The effect of a group of obstacles on flow and dispersion over a surface

Neil Jerram
King's College

September 25, 1995

A dissertation submitted for the degree of Doctor of Philosophy
in the University of Cambridge

The effect of a group of obstacles on flow and dispersion over a surface

Neil Jerram

In this thesis we develop analytical models for boundary layer flow through a two-dimensional group of obstacles, based on the "distributed force" model. An array of obstacles is represented as a region without solid obstructions but with distributed body forces resisting the flow. Linear analyses are presented of inviscid, laminar (or constant eddy viscosity) and turbulent flow through such force distributions. For any group of obstacles, we show how to calculate the model force distribution which becomes the input for the linear analyses. The entire procedure can be iterated to take account of non-linear upstream sheltering effects. In general the model distributed force integrates to equal the actual force exerted by obstacles on the flow divided by the fraction of the array volume not occupied by solid obstacles.

Turbulent stresses are modelled using a mixing length that is uniform up to a specified height and increases linearly above. Our physical arguments for a *displaced* mixing length above the obstacles provide an explanation for the observed coincidence between displacement height and the level of mean momentum absorption. Comparisons of the turbulent analysis results with numerical simulations and experimental data show very encouraging agreement and so support both the distributed force model and the assumptions of the mathematical analysis.

From the results of the turbulent flow analysis, effective roughness and displacement heights can be *calculated* for the flow above the obstacles. When the displacement of the turbulent mixing length is correctly taken into account, the calculated parameters are comparable with those obtained experimentally.

An analysis of plume dispersion through a group of obstacles shows how the flow field results can be applied to practical situations, and highlights the dominant effect of enhanced perturbation shear stress, especially in the obstacle rooftop layer, on changes to the downstream evolution of the plume.

Acknowledgements

To lose one supervisor may be regarded as a misfortune;
to lose both looks like carelessness.
— after Oscar Wilde

Over the past four years my two supervisors, Stephen Belcher and Julian Hunt, have guided and encouraged me, cajoled and implored me, and provided just the right mix of teaching, day-to-day help and inspiration. Four years ago Julian suggested the subject of this dissertation, and I feel very fortunate to have been given such a coherent and fruitful problem to work on. In the last few months, Stephen's and Julian's careful comments on my writing have considerably improved the final result. For their committed supervision, sustained throughout the duration of my research, I am enormously grateful to them both.

I trust that supervising me was not the reason why Stephen and Julian left Cambridge. In their absence Paul Linden adopted me as a member of his research group, and has ever since been a valuable source of willing advice on both administrative and research matters. I am very grateful to Paul for being so helpful and accessible.

I would like to thank Jenny Cohen for interesting discussions on the asymptotic analysis of chapter 3, and all the members of Julian Hunt's and Paul Linden's research groups for providing a friendly and helpful environment in which to work.

The staff of the Department of Applied Mathematics and Theoretical Physics have given me a lot of assistance over the years. Among them I would particularly like to thank Jon Peatfield, for sorting out so many of my computer problems, and David Cheesley and David Lipman, for their help and advice in setting up a field experiment.

Finally I would like to acknowledge the continual encouragement, support and scientific interest of my wife, Marisha Ray, and of our combined families.

The work of this dissertation was funded by the U.K. Ministry of Defence. This dissertation is the result of my own work and includes nothing which is the outcome of work done in collaboration.

Neil Ferrar

September 1995

Contents

Chapter 1

Modelling a group of obstacles as a distributed resistance

1.1 The problem

Perturbed turbulent boundary layers have been a subject of mathematical and experimental research for at least four decades. Driving this research is an abundance of practical applications in engineering and environmental flows that may be summarised by the question, "What are the effects of surface obstructions and surface curvature on flow and dispersion in a turbulent boundary layer?" Despite the considerable variety of such applications, two rather general mathematical ideas seem to be useful in most situations.

1. The disturbed flow can often be divided into regions where different physical processes dominate, particularly as regards the role of turbulent stresses. Witness the "internal boundary layer" of classical theories (*e.g.* Elliot 1958, Garratt 1990) and the inner/outer/wake regions of asymptotic theories (*e.g.* Counihan *et al.* 1974, Sykes 1980).

2. Far enough away from the source of the disturbance it should be possible to parameterise the flow in some universal way. Any surface obstructions or topo-

logical variation, when viewed at a large enough length scale, just make the surface appear rough; hence a natural parameterisation is in terms of an effective roughness height, displacement height and friction velocity as for turbulent flow over a rough surface.

The problem, that this thesis addresses, is that most attempts to model a set of obstructions in a turbulent boundary layer jump straight to the parameterisation. Rules of thumb and empirical values are used to estimate appropriate roughness parameters for a given distribution of obstructions (*e.g.* Kung's formula in Hsi & Nath 1970, table 6.2 in Panofsky & Dutton 1984). Then the problem of modelling flow in a region where the distribution of obstructions changes is usually recast as an investigation of flow over a change of roughness, even though there is no evidence that the roughness parameterisation is applicable in such a region.

For example, forests and large urban areas can modify the wind both within and *above* themselves sufficiently to affect prediction of the local micro-meteorology. For weather prediction purposes such effects have traditionally been modelled by representing the forest or urban area as a patch on the ground of increased roughness (*e.g.* André & Blondin 1986). It is generally believed that this is a reasonable model as long as the model roughness does not vary too rapidly in the direction of the wind, but the formalism gives no indication of what "too rapidly" actually means, neither does it attempt to describe the flow in regions where the roughness variation *is* too rapid. Anthropocentrically speaking this is unfortunate, since regions of rapid "roughness change" tend to exist next to high densities of human population, *e.g.* near transitions between relatively smooth countryside and significantly rougher urban areas.

Hence three key difficulties beset direct use of the roughness parameterisation for flow above a group of obstacles.

1. There is no reliable method for calculating roughness parameters.

2. There is no evidence that the parameterisation is valid where the distribution of obstacles is changing.

3. The parameterisation only describes the flow, when at all, well above the group of obstacles. What happens within the group?

The first of these difficulties is exacerbated by confusion over what the roughness parameters mean physically.

Thom (1971) discovered experimentally that the displacement height of the velocity profile above an artificial crop of roughness elements coincided remarkably closely with the height at which the drag force on the roughness elements appears to act (*i.e.* the height about which the force profile upon a roughness element has no moment). Jackson (1981) showed that the existence of some significant reference height d within the roughness element canopy is implicit in the usual derivation of the logarithmic velocity profile. Following Thom's experimental result, Jackson took d to be the height at which the canopy drag appears to act, and then demonstrated that d was also related to the displacement thickness of the total shear stress (which includes, for a periodic array of roughness elements, the "wave stress" $\langle \rho uw \rangle$, u and w being the streamwise and vertical mean velocities.). Given a non-zero displacement height d (relative to the surface on which roughness elements are mounted), Thom and Jackson both suggested that the roughness height z_o observed in the flow above was more likely to be related to the distance $h - d$ between the displacement height and the top of the roughness elements than to the height h itself; hence they explained some of the considerable scatter in experimental values of z_o/h.

These arguments are plausible, but neither Thom nor Jackson offered any physical picture to underlie this definition of d and the $h - d$ dependence of z_o.

A solution to all three difficulties described above is to construct a theory that describes a group of obstacles at a more basic level than the roughness parameterisation. Such a theory should aim to describe the flow field around the group of obstacles, amongst the obstacles as well as above them. Variation of the flow field above the obstacles could then be used to determine whether a roughness parameterisation is

applicable and, where applicable, to predict the roughness parameters.

Some progress in a parallel problem, that of boundary layer flow over complex terrain, has been made by Wood & Mason (1993), who used the detailed flow field results of Belcher *et al.* (1993) to derive an effective roughness height for turbulent flow over low hills. Their results relate the predicted roughness height to the form drag acting on the hills and to a scale height h_m that depends upon hill geometry and boundary layer depth. If an effective roughness height can be similarly derived for flow above a group of obstacles, it will be interesting to see whether the form of our predictions resembles that of Wood & Mason's results.

1.2 Motivating applications

Before beginning the construction of such a theory, we consider two particular applications that strongly motivate the present investigation of turbulent flow through groups of obstacles: the description of wind flow and scalar fluxes within forest canopies and the modelling of pollution dispersion within urban areas.

1.2.1 Wind flow and scalar fluxes within forest canopies

Many aspects of forestry research would be enhanced by better understanding of the wind field within the forest canopy. Plantations of Sitka spruce in Europe are regularly harvested well before the trees reach their optimum height and the wood attains its best quality, because experience has shown that plantations above a critical height are susceptible to extensive wind damage (Stacey *et al.* 1994); such damage results when the bending moments at the base of trees become large enough to uproot them. A good model of the forest canopy flow could predict these bending moments and therefore explain why wind damage is so prevalent above a certain tree height. Stacey *et al.* also consider the effects of a clearing within a forest, demonstrating that trees around a clearing are far more susceptible to damage than those in the bulk of the forest. This is of obvious importance for deforestation policy in many countries and

deserves to be better understood.

Forests are also important as diurnal sources or sinks of oxygen, carbon dioxide and water vapour. As a result of their high heat capacity, forests tend to stabilise the temperature variations of their local environment, and forest air can have a cathartic effect on the otherwise polluted environment of a built-up area nearby. Such effects have been considered by Gross (1987, 1988) in investigations of the consequences of deforestation.

1.2.2 Modelling pollution dispersion within urban areas

With 90% of the UK population designated as living in urban areas (Phillips World Atlas 1993), urban pollution is increasingly a subject of debate. Everyday sources of pollution are widely distributed around a city: car exhausts and industrial or domestic chimneys are primary sources of pollution and processes like the catalysis of ozone production by ultraviolet light can lead to sources of new pollutants at some distance from the origin of the reagent chemicals. More localised pollution may arrive in plumes or clouds from sources outside the city: accidental release of toxic or radioactive material as in the cases of Bhopal and Chernobyl, or deliberate release of nerve poisons in the eventuality of chemical warfare. In all cases the problem is to understand how the dispersion of such pollutants by the wind is modified by the presence of a large group of obstacles. The dispersion of pollutants in a turbulent flow over unobstructed level terrain is now reasonably well understood, but as yet there has been little work, either theoretical or experimental, on the effects on dispersion of a group of obstacles. Notable exceptions are the set of experiments by Davidson *et al.* (1995a,b) and the theoretical work of Fung & Hunt (1991).

Furthermore, such a theory may offer a better understanding of the processes surrounding a sudden change in roughness, as modelled in numerous experiments, for example Bradley (1968), Antonia & Luxton (1971) and Counihan (1971).

1.3 Previous work on plant and urban canopies

Early experiments on flow through crops were performed by Plate & Quraishi (1965), who used flexible plastic strips to represent the crop, and by Meroney (1968) and Hsi & Nath (1970), using metal and brush model trees to constitute a forest. Many other early experiments are reported in these papers. More recent experiments in the field (so to speak) have been performed by Amiro & Davis (1988) and Gardiner (1994), both in spruce forest, and by Rotach (1993) in the centre of Zürich. Model plant or forest canopies have been investigated in the wind tunnel by Thom (1971), Raupach *et al.* (1980), Raupach *et al.* (1986) and Stacey *et al.* (1994).

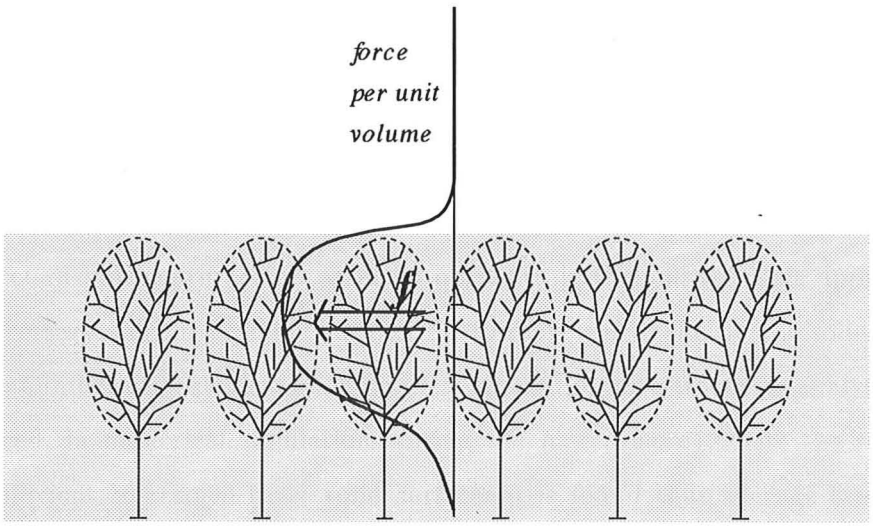

Figure 1.1: Using a distributed force profile to model a forest model.

Cionco (1965) used a distributed force to model the resistive effects of canopy elements in a one-dimensional model of the velocity profile within a forest (figure 1.1). Any attempt to represent exactly the branches and leaves of each tree, as solid surfaces within the flow field, would be wildly impractical, so instead Cionco modelled the trees by their most significant physical effect: drag on the mean flow. In his model the distributed force is proportional to the square of the local velocity, and the turbulent

shear stress is related via a mixing length model to the vertical gradient of total streamwise velocity. Because the flow is homogeneous in the streamwise direction, the distributed force is balanced not by mean flow deceleration but by the turbulent stress gradient, and this balance leads to the prediction of an exponential wind profile in the upper half of the canopy. Such exponential profiles were characterised by an "attenuation index" a which describes the decay of streamwise velocity moving down from the crown of a forest into its interior. Cionco (1972) collated the data from several experiments on (real or model) cereal crops and orchards and classified them according to their observed value of a, finding that low a-values are found in sparse arrays of rigid obstacles while high a-values are found in dense arrays of flexible obstacles. Smith *et al.* (1972) used this exponential wind profile to demonstrate the possibility of mean wind direction shear in forests with a relatively open understorey, and supported their theory with measurements from Thetford Forest.

Following Cionco (1965), essentially all modelling work since then has used a distributed force in the streamwise momentum equation to model obstacles, since the main effect of both natural and artificial obstacles is their drag. This approach remains necessary since it remains impractical to represent explicitly the solid surfaces of a large number of obstacles in a numerical simulation or a tractable analytical theory. Indeed, in numerical simulations (using the K–ϵ closure) where the resolution is just sufficient to resolve these solid surfaces it is found that average flow predictions are worse than those obtained from a distributed force model because the strong shear layers near obstacle surfaces are not adequately resolved (Savill & Solberg 1994). These shear layers produce a lot of turbulent kinetic energy, which distributed resistance models using K–ϵ or higher order turbulence closures can model by adding a production term to the turbulent kinetic energy equation in parallel with the drag term in the momentum equation (*e.g.* Svensson & Häggkvist 1990).

Numerical simulations of canopy flow using a distributed force representation have been carried out by Yamada (1982) and Hiraoka (1993), using second-order turbulence closures, Shaw & Schumann (1992) and Kanda & Hino (1994), using large eddy sim-

ulations, and Svensson & Häggkvist (1990), using a K–ϵ turbulence closure.

The distributed force approach was formalised somewhat by Raupach & Shaw (1982), who showed that force-like terms in the momentum equation emerge naturally from a spatial averaging operation over a limited horizontal area. Specifically, the force term is the difference between the gradient of horizontally averaged pressure and the horizontally averaged pressure gradient, plus similar but less significant differences arising from turbulent stress variations. The formalisation is not exact to the extent that the horizontal averaging operation is not idempotent, but it does indicate in principle how the model distributed force should be related to the actual drag upon the obstacles.

In recent years attention has focused more on aspects of canopy flow that cannot be predicted using gradient-transfer models of the turbulence. Wilson & Shaw (1977) first proposed the use of a second-order turbulence closure for canopy flow and demonstrated that such a model could account for the weak secondary maxima of mean velocity sometimes observed in forest canopies near the ground. Quadrant analysis of the turbulent velocities measured in experiments and numerical simulations (*e.g.* Raupach *et al.* 1986, Gao *et al.* 1989) has shown that turbulent transfer in canopies is dominated by strong intermittent sweep and ejection events.

Does such particular turbulent behaviour rule out the use of simple turbulence models in predicting the broad features of canopy flow? Perhaps surprisingly, it appears not. Westbury & Morrison (1994) have recently shown that momentum transfer in unobstructed turbulent boundary layers is also dominated by such strong intermittent events, yet it is well known (*e.g.* Tennekes & Lumley 1972, chapter 5) that the mean flow in turbulent boundary layers is well described by classical mixing length theory. The view that simple turbulence models remain useful will be supported by the good agreement between experimental data and the predictions of this thesis.

The literature on dispersion is relatively sparse compared with that on the flow field. Many of the physical mechanisms involved in dispersion of pollution around buildings were discussed by Puttock (1976) and Hunt (1982) and one process in

particular—wake diffusion—was analysed in detail by Puttock & Hunt (1979). The UK-ADMS model described by Carruthers *et al.* (1994) models dispersion around a single building by dividing the neighbourhood of the building into distinct regions: near wake, external flow, etc.; this model is not yet able to consider a large number of such obstacles. Theurer & Plate (1994) describe a semi-empirical model for dispersion from a point source in an urban area: the near field, where individual buildings are important, gives way to the far field, where buildings act more like roughness, at some characteristic "radius of homogenisation"; flow field information for this model is to be determined from a wind tunnel study.

Field and wind tunnel experiments on dispersion through an array of obstacles were performed at three different scales (1:20:200) by Davidson *et al.* (1995a,b); the key dispersive process observed in these experiments have been discussed by Jerram *et al.* (1994). Meroney (1968) measured the dispersion of a helium plume through his model forest canopy. Coppin *et al.* (1986) and Legg *et al.* (1986) measured the dispersion of heat from both line and plane sources in their model plant canopy experiments, and a theory for predicting dispersion from plane sources is given by Raupach (1989), the main point of which is the distinction between near field dispersion, where dispersing particles tend to move in straight lines, and far field dispersion, which is better modelled as a Fickian process.

1.4 Aims of this thesis

The existing literature may be summarised as follows. There is a substantial body of experimental data on canopy flows, ranging from "roughness change" experiments through model plant canopies in boundary layer tunnels to full scale field experiments in forests and city centres. In modelling, the concept of a distributed resistance is well established and supported theoretically by the averaging procedure of Raupach & Shaw (1982). Numerical experiments using a distributed resistance have been successful in one, two and three dimensions. Analytical treatments of distributed resistance in turbulent flow, however, have never ventured beyond one dimension.

Therefore the principal objective of this thesis is to develop the theory of two-dimensional turbulent flow through a region of distributed resistance. Drawing upon thoroughly tested asymptotic methods developed by Jackson & Hunt (1975), Sykes (1980) and Hunt *et al.* (1988a) for turbulent flow over low hills, the core analysis of chapter 3 calculates the flow field perturbations caused by a distributed force in a turbulent boundary layer. The results of this theory, interpreted as spatially averaged quantities applicable to urban and forest canopies, are tested against experimental data and numerical simulations in chapter 4. Then the parameterisations of chapter 5 show how the results of the analytical theory can be used to express the flow above an obstacle canopy in terms of effective roughness parameters, and relate appropriate roughness parameters to the underlying force distribution.

Before starting the turbulent analysis, however, it is instructive and well rewarded to consider inviscid and laminar viscous flows through a distributed force (chapter 2). Firstly, because the study of inviscid flow gives a sharper picture of the physical effects of distributed force, by stripping away turbulent processes that complicate the flow. Secondly, because there is in fact a close relation between the inviscid and turbulent flow solutions. Thirdly, because laminar viscous flow may be considered as turbulent flow with a constant eddy viscosity, and in some situations a constant eddy viscosity model may be more appropriate than the mixing length model used in the main turbulent flow analysis. The laminar analyses also throw up a counter-intuitive dependence of the overall flow structure on the form of the velocity profile that impinges upon the region of distributed force, which carries over into turbulent flow and has important consequences for dispersion. The inviscid analysis complements previous work by Taylor (1944), Lighthill (1957) and Newley *et al.* (1991).

In many practical situations it is the dispersion of some pollutant that is of overriding importance and not the flow field, albeit that the former is primarily determined by the latter. Therefore chapter 6 considers the processes that contribute to real dispersion and the difficulties involved in trying to model them. Following the work of Weng (1990) and Hunt *et al.* (1988c) a Fickian dispersion model is presented that

calculates the changes in scalar concentration distributions due to the addition of a distributed force to an originally unobstructed flow. The analysis is illustrated by sample results showing the perturbations to a Gaussian plume of contaminant passing through an array of obstacles.

1.5 Definition of the model problem

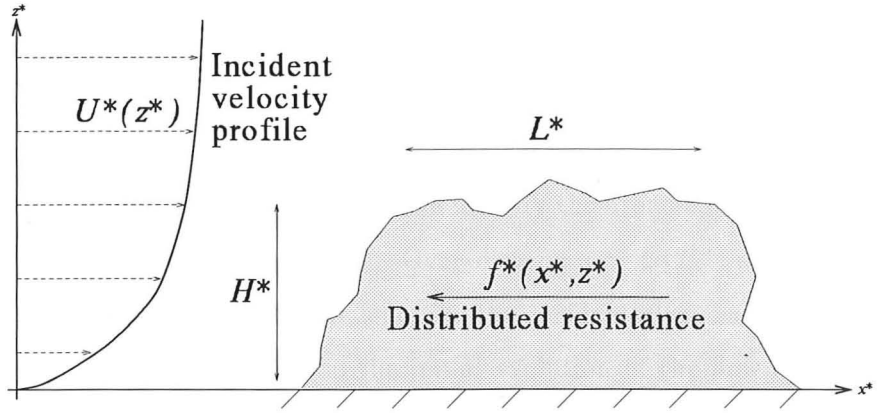

Figure 1.2: Illustration of the general problem: boundary layer flow through a region of distributed resistance.

The general arrangement of the flow to be studied is illustrated in figure 1.2. The region within which any body forces act is characterised by overall length scales L^* and H^* and sits in a boundary layer described by the incident velocity profile $U^*(z^*)$. It is understood that the boundary layer in the absence of any force distribution does not develop significantly over streamwise length scales of order L^*. The precise definitions of L^* and H^* are not critical for the analyses that follow. The general problem is to calculate the perturbations to the incident velocity field $(U^*(z^*), 0)$ that arise as a result of the distributed body force.

Building upon the ideas of Townsend (1965) for flow over a step roughness change and the recent field experiments of Davidson *et al.* (1995a) (where the observer could

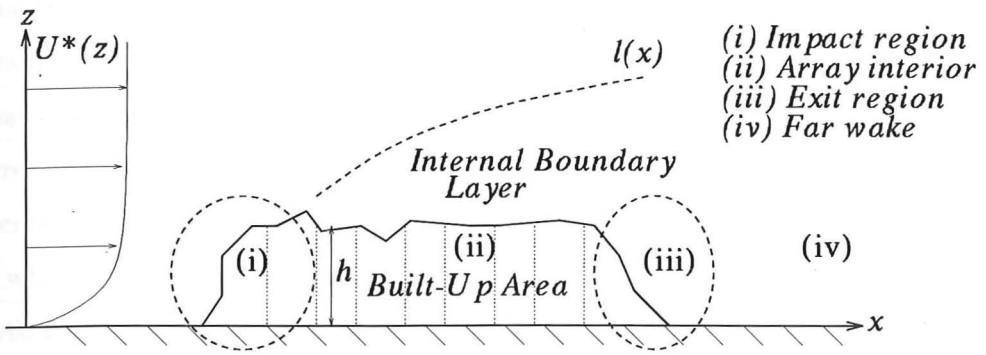

Figure 1.3: Regions of the flow where different physical processes dominate: (i) impact region (ii) array interior (iii) near wake (iv) far wake.

walk around among the obstacles!), one can identify the broad features of flow through such a force distribution (figure 1.3). Over distances of $O(H^*)$ around the leading edge of the distribution, the turbulence in the incident flow has not had time to adjust to the sudden resistance, so the initial evolution of the flow is quasi-inviscid, *i.e.* dominated by inertial rather than turbulent stress effects. Hence the mean flow around the leading edge decelerates rapidly in proportion to the force acting upon it. Further downstream turbulent stresses become significant, while inertial effects are reduced since the flow as a whole has decelerated: hence the dominant balance within the interior of the distribution is between the turbulent stress gradient and the distributed force, as modelled in the one-dimensional treatment of Cionco (1965). The deceleration of the mean flow lessens and finally vanishes as an increasing proportion of the distributed force is balanced by turbulent stress gradients. Hence in a long enough obstacle canopy the mean flow attains an equilibrium state within the array interior, in which the velocity defect no longer increases with distance downstream. Around the trailing edge, the sudden disappearance of any resistance gives rise to a second period of quasi-inviscid evolution, in this case acceleration. Turbulent stress gradients become dominant again in the far wake. Above the force distribution an internal boundary layer (IBL) develops. (This IBL is similar to that found after a step

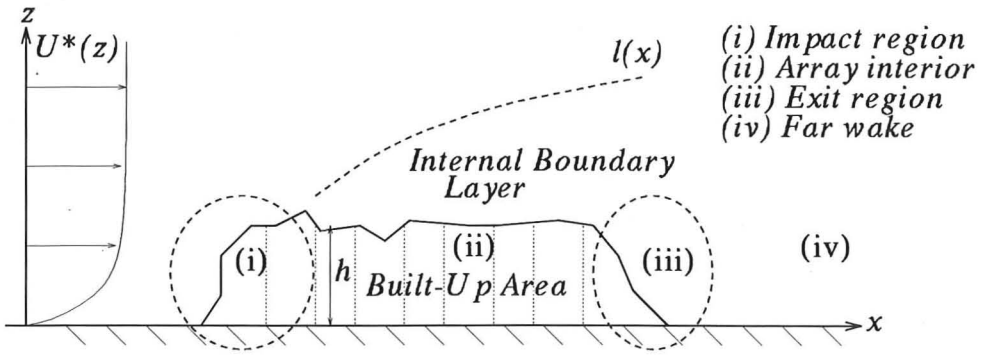

Figure 1.3: Regions of the flow where different physical processes dominate: (i) impact region (ii) array interior (iii) near wake (iv) far wake.

walk around among the obstacles!), one can identify the broad features of flow through such a force distribution (figure 1.3). Over distances of $O(H^*)$ around the leading edge of the distribution, the turbulence in the incident flow has not had time to adjust to the sudden resistance, so the initial evolution of the flow is quasi-inviscid, *i.e.* dominated by inertial rather than turbulent stress effects. Hence the mean flow around the leading edge decelerates rapidly in proportion to the force acting upon it. Further downstream turbulent stresses become significant, while inertial effects are reduced since the flow as a whole has decelerated: hence the dominant balance within the interior of the distribution is between the turbulent stress gradient and the distributed force, as modelled in the one-dimensional treatment of Cionco (1965). The deceleration of the mean flow lessens and finally vanishes as an increasing proportion of the distributed force is balanced by turbulent stress gradients. Hence in a long enough obstacle canopy the mean flow attains an equilibrium state within the array interior, in which the velocity defect no longer increases with distance downstream. Around the trailing edge, the sudden disappearance of any resistance gives rise to a second period of quasi-inviscid evolution, in this case acceleration. Turbulent stress gradients become dominant again in the far wake. Above the force distribution an internal boundary layer (IBL) develops. (This IBL is similar to that found after a step

change in roughness.) Momentum from the flow above is drawn down by turbulent stress gradients to balance obstacle drag near the ground.

In many practical situations the force acting at some point within the distribution is an increasing function of the local wind speed. Hence the strength of the distributed force decreases as the mean flow decelerates and the flow approaches an equilibrium state in which streamwise velocity gradients vanish. This tendency to equilibrium is clearly visible in the results of Meroney's (1968) experiment. It also follows that the force acting on the flow near the trailing edge of the distribution is much less than at the leading edge.

In order to describe how the force f^* should be calculated for a given set of obstacles and to understand how the results of a distributed force analysis are related to actual wind velocities, it is necessary to consider the spatial averaging operation $\mathcal{A}$ discussed by Raupach & Shaw (1982). The interesting point is that the horizontal average $\mathcal{A}\{\phi\}$ of a quantity ϕ could be defined in two ways:

$$\text{either} \qquad \mathcal{A}_1\{\phi\}(\mathbf{x}) \equiv \frac{\iint_{\text{fluid}} \phi(\mathbf{x}')A(\mathbf{x}'-\mathbf{x})\,d\mathbf{x}'}{\iint_{\text{fluid}} A(\mathbf{x}'-\mathbf{x})\,d\mathbf{x}'} \tag{1.1}$$

$$\text{or} \qquad \mathcal{A}_2\{\phi\}(\mathbf{x}) \equiv \frac{\iint_{\text{fluid}} \phi(\mathbf{x}')A(\mathbf{x}'-\mathbf{x})\,d\mathbf{x}'}{\iint_{\text{all space}} A(\mathbf{x}'-\mathbf{x})\,d\mathbf{x}'}. \tag{1.2}$$

Here $A(\mathbf{x})$ is some distribution about the origin that specifies the averaging operation precisely, for example

$$A(x,y,z) = e^{-(x^2+y^2)/L_A^2}\delta(z). \tag{1.3}$$

Now $\mathcal{A}_1$ is the more intuitive definition of a spatial average, since it has the property that $\mathcal{A}_1\{1\} = 1$, *i.e.* that the average value of a constant quantity is equal to the constant value. Whereas $\mathcal{A}_2\{1\}(\mathbf{x}) = \beta(\mathbf{x})$, where $\beta(\mathbf{x})$ is the fraction of the area around $\mathbf{x}$ not occupied by obstacles (weighted by the distribution A). However, $\mathcal{A}_2$ is much more convenient to differentiate than $\mathcal{A}_1$ since the denominator of (1.2) is constant, and therefore the horizontal averaging formalism uses $\mathcal{A}_2$ as its definition

rather than $\mathcal{A}_1$. The fact that careless use of $\mathcal{A}_1$ leads to incorrect answers is well known in the literature on multiphase flow—see for example Kowe *et al.* (1988).

Raupach & Shaw (1982) describe in detail how $\mathcal{A}_2$ is applied to the Navier Stokes equations to give a new set of equations for the horizontally averaged flow quantities, but they assume the obstacle array to be sufficiently sparse that departures of $\beta(\mathbf{x})$ from unity may be neglected (and hence the distinction between $\mathcal{A}_1$ and $\mathcal{A}_2$ does not arise). When $\beta(\mathbf{x})$ is included in the analysis it is found that the force term in the resulting momentum equation is enhanced by the factor β^{-1}. In other words, the distributed force per unit volume used to model an obstacle should integrate over the region surrounding that obstacle to give the actual force upon the obstacle divided by β.

Now consider an array of N obstacles each with frontal area A_f, height h and drag coefficient C_d, distributed over a total ground area A_t. Then the total force acting is $\frac{1}{2}\rho U_o^2 N C_d A_f$, where U_o is the characteristic velocity of the wind hitting the obstacles, and the volume over which this force acts is hA_t. Hence the distributed force that should be used to model this array is given by

$$f^* = \frac{1}{2}\rho U_o^2 \frac{N C_d A_f}{\beta h A_t} = \frac{1}{2}\rho U_o^2 \frac{a C_d}{\beta} = \frac{1}{2}\rho U_o^2 D^*. \tag{1.4}$$

$a \equiv N A_f / h A_t$ is known in the literature on forests and plant canopies as the leaf area index (LAI). $D^* \equiv a C_d / \beta$ will be called the "drag parameter" (with dimensions L^{-1}): it encapsulates all the geometrical and dynamical information about a canopy that is known *a priori*. Values of D^* may be reduced by sheltering effects (*e.g.* Thom 1971) if, for example, some obstacles are positioned so closely behind others that their exposure to the spatially averaged wind speed is reduced. Since most force distributions are a function of wind speed in the way suggested by (1.4), and the deceleration of the mean flow within the canopy is not known *a priori*, it is usually more appropriate to specify a distribution a drag parameter D^* rather than of force f^*

D^* is not required to be uniform over an entire canopy. Where systematic trends in obstacle density, size or wind resistance occur it is reasonable to expect horizontal variations in the drag parameter. It would not however be consistent for D^* to vary on

length scales smaller than the size L_A of the averaging operation $\mathcal{A}_2$, tempting though it may be to try to represent individual obstacles by strongly localised distributions of D^*. Note that there is no similar restriction on the vertical variation of D^* or f^*, since spatial averaging operates only in the horizontal plane.

With suitably defined distributions of force f^* or drag parameter D^*, the distributed force model is in principle capable of predicting the large scale mean flow changes that are observed in real flow through groups of obstacles. The partial blocking of flow approaching an array, causing flow over or (in three dimensions) around the obstacles, the mean deceleration of the wind within the array and the growth of an internal boundary layer above the obstacles are all significant effects that should be accurately captured by the concept of distributed resistance.

Chapter 2

Inviscid and laminar flow through a distributed force

2.1 Introduction

Taylor (1944) investigated the perturbations to a uniform flow due to a thin porous plate placed perpendicular to the stream. The plate in his analysis is represented as a uniform distribution of centres of resistance. By noting that the perturbed flow outside the wake of each centre of resistance is equivalent to the outflow from a source, it is possible to calculate the lateral deflection of streamlines approaching the plate and the overall drag coefficient in terms of the pressure drop across the plate. Thus Taylor exploited the important relationship between point forces and point sources in inviscid flow: the velocity perturbations due to these two types of disturbance are identical except for an additional, constant velocity defect in the wake of the point force.

The relationship is important because it enables us to translate any results obtained for a point source so as to apply to a point force. Specifically, if (u^*, v^*, w^*) are the velocity perturbations due to a point source at the origin of strength m^* (with dimensions T^{-1}), then the equivalent point force has strength $f^* \equiv \rho U^* m^*$, directed against the incident velocity at the origin U^*, and the corresponding velocity pertur-

bations are $(u^* - m^* H(x^*)\delta(y^*)\delta(z^*), v^*, w^*)$, where H and δ are the Heaviside and Dirac delta functions respectively.

Lighthill (1957) analysed the three-dimensional disturbances to a parallel shear flow that are caused by just such a point source; his results may therefore be translated so as to apply to a point force in the way just described. In order to avoid the "critical layer" analysis required around singularities in the governing equations, he limited his analysis to unbounded shear flows in which the incident velocity is nowhere zero. For general shear flow the governing equations cannot be solved exactly, so Lighthill sought to illustrate the form of the point source Green's function in such a flow by calculating aspects of it in three particular approximations: (i) for large horizontal wavenumber k, which he showed determined the Green's function near the point source; (ii) for small horizontal wavenumber k, which determines the Green's function far from the point source; (iii) for general k in shear flows where the total variation of incident velocity $\Delta U/U_{\max}$ is small.

The work of this chapter differs from and complements Lighthill's analysis in two ways. Firstly, we are here interested in finite regions of resistance rather than in isolated point forces. Secondly, these regions of resistance lie close to rigid surfaces where it is reasonable to expect the incident velocity to vanish. Therefore this chapter considers several special cases in which exact integrated solutions can be found for inviscid or laminar viscous flow through finite regions of resistance. Hence the results of Lighthill's analysis are not used directly, but there are several points of contact where the earlier work throws light upon the current study.

The special cases considered all fix the form of the incident velocity profile near the ground $U(z)$. In inviscid flow the difficulties of critical layer analysis can be avoided altogether if the incident vorticity gradient U''/U vanishes identically, so it is natural to consider constant shear flows in which this is the case. Two particular examples and a general far field analysis of such flows are presented in §§2.3–2.6.

As expected following Taylor's relationship between distributed forces and distributed sources, the general analysis shows that in most cases the far field pertur-

bations have the structure of outflow from a source whose strength is related to the integral of all the force acting. Perhaps surprisingly, however, the analysis shows that the strength of the far field source is also proportional to the incident velocity at the ground $U(0)$. Consequently, for a linear velocity profile with $U(0) = 0$, the far field source actually vanishes completely, leaving a much weaker quadrupolar structure in its place. §2.7 demonstrates that this unexpected result remains valid when the incident velocity profile $U(z)$ departs from a linear form above the top of the distributed force.

The significant differences between a source-dominated and a quadrupole-dominated flow structure affect the character of the flow within the region of resistance as well as in the far field (see §2.5). Furthermore, since the main results of inviscid analysis carry over into a real turbulent flow, such differences in flow structure would have important implications for scalar dispersion. Therefore it seems worthwhile to investigate the phenomenon further. A second class of incident shear flows, $U = (y/H)^{\alpha}$ with $0 < \alpha < 1$, is considered in §2.8, with the result that the source-like structure dominates for $\alpha < \frac{1}{2}$ but vanishes for $\alpha > \frac{1}{2}$.

An inviscid analysis similar to that of this chapter was performed by Newley *et al.* (1991) in an investigation of obstacles in a strongly stratified, rotating, uniform flow. Strong stratification, however, calls for a radiation boundary condition at the upper edge of the flow and the strongly stratified equations give internal wave solutions as $z \to \infty$, whereas the current analysis is intended for neutral stratification and so gives rise to exponentially decaying solutions aloft. A second significant difference between the two analyses is that Newley *et al.* were interested primarily in the region near the top of a top of a distributed resistance (modelling a group of hills) where vertical inertia forces are strong enough to overcome the stratification, whereas here we solve for the complete flow field and are particularly interested in the overall structure.

Shibata & Mei (1990) calculated the far-field perturbations due to a localised force distribution near a wall in a low Reynolds number shear flow as part of a model for sand particle interactions, retaining in their analysis the laminar viscous terms

while neglecting inertial acceleration terms. For the special case in which the incident velocity is uniform, it is possible to generalise this calculation by retaining the inertial terms in a linearised form. This generalised analysis of uniform laminar viscous flow through a distributed force is given in §2.9.

The dominant theme of this chapter is the dependence of predicted flow structure on the form of the incident velocity profile, demonstrated both for the constant shear flow analysis of §§2.5–2.6 and for the power law analysis of §2.8. Although the mathematical origins of this dependence are clear, a simple physical explanation is elusive. New light, however, is cast upon the phenomenon by a discussion in §2.10 of symmetry in the inviscid flow problem. By applying two symmetry operations to the flow system, the source-like flow structure can be understood as the product of an incident velocity discontinuity or region of strong shear in an unbounded flow, while the quadrupolar flow structure emerges naturally whenever discontinuities and strong shear are absent. The discussion concludes with some important implications for modelling the turbulent flow problem.

2.2 Governing equations for laminar flow

Our starting point is the steady incompressible Navier Stokes equation with a distributed force field $\mathbf{f}^*$ (force per unit volume):

$$\rho\hat{\mathbf{u}}^* \cdot \nabla\hat{\mathbf{u}}^* = -\nabla\hat{p}^* + \mu\nabla^2\hat{\mathbf{u}}^* - \mathbf{f}^*.$$

Following Taylor (1944), we separate the velocity $\hat{\mathbf{u}}^*$ into two parts: the incident velocity profile $\mathbf{i}U^*(z)$ and the velocity perturbations caused by the force distribution. The variables are non-dimensionalised as follows:

$$\mathbf{x}^* = L^*\mathbf{x}, \quad \hat{\mathbf{u}}^* = U_o^*(\mathbf{i}U(z) + \mathbf{u}(\mathbf{x})), \quad p^* = \rho U_o^{*2}p, \quad \mathbf{f}^* = \rho U_o^{*2}\mathbf{f}/L^*.$$

The non-dimensionalised force may be written as $f = L^*/L_f^*$, where $L_f^* \equiv \rho U_o^{*2}/f^*$ is a length scale characterising the strength of the force distribution. In the absence of pressure and frictional forces, L_f^* would be the distance over which a constant force f^*

would have to act in order to rob a fluid particle of its incident momentum ρU_o^*. Thus the non-dimensional force f would be a measure of how many times a fluid particle loses its momentum in traversing the force distribution. In real flows, however, this interpretation is made approximate firstly by the usual dependence of f^* on the local fluid velocity, secondly by turbulent stress gradients, which can balance a large fraction of the applied force f^* in place of inertia forces, and thirdly by pressure effects.

Assume now that $|\mathbf{u}| \ll 1$, so then the governing equation may be linearised:

$$U\frac{\partial \mathbf{u}}{\partial x} + \mathbf{u}\cdot\nabla U\mathbf{i} = -\nabla p + \frac{\nu}{L^*U_o^*}\nabla^2\mathbf{u} - \mathbf{i}f. \tag{2.1}$$

It is convenient here to specify a streamwise-directed force $-\mathbf{i}f$, since in most cases of interest resistance acts against the local velocity $\tilde{\mathbf{u}}$ and in the linear approximation the latter lies close to the incident velocity direction $\mathbf{i}$. Pressure is eliminated and the physics of the flow revealed by taking the curl of (2.1):

$$U\frac{\partial \omega}{\partial x} - U'\left(\mathbf{i}\frac{\partial v}{\partial x} + \mathbf{j}\frac{\partial v}{\partial z} + \mathbf{k}\frac{\partial w}{\partial z}\right) + U''w\mathbf{j} = \frac{\nu}{L^*U_o^*}\nabla^2\omega - \nabla\times\mathbf{i}f, \tag{2.2}$$

where ω is the vorticity. Physically, this is

$$\frac{D\omega}{Dt} - \{\text{vortex stretching}\} + U''w\mathbf{j} = \{\text{diffusion}\} - \{\text{rotational force gradients}\}.$$

Thus the essence of flow through a distributed force is that rotational force gradients act as sources of fluid vorticity. A fluid particle's vorticity may subsequently be modified by diffusion or by vortex stretching, as in any flow, but negative or positive vorticity is created, even in an initially irrotational, inviscid flow, by local gradients of the distributed force. The term $U''w\mathbf{j}$ here represents vertical transport of incident vorticity by the perturbation flow.

In two-dimensional, inviscid flows, the vorticity stretching and vorticity diffusion terms both disappear. Then the non-dimensional equations read

$$U\frac{\partial u}{\partial x} + w\frac{\partial U}{\partial z} = \frac{\partial p}{\partial x} - f; \tag{2.3}$$

$$U\frac{\partial w}{\partial x} = \frac{\partial p}{\partial z}; \tag{2.4}$$

$$\frac{\partial u}{\partial x} + \frac{\partial w}{\partial z} = 0; \tag{2.5}$$

eliminating the pressure gives the following equation for w:

$$U\left(\frac{\partial^2 w}{\partial x^2}+\frac{\partial^2 w}{\partial z^2}\right)-w\frac{\partial^2 U}{\partial z^2}=\frac{\partial f}{\partial z}. \tag{2.6}$$

The vertical perturbation velocity $w(x,z)$ is completely determined by the functions $U(z)$ and $f(x,z)$ and by the boundary conditions that $w(x,0)=0$ and $w\to 0$ as $x\to-\infty$ and as $z\to\infty$. The horizontal perturbation velocity may then be obtained from the continuity equation together with the boundary condition that $u\to 0$ as $x\to-\infty$.

For a point force at the origin with strength F the right hand side of (2.6) is $F\delta(x)\delta'(z)$ and then (2.6) is equivalent to Lighthill's (1957, eq. 14) equation of motion for a point source if the source strength m is given by $F=mU(0)$. Lighthill's equation is derived for three-dimensional perturbations, whereas (2.6) was obtained in two dimensions only. Following Lighthill's derivation for a generally directed force distribution $\mathbf{f}$, we obtain the more general three-dimensional inviscid governing equation

$$U\left(\frac{\partial^2 w}{\partial x^2}+\frac{\partial^2 w}{\partial y^2}+\frac{\partial^2 w}{\partial z^2}\right)-w\frac{\partial^2 U}{\partial z^2}=\frac{\partial f_x}{\partial z}-\frac{\partial f_z}{\partial x}+\frac{\partial}{\partial y}\int_{-\infty}^{x}\frac{\partial f_y}{\partial z}-\frac{\partial f_z}{\partial y}\,dx', \tag{2.7}$$

of which (2.6) is a special case.

Note that the first derivative of U is absent from (2.6) and (2.7) by continuity. When the shear of the incident velocity profile is constant or has negligible variation within the domain of the force distribution, the second derivative term U'' disappears as well. In this case the general solution of (2.6) is

$$w(x,z)=\int_{-\infty}^{\infty}d\xi\int_{0}^{\infty}d\zeta\frac{G(x,y;\xi,\zeta)}{U(\zeta)}\frac{\partial f}{\partial\zeta}, \tag{2.8}$$

where $G(x,y;\xi,\zeta)$ is the two-dimensional Green's function

$$G(x,y;\xi,\zeta)=\frac{1}{4\pi}\ln\frac{(\xi-x)^2+(\zeta-z)^2}{(\xi-x)^2+(\zeta+z)^2},$$

and has been constructed so as to ensure that w vanishes on the ground $z=0$. The horizontal perturbation velocity u is obtained from (2.8) by continuity.

2.3 A constant force in uniform incident flow

In the simplest possible arrangement, in a uniform incident flow, consider a distributed force that is a constant F in the rectangular region defined by $-1 < x < 1$ and $0 < z < H$, where $H \equiv H^*/L^*$. Then $\partial f/\partial z$ is a δ-function at $z = H$ and, in this inviscid approximation, any constant shear in the velocity profile has no effect upon the velocity perturbation produced by the force. There is a multiplicative factor of $U(H)^{-1}$, but our choice of non-dimensionalisation, using the advective velocity scale $U_o^* \equiv U^*(H^*)$, makes this factor 1. The integral (2.8) then reduces to

$$\begin{aligned} \frac{w(x,z)}{F} &= \frac{-1}{4\pi}\int_{-1}^{1} \ln\frac{(\xi-x)^2+(H-z)^2}{(\xi-x)^2+(H+z)^2}\,d\xi \\ &= \frac{-1}{4\pi}\Big[h_2(x-1,z-H)-h_2(x+1,z-H) \\ &\qquad -h_2(x-1,z+H)+h_2(x+1,z+H)\Big], \end{aligned}$$

where F is the magnitude of the distributed force (defined to be *positive* when the force *resists* the flow) and

$$h_2(x,z) \equiv -x\ln(x^2+z^2) - 2z\tan^{-1}\frac{x}{z}.$$

The horizontal perturbation velocity is calculated via the continuity equation:

$$\frac{u(x,z)}{F} = \frac{1}{4\pi}\Big[h_1(x-1,z-H)-h_1(x+1,z-H) \\ -h_1(x-1,z+H)+h_1(x+1,z+H)\Big] - S(z-H),$$

where

$$h_1(x,z) \equiv z\ln(x^2+z^2) - 2x\tan^{-1}\frac{x}{z},$$

and the step function $S(z-H) = 1$ if $z < H$ and 0 otherwise; this term appears via the boundary condition that $u \to 0$ as $x \to -\infty$. The inverse tangents are defined to lie in the range $-\pi/2 \le \tan^{-1}\theta < \pi/2$. $h_1(x,z)$ and $h_2(x,z)$ may be expressed as the real and imaginary parts of a single function of the complex variable $s \equiv x + iz$:

$$h(s) \equiv h_1 + ih_2 = -2is\ln s - \pi s.$$

According to the convention chosen for the inverse tangent, this complex logarithm has a branch cut along the real axis $z = 0$. If we now define a complex parameter

$s_1 \equiv 1 + iH$ describing the extent of the force distribution, the perturbation velocity field may be written compactly as

$$\frac{u - iw}{F} = \frac{1}{4\pi}\left[h(s - s_1) - h(s - s_1^*) - h(s + s_1^*) + h(s + s_1)\right] - S(z - H). \tag{2.9}$$

Far from the force distribution, where $|s| \gg |s_1|$ and $z > H$ so that all four logarithm arguments lie on the same side of the branch cut, we can expand $\ln(s+\Delta s)$ in a Taylor series: $\ln(s + \Delta s) \approx \ln s + \Delta s/s - \frac{1}{2}(\Delta s/s)^2 + \ldots$. Then the far field velocities are

$$u - iv = \frac{2FH(x - iz)}{\pi(x^2 + z^2)} + O\left(\frac{s_1^3}{s^2}\right). \tag{2.10}$$

This agrees with Taylor (1944), since (2.10) is the perturbation flow field associated with a source near the origin. Integrating (2.10) around a large semicircle, we find that the total outflow from this source is $2FH$. Below the height H, in $z < H$, the horizontal perturbation velocity tends to 0 far upstream and $-2F$ in the wake far downstream. Thus the mass outflow from the source is balanced by a mass flux deficit of $2FH$ in the wake. The wake never decays because the mechanism for diffusion, namely viscosity, has been neglected in the current calculation.

At $z = H$, discontinuities in two of the logarithmic terms and in $S(z-H)$ combine to produce a jump in perturbation velocity u which increases linearly with distance from the leading edge of the force distribution, i.e. $\Delta u \propto x + 1$, until the trailing edge, after which the velocity jump remains constant. The same result can be obtained directly by considering the change in the horizontal component (2.3) of the governing equation across a discontinuity in the distributed force:

$$\frac{\partial}{\partial x}[u(H^+) - u(H^-)] = \frac{\partial \Delta u}{\partial x} = f(H^-) - f(H^+) = \begin{cases} F, & |x| < 1 \\ 0, & |x| > 1 \end{cases}$$

$$\Rightarrow \Delta u = \begin{cases} 0, & x < -1 \\ F(x+1), & -1 < x < 1 \\ 2F, & x > 1 \end{cases}$$

The vertical discontinuity in f cannot be matched by $\partial^2 p/\partial x \partial z$, as that would create infinite forces in the vertical momentum equation.

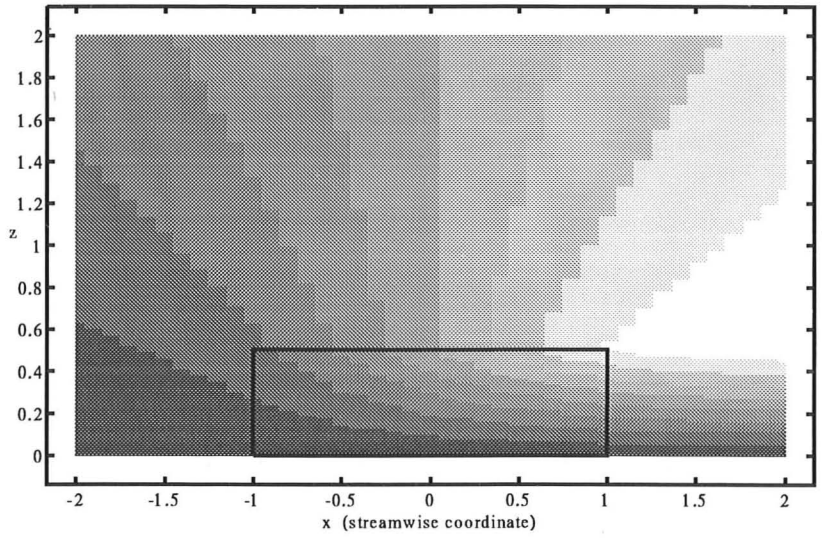

Figure 2.1: Constant force in uniform flow with $F = 0.45$ and $H = 0.5$. (a) Contours of the perturbation streamfunction.

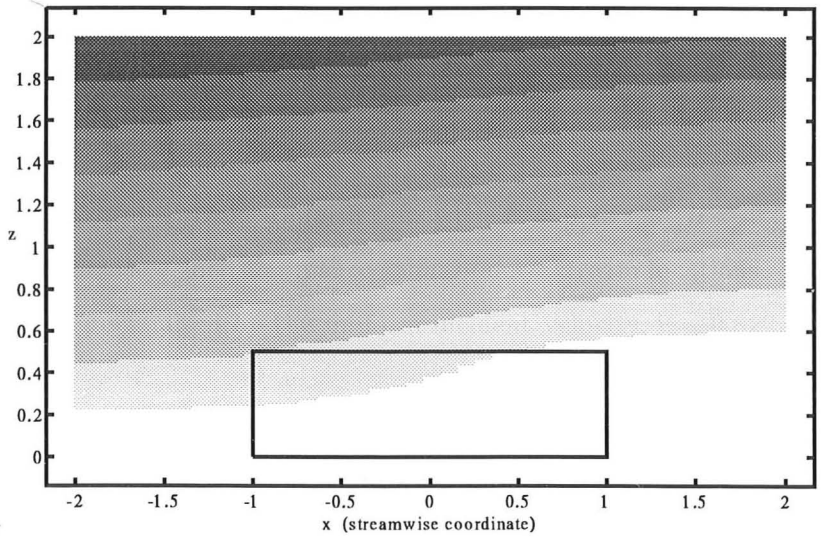

Figure 2.2: Constant force in uniform flow with $F = 0.45$ and $H = 0.5$. (b) Contours of the total streamfunction.

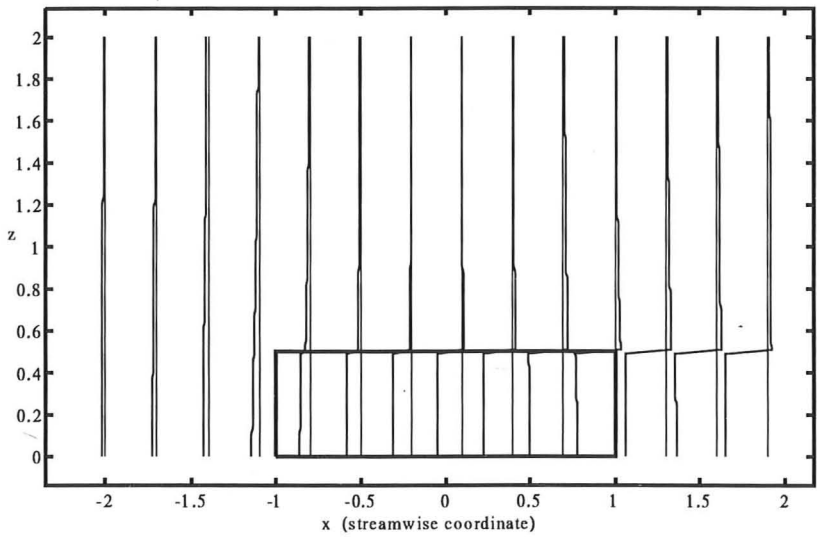

Figure 2.3: Constant force in uniform flow with $F = 0.45$ and $H = 0.5$. (c) The perturbation streamwise velocity at a succession of downstream locations. The maximum velocity deficit, normalised by the uniform incident velocity, is -0.827.

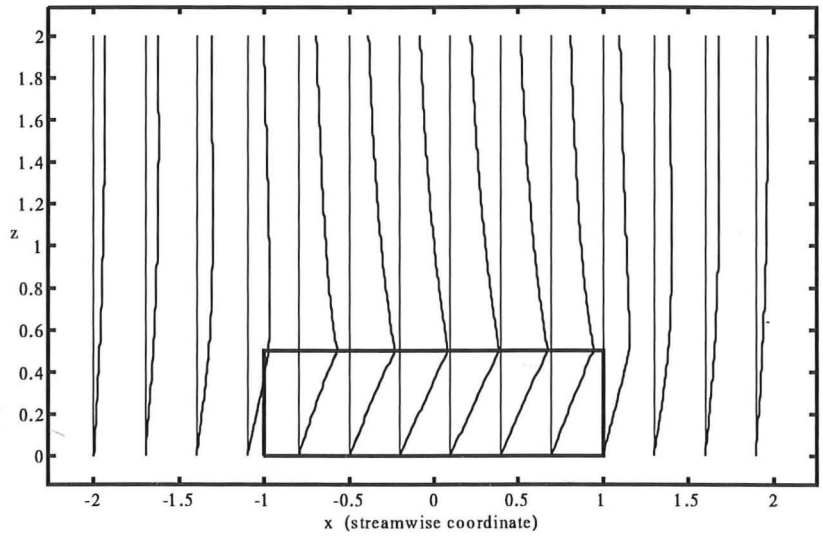

Figure 2.4: Constant force in uniform flow with $F = 0.45$ and $H = 0.5$. (d) The perturbation vertical velocity at a succession of downstream locations. The maximum vertical velocity, normalised by the uniform incident velocity, is 0.358.

Figures 2.1–2.4 show the result of this calculation for $F = 0.45$ and $H = 0.5$. The plot of perturbation streamfunction in figure 2.1 shows the physical structure of the flow: outside the force distribution and its wake the perturbations resemble those from a point source at the origin, and the total mass outflow from this effective source is balanced by an equal mass flux deficit in the wake. The plot of total streamfunction in figure 2.2 shows the blocking effect: flow is forced up and over the region of resistance rather than through it. The plots of streamwise and vertical velocities (figures 2.3 and 2.4) show how the flow is progressively decelerated by the resistance, how the velocity jump at $z = H$ increases linearly between the leading and trailing edges, and how the disturbance in vertical velocity is very small outside the immediate vicinity of the resistance. The physical picture of §1.5 suggests that this inviscid calculation is qualitatively correct for the part of the force distribution where quasi-inviscid dynamics prevail, *i.e.* for the rapid mean flow deceleration of the flow near the leading edge.

2.4 Quadratic force in a constant shear flow

For a second example calculation, the incident velocity profile is chosen to be $U = z/H$ and, by analogy with the usual form of drag laws for bluff bodies (*e.g.* Batchelor 1967), the distributed force is proportional to the square of the local velocity: $f = C_d U^2(z)$. The dimensionless drag coefficient C_d then becomes the characteristic length ratio L^*/L_f^* discussed in §2.2; it is assumed to be constant within the rectangular region $\{|x| < 1,\ 0 < z < H\}$ and zero elsewhere. The governing equation for this flow is, from (2.6),

$$\frac{\partial^2 w}{\partial x^2} + \frac{\partial^2 w}{\partial z^2} = U\frac{\partial C_d}{\partial z} + 2C_d\frac{\partial U}{\partial z}; \tag{2.11}$$

the boundary conditions are $w = 0$ on $z = 0$ and $w \to 0$ as $x \to -\infty$ and $z \to \infty$. The first term on the right is a δ-function at $z = H$ and so its particular integral is the solution derived in §2.3, except that F is replaced by C_d. The second term on the right is a step function: constant $2C_d/H$ in $z < H$ and zero in $z > H$. This is the integral of a δ-function; hence the particular integral of this term can be calculated

by integrating the solution of §2.3. The complex representation pays dividends in facilitating this integration. For example

$$\int_1^{s_1} (s-s')\ln(s-s')\,ds' = \left[\frac{1}{4}(s-s')^2 - \frac{1}{2}(s-s')^2\ln(s-s')\right]_1^{s_1} \tag{2.12}$$

$$= \frac{1}{4}(s-s_1)^2 - \frac{1}{2}(s-s_1)^2\ln(s-s_1) - \frac{1}{4}(s-1)^2 + \frac{1}{2}(s-1)^2\ln(s-1).$$

Care is required when the path of integration crosses the branch cut along the real axis in the definition of $\ln(s-s')$. When $0 < \mathrm{Im}(s) < H$, there is an extra contribution to (2.12) from the branch cut, namely

$$\frac{i\pi}{2}(x-1)^2\mathrm{sgn}(x-1).$$

Similar care is required when integrating $h(s+s_1^*)$. The complete solution for the quadratic force distribution is

$$\begin{aligned}\frac{u-iw}{C_d} &= \frac{1}{4\pi}\left[h(s-s_1) - h(s-s_1^*) - h(s+s_1^*) + h(s+s_1)\right] - S(z-H)\\ &\quad -\frac{1}{2\pi H}\left[j(s-s_1) + j(s-s_1^*) - j(s+s_1^*) - j(s+s_1)\right.\\ &\qquad\qquad \left. -2j(s-1) + 2j(s+1)\right]\\ &\quad +\frac{i}{2H}S(z-H)\left[(x-1)^2\,\mathrm{sgn}(x-1) - (x+1)^2\,\mathrm{sgn}(x+1)\right]\\ &\quad +\frac{2}{H}(H-z)S(z-H),\end{aligned} \tag{2.13}$$

where $j(s) \equiv s^2\ln s$. Approximating this expression for $|s| \gg |s_1|$, $z > H$, and writing $s = re^{i\theta}$, we find that the far field for this quadratic force distribution is given by

$$u - iw \sim -\frac{C_d H^3}{3\pi s^3} = -\frac{C_d}{3\pi}\left(\frac{H}{r}\right)^3 \exp(-3i\theta) \qquad \text{as} \quad r \to \infty. \tag{2.14}$$

This is fundamentally different from the the source-like far field obtained in §2.3. Velocity perturbations fall off rapidly like r^{-3} rather than r^{-1} and integration of (2.14) around a large semicircle shows that there is no net outflow associated with this far field.

The exact flow field is illustrated in figures 2.5–2.9. The plots of perturbation streamlines (figures 2.5 and 2.6) show the weak quadrupolar circulation above the force

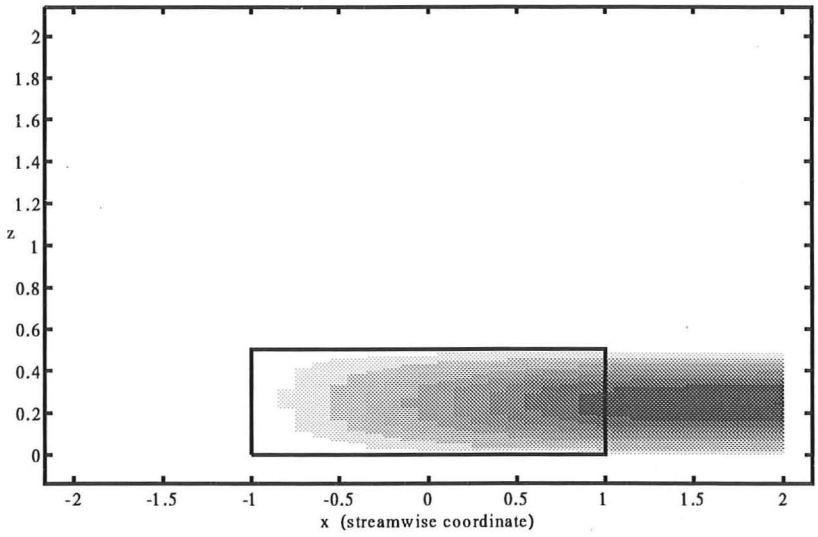

Figure 2.5: Quadratic force in linear flow with $F = 0.45$ and $H = 0.5$. (a) Contours of the perturbation streamfunction.

distribution and the much stronger recirculation of fluid within the force distribution and wake from the upper half $H/2 < z < H$ to the lower half $0 < z < H/2$. The plot of total streamlines (figure 2.7) shows that the blocking effect of the resistance has all but vanished in comparison with the uniform flow (figure 2.2): streamlines pass through the force distribution with little net vertical displacement. The plots of streamwise and vertical velocities (figures 2.8 and 2.9) show that the distributed resistance acts to equalise wind velocities within the force distribution and that there is no flow through the roof of the force distribution. The velocity jump at $z = H$ increases from the leading edge in the same way as in §2.3.

2.5 Flow structure analysis

Prior to the second example calculation of §2.4, one might reasonably have guessed that the far field behaviour of the velocity perturbations depends only upon the total

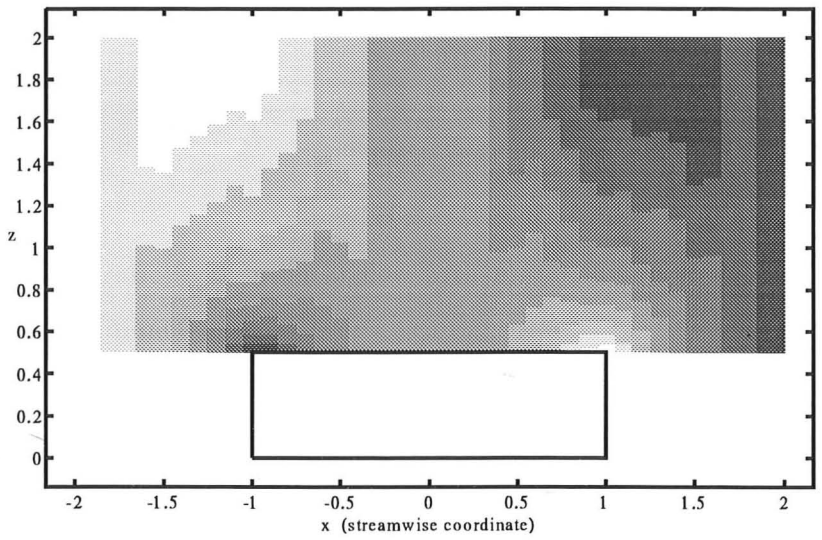

Figure 2.6: Quadratic force in linear flow with $F = 0.45$ and $H = 0.5$. (b) Contours of the perturbation streamfunction above the force distribution, showing the quadrupolar structure.

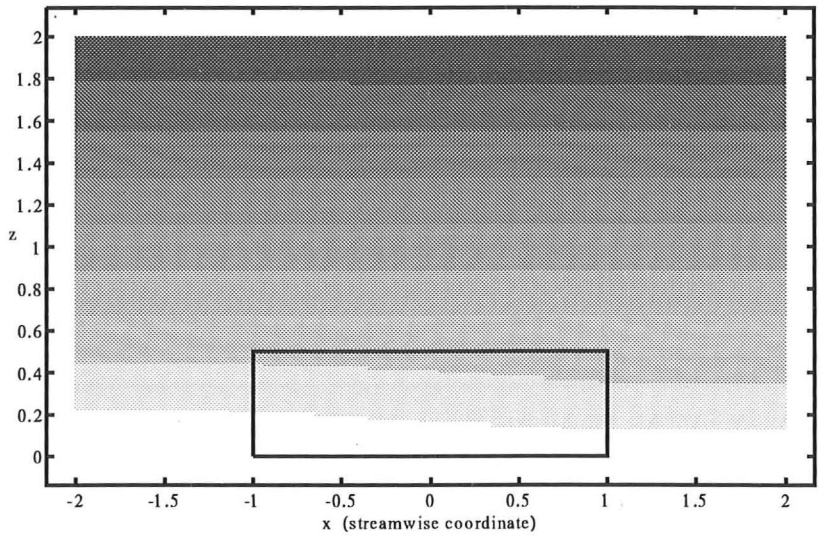

Figure 2.7: Quadratic force in linear flow with $F = 0.45$ and $H = 0.5$. (c) Contours of the total streamfunction.

force acting, *i.e.* the area integral of the distributed force. This proposition may be investigated in general by integrating (2.8) by parts:

$$w(x,z) = \iint d\xi d\zeta \left\{ \frac{G(x,z;\xi,\zeta) f(\xi,\zeta) U'(\zeta)}{U^2(\zeta)} - \frac{G'(x,z;\xi,\zeta) f(\xi,\zeta)}{U(\zeta)} \right\}, \qquad (2.15)$$

where the primes indicate differentiation with respect to ζ. It is assumed that

$$G(x,z;\xi,\zeta) f(\zeta)/U(\zeta) \to 0 \quad \text{as} \quad \zeta \to 0 \qquad (2.16)$$

so that the integrals in (2.15) are regular. Since $G(x,z;\xi,\zeta) \sim \zeta$ as $\zeta \to 0$, (2.16) implies that f and U must satisfy $f(\zeta)/U(\zeta) \sim \zeta^\alpha$ with $\alpha > -1$ as $\zeta \to 0$. This restriction excludes the case of a constant force in the linear shear flow $U = z/H$, which is covered in §2.3. When $U = z/H$, the restriction is obeyed by any force distribution that vanishes at the ground (*e.g.* a quadratic force $f \propto z^2$).

The far field of the flow is now investigated. First write $(x,z) = r(\cos\theta, \sin\theta)$.

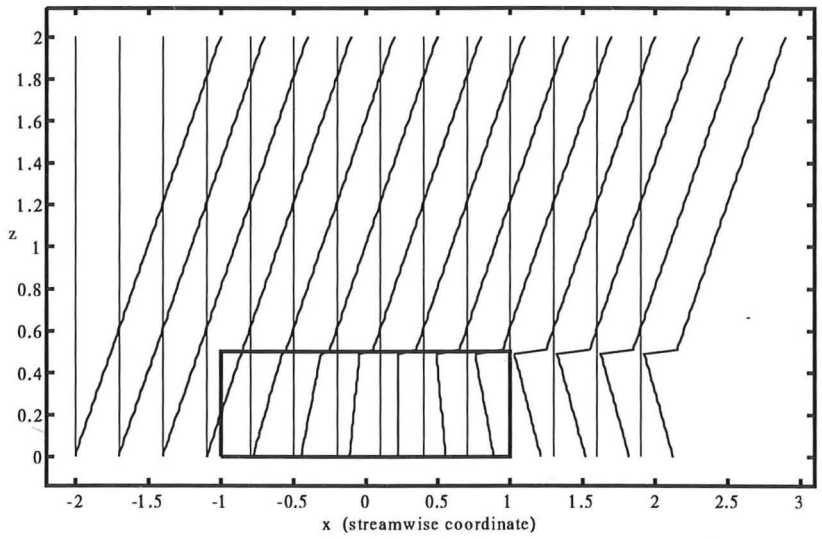

Figure 2.8: Quadratic force in linear flow with $F = 0.45$ and $H = 0.5$. (d) The streamwise velocity at a succession of downstream locations. The perturbation velocity, normalised by the incident velocity at $z = H$, lies between -0.858 and 0.899.

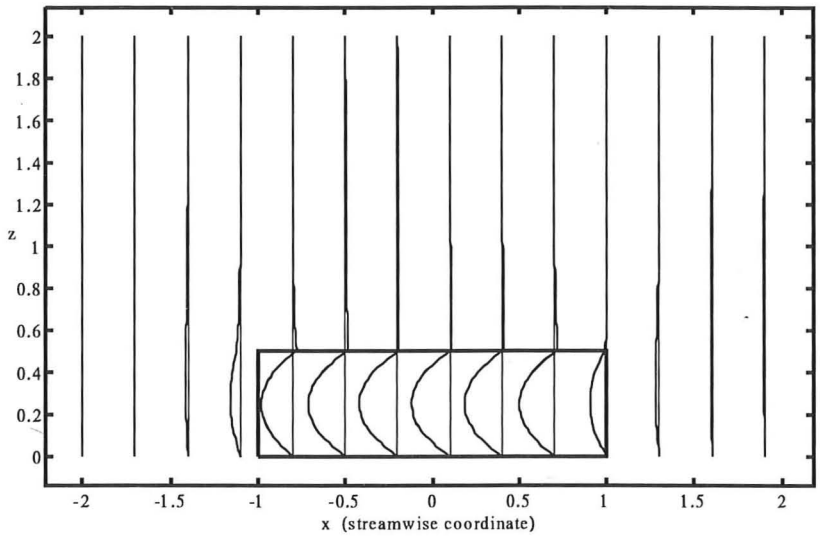

Figure 2.9: Quadratic force in linear flow with $F = 0.45$ and $H = 0.5$. (e) The perturbation vertical velocity at a succession of downstream locations. The maximum downwards vertical velocity, normalised by the incident velocity at $z = H$, is -0.055.

Then for $\xi^2 + \zeta^2 \ll r^2$, G is approximately

$$G(r,\theta;\xi,\zeta) \approx \frac{-\zeta}{\pi}\left\{\frac{\sin\theta}{r} + \frac{\xi\sin 2\theta}{r^2} + \frac{\xi^2\sin 3\theta}{r^3}\right\} + \frac{\zeta^3\sin 3\theta}{3\pi r^3} + O(r^{-4}). \qquad (2.17)$$

The dipole ($r^{-2}\sin 2\theta$) term here serves only to shift the effective origin of coordinates: it vanishes when the centroid of the force distribution lies at $\xi = 0$. The monopole ($r^{-1}\sin\theta$) term dominates the far field provided its integral in (2.15) does not vanish. Writing the most general uniform or uniform shear velocity profile as $U(\zeta) = U(0)+\sigma\zeta$, the far field monopole velocity field is given, from (2.15), (2.16) and (2.17), by

$$w_1(x,z) \approx \frac{\sin\theta}{\pi r}\iint d\xi d\zeta \frac{f(\xi,\zeta)}{U(\zeta)}\left(1 - \frac{\zeta U'}{U}\right) = \frac{U(0)\sin\theta}{\pi r}\iint d\xi d\zeta \frac{f(\xi,\zeta)}{U^2(\zeta)}. \qquad (2.18)$$

If $f \equiv C_d U^2(z)$, as in the analysis of §2.4, the integrand is constant and (2.18) reduces to

$$w_1(x,z) \approx \frac{U(0)C_d A\sin\theta}{\pi r}, \qquad (2.19)$$

where A is the area occupied by the distributed force.

A surprising feature of the monopole velocity field (2.18) is that it vanishes if $U(0) = 0$, *i.e.* if the incident velocity is zero at the ground and increases linearly with height. In this case $w_1 = 0$ identically and the largest non-vanishing term is the quadrupole solution

$$w_3(x,z) \approx \frac{2\sin 3\theta}{3\pi r^3}\iint d\xi d\zeta \frac{\zeta f(\xi,\zeta)}{\sigma}. \qquad (2.20)$$

Note that this general result depends only upon the form of the incident velocity profile, not on the force distribution. It shows that a region of net resistance near a solid boundary does not always give rise to a flow structure composed of a source and a wake. Instead a quadrupolar structure may prevail because the incident velocity profile is linear and vanishes at the boundary. (Equation (2.18) shows that a quadrupolar structure can also result from distributions of f/U^2 that integrate to zero, in the same way that a balanced source/sink pair in potential flow generates a dipolar rather than a source-like far field, but this result was to be expected.) More specifically, the strength of the source-plus-wake flow structure is directly proportional to the incident

boundary velocity $U(0)$. For any velocity profile which is non-zero at the ground, the flow structure is monopolar and its magnitude is related to the total force acting on the flow; but for the simple shear profile $U = \sigma z$ the flow structure is quadrupolar and its magnitude is related to the total couple on the flow about $z = 0$.

This difference in flow structure is not a mere mathematical curiosity of inviscid flow. The following chapter will show that the results of a turbulent analysis may be understood as inviscid results plus turbulent stress corrections; the pressure field in particular is determined almost entirely by inviscid dynamics. Hence some broad features of the inviscid results carry over into the turbulent analysis. Consider then the influence of these flow structures on scalar dispersion. Referring back to the uniform flow streamline plots of figures 2.1 and 2.2, we note (i) that incident streamlines are partially blocked by the resistance, so that an approaching plume will have its centreline lifted, and (ii) that all the perturbation source flow comes from the wake via the resistance, so that scalar concentrations initially within the resistance will be rapidly dispersed into the flow above. In strong contrast, the linear flow plots of figures 2.5 and 2.7 show that the centreline of an incident plume is hardly affected by the resistance and that there is negligible exchange of fluid and scalar concentrations between the interior of the resistance and the flow above it. These are significant qualitative differences for scalar dispersion.

In turbulent flow, the incident velocity profile is neither uniform, $U = 1$ nor linear, $U = z/H$. It is not at all clear which of these two idealised velocity profiles is the better model and, therefore, which of the two distinct flow structures is likely to be observed in practice. To resolve this issue, the following sections investigate the dependence of overall flow structure on varying shear above the region of resistance and on a second class of incident velocity profiles, with the assumption, as suggested by the two preceding calculations, that the flow as a whole can be adequately characterised by the behaviour of velocity perturbations in the far field.

2.6 The view from Fourier space

The same far field results may be obtained in a complementary way by solving the constant and quadratic force problems in Fourier space. Equivalence between the results obtained in real and in Fourier space is important because the results of §§2.7–2.8 can only be obtained by Fourier methods. When the force distribution is constant, the Fourier transform of the governing equation is

$$\frac{\partial^2 w}{\partial z^2} - k^2 z = -\delta(z-H)\frac{\sin k}{k},$$

whose solution for $z > H$ is

$$w_c(k,z;H) = k^{-2}e^{-kz}\sin k \sinh kH. \tag{2.21}$$

The quadratic force solution is obtained from w_c by integration:

$$\begin{aligned} w_q(k,z;H) &= w_c(k,z;H) - \frac{2}{H}\int_0^H w_c(k,z;\eta)\,d\eta \\ &= k^{-2}e^{-kz}\sin k \times \left\{\sinh kH - \frac{2(\cosh kH - 1)}{kH}\right\}. \end{aligned} \tag{2.22}$$

The order of the multipole far field behaviour in real space is represented in Fourier space by the behaviour of the Fourier transform for small k. Specifically, the Fourier transform of an n-pole behaves as k^{n-1} as $k \to 0$. Therefore we can find the "pole order" n for each of our two Fourier solutions by examining them as $k \to 0$. In this limit, the constant force solution (2.21) tends to H and the quadratic force solution (2.22) to $k^2H^3/12$. Thus a constant force gives a monopole far field perturbation ($n = 1$) while the quadratic force in constant shear flow produces a quadrupole far field perturbation ($n = 3$), in agreement with the real space analysis.

To investigate this phenomenon for a wider class of force distributions, take $U = (z/H)^\alpha$, where $\alpha = 0$ or 1, and the force distribution as $f = C_d(z/H)^\beta$. Then the Fourier transformed governing equation is

$$\frac{\partial^2 w}{\partial z^2} - k^2 w = -C_d\left(\frac{z}{H}\right)^{\beta-\alpha}\delta(z-H) + \frac{\beta C_d}{H}\left(\frac{z}{H}\right)^{\beta-\alpha-1},$$

of which the solution is

$$w(k,z;H) = C_d w_c(k,z;H) - \frac{\beta C_d}{H^{\beta-\alpha}} \int_0^H \eta^{\beta-\alpha-1} w_c(k,z;\eta)\, d\eta.$$

In order to ensure that the integral is finite we must impose the condition that $\beta - \alpha > -1$. The limit of this solution as $k \to 0$ is

$$w(k \to 0, z; H) = \frac{C_d H(1-\alpha)}{\beta - \alpha + 1}\left[1 + O(k)\right] + \frac{C_d H^3(3-\alpha)}{6(\beta-\alpha+3)}\left[k^2 + O(k^3)\right].$$

Hence $w(k,z;H) \sim k^0$ if $\alpha = 0$ and $w(k,z;H) \sim k^2$ if $\alpha = 1$, for any value of $\beta > \alpha - 1$. This is equivalent to the real space results of §2.5.

2.7 Varying shear above the force distribution

How is the structure of the far-field perturbations modified by non-uniform shear above the force distribution? Specifically, is the quadrupole structure found for a linear velocity profile just an artefact associated with an unphysical choice of velocity which becomes unbounded as $z \to \infty$? To answer these questions, we consider a flow in which the incident velocity shear changes abruptly at some height $z' > H$. Thus $U''(z)$ is non-zero only at $z = z'$ and the modified governing equation has the form (in Fourier space)

$$\frac{\partial^2 w}{\partial z^2} - k^2 z - aw\delta(z - z') = g(k,z), \tag{2.23}$$

where $aU(z')$ is the jump in incident shear and g is the distributed force gradient. In $H < z < z'$, the solution of this equation is

$$w(k,z) = C \sinh kz + \int_0^H \frac{g(k,\eta)}{k} \sinh k(z-\eta)\, d\eta,$$

where C is an arbitrary constant. It is convenient to rewrite this as

$$w(k,z) = C \sinh kz + I_1 e^{kz} + I_2 e^{-kz},$$

where I_1 and I_2 are known integrals over g. In the absence of the shear jump at $z = z'$, the boundary condition as $kz \to \infty$ determines C by requiring that the coefficient of e^{kz} must vanish, which leads to

$$\frac{1}{2}C + I_1 = 0.$$

Hence the solution in $z > H$ is $w(k,z) = (I_1 + I_2)e^{-kz}$.

When the incident velocity switches from linear to constant, there are jump conditions to be incorporated at $z = z'$, namely

$$[w]_{z'-}^{z'+} = 0, \qquad \text{and} \qquad \left[\frac{\partial w}{\partial z}\right]_{z'-}^{z'+} = aw(z'),$$

so that the solution in $z > z'$ is

$$\begin{aligned} w &= C\sinh kz + I_1 e^{kz} + I_2 e^{-kz} \\ &\quad + \frac{a}{k}\left(C\sinh kz' + I_1 e^{kz'} + I_2 e^{-kz'}\right)\sinh k(z - z'). \end{aligned}$$

The coefficient of e^{kz} must vanish, so

$$\frac{1}{2}C + I_1 + \frac{a}{2k}\left(C\sinh kz' + I_1 e^{kz'} + I_2 e^{-kz'}\right)e^{-kz'} = 0$$

and then the solution in $z > z'$ is

$$w = \frac{(I_1 + I_2)e^{-kz}}{1 + (a/2k)(1 - e^{-2kz'})}.$$

Thus the solution in the presence of the shear jump is modified by the multiplicative "transfer function" $\{1 + (a/2k)(1 - \exp(-2kz'))\}^{-1}$ which depends only upon the wavenumber k and on the position z' and strength a of the jump, and *not* upon $g(x,z)$.

If this transfer function is to alter the structure of far field velocity perturbations produced by the distribution, it must behave like some non-zero power of k as $k \to 0$. In fact it is evident that the transfer function tends in this limit to $\{1 + az'\}^{-1}$, which is independent of k. It follows that the shear jump has no effect on the structure of the far field. Clearly this conclusion may be generalised to cover any velocity profile with varying shear above the force distribution, by treating $U''(z)$ as the composition of a number of δ-functions none of which alter the far field structure. Therefore the quadrupole structure must be a direct consequence of the variation of incident velocity near the ground where the distributed force acts and vorticity is created.

Hence the solution in $z > H$ is $w(k,z) = (I_1 + I_2)e^{-kz}$.

When the incident velocity switches from linear to constant, there are jump conditions to be incorporated at $z = z'$, namely

$$[w]_{z'-}^{z'+} = 0, \qquad \text{and} \qquad \left[\frac{\partial w}{\partial z}\right]_{z'-}^{z'+} = aw(z'),$$

so that the solution in $z > z'$ is

$$\begin{aligned} w &= C\sinh kz + I_1 e^{kz} + I_2 e^{-kz} \\ &\quad + \frac{a}{k}\left(C\sinh kz' + I_1 e^{kz'} + I_2 e^{-kz'}\right)\sinh k(z-z'). \end{aligned}$$

The coefficient of e^{kz} must vanish, so

$$\frac{1}{2}C + I_1 + \frac{a}{2k}\left(C\sinh kz' + I_1 e^{kz'} + I_2 e^{-kz'}\right)e^{-kz'} = 0$$

and then the solution in $z > z'$ is

$$w = \frac{(I_1 + I_2)e^{-kz}}{1 + (a/2k)(1 - e^{-2kz'})}.$$

Thus the solution in the presence of the shear jump is modified by the multiplicative "transfer function" $\{1 + (a/2k)(1 - \exp(-2kz'))\}^{-1}$ which depends only upon the wavenumber k and on the position z' and strength a of the jump, and *not* upon $g(x,z)$.

If this transfer function is to alter the structure of far field velocity perturbations produced by the distribution, it must behave like some non-zero power of k as $k \to 0$. In fact it is evident that the transfer function tends in this limit to $\{1 + az'\}^{-1}$, which is independent of k. It follows that the shear jump has no effect on the structure of the far field. Clearly this conclusion may be generalised to cover any velocity profile with varying shear above the force distribution, by treating $U''(z)$ as the composition of a number of δ-functions none of which alter the far field structure. Therefore the quadrupole structure must be a direct consequence of the variation of incident velocity near the ground where the distributed force acts and vorticity is created.

2.8 Power law shear flows

It is possible to obtain analytical results for a further class of incident velocity profiles: $U = (z/H)^\alpha$, where $0 < \alpha < 1$. Power law profiles merit investigation for two reasons:

1. They are sometimes used as approximations to atmospheric boundary layer profiles; specifically, a value of $\alpha \approx \frac{1}{7}$ is sometimes used to model turbulent boundary layers. (See Barenblatt 1993 for a discussion of power law and logarithmic profiles in turbulent flows.)

2. They lie intermediate between uniform velocity profiles ($a = 0$) and constant shear profiles ($a = 1$) and throw further light on the problem of far field perturbation structure.

For power law profiles $U''/U = \alpha(\alpha - 1)/z^2$, so the Fourier transformed governing equation is

$$\frac{\partial^2 w}{\partial z^2} - k^2 w - \alpha(\alpha - 1)\frac{w}{z^2} = \frac{1}{U}\frac{\partial f}{\partial z}. \tag{2.24}$$

(2.24) may be transformed into a modified Bessel equation of order $\nu \equiv |\alpha - \frac{1}{2}|$:

$$\xi^2 \frac{\partial^2 W}{\partial \xi^2} + \xi \frac{\partial W}{\partial \xi} - \left(\xi^2 + \alpha(\alpha - 1) + \frac{1}{4}\right) W = \frac{z^2}{\xi^{1/2} U}\frac{\partial f}{\partial z}, \tag{2.25}$$

where $\xi \equiv kz$ and $W \equiv \xi^{-1/2} w$. The coefficient ν is not a whole number for the range of α that we are interested in (we exclude $\alpha = \frac{1}{2}$). The homogeneous solution of (2.24) is

$$w = A(kz)^{\frac{1}{2}} I_\nu(kz) + B(kz)^{\frac{1}{2}} I_{-\nu}(kz).$$

The general solution for an arbitrary force distribution is calculated using the Green's function method. The Green's function for a δ-function at $z = \eta$ on the right hand side of (2.24) must satisfy boundary conditions on $z = 0$ and as $kz \to \infty$ and the jump conditions

$$[w]_{\eta-}^{\eta+} = 0 \qquad \text{and} \qquad [w']_{\eta-}^{\eta+} = 1.$$

The boundary condition at the ground is $w = 0$. Since $0 < \nu < \frac{1}{2}$ and $I_\nu(\xi) \sim \xi^\nu$ for small ξ, the homogeneous solution in fact satisfies the ground boundary condition

for any choice of A and B. Also, the gradient of w is infinite at $z = 0$ for any non-trivial choice of A and B. This difficulty arises because the incident velocity gradient is singular at $z = 0$, indicating that a physical analysis of the flow near $z = 0$ would require consideration of viscosity. In order to establish the far field structure, however, it suffices to retain the complementary function whose gradient is "less infinite," *i.e.* $B = 0$. This choice is consistent with what happens in the limiting cases when α is 0 or 1: in both cases $\nu = \frac{1}{2}$, so $I_\nu(kz) = (\pi kz/2)^{-1/2}\sinh kz$, $I_{-\nu}(kz) = (\pi kz/2)^{-1/2}\cosh kz$, and the ground boundary condition is satisfied by rejecting the complementary function in $I_{-\nu}(kz)$. Hence in $z < \eta$ the Green's function is given by

$$w_g(k, z; \eta) = A(k, \eta)(kz)^{\frac{1}{2}} I_\nu(kz).$$

In $z > \eta$ we need to add a general solution which at $z = \eta$ has a value of 0 and a gradient of 1. Thus in $z > \eta$

$$w_g(k, z; \eta) = A(kz)^{\frac{1}{2}} I_\nu(kz) + \frac{\pi(z\eta)^{\frac{1}{2}}}{2\sin\nu\pi}\left\{I_{-\nu}(k\eta)I_\nu(kz) - I_\nu(k\eta)I_{-\nu}(kz)\right\},$$

using the relation $I_{-\nu}(\xi)I'_\nu(\xi) - I_\nu(\xi)I'_{-\nu}(\xi) = 2\sin\nu\pi/\pi\xi$ (Abramowitz & Stegun 1972, §9.6). A is now determined by applying the boundary condition that $w_g \to 0$ as $z \to \infty$. For large ξ, $I_\nu(\xi) \sim e^\xi/\sqrt{2\pi\xi}$, thus

$$Ak^{\frac{1}{2}} + \frac{\pi\eta^{\frac{1}{2}}}{2\sin\nu\pi}\left\{I_{-\nu}(k\eta) - I_\nu(k\eta)\right\} = 0$$

$$\Rightarrow A = \pi\frac{I_\nu(k\eta) - I_{-\nu}(k\eta)}{2\sin\nu\pi}\left(\frac{\eta}{k}\right)^{\frac{1}{2}}.$$

The fully determined Green's function is therefore

$$\begin{aligned} w_g(k, z; \eta) &= \frac{\pi(z\eta)^{\frac{1}{2}} I_\nu(kz)}{2\sin\nu\pi}\left\{I_\nu(k\eta) - I_{-\nu}(k\eta)\right\}, \quad z < \eta; \\ &= \frac{\pi(z\eta)^{\frac{1}{2}} I_\nu(k\eta)}{2\sin\nu\pi}\left\{I_\nu(kz) - I_{-\nu}(kz)\right\}, \quad z > \eta. \end{aligned} \tag{2.26}$$

Now consider the general force distribution $f = C_d(z/H)^\beta$. Then the right hand side of the governing equation becomes

$$\frac{1}{U}\frac{\partial f}{\partial z} = \frac{\beta C_d}{H^{\beta-\alpha}} z^{\beta-\alpha-1} - C_d\delta(z - H).$$

The perturbation vertical velocity produced by such a force distribution is

$$w_{\alpha\beta}(k,z;H) = \frac{\beta C_d}{H^{\beta-\alpha}} \int_0^H \eta^{\beta-\alpha-1} w_g(k,z;\eta)\, d\eta - C_d w_g(k,z;H).$$

For $z > H$, on substituting the Green's function (2.26), this is

$$\frac{\pi z^{\frac{1}{2}}}{2\sin\nu\pi} \{I_\nu(kz) - I_{-\nu}(kz)\} \left\{ \frac{\beta C_d}{H^{\beta-\alpha}} \int_0^H \eta^{\beta-\alpha-\frac{1}{2}} I_\nu(k\eta)\, d\eta - C_d H^{\frac{1}{2}} I_\nu(kH) \right\}.$$

In order to complete the flow field calculation for given values of α and β this integral must be calculated numerically for several values of k; then the resulting profiles are inverse Fourier transformed to obtain the real space flow field. For the purpose of establishing the structure of the far field velocity perturbations, however, it is sufficient to obtain the limiting form of the Fourier transform as $k \to 0$. This limit is found to be

$$\frac{w_{\alpha\beta}(k \to 0, z > H; H)}{C_d H} = \left[O(k^{2\nu}) - \frac{(z/H)^{\frac{1}{2}-\nu}}{2\nu} \right] \left[\frac{\alpha - \frac{1}{2} - \nu}{\beta - \alpha + \frac{1}{2} + \nu} + O(k^2) \right].$$

Recall that $\nu \equiv |\alpha - \frac{1}{2}|$. If $\alpha < \frac{1}{2}$, $\nu = \frac{1}{2} - \alpha$ and the second square bracket is $O(1)$. If, on the other hand, $\alpha > \frac{1}{2}$, $\nu = \alpha - \frac{1}{2}$ and the second square bracket is $O(k^2)$. As the rest of the limiting expression is $O(1)$, the result is that for power law incident velocity profiles $U = (z/H)^\alpha$ with $0 < \alpha < 1$, the far field velocity perturbations will have a monopole structure if $\alpha < \frac{1}{2}$ and a quadrupole structure if $\alpha > \frac{1}{2}$.

2.9 Uniform laminar viscous flow

The final calculation of this chapter includes fluid stress with a constant viscosity ν. This may be considered a crude model of turbulent flow, in which case ν should be interpreted as a turbulent eddy viscosity, *i.e.* the product of a typical eddy length scale and a typical eddy velocity. In some situations (see §3.8) this model may in fact be more appropriate *within the force distribution* than the mixing length model, since the small scale intense eddies generated by obstacles and their wakes can mix fluid efficiently over the whole depth of the distribution.

When the incident velocity profile is uniform, the governing vorticity equation in two dimensions (2.2) becomes

$$U\frac{\partial\omega}{\partial x} = \frac{\nu}{L^*U_o^*}\nabla^2\omega - \frac{\partial f}{\partial z}.$$

Write the vorticity ω in terms of a streamfunction ψ such that $\omega = -\nabla^2\psi$ and then take the Fourier transform of the equation to give

$$\frac{1}{Re}\frac{\partial^4\psi}{\partial z^4} - \left(\frac{2k^2}{Re} + ik\right)\frac{\partial^2\psi}{\partial z^2} + \left(\frac{k^4}{Re} + ik^3\right)\psi = \frac{\partial f}{\partial z}, \tag{2.27}$$

where the Reynolds number is $Re \equiv L^*U_o^*/\nu$ and ψ and f are now Fourier transforms with respect to streamwise coordinate x and so are functions of (k, z). The complementary function of (2.27) has the form:

$$A_1e^{\beta z} + A_2e^{-\beta z} + A_3e^{\alpha z} + A_4e^{-\alpha z}, \tag{2.28}$$

where $\beta = |k|$, $\alpha^2 = k^2 + ikRe$ and the real part of α is non-negative to satisfy the boundary condition that $\psi \to 0$ as $z \to \infty$. We require the Green's function G_v for (2.27) when the right hand side is a δ-function at $z = z_1$. This will have the form of (2.28) and must also satisfy the following boundary and jump conditions:

1. $G_v(k, z = 0; z_1) = G_v'(k, z = 0; z_1) = 0 \ \ \forall k$;
2. $[G_v]_{z=z_1^-}^{z=z_1^+} = [G_v']_{z=z_1^-}^{z=z_1^+} = [G_v'']_{z=z_1^-}^{z=z_1^+} = 0 \ \ \forall k$;
3. $[G_v''']_{z=z_1^-}^{z=z_1^+} = 1 \ \ \forall k$;
4. G_v and its derivatives tend to zero as $z \to \infty$;

where a prime $'$ denotes differentiation with respect to z. The Green's function which satisfies all these conditions is given in $z > z_1$ by

$$\begin{aligned} G_v = G_v^+ \equiv & \frac{\exp(-\alpha z_1) + (\alpha/\beta)\sinh(\beta z_1) - \cosh(\beta z_1)}{(\alpha-\beta)(\alpha^2-\beta^2)}\exp(-\beta z) \\ & + \frac{\exp(-\beta z_1) + (\beta/\alpha)\sinh(\alpha z_1) - \cosh(\alpha z_1)}{(\alpha-\beta)(\alpha^2-\beta^2)}\exp(-\alpha z) \end{aligned} \tag{2.29}$$

and in $z < z_1$ by

$$G_v = G_v^+ + \frac{\sinh \beta(z - z_1)}{\beta(\alpha^2 - \beta^2)} + \frac{\sinh \alpha(z - z_1)}{\alpha(\beta^2 - \alpha^2)} \tag{2.30}$$

Given this Green's function, the streamfunction is obtained from the integral

$$\psi(x, z) = Re \int_{-\infty}^{\infty} dk\, e^{ikx} \int_0^{\infty} dz' \frac{\partial f(k, z')}{\partial z'} G_v(k, z; z'). \tag{2.31}$$

Streamwise and vertical perturbation velocities can then be found by differentiation: $u = \partial\psi/\partial z$; $w = -\partial\psi/\partial x$.

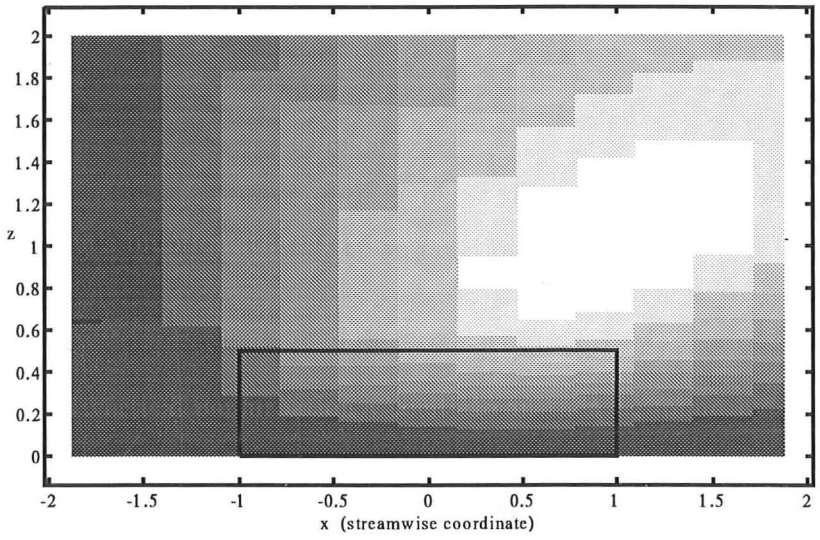

Figure 2.10: Constant force in uniform laminar viscous with $F = 0.45$, $Re = 10$ and $H = 0.5$. (a) Contours of the perturbation streamfunction.

The streamfunction and perturbation velocities given by (2.31) are calculated numerically for the uniform force distribution of §2.3 and $Re = 10$ and the results are shown in figures 2.10–2.13. The plot of perturbation streamlines (figure 2.10) shows fluid being sucked in from the wake and expelled through the top of the array. With the addition of an incident flow, the streamlines (figure 2.11) again exhibit the blocking effect of the array, but now they also show the wake beginning to decay as some

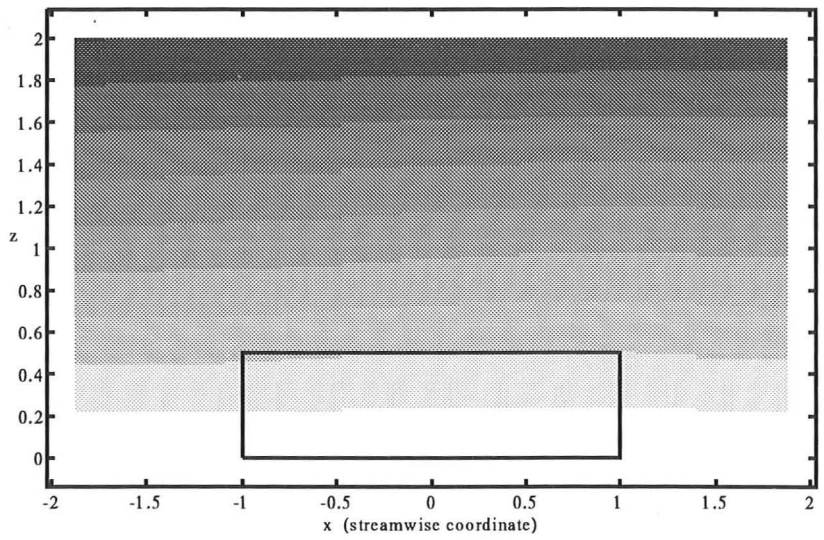

Figure 2.11: Constant force in uniform laminar viscous with $F = 0.45$, $Re = 10$ and $H = 0.5$. (b) Contours of the total streamfunction.

fluid flows downwards downstream of the array. Figure 2.12 shows that the streamwise perturbation velocity becomes positive above the array soon after the leading edge in contrast to the inviscid case where the perturbation is negative until halfway along the array. It is also clear that there is far more deceleration in the first half of the array than in the second, consistent with the idea that the flow approaches an equilibrium state in the array interior with stress gradients making a significant contribution to the momentum balance. Figure 2.13 shows a dramatic streamwise gradient of vertical velocity in the exit region of the array where the applied force suddenly disappears. This gradient is less dramatic if f^* is a function of the local fluid velocity.

The n-pole decomposition of the far field structure that has been pursued in the inviscid analysis depends implicitly upon the far field perturbations obeying Laplace's equation $\nabla^2 w = 0$ either exactly or approximately (which is true for the power law profile analysis of §2.8 because $U''/U \to 0$ as $z \to \infty$). The laminar viscous far field cannot be decomposed in this way because its perturbations obey the fourth order

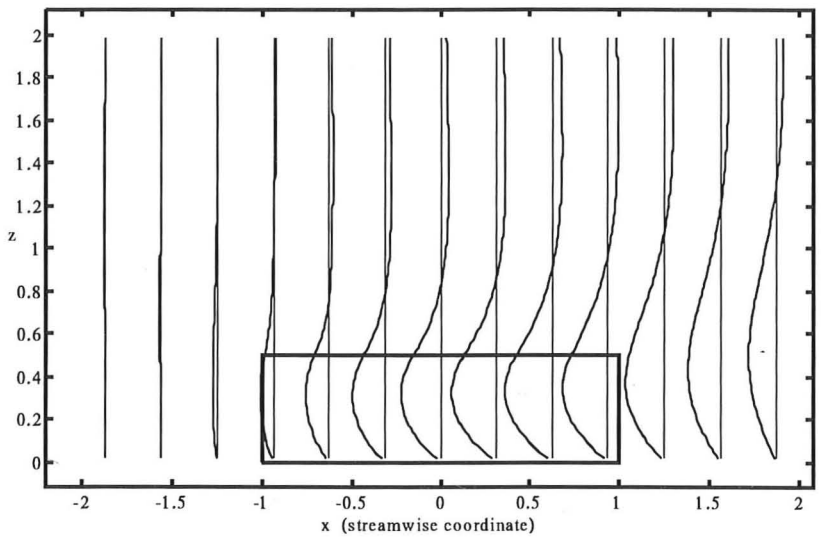

Figure 2.12: Constant force in uniform laminar viscous with $F = 0.45$, $Re = 10$ and $H = 0.5$. (c) The perturbation streamwise velocity at a succession of downstream locations. The maximum velocity deficit, normalised by the uniform incident velocity, is -0.176.

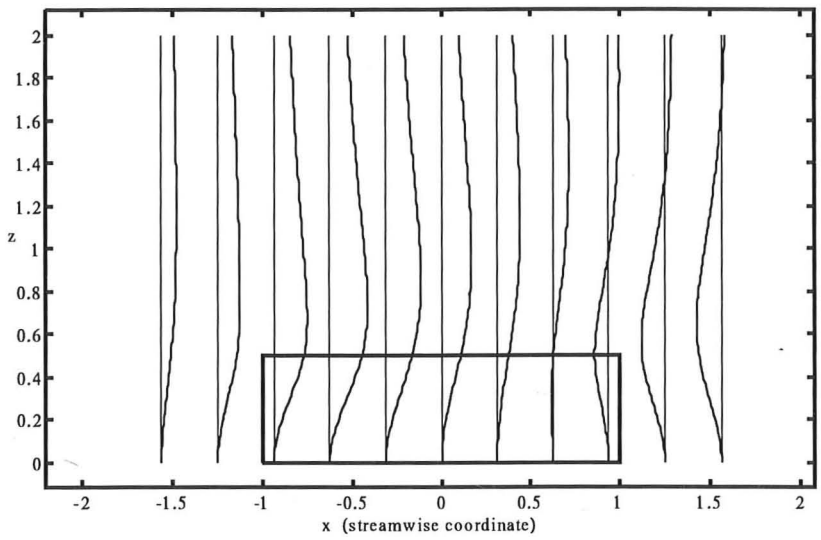

Figure 2.13: Constant force in uniform laminar viscous with $F = 0.45$, $Re = 10$ and $H = 0.5$. (d) The perturbation vertical velocity at a succession of downstream locations. The maximum upwards vertical velocity, normalised by the uniform incident velocity, is 0.0525.

equation (2.27) which does not reduce to Laplace's equation in the far field. However, comparison of the streamline plots from figures 2.1, 2.5, 2.6 and 2.10 clearly shows that the laminar viscous results obtained here are qualitatively closer to the source-like inviscid results of §2.3 than to the quadrupole structure results of §2.4.

2.10 Symmetry in inviscid flow

The different flow structures observed in inviscid flow can be understood, or at least viewed from a new vantage point, by considering the symmetry of the flow configuration. The following arguments attempt to explain the observed flow structure in terms of this symmetry and have significant implications for turbulent flow and the way that turbulent flow should be modelled.

2.10.1 Explaining the observed flow structures

In inviscid flow, the function of the solid boundary is to suppress any normal flow. The same effect can be achieved without a solid boundary by placing an image system of incident velocity and force distribution below the line where perpendicular velocities are required to vanish. Thus the solid boundary in figure 2.14a becomes a line of symmetry for the equivalent flow system in figure 2.14b.

A second symmetry operation derives from the governing equations (2.6), which show that it is f'/U, not f' alone, that acts as the source of perturbation vorticity and hence of vertical velocity perturbations. Therefore we could change the sign both of the incident velocity and of the distributed force below the line of symmetry and still have an equivalent flow system (figure 2.14c) for the flow above the symmetry line. (The physical behaviour of the flow below the line then becomes rather counter-intuitive, since the boundary condition is still that $u \to 0$ as $x \to -\infty$, but mathematically the symmetry operation is valid.)

Now consider the effect of these two symmetry operations on the inviscid distributed

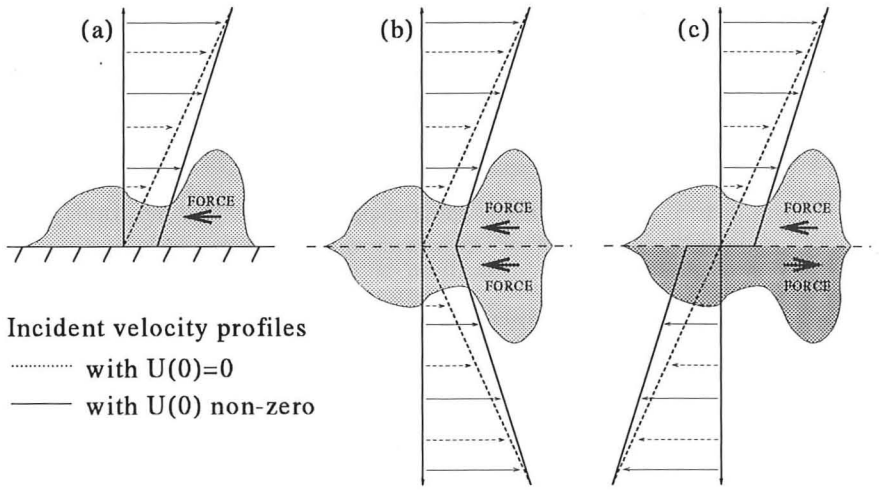

Figure 2.14: Equivalent flow systems: (a) with a solid boundary; (b) reflected about the line where the solid boundary used to be; (c) after changing the sign of both f and U in the lower half of the system.

force problem with linear incident velocity profiles, $U = U(0) + \sigma z$. When $U(0) = 0$, the reflected velocity profile in the equivalent flow system of figure 2.14c (shown as a dashed line) is continuous. Then the complete system constitutes a force dipole in an unbounded shear flow and there is consequently no source-like contribution to the far field perturbations. When $U(0) \neq 0$ (shown as a solid line) the reflected velocity profile is discontinuous on the line of symmetry. It appears that this discontinuity prevents complete transmission of the perturbations from above the symmetry line to the region below so that cancellation of the upper and lower monopole fields is not exact and there is a source-like contribution to the far field perturbations whose strength is directly proportional to the size of the discontinuity $U(0)$ (equation 2.18).

A mathematical explanation is provided by Lighthill (1957). He describes an argument due to Prof. M.B. Glauert, based on the method of images, which shows the effect of a velocity discontinuity on the far field perturbations from a point source. If a point source of strength m lies above a vortex sheet separating two regions with velocities V_- and V_+, the effective source strengths of far field perturbations above

and below the vortex sheet become m_+ and m_- respectively, where

$$m_+ = \frac{2V_-^2}{V_+^2 + V_-^2} m \qquad \text{and} \qquad m_- = \frac{2V_+V_-}{V_+^2 + V_-^2} m.$$

If $V_- = -V_+$ as in figure 2.14c then $m_+ = m$ and $m_- = -m$. Hence the perceived source strength above the vortex sheet is unchanged, but the source strength below the sheet is reversed in sign. Now the equivalent flow system of figure 2.14c has a source above the symmetry line and a sink below the symmetry line for every element of the distributed force in figure 2.14a. In the presence of a velocity discontinuity, Glauert's image approach shows that sinks below the line will be perceived in the upper half of the flow as extra sources, supplementing the original sources in the upper half, thus producing a monopolar far field.

For the case of uniform flow, therefore, it is demonstrated that the velocity discontinuity in the equivalent flow system modifies the source strength of velocity perturbations crossing the discontinuity such that the upper and lower sources do not cancel each other out in the far field. It is reasonable to infer that any discontinuous velocity profile will modify the transmitted source strength in a similar way to an extent depending upon the size of the discontinuity. The action of the discontinuity here is somewhat reminiscent of the effects of a strong shear layer in blocking the motion of turbulent eddies across it, discussed later in §3.8.

The more general shear flow profiles $U = (z/H)^\alpha$, $0 < \alpha < 1$, lie intermediate between the strongly discontinuous (after reflection) uniform flow $U = 1$ ($\alpha = 0$) and the continuous linear flow $U = z/H$ ($\alpha = 1$). The exponent α describes the spread of the incident velocity shear layer around the symmetry line. Thus the results of §2.8 show that shear layers with $\alpha < \frac{1}{2}$ are sufficiently strong to behave in the same way as discontinuous velocity profiles, while those with $\alpha > \frac{1}{2}$ are apparently not.

2.10.2 Implications for turbulent flow modelling

The flow structure results obtained in inviscid flow and the explanation offered here have important implications for turbulent flow and any attempts to model turbulent

flow. When represented by a power law (*e.g.* Barenblatt 1993), turbulent boundary layer profiles have power law exponents around $\alpha \approx \frac{1}{7}$; hence they should be classified with the $\alpha < \frac{1}{2}$ velocity profiles of §2.8. Physically this classification reflects the fact that the shear in a turbulent boundary layer is concentrated in a thin layer near the ground. It follows that we should always expect to observe a source-like flow structure above the force distribution in a turbulent boundary layer. It also follows that the incident velocity in a turbulent flow analysis should only be modelled by a profile that correctly represents strong shear or a velocity discontinuity near the ground. This excludes use of the linear profile $U = z/H$ and favours the uniform profile $U = 1$, even though the latter does not satisfy a no-slip boundary condition at the ground.

In a laminar viscous flow it is not clear to what extent the results of inviscid analysis apply. In contrast to turbulent boundary layers, typical laminar viscous boundary layers have a velocity variation described by the Blasius profile (*e.g.* Tritton 1988, pp. 127–130), which is almost linear over a large part of the boundary layer near the wall. However, the results of §2.9 with a *uniform* incident velocity are qualitatively source-like, and it may be that this resemblance is a consequence of the uniform velocity and that an analysis with $U = z/H$ would lead to a more quadrupole-like flow structure. In this case the response of a laminar boundary layer to a distributed force would be very different from that of a turbulent boundary layer simply because of differences in their undisturbed velocity profiles, essentially because the laminar profile lacks a layer of concentrated shear. Therefore when a laminar analysis is used to model a turbulent flow, as in §3.8, care must be taken to ensure that the resulting flow structure is qualitatively correct. Use of a linear or Blasius profile in the laminar analysis could result in a perturbation structure completely inappropriate *to turbulent flow*, while use of a uniform profile at least guarantees a source-like far field such as prevails in turbulent flows.

Chapter 3

Analytical models for turbulent canopy flows

3.1 Introduction

The interesting flows that can be modelled using the concept of distributed force—forests, urban areas, etc.—are generally characterised by large enough Reynolds numbers for the flow to be fully turbulent. Given such practical importance, the remaining chapters of this thesis are concerned specifically with *turbulent* flow and dispersion through a distributed force.

Turbulent flow field modelling in this thesis has two main objectives. Firstly we aim to produce practical analytical models for the detailed perturbation velocities and shear stresses within and above a region of distributed resistance. Such models are developed by the following analyses in this chapter, and have been incorporated into a working computer software package. The input to this computer package is a description of the incident wind and of the distributed resistance; the output is a two-dimensional array of perturbation flow quantities. In chapter 4 these models are used to simulate a number of experiments on flow through a group of obstacles and the simulation results are compared against the experimental data.

Secondly we aim to produce "equivalent" parameterisations, that usefully describe

broad aspects of the calculated flow fields in an accessible way. The most important of such parameterisations calculates effective roughness parameters—displacement height, roughness height and friction velocity—for the flow above a region of resistance that varies slowly in the streamwise direction. Chapter 5 derives two equivalent parameterisations from the detailed flow field results of chapter 3 and indicates the regions of the flow where these parameterisations are valid.

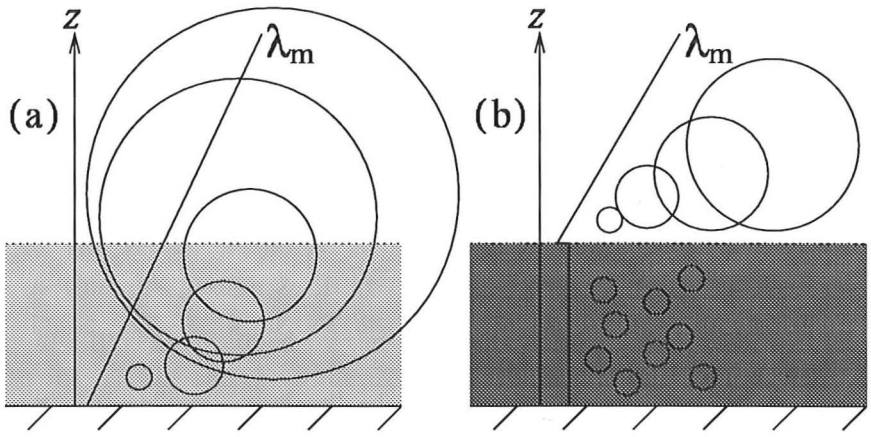

Figure 3.1: The two turbulent mixing length models used here. (a) The "standard" mixing length (SML) model. (b) The "displaced" mixing length (DML) model.

A turbulent analysis requires a model for the turbulent stresses. If a standard model such as mixing length or K–ϵ is to be used, new effects particular to distributed force flow or to the underlying canopy flow must be taken into account. For example, Svensson & Häggkvist (1990) and Savill & Solberg (1994) add terms to the K–ϵ turbulent kinetic energy (TKE) equation to represent the shear production of TKE in obstacle boundary layers.

In this chapter we use two variants of the mixing length model. The "standard" mixing length (SML) model (figure 3.1a) assumes that the mean flow perturbations due to a distributed force are too weak to alter the turbulence structure of the incident boundary layer flow. Hence the mixing length λ_m is proportional to height above the

ground. In the "displaced" mixing length (DML) model (figure 3.1b), the flow domain is divided into two. A constant mixing length within the canopy models intense small scale turbulence due to the eddies shed from individual obstacles, while a linear mixing length above, with a non-zero displacement height, models the blocking effect on turbulent eddies of a strong shear layer such as might be produced at the rooftop level of a group of obstacles. Thus the DML model assumes that individual obstacles and large scale mean flow changes significantly alter the turbulence structure within and above the obstacle canopy. The ideas behind these two contrasting turbulence models are further discussed in §3.2 and §3.8. The sensitivity of our results to turbulence modelling will be assessed by comparing results from these two models with each other and with numerical simulations using the K–ϵ closure.

For the SML turbulence model, the method of analysis of the perturbation flow field follows that of Jackson & Hunt (1975), Sykes (1980), Hunt *et al.* (1988a) and Belcher *et al.* (1990), developed by these authors in investigations of turbulent boundary layer flow over changes in ground elevation and surface roughness. The key points of this method are that

- the analysis is linear: we specify the form of the incident velocity upstream of any distributed force and assume that any perturbations from this incident profile are small;
- the flow domain is divided into dynamically distinct layers (described in §3.3): turbulent shear stresses usually affect the mean flow perturbations only within a thin layer near the ground (Townsend 1965);
- linear perturbations are calculated separately in each layer and then matched with each other using the method of matched asymptotic expansions.

Rapidly varying force distributions, however, can make turbulent shear stresses significant outside the thin stress layer near the ground (§3.4). This feature is specific to the distributed force problem, because a distributed force extends vertically into the flow domain, whereas the previously studied elevation and roughness changes are

surface perturbations. Hence separate analyses are presented for slowly varying (§3.5) and rapidly varying (§3.6) force distributions. Sample results for the SML analysis are presented in §3.7.

For the DML turbulence model (§3.8), the upper part of the flow, where mixing length increases linearly with height, is calculated using the same asymptotic method but with extensions to allow for a non-zero displacement height. The lower part of the flow, where mixing length is uniform, is calculated using the laminar viscous analysis of §2.9.

The chapter concludes in §3.9 by evaluating the sensitivity of the key features of the calculated flow fields to the turbulence model.

3.2 The SML turbulent stress model

As in the laminar analyses of chapter 2, the region of distributed force is characterised by horizontal and vertical extents L^* and H^*. The incident boundary layer flow is understood to be developing slowly only on time scales longer than the time L^*/U_o^* for flow to pass through the region of resistance, and the distributed force is taken to lie within the lower 20% of the total boundary layer depth. Hence the incident mean velocity profile is logarithmic (*e.g.* Panofsky & Dutton 1984, chapter 6) and characterised by friction velocity u_* and roughness height z_o^*:

$$U^*(z^*) = \frac{u_*}{\kappa} \ln \frac{z^*}{z_o^*}, \tag{3.1}$$

where $\kappa \approx 0.41$ is von Karman's constant. Hence the mixing length model for the undisturbed boundary layer shows that turbulent shear stress in the incident flow is uniform:

$$T^* = \rho u_*^2. \tag{3.2}$$

Throughout the analysis, capital letters denote incident flow quantities and lowercase letters perturbation quantities.

Following Townsend (1965), turbulent stress perturbations are modelled by the

equation

$$\tau^* = 2\rho u_* \kappa z^* \frac{\partial u^*}{\partial z^*}, \tag{3.3}$$

in which κz^* is the SML model turbulent mixing length. Equation (3.3) is the linear perturbation of the mixing length model for total shear stress, namely

$$\hat{\tau}^* = \rho \kappa^2 z^{*2} \frac{\partial \hat{u}^*}{\partial z^*} \left| \frac{\partial \hat{u}^*}{\partial z^*} \right|. \tag{3.4}$$

The factor of two in (3.3) arises because (3.4) makes total shear stress $\hat{\tau}^*$ quadratic in the total streamwise velocity gradient $\partial \hat{u}^*/\partial z^*$.

The normal stress perturbations τ_{11}^* and τ_{33}^* are far less important dynamically than the shear stress τ_{13}^* (also written here as τ^*). The flow within the thin layer where turbulent stress perturbations are non-negligible is largely determined by the balance of streamwise momentum, which is influenced by the *vertical* gradient of τ_{13}^* and the *streamwise* gradient of τ_{11}^*. Given that τ_{11}^* and τ_{13}^* are of similar order (as established by numerous experiments, *e.g.* Laufer 1955), the thinness of the turbulent stress layer makes $\partial \tau_{11}^*/\partial x^*$ negligible in comparison with $\partial \tau_{13}^*/\partial z^*$. In terms of the ratio ϵ between vertical and streamwise length scales in this layer, the normal stress τ_{11}^* makes only an $O(\epsilon^2)$ correction to the flow.

The vertical normal stress τ_{33}^* affects streamwise momentum transfer only indirectly, as it gives rise to a pressure variation across the thin layer at $O(\epsilon)$ and hence to an $O(\epsilon)$ correction to the streamwise velocity perturbation. This is omitted in the analysis below, even though corrections of similar order are included, because it exhibits no new interesting physics and because the analysis clearly indicates how an arbitrary number of further such corrections could be incorporated if so desired.

Thus closure models for τ_{11}^* and τ_{33}^* are not used in the following analysis. If models were required, for example to calculate further corrections to the asymptotic results below, then observations would suggest proportionality: $\tau_{11}^* = -\alpha \tau_{13}^*$ and $\tau_{33}^* = -\beta \tau_{13}^*$. Appropriate values for α and β, measured in the laboratory and in the atmosphere, are given by Townsend (1976, Table 5.2).

All quantities in the following analysis will be non-dimensionalised using the length L^*, advective velocity scale $U_o^* \equiv U^*(H^*)$ and fluid density ρ, with the exception of

turbulent shear stresses which scale on u_*^2 and so are conveniently non-dimensionalised by the incident shear stress ρu_*^2. Dimensional quantities are marked with an asterisk.

3.3 Asymptotic flow structure

3.3.1 The domain of importance of turbulent stresses

Implicit in the derivation of the mixing length model (3.3) is the idea that turbulent eddies are in a state of "local equilibrium" (Townsend 1961), such that there is enough time for turbulent eddies to move and transfer momentum before the mean flow has changed much. If, however, the mean flow changes too rapidly, eddies are distorted by the mean flow changes before there is time to establish the local equilibrium. The analogy with molecular diffusion then breaks down. In the limit of very rapidly changing mean flow, rapid distortion theory (RDT) can be used to model the turbulence. Following Britter *et al.* (1981) and Belcher *et al.* (1993), the height l^* of an inner region within which (3.4) applies is established by comparing time scales for turbulent eddy diffusion and for distortion of the mean flow.

Consider boundary layer flow past an obstacle of length L^*. The time taken for a fluid particle or an eddy to be advected past the obstacle at a height z^* is

$$t_a^* \approx L^*/U^*(z^*). \tag{3.5}$$

t_a^* decreases with height because the wind speed increases. The mean flow is distorted most somewhere near the obstacle, while far upstream and downstream the perturbations tend to zero. Hence t_a^* is also the characteristic time scale for mean flow distortion.

A turbulent equilibrium time t_e^* is determined by the turbulent length scale, which according to the mixing length theory is the height above the ground, and the characteristic velocity fluctuation u_*. The equilibrium time scale is therefore

$$t_e^* \approx z^*/u_*. \tag{3.6}$$

t_e^* increases with height as the typical eddy size increases, because more time is required to mix momentum over greater distances.

The two time scales t_a^* and t_e^* are of similar order at a height l^* defined implicitly by

$$\frac{L^*}{U^*(l^*)} \approx \frac{l^*}{u_*} \Rightarrow l^* \ln \frac{l^*}{z_o^*} \approx \kappa L^*. \tag{3.7}$$

In the region $z^* < l^*$ where the equilibrium time t_e^* is less than the advection time, the local equilibrium hypothesis is appropriate and the perturbation turbulence closure (3.3) can be used. For $z^* \gg l^*$, $t_e^* \gg t_a^*$ and so turbulence is governed by RDT. RDT implies that perturbation turbulent stresses are $O(\epsilon^2)$, where ϵ is the ratio of turbulent velocity u_* to characteristic advection velocity U_o^*. It follows that these rapidly distorted eddies have no effect on the leading order mean flow perturbations.

Thus consideration of these two time scales divides the flow domain into two regions at an approximate height l^*. In the inner region, *i.e.* $z^* < l^*$, turbulent stress perturbations are significant and can be modelled by the mixing length closure (3.3). In the outer region, $z^* > l^*$, turbulent stresses do not affect the mean flow perturbations at leading order, indicating that the outer region flow perturbations are effectively controlled by inertia gradients and pressure forces.

Belcher *et al.* (1993) have shown that this layered turbulence model is significantly more accurate than using a mixing length model throughout the flow domain when applied to the calculation of pressure drag on a low hill: the results of their linear asymptotic analysis are comparable with those of numerical simulations using a second-order turbulence closure. If an SML closure is used incorrectly outside the inner region, turbulent stress appears to affect the mean flow perturbations at $O(\epsilon)$, where ϵ is the ratio of turbulent friction velocity to the advective velocity scale. Belcher *et al.* used rapid distortion theory outside the inner region to show that turbulent stress in fact affects mean flow perturbations only at $O(\epsilon^2)$.

3.3.2 The use of Fourier analysis

Following Lighthill (1957) and many others, the application of Fourier analysis to the linearised distributed force problem allows arbitrary force distributions to be treated by the Fourier synthesis of a set of harmonic distributions. The inconvenience of inverse Fourier transformation at the end of the analysis is far outweighed by the simplification that results from reducing partial differential equations in two or three independent variables to ordinary differential equations in just one vertical coordinate.

Moreover, in the distributed force problem the reponse of the incident flow is quite different, depending on whether the force distribution varies rapidly or slowly in the streamwise direction, *i.e.* according to the ratio between streamwise variation length scale and force distribution height. Fourier analysis provides a formal method for separating out these differently behaving components of an arbitrary force distribution. This is an important extra consideration for the distributed force and roughness change problems because the imposed flow disturbance can include a wide spectrum of streamwise wavenumbers (consider the step change in roughness).

In a Fourier analysis, it is appropriate to calculate the height l^* separately for each Fourier component of the force distribution, taking the Fourier wavelength $2\pi/k^*$ as the horizontal length scale for advection. Thus, from (3.7), at each wavenumber k^* we define $l^*(k^*)$ implicitly by

$$k^* l^* \ln \frac{l^*}{z_o^*} \approx 2\pi\kappa. \tag{3.8}$$

This wavenumber dependent scaling leads naturally to the physical picture described in §1.5. The impact and exit regions of the flow correspond to short wavelength components of the force distribution. For these Fourier components l^* is small compared to the height of the force distribution and most of the perturbation flow will be inviscid as the physical arguments of §1.5 suggest. By contrast, in the array interior and far wake regions, which correspond to long wavelength components, l^* is large and well above the top of the force distribution; hence turbulent stresses are crucial to the dynamics of these regions.

To fix the value of l^* the right hand side of (3.8) is chosen to be 1. Note that

this choice is slightly different to that made by Hunt *et al.* (1988a) and Belcher *et al.* (1990) and is made here for notational convenience. Since l^* is interpreted as an order of magnitude estimate for the transition height between inner and outer regions, the choice of this $O(1)$ constant in no way affects the results. Thus l^* is defined implicitly by

$$k^* l^* \ln \frac{l^*}{z_o^*} = 1. \tag{3.9}$$

At very small wavenumbers (3.9) gives the inner region height l^* increasing without limit. In practice l^* must be limited by that fraction of the *incident* boundary layer depth in which there is local equilibrium, typically about one fifth of the total boundary layer depth. Denoting this limiting height by δ^*, there is a critical wavenumber k_c^* below which l^* as defined by (3.9) would exceed δ^*. k_c^* is given by

$$k_c^* = \left(\delta^* \ln \frac{\delta^*}{z_o^*} \right)^{-1}. \tag{3.10}$$

To estimate a typical value for k_c^* in the atmospheric boundary layer, we take $\delta^* = 200\text{m}$ and $z_o^* = 0.1\text{m}$, giving $k_c^* = 6.6 \times 10^{-4}\text{m}^{-1}$ or a critical horizontal scale of about 10km. This restriction is always significant for the smallest woods and villages as well as the largest cities and forests because, assuming that all of a force distribution acts in the same direction, the zero wavenumber Fourier component is larger in magnitude than any non-zero wavenumber component:

$$|f(k)| = \left| \int_{-\infty}^{\infty} f(x) e^{-ikx}\, dx \right| \leq \int_{-\infty}^{\infty} |f(x)|\, dx = |f(0)|. \tag{3.11}$$

In a numerical implementation of the results of the present analysis, (3.9) is modified to give

$$l^* \equiv \delta^* \tanh \frac{l_1^*}{\delta^*}, \quad \text{where} \quad k^* l_1^* \ln \frac{l_1^*}{z_o^*} = 1. \tag{3.12}$$

The value of l^* given by (3.12) differs negligibly from that of (3.9) when $k^* \gg k_c^*$, so the physical reasoning behind (3.9) is preserved until l^* approaches δ^*; then the modified definition (3.12) ensures that the stronger constraint $l^* \leq \delta^*$ is obeyed.

3.3.3 The asymptotic small parameter ϵ

The small parameter ϵ of the analysis is defined as the ratio between turbulent velocity scale u_* and advective velocity scale U_o^*:

$$\epsilon \equiv \frac{u_*}{\kappa U_o^*}. \tag{3.13}$$

Non-dimensionalisation of the advective velocity scale, $U_o^* = U^*(H^*)$, gives the relation

$$\epsilon \ln \frac{H}{z_o} = 1. \tag{3.14}$$

This is perhaps a more useful definition of ϵ since it relates the small parameter directly to the geometry of the problem. (3.14) shows that the condition for ϵ to be small is equivalent to the condition that there should be a clear separation of scales between z_o and H. The surface roughness could also be modelled as a part of the distributed force. Therefore a clear separation of scales between z_o and H is required for the surface roughness to be treated consistently as a roughness length rather than as a force distribution.

Equation of (3.9) and (3.14) gives a relation between ϵ and kl:

$$\frac{kl}{\epsilon} = \frac{\ln(H/z_o)}{\ln(l/z_o)} = 1 + \frac{\ln(H/l)}{\ln(l/z_o)} = \frac{1}{1 - \epsilon \ln(H/l)}. \tag{3.15}$$

Hence $kl = O(\epsilon)$ as long as $1 - \epsilon \ln(H/l) = O(1)$, which is true unless l is as small as $O(z_o)$. Typically the smallest significant wavelengths of the force distribution are $O(H)$, and for such small scales $l \sim \lambda = O(H)$. Overall, therefore, it is safe to scale $kl = O(\epsilon)$, which shows that ϵ also characterises the ratio of vertical to horizontal length scales in the inner region.

3.3.4 Subdividing the inner region

A velocity scale for the inner region is defined by

$$U_l \equiv U(l) = \epsilon \ln \frac{l}{z_o} \tag{3.16}$$

and then the incident velocity in the inner region may be written

$$U(z) = U_l + \epsilon \ln \frac{z}{l}. \tag{3.17}$$

Hence $U(z) = U_l + O(\epsilon)$ throughout the inner region except very near the ground where $z \sim z_o$. Therefore the inner region is divided into two sub-layers. In the inner surface layer (ISL), $z \sim z_o$, the natural $O(1)$ vertical coordinate is $\zeta_i \equiv z/z_o$ and the incident velocity profile is $U(z) = \epsilon \ln \zeta_i = O(\epsilon)$. The shear stress layer (SSL) is defined as the rest of the inner region. Here the $O(1)$ vertical coordinate is $\zeta \equiv z/l$ and the incident velocity is $U(z) = U_l + O(\epsilon)$. The need to subdivide the inner region in this way was first recognised by Sykes (1980) and will be clarified in §§3.5.2–3.5.3.

3.4 Effects of strong force gradients

The remark made in §3.1, that rapidly varying force distributions can make turbulent stresses significant outside of the thin stress layer near the ground, is a manifestation of the fact that a *distributed* force can impose new vertical length scales upon the flow. Since the basic physics of distributed body forces is that force gradients create vorticity (§2.2), new length scales are most clearly defined by locations within the force distribution where the force gradient is strong.

When significant new vertical length scales exist, a mathematical problem for the SML analysis arises because the asymptotic flow structure of §3.3 implicitly ignore all vertical length scales except height above the ground. Although a general force distribution may have several places where the force gradient $\partial f/\partial z$ becomes large, the issues involved are demonstrated most clearly by consideration of a force distribution that is slowly varying up to a height h and zero above h, so that there is a single discontinuous change in distributed force at $z = h$.

3.4.1 Mathematical resolution of flow discontinuities in the outer region

The analysis of chapter 2 showed that in *inviscid* flow force discontinuities at height h lead to discontinuities in the streamwise velocity at height h. This result is equally valid for a force discontinuity in the outer region of the proposed turbulent flow structure. Therefore, given the dependence (3.9) of inner region height l on wavenumber k, for any height h there will be a range of wavenumbers such that the discontinuity lies in the outer region. Hence the Fourier components of perturbation velocity in this wavenumber range will be discontinuous at $z = h$.

Such unphysical flow discontinuities betray a limitation of the asymptotic flow structure as described in §3.3. What happens physically is that in any region of high flow gradients, turbulent stresses become large and dynamically important. Mathematically, therefore, turbulent stresses must be retained in the governing equations near any point of potential discontinuity. To reflect this, the asymptotic flow structure must be modified so as to include new turbulent stress layers around any height where strong force gradients occur outside the inner region.

Hence the analysis of the SML model is presented in two parts. The slowly varying analysis of §3.5 is valid at smaller wavenumbers for which any strong force gradients lie well within the inner region. The rapidly varying analysis of §3.6 considers the idealised case of a uniform force distribution which vanishes discontinously at a height within the outer region, for which a new shear stress layer is added to the flow structure around the discontinuity. By comparing the analyses of §3.5 and §3.6, it becomes clear how their results can be blended together to allow a practical treatment of any number of force discontinuities anywhere within the flow domain.

3.4.2 Effect of a strong elevated shear layer on turbulence

As well as the asymptotic flow structure, the SML turbulence model also ignores any vertical length scales other than height above the ground. This is a physical limitation of the SML model that is addressed by the more general DML turbulence model in

the analysis of §3.8.

3.5 Analysis of slowly varying force distributions

3.5.1 Governing equations

We begin with the steady, incompressible, Reynolds averaged Navier Stokes equations for total (*i.e.* undisturbed + perturbation) pressure, velocities and turbulent stresses, supplemented by a distributed force in the streamwise momentum equation:

$$\rho\hat{\mathbf{u}}^* \cdot \nabla^*\hat{\mathbf{u}}^* + \nabla^*\hat{p}^* = \nabla^* \cdot \hat{\boldsymbol{\tau}}^* - \mathbf{i}f^*, \tag{3.18}$$

$$\nabla^* \cdot \hat{\mathbf{u}}^* = 0. \tag{3.19}$$

The total velocity is the sum of the undisturbed streamwise flow $(U^*, 0)$ and the perturbation velocities (u^*, w^*) due to the force $\mathbf{i}f^*$. Similarly, $\hat{p}^* = P^* + p^*$ and $\hat{\boldsymbol{\tau}}^* = \boldsymbol{T}^* + \boldsymbol{\tau}^*$, but in the undisturbed boundary layer there are no gradients of pressure or turbulent stress, so the constant pressure P^* is dynamically irrelevant and the constant stress tensor $\boldsymbol{T}^*$ serves only to define the friction velocity u_*. Expanding flow quantities into their undisturbed and perturbation parts, neglecting the normal turbulent stress perturbations, and linearising the inertia terms by assuming that $|\mathbf{u}^*(z^*)| \ll U^*(z^*)$, we obtain in component form

$$\rho U^*\frac{\partial u^*}{\partial x^*} + \rho w^*\frac{\partial U^*}{\partial z^*} + \frac{\partial p^*}{\partial x^*} = \frac{\partial \tau^*}{\partial z^*} - f^*, \tag{3.20}$$

$$\rho U^*\frac{\partial w^*}{\partial x^*} + \frac{\partial p^*}{\partial z^*} = \frac{\partial \tau^*}{\partial x^*}, \tag{3.21}$$

$$\frac{\partial u^*}{\partial x^*} + \frac{\partial w^*}{\partial z^*} = 0. \tag{3.22}$$

The coordinates and physical quantities in these equations are non-dimensionalised using the characteristic length and velocity scales defined in §3.2:

$$\begin{aligned} k^* = k/L^*, \qquad & \mathbf{x}^* = L^*\mathbf{x}, \\ U^* = U_o^*U, \qquad & f^* = \rho U_o^{*2} f/L^*, \\ \mathbf{u}^* = U_o^*\mathbf{u}, \qquad & p^* = \rho U_o^{*2} p, \qquad \tau_{ij}^* = \rho u_*^2 \tau_{ij}. \end{aligned} \tag{3.23}$$

The non-dimensionalised equations read

$$U\frac{\partial u}{\partial x} + w\frac{\partial U}{\partial z} + \frac{\partial p}{\partial x} = \epsilon^2\kappa^2\frac{\partial \tau}{\partial z} - f, \tag{3.24}$$

$$U\frac{\partial w}{\partial x} + \frac{\partial p}{\partial z} = \epsilon^2\kappa^2\frac{\partial \tau}{\partial x}, \tag{3.25}$$

$$\frac{\partial u}{\partial x} + \frac{\partial w}{\partial z} = 0. \tag{3.26}$$

The factor $\epsilon^2\kappa^2 = (u_*/U_o^*)^2$ appears here because the stress and inertia terms are non-dimensionalised using different velocity scales. Now the physical quantities in (3.24)–(3.26) are expressed in terms of their Fourier transforms, for example

$$u(x,z) = \int_{-\infty}^{\infty} u(k,z)e^{ikx}dk. \tag{3.27}$$

Note that a physical quantity is represented by the same symbol in both real and Fourier space; where there is any ambiguity as to whether the real space or Fourier space quantity is intended, the intention is clarified by writing the argument list explicitly as in (3.27). After a set of transformations like (3.27), (3.24)–(3.26) become

$$ikUu + wU' + ikp = \epsilon^2\kappa^2\tau' - f, \tag{3.28}$$

$$ikUw + p' = \epsilon^2\kappa^2 ik\tau, \tag{3.29}$$

$$iku + w' = 0. \tag{3.30}$$

Here the primes denote vertical differentiation $\partial/\partial z$.

Throughout the analysis that follows, it is convenient to assume that the wavenumber k is non-negative; this saves a lot of notational trouble involving $|k|$ and $\operatorname{sgn} k$. This assumption is not restrictive since $u(x,z)$, $p(x,z)$ etc. are real, and so their Fourier transforms for negative k may be obtained from those for non-negative k via the Hermitian relationship $u(-k) = [u(k)]^*$ (where the asterisk *here* denotes complex conjugation).

It is not possible to solve (3.28)–(3.30) exactly. Further progress must be made by considering the behaviour of (3.28)–(3.30) in each layer of the flow structure defined in §3.3 and applying the turbulence closure and approximations that are appropriate to each layer.

3.5.2 The shear stress layer

The natural vertical coordinate for the shear stress layer is $\zeta \equiv z/l$. Turbulent shear stresses are modelled by the eddy viscosity closure (3.3), which after non-dimensionalisation (3.23) takes the form

$$\tau = \frac{2z}{\epsilon}\frac{\partial u}{\partial z}. \tag{3.31}$$

Rewriting (3.28)–(3.30) in terms of ζ, making use of this turbulence closure, and writing the incident wind velocity as $U = U_l + \epsilon \ln \zeta$, we obtain

$$ikl(U_l + \epsilon \ln \zeta)u + \epsilon w/\zeta + iklp = 2\epsilon\kappa^2(\zeta u')' - lf, \tag{3.32}$$

$$ikl(U_l + \epsilon \ln \zeta)w + p' = 2ikl\epsilon\kappa^2\zeta u', \tag{3.33}$$

$$iklu + w' = 0. \tag{3.34}$$

Recall that kl, which multiplies many of the terms here, is $O(\epsilon)$. These equations are to be solved asymptotically in the limit $\epsilon \to 0$. The perturbation velocities and pressure are expanded as asymptotic series in ϵ:

$$u = u_o + \epsilon u_1 + \epsilon^2 u_2 + \cdots \tag{3.35}$$

$$w = \epsilon w_1 + \epsilon^2 w_2 + \cdots \tag{3.36}$$

$$p = p_o + \epsilon p_1 + \epsilon^2 p_2 + \cdots \tag{3.37}$$

The continuity equation (3.34) shows that there is no leading order vertical velocity perturbation, hence w_o has been omitted. The vertical momentum equation (3.33) shows that any pressure variation in the SSL must be $O(\epsilon^2)$; hence $p_o' = p_1' = 0$.

There are two mechanisms which give rise to a pressure perturbation in turbulent flow through a distributed force. The first is an inviscid mechanism. In the inviscid analysis, we found that the flow perturbations can be characterised as outflow from a source balanced by a constant velocity deficit in the wake of the force distribution. A pressure perturbation is associated with the source flow part of the inviscid solution. In the turbulent flow analysis, the outer region is quasi-inviscid and we shall see that a large part of the inner region also acts inviscidly, so this inviscid mechanism for

pressure perturbation is just as important for turbulent flow as it is for inviscid flow. A simple scaling analysis shows that this inviscid pressure perturbation is $O(fH/r)$, where r is the distance in real space from the measurement point to the centroid of the force distribution (the apparent origin of the source flow); this is formally $O(1)$ so far as our asymptotic expansion in ϵ is concerned.

The second mechanism is due to turbulent stress effects in the inner region, which give rise to an extra vertical velocity perturbation at $z \approx l$. This extra vertical velocity perturbation appears to the outer region like a wavy surface. An associated pressure perturbation is induced in the outer region, in the same way as in hill flow, and this pressure is transmitted back to the inner region. The extra vertical velocity at $z \approx l$ turns out, however, to be $O(\epsilon^2)$, so the corresponding pressure perturbation is much weaker then that produced by the inviscid mechanism.

Substituting (3.35)–(3.37) into (3.32)–(3.34) we can identify the following equations at $O(\epsilon)$ and $O(\epsilon^2)$:

$$iklU_l u_o - 2\epsilon\kappa^2(\zeta u_o')' = -lf - iklp_o, \tag{3.38}$$

$$iklU_l u_1 - 2\epsilon\kappa^2(\zeta u_1')' = -iklu_o \ln\zeta - \epsilon w_1/\zeta - iklp_1, \tag{3.39}$$

$$p_o' + \epsilon p_1' = 0, \tag{3.40}$$

$$iklU_l w_1 + \epsilon p_2' = 2ikl\kappa^2\zeta u_o', \tag{3.41}$$

$$iklu_o + \epsilon w_1' = 0, \tag{3.42}$$

$$iklu_1 + \epsilon w_2' = 0. \tag{3.43}$$

The first of these equations governs the leading order streamwise perturbation velocity u_o. By means of a change of variables, defining the new Bessel function coordinate Z by

$$Z \equiv e^{3i\pi/4}\sqrt{\frac{2U_l kl\zeta}{\epsilon\kappa^2}}, \tag{3.44}$$

(3.38) is transformed into the Bessel equation

$$u_o'' + \frac{u_o'}{Z} + u_o = \frac{if}{kU_l} - \frac{p_o}{U_l}. \tag{3.45}$$

Solutions to (3.45) are expressed in terms of the Bessel functions $J_o(Z)$ and $K_o(-iZ)$ (Abramowitz & Stegun 1972, chapter 9). This somewhat unusual combination is advantageous for two reasons. Firstly, $J_o(Z)$ and $K_o(-iZ)$ are respectively exponentially large and exponentially small as $|Z| \to \infty$, which is useful when matching with the outer region. Secondly, $J_o(Z)$ and $K_o(-iZ)$ are related to the Kelvin functions: $J_o(Z) = \mathrm{ber}(\mathcal{Z}) + i\,\mathrm{bei}(\mathcal{Z})$ and $K_o(-iZ) = \mathrm{ker}(\mathcal{Z}) + i\,\mathrm{kei}(\mathcal{Z})$ where $\mathcal{Z} \equiv Z\exp(-3i\pi/4) = |Z|$, which is useful in practical implementations of the theory because $\mathrm{ber}(\mathcal{Z})$ etc. are real.

The general solution of (3.45) is

$$\begin{aligned} u_o &= A_o J_o(Z) + B_o K_o(-iZ) - \frac{p_o}{U_l} \\ &\quad + \frac{i}{kU_l}\int_{Z_o}^{Z} Z' f(z')\left\{J_o(Z)K_o(-iZ') - J_o(Z')K_o(-iZ)\right\} dZ', \end{aligned} \tag{3.46}$$

where A_o and B_o are to be determined by matching with the inner surface layer below and the outer region above. The SSL and outer region coordinates are related to each other by $\zeta = kz/(kl) = kz \times O(\epsilon^{-1})$, so an $O(1)$ coordinate for the matching region is given by

$$\chi = \epsilon^{-\alpha} kz \qquad \text{where} \qquad 0 < \alpha < 1. \tag{3.47}$$

In the matching region $|Z|$ therefore becomes large like $\epsilon^{\alpha-1}$, so the terms in (3.46) containing $J_o(Z)$ are exponentially large as $\epsilon \to 0$. Anticipating that there are no exponentially large terms in the outer region solution to match this behaviour, it follows that the coefficients in (3.46) of $J_o(Z)$ must cancel as $|Z| \to \infty$. This matching condition fixes A_o:

$$A_o + \frac{i}{kU_l}\int_{Z_o}^{\infty} Z' f(z') K_o(-iZ') dZ' = 0. \tag{3.48}$$

At $O(\epsilon)$ the governing equation for u_1 is (3.39). The general solution is

$$\begin{aligned} u_1 &= A_1 J_o(Z) + B_1 K_o(-iZ) - \frac{p_1}{U_l} \\ &\quad + \frac{i}{kU_l}\int_{Z_o}^{Z} Z' \left(f_1^{(\mathrm{U})} + f_1^{(\mathrm{w})}\right)\left\{J_o(Z)K_o(-iZ') - J_o(Z')K_o(-iZ)\right\} dZ', \end{aligned} \tag{3.49}$$

where $f_1^{(\mathrm{U})} \equiv iku_o \ln\zeta$ and $f_1^{(\mathrm{w})} \equiv \epsilon w_1/z$. The particular integrals in (3.49) are formally the same as additional force distributions, so we could think of the corrections as contributing to an effective total force distribution

$$f_{\mathrm{eff}} = f + \epsilon f_1^{(\mathrm{U})} + \epsilon f_1^{(\mathrm{w})} + \epsilon^2 f_2 + \cdots. \tag{3.50}$$

The leading order pressure p_o is determined by the original force distribution f, and in the same way the first order pressure perturbation may be split into two parts and ascribed to $f_1^{(\mathrm{U})}$ and $f_1^{(\mathrm{w})}$. Thus the first order streamwise velocity u_1 can be divided into three components:

$$u_1 \equiv u_1^{(\mathrm{cf})} + u_1^{(\mathrm{U})} + u_1^{(\mathrm{w})}, \tag{3.51}$$

where

$$u_1^{(\mathrm{cf})} = B_1 K_o(-iZ), \tag{3.52}$$

$$u_1^{(\mathrm{U})} = A_1^{(\mathrm{U})} J_o(Z) - \frac{p_1^{(\mathrm{U})}}{U_l} + \frac{i}{kU_l}\int_{Z_o}^{Z} Z' f_1^{(\mathrm{U})} \left\{J_o(Z)K_o(-iZ') - J_o(Z')K_o(-iZ)\right\} dZ', \tag{3.53}$$

$$u_1^{(\mathrm{w})} = A_1^{(\mathrm{w})} J_o(Z) - \frac{p_1^{(\mathrm{w})}}{U_l} + \frac{i}{kU_l}\int_{Z_o}^{Z} Z' f_1^{(\mathrm{w})} \left\{J_o(Z)K_o(-iZ') - J_o(Z')K_o(-iZ)\right\} dZ'. \tag{3.54}$$

Then $A_1^{(\mathrm{U})}$ and $A_1^{(\mathrm{w})}$ are determined by equations similar to (3.48), while B_1 is to be determined by matching with the ISL.

3.5.3 The inner surface layer

In the inner surface layer the natural vertical coordinate is $\zeta_i \equiv z/z_o$. Using the turbulence closure (3.31) and rewriting (3.28)–(3.30) in terms of the ISL coordinate ζ_i, we obtain

$$ikz_oUu + \epsilon w/\zeta_i + ikz_o p = 2\epsilon\kappa^2(\zeta_i u')' - z_o f, \tag{3.55}$$

$$ikz_oUw + p' = 2\epsilon\kappa^2 ikz_o\zeta_i u', \tag{3.56}$$

$$ikz_o u + w' = 0, \tag{3.57}$$

primes now indicate differentiation with respect to ζ_i. From (3.12) and (3.14) we can calculate the order of kz_o:

$$kz_o = \frac{kl}{l/z_o} \leq \epsilon e^{-U_l/\epsilon}, \tag{3.58}$$

i.e. kz_o is exponentially small as $\epsilon \to 0$. We could therefore solve (3.55)–(3.57) for the perturbation velocities and pressure expressed as asymptotic series in the small parameter kz_o. However, the SSL analysis contains only algebraically small corrections; hence there will be nothing small enough to match any $O(kz_o)$ corrections from the ISL. It is sufficient therefore to calculate only the leading order ISL solution, which should match the leading order solution in the SSL and all its algebraically small corrections (Belcher 1990).

To obtain the leading order solution (denoted by the subscript i) we neglect all terms that are $O(kz_o)$. The streamwise momentum equation reduces to

$$2\epsilon\kappa^2(\zeta_i u_i')' = z_o f. \tag{3.59}$$

When integrated once (3.59) gives the ISL shear stress:

$$\tau_i = \frac{2z}{\epsilon}\frac{\partial u_i}{\partial z} = \tau_w + \frac{1}{\epsilon^2\kappa^2}\int_{z_o}^{z} f(z')dz'. \tag{3.60}$$

The turbulent stress above a group of obstacles is transmitted to the ground partly through obstacle drag and partly through shear stresses at the ground. (3.60) describes the transfer of drag force between these two mechanisms in the absence of other dynamical contributions to the streamwise momentum balance. A second integration gives the leading order streamwise velocity:

$$u_i = \frac{\epsilon\tau_w}{2}\ln\frac{z}{z_o} + \frac{1}{2\epsilon\kappa^2}\int_{z_o}^{z} f(z')\ln\frac{z}{z'}dz'. \tag{3.61}$$

Reynolds stress gradients are of great practical importance in determining near-surface transport processes such as heat transfer and deposition of pollutants. In the absence of any force in the ISL, (3.60) shows that the turbulent shear stress is constant across the layer. But the ISL is a transcendentally thin layer, so the constancy of τ_i does not exclude the possibility of *algebraically large* stress gradients existing in the

ISL. The unscaled streamwise momentum equation (3.28) gives

$$\epsilon^2\kappa^2\tau_i' = f + iku_i\epsilon \ln\frac{z}{z_o} - \frac{ik\epsilon}{z}\int_{z_o}^{z} u_i(z')\,dz' + ikp_i. \tag{3.62}$$

Substituting for the ISL streamwise perturbation u_i (3.61) and ignoring terms involved the distributed force f (which in practical flows is small very near the ground), we find that

$$\epsilon^2\kappa^2\tau_i' = \frac{ik\epsilon^2\tau_w}{2}\left[\ln^2\frac{z}{z_o} - \ln\frac{z}{z_o} + 1 - \frac{z_o}{z}\right] + ikp_i. \tag{3.63}$$

Equation (3.63), which was also obtained by Hunt *et al.* (1988a) by a different method, shows that there is an $O(1)$ turbulent stress gradient at the ground that matches the streamwise pressure gradient. In the leading order SSL solution this pressure gradient is balanced by the force distribution and streamwise accelerations and the most significant turbulent stress gradient is $O(\epsilon)$. Thus, following Hunt *et al.* (1988a), the ISL may be characterised as a layer where the stress gradient increases dramatically from $O(\epsilon)$ to $O(1)$, as the balance of streamwise momentum changes to meet the surface boundary condition.

3.5.4 Matching the ISL and SSL

To match (3.46) and (3.52)–(3.54) with the ISL solution (3.61), it is convenient to separate out the terms of the SSL solution that are non-zero at $z = z_o$:

$$\begin{aligned} u_o \;=\; & A_oJ_o(Z_o) + B_oK_o(-iZ_o) - \frac{p_o}{U_l} \\ & + A_o\left\{J_o(Z) - J_o(Z_o)\right\} + B_o\left\{K_o(-iZ) - K_o(-iZ_o)\right\} \\ & + \frac{i}{kU_l}\int_{Z_o}^{Z} Z'f(z')\left\{J_o(Z)K_o(-iZ') - J_o(Z')K_o(-iZ)\right\}dZ'. \end{aligned} \tag{3.64}$$

The ISL coordinate ζ_i is related to the SSL coordinate ζ by

$$\zeta_i = \frac{z}{z_o} = \frac{z}{l} \div \frac{z_o}{l} = \zeta e^{U_l/\epsilon}; \tag{3.65}$$

this shows that in the SSL, where $\zeta = O(1)$, the ISL coordinate would be very large, $O(\exp(U_l/\epsilon))$. An $O(1)$ coordinate ϕ for the ISL/SSL matching region is defined by

$$\phi \equiv \zeta e^{\alpha U_l/\epsilon} \qquad \text{where} \qquad 0 \le \alpha \le 1. \tag{3.66}$$

($\alpha = 0$ gives $\phi = \zeta$, placing us in the SSL, while $\alpha = 1$ gives $\phi = \zeta_i$, placing us in the ISL, so an intermediate value of α corresponds to a matching region between these two layers.) In the matching region, $|Z| \sim \zeta^{\frac{1}{2}}$ is exponentially small like $\exp(-\alpha U_l/(2\epsilon))$, so it is appropriate to use small argument expansions (Abramowitz & Stegun 1972, §§9.6 and 9.1) for the Bessel functions in (3.64):

$$J_o(Z) = 1 - \frac{1}{4}Z^2 + O(Z^4), \tag{3.67}$$

$$K_o(-iZ) = -\left\{\gamma + \ln\frac{-iZ}{2}\right\}\left\{1 - \frac{Z^2}{4}\right\} - \frac{Z^2}{4} + O(Z^4, Z^4 \ln Z). \tag{3.68}$$

Using these small argument expansions for the non-constant terms in (3.64), we find that the leading order SSL solution in the matching region takes the form

$$u_o \approx A_o J_o(Z_o) + B_o K_o(-iZ_o) - \frac{p_o}{U_l} - \frac{B_o}{2}\ln\frac{z}{z_o} + \frac{1}{2\epsilon\kappa^2}\int_{z_o}^{z} f(z')\ln\frac{z}{z'}\,dz'. \tag{3.69}$$

Similarly, the first order corrections become

$$u_1^{(\mathrm{cf})} \approx B_1 K_o(-iZ_o) - \frac{B_1}{2}\ln\frac{z}{z_o}, \tag{3.70}$$

$$u_1^{(\mathrm{U})} \approx A_1^{(\mathrm{U})} J_o(Z_o) - \frac{p_1^{(\mathrm{U})}}{U_l} + \frac{1}{2\epsilon\kappa^2}\int_{z_o}^{z} f_1^{(\mathrm{U})}(z')\ln\frac{z}{z'}\,dz', \tag{3.71}$$

$$u_1^{(\mathrm{w})} \approx A_1^{(\mathrm{w})} J_o(Z_o) - \frac{p_1^{(\mathrm{w})}}{U_l} + \frac{1}{2\epsilon\kappa^2}\int_{z_o}^{z} f_1^{(\mathrm{w})}(z')\ln\frac{z}{z'}\,dz', \tag{3.72}$$

The highest order term of the ISL solution (3.61) is $O(\epsilon)$. Hence matching with the ISL means that all the $O(1)$ or higher terms of (3.69)–(3.72) must add to zero. Now $K_o(-iZ_o) \sim \ln(z_o/l) = O(\epsilon^{-1})$, so part of the $u_1^{(\mathrm{cf})}$ correction becomes $O(1)$ as $z/l \to 0$ and contributes to this leading order match:

$$A_o J_o(Z_o) + (B_o + \epsilon B_1) K_o(-iZ_o) - \frac{p_o}{U_l} = 0. \tag{3.73}$$

In (3.73), A_o, $J_o(Z_o)$, B_o, B_1, p_o and U_l are all $O(1)$, while $K_o(-iZ_o)$ is $O(\epsilon^{-1})$; at $O(\epsilon^{-1})$ it follows that $B_o = 0$ and hence that we must reject the term in $K_o(-iZ)$ as a part of the leading order solution. The remaining terms of (3.73), namely

$$A_o J_o(Z_o) + \epsilon B_1 K_o(-iZ_o) - \frac{p_o}{U_l} = 0, \tag{3.74}$$

determine the first order coefficient B_1 in terms of A_o and p_o.

Since all corrections in the ISL are exponentially small, it is necessary to show that the leading order solution in the ISL matches the leading order solution and all its algebraically small corrections in the SSL. For this purpose it is convenient to lump together all contributions to an additional distributed force for the first order correction—

$$f_1 = f_1^{(\mathrm{U})} + f_1^{(\mathrm{w})}, \quad p_1 = p_1^{(\mathrm{U})} + p_1^{(\mathrm{w})}, \quad A_1 = A_1^{(\mathrm{U})} + A_1^{(\mathrm{w})} \tag{3.75}$$

—and similarly for all higher order corrections. The nth order corrections are given by a set of equations like (3.70)–(3.72) and matching at $O(\epsilon^n)$ with the ISL and with the outer region gives

$$A_n J_o(Z_o) + \epsilon B_{n+1} K_o(-iZ_o) - \frac{p_n}{U_l} = 0, \tag{3.76}$$

$$A_n + \frac{i}{kU_l}\int_{Z_o}^{\infty} Z' f_n(z') K_o(-iZ')\, dZ' = 0. \tag{3.77}$$

There are algebraic contributions to the ground shear stress from all orders:

$$\tau_w = -B_1 - \epsilon B_2 - \epsilon^2 B_3 - \ldots \tag{3.78}$$

$$= -\frac{1}{\epsilon^2\kappa^2}\int_{z_o}^{\infty} f(z')\frac{K_o(-iZ')}{K_o(-iZ_o)}\, dz' - \frac{p_o}{\epsilon U_l K_o(-iZ_o)} + O(\epsilon). \tag{3.79}$$

Here we have used (3.48) and (3.74) to express the ground shear stress in terms of the distributed force and the inner region pressure p_o.

The shear stress gradient in the SSL is easily obtained by inspection of the streamwise momentum equations that u_o and u_1 satisfy; thus

$$\epsilon^2\kappa^2\frac{\partial \tau}{\partial z} = ikU(u_o + \epsilon u_1) + f + ik(p_o + \epsilon p_1) + \epsilon w_1 U' - \epsilon^2 ik \ln\zeta u_1 + O(\epsilon^2)$$

$$= ikU u + f + ikp + wU' + O(\epsilon^2). \tag{3.80}$$

It follows that u_o and u_1 have associated stress gradients which match the ISL stress gradient to $O(\epsilon^2)$; clearly the stress gradient of the next order velocity perturbation u_2 will improve the match to $O(\epsilon^3)$, and so on.

Finally we consider the particular integrals over distributed force f that appear in (3.61) and (3.69), and the additional force integrals that contribute to higher order corrections like (3.71). The former integrals match exactly. Corrections arising from the latter integrals are algebraically small within the SSL, but become exponentially small in the ISL/SSL matching region. Note that all contributions to additional distributed forces contain the factor k. Then in the matching region defined by (3.66) the typical force integral becomes

$$\int_{z_o}^{z} f_n(z') \ln \frac{z}{z'} \, dz' = kle^{-\alpha U_l/\epsilon} \int_{\phi_o}^{\phi} k^{-1} f_n(\phi') \ln \frac{\phi}{\phi'} \, d\phi' = O(\epsilon e^{-\alpha U_l/\epsilon}), \tag{3.81}$$

which is exponentially small. Hence the only $O(\epsilon^n)$ SSL corrections that remain $O(\epsilon^n)$ in the matching region are contributions to the constant turbulent stress and are matched by the ISL's τ_w as given by (3.78).

Jackson & Hunt (1975), in their analysis of flow over a low hill, did not subdivide their inner region, but instead used solutions like those of the SSL here all the way down to the ground. Consider applying the ground boundary condition $u(z_o) = 0$ to the SSL solution. At $O(1)$, (3.46) gives

$$A_o + B_o K_o(-iZ_o) - p_o/U_l = 0. \tag{3.82}$$

A_o, B_o, p_o and U_l are by definition $O(1)$, but $K_o(-iZ_o) \sim \ln l/z_o = O(\epsilon^{-1})$. Hence B_o must be zero. Since A_o and p_o are not free to be determined by (3.82) with $B_o = 0$, it follows that the leading order SSL solution cannot satisfy $u_o(z_o) = 0$. Hence the need for an inner surface layer very close to the ground.

Put more formally, the SSL solution cannot satisfy the ground boundary condition because the ground at $z = z_o$ lies far below the region where the definition of the SSL, $z/l = O(1)$, is reasonable. In the SSL, functions of the $O(1)$ layer coordinates ζ and Z ought themselves to be $O(1)$; but as $z \to z_o$ we have $\zeta = z/l = O(\exp(-U_l/\epsilon)) \ll O(1)$ and consequently $K_o(-iZ) = O(\epsilon^{-1}) \gg O(1)$.

Therefore, as first recognised by Sykes (1980) and later developed by Hunt *et al.* (1988a), correct treatment of the ground boundary condition is impossible without an ISL analysis.

3.5.5 SSL shear stress and vertical velocity perturbations

The scaling of shear stress means that nth order streamwise velocity perturbations are associated via the turbulence closure model (3.31) with $(n-1)$th order shear stress perturbations. Thus the shear stress perturbation τ is expanded as

$$\tau = \epsilon^{-1}\tau_{-1} + \tau_o + \epsilon\tau_1 + \cdots. \tag{3.83}$$

By differentiation of (3.45) (with $B_o = 0$) and (3.70), the shear stress profiles associated with u_o and $u_1^{(\mathrm{cf})}$ are

$$\tau_{-1} = -A_o Z J_1(Z) - \frac{iZ}{kU_l}\int_{Z_o}^{Z} Z' f(z')\left\{J_1(Z)K_o(-iZ') + iJ_o(Z')K_1(-iZ)\right\} dZ', \tag{3.84}$$

$$\tau_o^{(\mathrm{cf})} = iB_1 Z K_1(-iZ). \tag{3.85}$$

The corresponding vertical velocity perturbations are conveniently calculated by using continuity to rewrite the streamwise momentum equations as

$$-\epsilon U_l w_1' - \epsilon\kappa^2\tau_{-1}' = -ikl p_o - lf, \tag{3.86}$$

$$-\epsilon U_l w_2'^{(\mathrm{cf})} - \epsilon\kappa^2\tau_o'^{(\mathrm{cf})} = 0. \tag{3.87}$$

Hence by integration,

$$\epsilon U_l w_1 = ikp_o(z - z_o) + \int_{z_o}^{z} f(z')\,dz' - \epsilon\kappa^2\{\tau_{-1} + A_o Z_o J_1(Z_o)\}, \tag{3.88}$$

$$\epsilon U_l w_2^{(\mathrm{cf})} = -\epsilon\kappa^2\{\tau_o^{(\mathrm{cf})} - iB_1 Z_o K_1(-iZ_o)\}. \tag{3.89}$$

At the top of the inner region, where the shear stresses τ_{-1} and $\tau_o^{(\mathrm{cf})}$ decay exponentially, equation (3.88) shows that there is no first order contribution to the vertical velocity from Reynolds stress effects. This means that although turbulent stress effects are important at leading order *within* the SSL, they make no contribution to the leading order match with the outer region. The terms in (3.88) which do contribute to a vertical velocity at the top of the inner region represent purely inviscid behaviour. At second order Reynolds stress effects produce a perturbation vertical velocity whose limiting value is

$$\epsilon^2 w_2^{(\mathrm{cf})} \to i\epsilon^2\kappa^2 B_1 Z_o K_1(-iZ_o)/U_l \approx -\epsilon^2\kappa^2 B_1/U_l \approx \epsilon^2\kappa^2\tau_w/U_l. \tag{3.90}$$

3.5.6 Discussion of the inner region solutions

The leading order solutions $\{u_o, \tau_{-1}, w_1\}$ represent a largely inviscid response to the applied distributed force. Leading order Reynolds stresses are significant within the SSL but not at its lower or upper boundaries. The streamwise perturbation velocity u_o tends to a constant non-zero value as $z/l \to 0$, hence the leading order solution alone does not match with the ISL.

At $O(\epsilon)$ there are three first order corrections, labelled (cf), (U) and (w). The (cf) correction behaves logarithmically as $z/l \to 0$, giving a ground shear stress and combining with the leading order solution to match with the ISL. At leading order, therefore, the sum $u_o + \epsilon u_1^{(\mathrm{cf})}$ is a uniformly valid approximation for the complete inner region.

The (U) and (w) corrections are conveniently represented as perturbations resulting from additional distributed forces. They arise respectively from approximating the incident velocity $U(z)$ as a constant, $U(z) \approx U_l$, and from neglect of the $O(\epsilon)$ incident velocity shear dU/dz, and are calculated as the results of additional force distributions $\epsilon f_1^{(\mathrm{U})} \equiv \epsilon i k u_o \ln \zeta$ and $\epsilon f_1^{(\mathrm{w})} \equiv \epsilon^2 w_1 / z$.

Further evaluation of the general expressions (3.71) and (3.72), for the flow perturbations due to $f_1^{(\mathrm{U})}$ and $f_1^{(\mathrm{w})}$, is not attempted here since (i) the results would not be very illuminating and (ii) a practical implementation of this analysis can compute these expressions using the leading order results already presented (but for additional $O(\epsilon)$ force distributions). It will be necessary, however, to consider all the $O(\epsilon)$ corrections at the top of the inner region when matching with the outer region.

3.5.7 Analysis of the outer region

Take the curl of (3.28)–(3.30) and neglect the turbulent stress gradients, to obtain the governing equations for the outer region,

$$w'' - \left(k^2 + \frac{U''}{U}\right) w = \frac{f'}{U}, \tag{3.91}$$

$$ikUu + wU' + ikp = -f, \tag{3.92}$$

$$ikUw + p' = 0, \tag{3.93}$$

$$iku + w' = 0. \tag{3.94}$$

Equations (3.92)–(3.94) may be used to calculate the perturbation pressure and streamwise velocity once (3.91) has been solved for the vertical velocity w. For a logarithmic boundary layer, the incident shear term in (3.91) may be written

$$\frac{U''w}{U} = \frac{-\epsilon w}{z^2 U}, \tag{3.95}$$

so it is appropriate to solve (3.91) by writing w as an asymptotic series in ϵ:

$$w = w_o + \epsilon w_1 + \epsilon^2 w_2 + \ldots \tag{3.96}$$

Substitute (3.96) into (3.91) and group terms of similar order, then

$$w_o'' - k^2 w_o = \frac{f'}{U}, \tag{3.97}$$

$$w_1'' - k^2 w_1 = \frac{-w_o}{z^2 U}, \tag{3.98}$$

and so on. The general solution to (3.97) is

$$w_o = C_o e^{-kz} + D_o e^{kz} + \int_{z_o}^{z} \frac{f(z')\cosh k(z-z')}{U(z')}\, dz', \tag{3.99}$$

where the lower limit of the integral has been chosen for later convenience. Then by continuity the leading order streamwise velocity is

$$u_o = -iC_o e^{-kz} + iD_o e^{kz} + \frac{if}{kU} + i\int_{z_o}^{z} \frac{f(z')\sinh k(z-z')}{U(z')}\, dz', \tag{3.100}$$

and the leading order pressure is

$$p_o = \frac{if}{k} - Uu_o = iUC_o e^{-kz} - iUD_o e^{kz} - iU\int_{z_o}^{z} \frac{f(z')\sinh k(z-z')}{U(z')}\, dz'. \tag{3.101}$$

The constant D_o is determined by applying the upper boundary condition that w_o must be bounded as $kz \to \infty$. This means that the terms in $\exp(kz)$ must cancel each other above the force distribution, hence

$$D_o + \frac{1}{2}\int_{z_o}^{\infty} \frac{f(z')\exp(-kz')}{U(z')}\, dz' = 0. \tag{3.102}$$

It remains to determine the other constant C_o and the inner region pressure p_o by matching (3.99)–(3.101) with the corresponding SSL solutions.

At first order, (3.98) shows that the $O(\epsilon)$ vertical velocity correction can be represented as the result of a secondary force distribution ϵf_1 defined by

$$f_1' = -w_o/z^2. \tag{3.103}$$

This correction is similar to the (w) correction in the inner region.

3.5.8 Matching the inner and outer regions

The detailed matching of the inner and outer regions is analysed by focusing on the vertical velocity perturbation w. Matching is a two-part process. The complementary functions of the inner and outer solutions contain constants of integration that remain to be determined by matching and by applying boundary conditions. The particular integrals, on the other hand, are already fully specified. The matching process includes checking that the particular integrals are mutually consistent, which provides a useful check on the individual layer analyses.

The shear stress layer is defined by $z/l = O(1)$, so $kz = O(\epsilon)$ in the SSL, while in the outer region $kz = O(1)$. Therefore an $O(1)$ matching coordinate, χ, for the overlap region between the SSL and the outer region is defined by

$$kz = \epsilon^\alpha \chi, \qquad \text{where} \quad 0 \leq \alpha \leq 1. \tag{3.104}$$

Hence the outer region coordinate kz is small in the overlap region where $\chi = O(1)$. The SSL Bessel function coordinate Z in the overlap region is

$$Z = \frac{\exp(3i\pi/4)}{\kappa}\sqrt{\frac{2U_l kz}{\epsilon}} = \frac{\exp(3i\pi/4)}{\kappa}\sqrt{2U_l\chi}\,\epsilon^{\alpha/2-1}, \tag{3.105}$$

which is large.

Consider the behaviour of the SSL vertical velocities (3.88) and (3.89) in the overlap region. For large $|Z|$, $K_o(-iZ)$ and $K_1(-iZ)$ tend exponentially to zero while $J_o(Z)$ and $J_1(Z)$ become exponentially large. Thus $\tau_o^{(\mathrm{cf})}$ is negligible. τ_{-1} is also

negligible if the matching region lies above the top of the force distribution, since the $J_1(Z)$ terms in (3.84) cancel each other (this condition determines A_o).

If the matching region does contain any distributed force, τ_{-1} can be rewritten:

$$\tau_{-1} = \frac{iZJ_1(Z)}{kU_l}\int_Z^\infty Z'f(z')K_o(-iZ')\,dZ' + \frac{ZK_1(-iZ)}{kU_l}\int_{Z_o}^Z Z'f(z')J_o(Z')\,dZ'. \quad (3.106)$$

As discussed in §3.4, the present analysis applies to slowly varying force distributions for which any strong force gradients $\partial f/\partial z$ lie well within the inner region. Hence $f(z)$ does not vary rapidly in the matching region. Then the exponential behaviour of the Bessel functions in (3.106) means that the two integrals derive mainly from contributions very close to $Z' = Z$, and τ_{-1} can be evaluated approximately in the matching region by moving $f(z)$ outside the integrals. Hence (3.106) becomes

$$\tau_{-1} \approx \frac{Z_oJ_1(Z_o)ZK_1(-iZ)f(z)}{kU_l}, \quad (3.107)$$

which is exponentially small. Hence τ_{-1} is also negligible in the matching region even if the force distribution extends above the inner region.

Thus the vertical velocity that matches at $O(\epsilon)$ and $O(\epsilon^2)$ with the outer region is

$$\epsilon w_1 + \epsilon^2 w_2^{(\mathrm{cf})} \approx \frac{ikp_o(z-z_o)}{U_l} + \int_{z_o}^z \frac{f(z')}{U_l}\,dz' + \frac{i\epsilon^2\kappa^2 B_1 Z_o K_1(-iZ_o)}{U_l}. \quad (3.108)$$

Similar arguments applied to u_o and $u_1^{(\mathrm{cf})}$ show that the SSL streamwise perturbation velocity for matching with the outer region is

$$u_o \approx \frac{if}{kU_l} - \frac{p_o}{U_l}, \quad (3.109)$$

which could equally have been obtained from (3.108) by continuity.

The inner/outer region matching is enhanced by consideration of the various $O(\epsilon)$ corrections to the inner and outer region solutions. In the outer region, the $O(\epsilon)$ correction due to neglect of incident velocity shear is represented as the result of an secondary force distribution given by (3.103). Noting the exponential behaviour of w_o, partial integration of (3.103) gives

$$f_1 = \frac{w_o}{z}\{1 + O(kz)\}; \quad (3.110)$$

hence as $kz \to 0$ the first order correction in the outer region matches with the (w) correction in the inner region. Therefore it is convenient to leave (3.110) and the inner region (w) correction to one side. Practical implementations of this analysis can calculate these corrections for the whole flow domain as the result of a uniformly valid additional force distribution defined by (3.103).

The inner region (cf) correction has already been shown to be negligible in the matching region. The inner region (U) correction is not negligible and has no counterpart in the outer region because it is not necessary to approximate $U(z)$ to obtain the outer region solutions. Therefore we calculate the effect of the (U) correction on the inner region solutions within the matching region. It is easiest to consider the streamwise velocity perturbation. Equation (3.109) shows that in the matching region,

$$u_1^{(\mathrm{U})} = \frac{if_1^{(\mathrm{U})}}{kU_l} - \frac{p_1^{(\mathrm{U})}}{U_l} = \frac{-u_o \ln(z/l)}{U_l} - \frac{p_1^{(\mathrm{U})}}{U_l}, \tag{3.111}$$

where the pressure perturbation $p_1^{(\mathrm{U})}$ is associated with the additional force $f_1^{(\mathrm{U})}$ in the same way as p_o arises from the imposed force distribution f. Therefore the corrected SSL solution in the matching region is

$$\begin{aligned} u_o + \epsilon u_1^{(\mathrm{U})} &= u_o\left(1 - \frac{\epsilon \ln(z/l)}{U_l}\right) - \frac{\epsilon p_1^{(\mathrm{U})}}{U_l} = \frac{u_o U_l}{U(z)} - \frac{\epsilon p_1^{(\mathrm{U})}}{U_l} + O(\epsilon^2) \\ &= \frac{if}{kU} - \frac{p_o}{U} + O(\epsilon), \end{aligned} \tag{3.112}$$

i.e. the effect of incorporating the (U) correction is to replace occurences of U_l by $U(z)$. This might have been anticipated simply because $U(z)$ varies much more slowly than the perturbation velocities u and w. Correcting the vertical velocity perturbations in a similar way (noting that $dU/dz = O(\epsilon)$), we obtain

$$\epsilon w_1 + \epsilon^2 w_2^{(\mathrm{cf})} + \epsilon^2 w_2^{(\mathrm{U})} \approx \frac{ikp_o(z - z_o)}{U} + \int_{z_o}^{z} \frac{f(z')}{U(z')}\, dz' + \frac{i\epsilon^2\kappa^2 B_1 Z_o K_1(-iZ_o)}{U}. \tag{3.113}$$

These solutions can now be matched with those in the outer region, each incorporating the same approximations and corrections.

The form of the outer region solutions in the matching region is obtained by

substituting the $O(1)$ coordinate χ into (3.99)–(3.101):

$$u_o^{(\mathrm{OR})} = i(D_o - C_o) + i\epsilon^\alpha (C_o + D_o)\chi + \frac{if}{kU} + O(\epsilon^{2\alpha}), \tag{3.114}$$

$$w_o^{(\mathrm{OR})} = C_o + D_o + \epsilon^\alpha (D_o - C_o)\chi + \int_{z_o}^{z} \frac{f(z')}{U(z')}\, dz' + O(\epsilon^{2\alpha}), \tag{3.115}$$

$$p_o^{(\mathrm{OR})} = iU(C_o - D_o) - i\epsilon^\alpha (C_o + D_o)\chi + O(\epsilon^{2\alpha}). \tag{3.116}$$

Comparison of (3.112) and (3.114), or of (3.113) and (3.115), shows that the particular force integrals already match at leading order. Then matching complementary functions in the inner and outer region solutions for perturbation velocities gives the following relations between C_o, D_o and the inner region pressure p_o:

$$C_o + D_o = \frac{i\epsilon^2 \kappa^2 B_1 Z_o K_1(-iZ_o)}{U_\alpha}, \tag{3.117}$$

$$i(C_o - D_o) = \frac{p_o}{U_\alpha}. \tag{3.118}$$

Here U_α is the characteristic velocity of the matching region. Together with the upper boundary condition (3.102), these relations determine all the remaining unknowns. We note that the $O(\epsilon^\alpha)$ linear term in (3.115) matches exactly the linear pressure term of the SSL solution (3.113), which in practice considerably improves the inner/outer region matching.

3.5.9 A uniformly valid approximation

The matching process shows that the constant and linear terms of the SSL vertical velocity match the first two terms of the Maclaurin expansion of the outer region's $C_o \exp(-kz) + D_o \exp(kz)$ for small kz. This suggests that a uniformly valid approximation may be formed by replacing the constant and linear terms of the SSL solution by $C_o \exp(-kz) + D_o \exp(kz)$ while retaining the other SSL terms that are important in the inner region but decay exponentially in the outer region:

$$w^{(\mathrm{UVA})} = C_o e^{-kz} + D_o e^{kz} + \int_{z_o}^{z} \frac{f(z') \cosh k(z - z')}{U_g(z')}\, dz' - \frac{\epsilon^2 \kappa^2 \tau^{(\mathrm{UVA})}}{U_l}, \tag{3.119}$$

where $\tau^{(\mathrm{UVA})} = \epsilon^{-1}\tau_{-1} + \tau_o^{(\mathrm{cf})}$. The "blend velocity" $U_g(z)$ is defined such that $U_g(z) \to U_l$ for $z \ll l$ and $U_g(z) \to U(z)$ for $z \gg l$; then the force integral in

(3.119) is a uniformly valid approximation to both inner and outer region particular integrals. A uniformly valid streamwise velocity perturbation may be obtained from (3.119) by continuity.

This approximation includes the leading order solution and all $O(\epsilon)$ corrections except that due to effects of incident velocity shear. Physically this correction accounts for the vertical displacement of upstream vorticity by $w^{(\mathrm{UVA})}$. It may be calculated as the leading order response to an extra distributed force $\epsilon f_1^{(\mathrm{w})} \equiv \epsilon w^{(\mathrm{UVA})}/z$.

3.6 Analysis of rapidly varying force distributions

In this second part of the SML analysis there is a strong force gradient outside the inner region, which was excluded from the analysis of §3.5 for the reasons discussed in §3.4.

3.6.1 A modified flow structure

If used incorrectly for a force distribution that is discontinuous in the outer region, the analysis of §3.5 gives a corresponding discontinuity in the streamwise perturbation velocity. In a real flow this is not permissible. What happens in practice is that regions of rapid variation locally create turbulent stresses that are dynamically important and must be included in the calculation, even though the flow outside these regions of rapid variation may behave inviscidly. Consequently the flow structure described in §3.3 must be modified to include new turbulent stress layers around any height where strong force gradients occur outside the inner region. Such a modified flow structure is illustrated in figure 3.2 for the case where just one new layer is required around the height h. In order to establish the precise effects of this new flow structure, it suffices to consider the canonical force distribution

$$\begin{aligned} f &= 1, \qquad z_o \leq z \leq h, \\ f &= 0, \qquad z > h. \end{aligned} \tag{3.120}$$

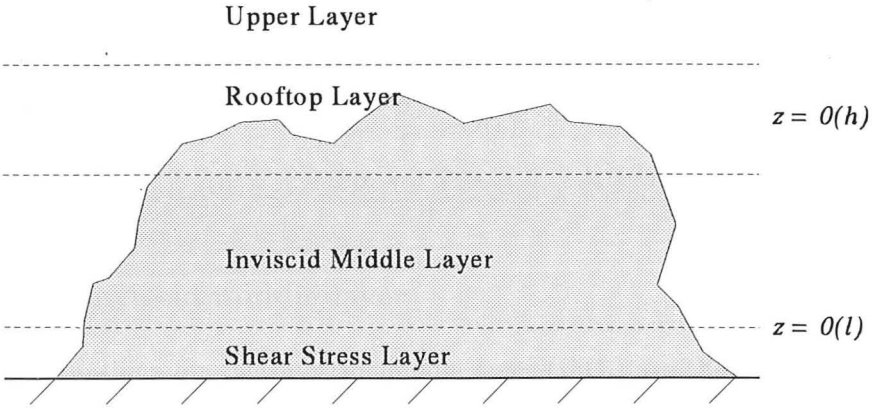

Figure 3.2: Modified flow structure for large wavenumbers such that $l \ll h$.

Much of the detailed analysis of the perturbations induced by this force distribution is similar to that of §3.5 and so will not be repeated unnecessarily. In the following subsections we concentrate on the differences from the analysis for slowly varying force distributions.

3.6.2 The inner surface and shear stress layers

The ISL and SSL analyses proceed as in §§3.5.3–3.5.6, but now the force is constant throughout these layers; hence uniformly valid solutions for the inner region are

$$u_o + \epsilon u_1^{(\mathrm{cf})} = \epsilon B_1 K_o(-iZ) - \frac{p_o}{U_l} + \frac{i}{kU_l}\left\{1 + Z_o J_1(Z_o) K_o(-iZ)\right\}, \tag{3.121}$$

$$\epsilon w_1 + \epsilon^2 w_2^{(\mathrm{cf})} = \frac{(ikp_o + 1)(z - z_o)}{U_l} - \frac{\epsilon^2\kappa^2(\tau_o^{(\mathrm{cf})} - iB_1 Z_o K_1(-iZ_o))}{U_l},$$

where

$$\tau_o^{(\mathrm{cf})} = iB_1 Z K_1(-iZ).$$

B_1 and p_o are related by the ISL/SSL matching condition (3.74) with

$$A_o = \frac{Z_o K_1(-iZ_o)}{kU_l}. \tag{3.122}$$

Thus as $z/l \to \infty$, the velocity perturbations that must match with the layer above, including the $\epsilon f_1^{(\mathrm{U})}$ corrections as in §3.5.8, are

$$u_o + \epsilon u_1^{(\mathrm{U})} \approx \frac{i}{kU} - \frac{p_o}{U} + O(\epsilon). \tag{3.123}$$

$$\epsilon w_1 + \epsilon^2 w_2^{(\mathrm{cf})} + \epsilon^2 w_2^{(\mathrm{U})} \approx \frac{(ikp_o + 1)(z - z_o)}{U} + \frac{i\epsilon^2\kappa^2 B_1 Z_o K_1(-iZ_o)}{U}. \tag{3.124}$$

3.6.3 The inviscid middle layer

Governing equations for the inviscid middle layer (IML) are the same as those used for the outer region analysis of §3.5.7. For a constant force, the general solutions are

$$w_o = C_o e^{-kz} + D_o e^{kz} + \int_{z_o}^{z} \frac{\cosh k(z - z')}{U(z')}\, dz', \tag{3.125}$$

$$u_o = -iC_o e^{-kz} + iD_o e^{kz} + \frac{i}{kU} + i\int_{z_o}^{z} \frac{\sinh k(z - z')}{U(z')}\, dz', \tag{3.126}$$

$$p_o = \frac{i}{k} - Uu_o = iUC_o e^{-kz} - iUD_o e^{kz} - iU\int_{z_o}^{z} \frac{\sinh k(z - z')}{U(z')}\, dz'. \tag{3.127}$$

Matching between the SSL and the IML proceeds exactly as between the inner and outer regions in §3.5.8, the only difference being that D_o is not yet determined. Hence the two matching conditions (3.117) and (3.118) link p_o, C_o and D_o as in §3.5. A third relation will follow from matching with the rooftop layer around $z \approx h$. To find the IML perturbations that match with the rooftop layer, the appropriate limiting process is $k(h - z) \to 0$. Therefore we substitute $kz = kh - \epsilon^\alpha \psi$, where $0 \le \alpha \le 1$ and $\psi = O(1)$, into (3.125)–(3.127) and obtain

$$w_o = C_o e^{-kh} + D_o e^{kh} + \epsilon^\alpha \psi (C_o e^{-kh} - D_o e^{kh}) - \frac{\epsilon^\alpha(\psi - \psi_o)}{kU_h} + O(\epsilon^{2\alpha}), \tag{3.128}$$

$$u_o = \frac{i}{kU_h} - iC_o e^{-kh} + iD_o e^{kh} + O(\epsilon^\alpha), \tag{3.129}$$

$$p_o = \frac{i}{k} - U_h u_o = iU_h C_o e^{-kh} - iU_h D_o e^{kh} + O(\epsilon^\alpha). \tag{3.130}$$

3.6.4 The rooftop layer

The rooftop layer (RL) requires new consideration. The effect of a discontinuity in f at $z = h$ is that the mean flow changes rapidly near $z = h$ and so turbulent stresses

become important in a region of the flow where they would otherwise be negligible. Mathematically, the shear stress gradient $\partial\tau/\partial z \approx \Delta\tau/\Delta z$ is large because the vertical length scale Δz over which the shear stress changes is smaller than it would otherwise be at a height h above the ground. Thus the rooftop layer is constructed by defining a new vertical coordinate relative to h and acknowledging that strong perturbation stress and velocity gradients may exist over distances that are $O(1)$ in the new coordinate.

To deduce the scaling of the new vertical coordinate ζ_h and the thickness of the rooftop layer, write

$$z = h + \epsilon^{\beta}\zeta_h/k, \tag{3.131}$$

$$U(z) \approx U_h + \epsilon^{\beta+1}\zeta_h/(kh). \tag{3.132}$$

These definitions are substituted into the streamwise momentum equation (3.32), which then becomes

$$ik\left(U_h + \frac{\epsilon^{\beta+1}\zeta_h}{kh}\right)u + \frac{\epsilon w}{h} + ikp = 2\epsilon^{1-2\beta}\kappa^2 k^2 h u'' + 2\epsilon^{1-\beta}\kappa^2 k^2(\zeta_h u')' - f, \tag{3.133}$$

where the prime indicates differentiation with respect to ζ_h. Of the two stress terms on the right hand side of (3.133), the first is larger and is of similar order to the advection term when $kh\epsilon^{1-2\beta} = O(1)$. Hence the vertical thickness l_r of the rooftop layer is

$$l_r = \epsilon^{\beta}/k = O(\sqrt{\epsilon h/k}) \approx O(\sqrt{hl}). \tag{3.134}$$

At leading order the pressure across the RL is a constant, p_h, since $kl_r = O(\epsilon^{\beta})$. (Although it is not necessarily the same as the constant leading order pressure in the SSL, because pressure may vary dramatically across the inviscid middle layer.) Equation (3.133) shows that the vertical velocity term $\epsilon w/h$ is negligible as in the SSL but for a different reason. In the SSL the incident velocity shear ϵ/z may be large, but proximity to the ground means that w itself is small. In the RL w may be significant, in fact we know that u and w are of similar order in the inviscid layer below, but the incident velocity shear ϵ/h is very small. Thus the leading order form of (3.133) is identical to that of the SSL governing equation, except that the reference

velocity and pressure are different. At leading order the general solution is

$$u_o = h_2 K_o(-iY) - \frac{p_h}{U_h} + \frac{i}{kU_h}\int_{Y_h}^{Y} Y' f(z')\left\{J_o(Y)K_o(-iY') - J_o(Y')K_o(-iY)\right\} dY'. \tag{3.135}$$

The new coordinate Y is defined by

$$Y \equiv e^{3i\pi/4}\sqrt{\frac{2U_h k l \zeta}{\epsilon\kappa^2}}; \tag{3.136}$$

here Y is used rather than Z to emphasise that the velocity scale in the definition is U_h rather than U_l. A possible term in $J_o(Y)$ has been omitted from (3.135) because the particular integral has been written so as to vanish for $z > h$. Below $z = h$ (3.135) becomes

$$u_o = h_2 K_o(-iY) - \frac{p_h}{U_h} + \frac{i}{kU_h}\left\{i - Y_h K_1(-iY_h)J_o(Y) + iY_h J_1(Y_h)K_o(-iY)\right\}, \quad z < h. \tag{3.137}$$

The Bessel function coordinate Y is very large in the RL, since $h/l \gg 1$. It follows that the Bessel functions around $z \approx h$ are either growing or decaying exponentially. Moving downwards from $z = h$, the terms in $K_o(-iY)$ grow exponentially. Since there is no similar exponential behaviour for these terms to match in the IML, their coefficients must cancel each other:

$$h_2 + \frac{iY_h J_1(Y_h)}{kU_h} = 0. \tag{3.138}$$

Thus the RL solution for $z < h$ reduces to

$$u_o = \frac{1}{kU_h}\left\{i - Y_h K_1(-iY_h)J_o(Y)\right\} - \frac{p_h}{U_h}, \quad z < h, \tag{3.139}$$

while that for $z > h$ is

$$u_o = -\frac{iY_h J_1(Y_h)}{kU_h}K_o(-iY) - \frac{p_h}{U_h}, \quad z > h. \tag{3.140}$$

In (3.139), the Bessel function term decays exponentially like $\exp(\sqrt{z} - \sqrt{h})$ as the RL coordinate $\zeta_h \to -\infty$ for matching with the IML. Then matching the IML and

RL streamwise velocities proceeds as in earlier examples, to give the rooftop pressure p_h as

$$p_h = iU_h(C_o e^{-kh} - D_o e^{kh}). \tag{3.141}$$

The change in vertical velocity w across the RL due to the shear stress correction terms is

$$\begin{aligned}\Delta w^{(\mathrm{RL})} &= \frac{\epsilon\kappa^2 Y_h}{kU_h^2}\left\{-K_1(-iY_h)\left[Y'J_1(Y')\right]_{Y_o}^{Y_h} - iJ_1(Y_h)\left[-iY'K_1(-iY')\right]_{Y_h}^{\infty}\right\} \\ &= \frac{\epsilon\kappa^2 Y_h K_1(-iY_h)Y_o J_1(Y_o)}{kU_h^2},\end{aligned} \tag{3.142}$$

which is exponentially small on several counts. Therefore the limiting values of vertical perturbation velocity above and below the RL are equal. Hence the streamwise and vertical velocities above the RL are

$$u_o^{(\mathrm{RL})} = -p_h/U_h, \tag{3.143}$$

$$w_o^{(\mathrm{RL})} = C_o e^{-kh} + D_o e^{kh}. \tag{3.144}$$

These must match the upper layer solution given by

$$w_o^{(\mathrm{UL})} = g_1 e^{-kz}, \tag{3.145}$$

$$u_o^{(\mathrm{UL})} = -ig_1 e^{-kz}. \tag{3.146}$$

Hence the final matching conditions are

$$g_1 e^{-kh} = C_o e^{-kh} + D_o e^{kh}, \tag{3.147}$$

$$-ig_1 e^{-kh} = -p_h/U_h, \tag{3.148}$$

$$\Rightarrow \quad i(C_o e^{-kh} + D_o e^{kh}) = p_h/U_h. \tag{3.149}$$

(3.141) and (3.149) together imply that $D_o = 0$ and that

$$p_h/U_h = iC_o e^{-kh} = e^{-kh} p_o/U_\alpha. \tag{3.150}$$

3.6.5 Comparison with a naive small k solution

By a "naive" solution we mean one which is obtained if we ignore the difficulties that motivated this large wavenumber analysis and blindly apply the small wavenumber solution of §3.5 to the current canonical force distribution. Substituting the canonical force distribution (3.120) into the uniformly valid small wavenumber solution (3.119), we obtain for $z < h$

$$\begin{aligned} w^{(\mathrm{UVA})} &= C_o e^{-kz} + D_o e^{kz} + \int_{z_o}^{z} \frac{\cosh k(z-z')}{U_g(z')}\, dz' \\ &\quad - \frac{\epsilon\kappa^2 Z J_1(Z) Z_h K_1(-iZ_h)}{kU_l^2} - \frac{i\epsilon^2\kappa^2 B_1 Z K_1(-iZ)}{U_l}, \end{aligned} \tag{3.151}$$

and for $z > h$

$$\begin{aligned} w^{(\mathrm{UVA})} &= C_o e^{-kz} + D_o e^{kz} + \int_{z_o}^{h} \frac{\cosh k(z-z')}{U_g(z')}\, dz' \\ &\quad - \frac{\epsilon\kappa^2 Z K_1(-iZ) Z_h J_1(Z_h)}{kU_l^2} - \frac{i\epsilon^2\kappa^2 B_1 Z K_1(-iZ)}{U_l}. \end{aligned} \tag{3.152}$$

The streamwise perturbation velocity is obtained by continuity. For $z < h$

$$\begin{aligned} u^{(\mathrm{UVA})} &= -iC_o e^{-kz} + iD_o e^{kz} + \int_{z_o}^{z} \frac{i\sinh k(z-z')}{U_g(z')}\, dz' + \frac{i}{kU_g(z)} \\ &\quad - \frac{J_o(Z) Z_h K_1(-iZ_h)}{kU_l} + \epsilon B_1 K_o(-iZ), \end{aligned} \tag{3.153}$$

and for $z > h$

$$\begin{aligned} u^{(\mathrm{UVA})} &= -iC_o e^{-kz} + iD_o e^{kz} + \int_{z_o}^{h} \frac{i\sinh k(z-z')}{U_g(z')}\, dz' \\ &\quad - \frac{iK_o(-iZ) Z_h J_1(Z_h)}{kU_l} + \epsilon B_1 K_o(-iZ). \end{aligned} \tag{3.154}$$

(3.153) and (3.154) show that the naive solution for $u^{(\mathrm{UVA})}$ is discontinuous at $z = h$ because the jump in the inviscid response terms, $i/(kU_g(h))$, is not cancelled exactly by the jump in the stress gradient terms, $-i/(kU_l)$. These terms *do* cancel each other under the conditions of the small wavenumber analysis, because then h lies well within the inner region and so $U_g(h) = U_l$, given the definition of $U_g(z)$ in §3.5.9; in the large wavenumber case, however, we have $h \gg l$ and $U_g(h) > U_l$.

Let us compare (3.151)–(3.154) with the solutions obtained for the five layers of the large wavenumber analysis in §§3.6.2–3.6.4. The IML solution for leading order pressure (3.127) shows that the first three terms of (3.153) are $-p(z)/U(z)$, local pressure divided by incident velocity. This tends at the bottom of the IML to $-p_o/U_l$, where p_o is the constant SSL pressure. In the SSL, therefore, noting that $U_g(z) \approx U_l$ and that $J_o(Z)K_1(-iZ_h)$ is exponentially small because $z \ll h$, (3.153) becomes identical to the large k SSL solution (3.121). In the IML, $J_o(Z)K_1(-iZ_h)$ is still exponentially small because $z \ll h$, but now $K_o(-iZ)$ is also small because $z \gg l$. Hence all the turbulent stress terms of (3.153) become negligible and the surviving inviscid response terms are plainly identical to the large k IML solution (3.126).

In the $z < h$ half of the RL, z is now close enough to h for $J_o(Z)K_1(-iZ_h)$ to become important, while $K_o(-iZ)$ remains negligible. The first three terms of (3.153) now give $-p_h/U_h$, where p_h and U_h are the constant pressure and incident velocity for the rooftop layer. Therefore the naive solution (3.153) has exactly the same form as the large k RL solution (3.139), except that the large k RL solution uses the local value of incident velocity, U_h, while the naive solution uses the value U_l from far below at $z \approx l$. This applies both to explicit appearances of U_l or U_h in the solutions and to the use of U_l or U_h in the definition of the Bessel function coordinates Z and Y. Exactly the same is true in the $z > h$ half of the RL: the naive solution and the large k solution (3.140) have identical forms but use different values for the incident velocity.

3.6.6 A uniform approximation for all wavenumbers

This detailed comparison shows that we can in fact obtain a uniformly valid approximation for all wavenumbers by means of a simple modification to the small wavenumber solutions (3.151)–(3.154): the SSL incident velocity U_l is replaced wherever it occurs by the blend velocity $U_g(z)$. The definition of Bessel function coordinate Z becomes

$$Z \equiv e^{3i\pi/4}\sqrt{\frac{2U_g(z)kz}{\epsilon\kappa^2}} \tag{3.155}$$

and explicit occurrences of U_l are also replaced by $U_g(z)$. When, as in the small wavenumber analysis, turbulent stresses are important only within the inner region, this replacement has no effect, since $U_g(z) \approx U_l$ in the inner region. When turbulent stresses become important outside the inner region, for example if there is a strong force gradient around $z = h \gg l$, the replacement modifies the small wavenumber solutions such that they become identical to the detailed solutions from a large wavenumber analysis.

Two characteristics of this simple modification should be noted. Firstly, its effect is similar to the effect in §3.5.8 of incorporating the (U) correction into the original SSL solutions. The replacement of a fixed characteristic velocity U_l by a varying velocity $U_g(z)$ might be justified in general terms by arguing that the perturbations in the SSL vary much more quickly than the incident velocity profile $U(z)$ and hence that any errors introduced by the replacement will be small. This explains why the (U) correction, which allows for the incident velocity profile being $U(z)$ rather than U_l, takes the form it does. The same argument is implicit in the IML solution, since $U(z)$ does not require approximation there.

Secondly, the modification makes no direct reference to the height h whence the problems arise. This is a very important feature. It justifies our use of the canonical force distribution (3.120) and shows that the same modification applies equally well to force distributions which may include strong force gradients at a number of different heights.

3.7 Sample results

To illustrate the analysis we present small and large wavenumber responses to a distributed force whose drag coefficient is constant up to the height $h^* = 60\text{mm}$ and then vanishes; consequently the force in $z_o^* \leq z^* \leq h^*$ varies as the square of incident velocity. The incident velocity is logarithmic with friction velocity $u_* = 0.64\text{ms}^{-1}$ and roughness height $z_o^* = 0.4\text{mm}$. For a single wavenumber k, real and imaginary parts of the results for a given quantity ϕ show the progression of that quantity in passing

through a sinusoidally varying force distribution with wavenumber k: $\mathrm{Re}\{\phi\}$ is the actual profile at points where the resistance is a maximum and $\mathrm{Im}\{\phi\}$ is the actual profile at points where the resistance is zero and increasing; see figure 3.3.

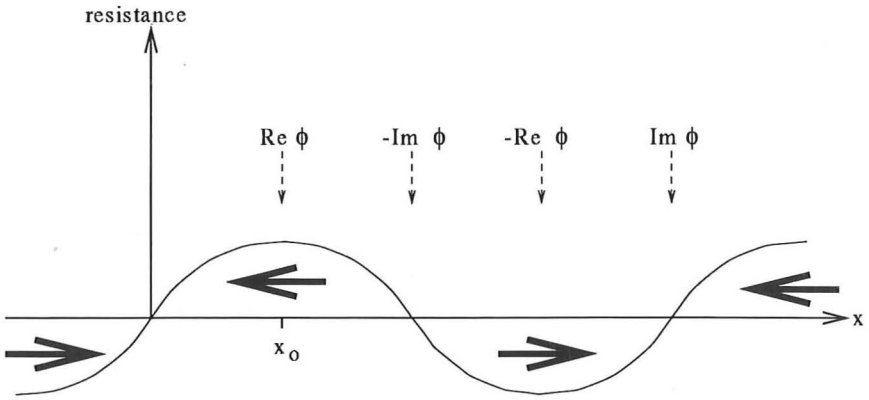

Figure 3.3: Real and imaginary parts of a solution represent the actual profile at different stages of passage through a sinusoidally varying resistance. The general profile at streamwise location x is $\mathrm{Re}\{\phi\}\cos k(x-x_o) - \mathrm{Im}\{\phi\}\sin k(x-x_o)$, where x_o is a location of maximum resistance.

3.7.1 Matching between the inner and outer regions

Figures 3.4 and 3.5 illustrate small and large wavenumber matching respectively. Each figure shows real and imaginary parts of the vertical velocity w as given by the inner region solution (3.88, 3.89), the outer region solution (3.99) and the uniformly valid approximation (3.119). In figure 3.4 $l^* = 0.65$m so that $l^* \gg h^*$ and significant force gradients are contained within the inner region. In figure 3.5 $l^* = 0.035$m so that $l^* \ll h^*$: the rooftop layer around h^* is noticeable as a region where the gradient of w varies rapidly. In both cases matching between inner and outer regions is good, such that the uniformly valid approximation asymptotes correctly to the inner and outer region solutions for $z \ll l$ and $z \gg l$ and makes a smooth transition between them for $z = O(l)$.

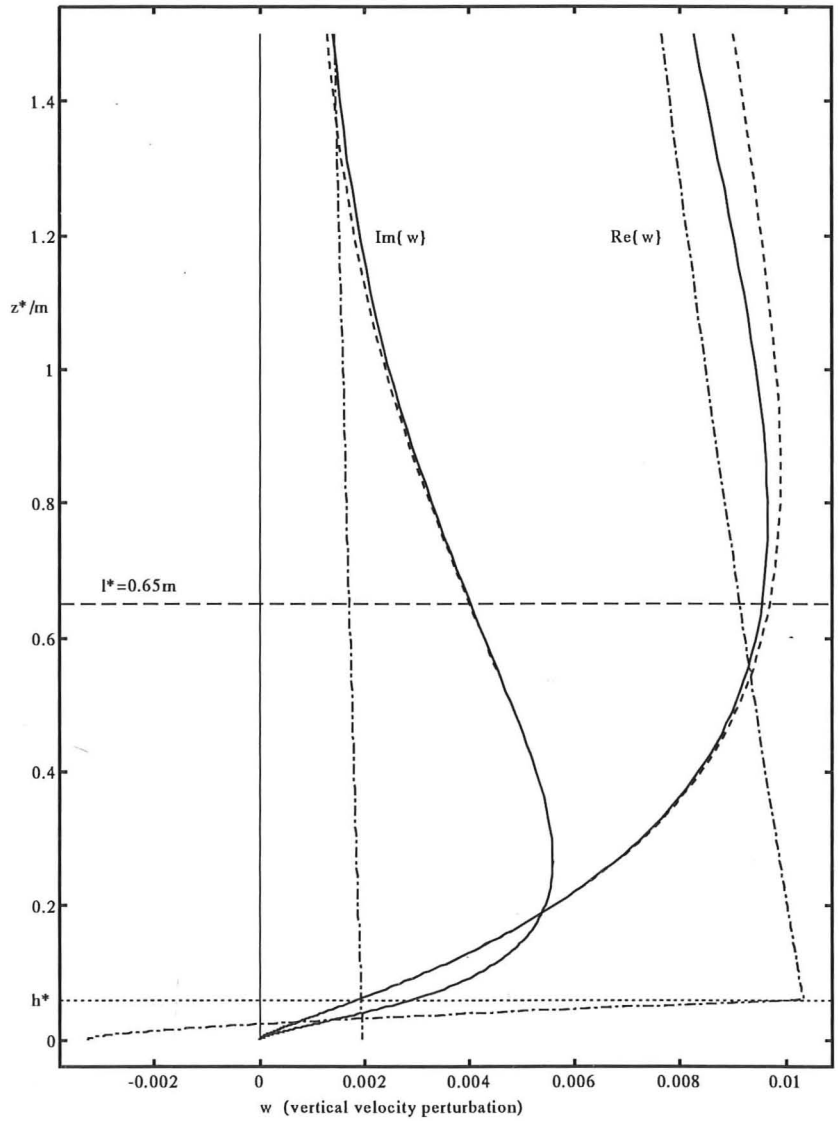

Figure 3.4: Illustration of inner/outer region matching at small wavenumbers, showing real (to the right) and imaginary (to the left) parts of the vertical velocity perturbation w. Single dashed lines show the inner region solution; double dashed lines show the outer region solution; solid lines show the uniformly valid approximation.

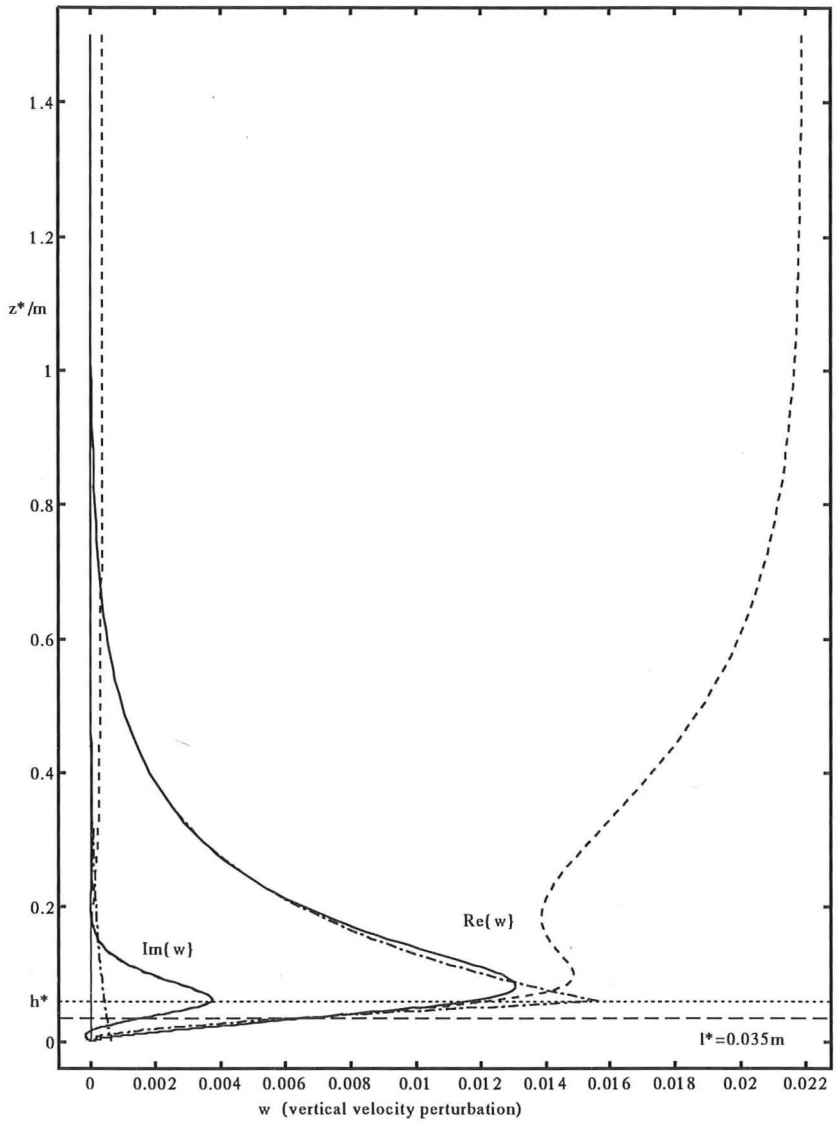

Figure 3.5: Illustration of inner/outer region matching at large wavenumbers, showing real (to the right) and imaginary (to the left) parts of the vertical velocity perturbation w. Single dashed lines show the inner region solution; double dashed lines show the outer region solution; solid lines show the uniformly valid approximation.

3.7.2 Small and large wavenumber responses

Figures 3.6–3.9 show the uniformly valid perturbation velocities, pressure and turbulent shear stress that comprise the response to a slowly varying force distribution. Dashed lines show the effect of including the $O(\epsilon)$ incident velocity shear correction. Notice how the spread of streamwise velocity defect increases as the flow moves downstream from the location of maximum resistance (profile = $\mathrm{Re}\, u$) to that of zero resistance (profile = $-\mathrm{Im}\, u$), showing the diffusive effects of turbulent stress. Correspondingly, $-\mathrm{Im}\, \tau$ shows a constant stress layer above $z^* = h^*$ which is not evident in the $\mathrm{Re}\, \tau$ profile further upstream.

Figures 3.10–3.13 present similar results for a rapidly varying force distribution. Here the flow is quasi-inviscid, except for turbulent stress effects which meet the no-slip condition at the ground and smooth out sharp gradients in the rooftop layer. Hence the streamwise velocity is largely confined to $z_o^* \leq z^* \leq h^*$, turbulent stress is small except near the ground and near $z^* = h^*$, and the pressure profile is like that associated with outflow from a source.

The effect of the incident velocity shear correction is generally to increase the magnitude of the streamwise velocity perturbations. In $z^* < h^*$ the *deceleration* due to resistance is increased by this correction, while in $z^* > h^*$ at large wavenumbers the *acceleration* over the top of the distribution is increased. Similarly, in turbulent flow over a low hill the incident shear correction increases the speed-up over the crest of the hill.

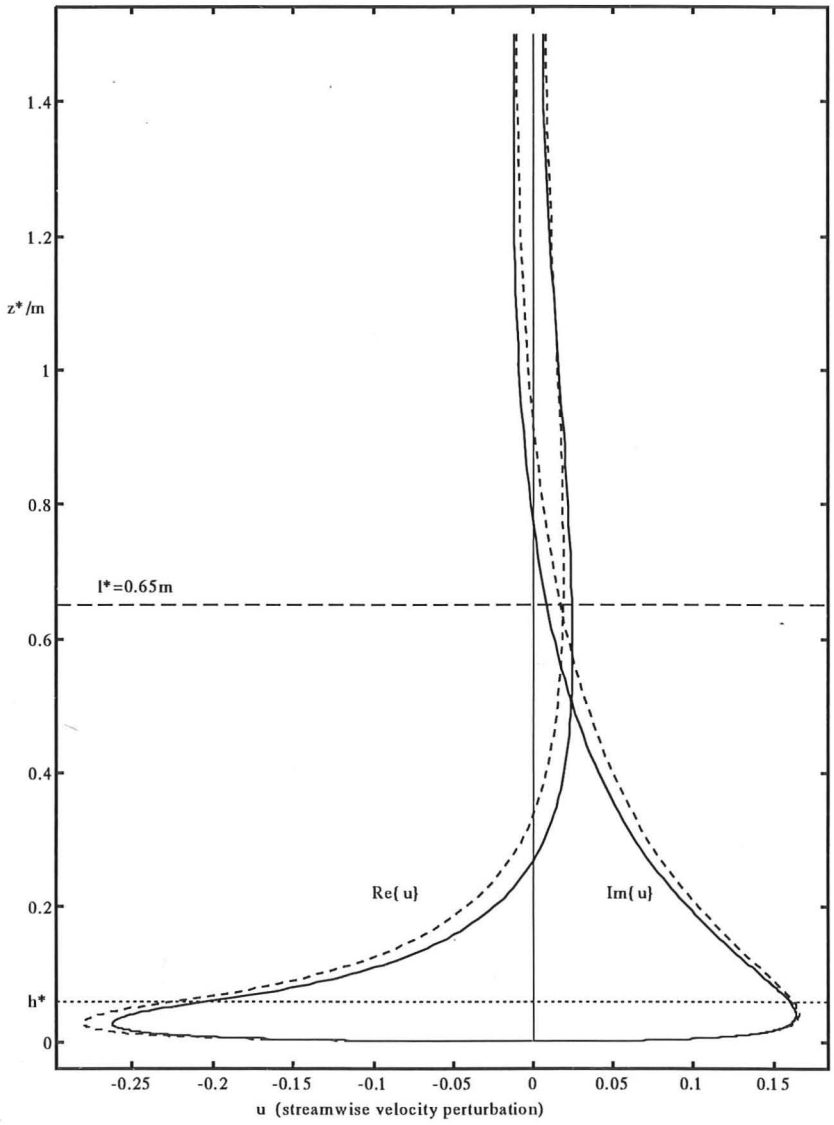

Figure 3.6: Perturbation streamwise velocity at small wavenumbers: real part to the left, imaginary part to the right. Dashed lines show the effect of including the incident velocity shear correction.

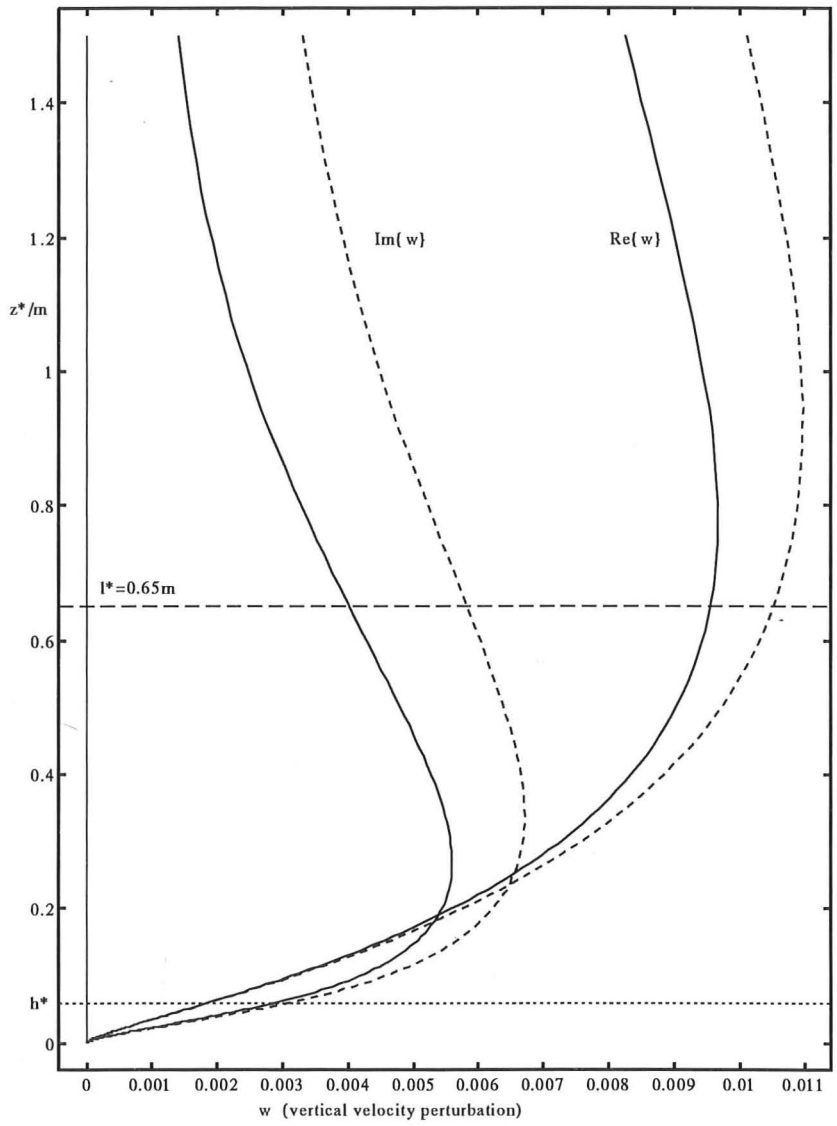

Figure 3.7: Perturbation vertical velocity at small wavenumbers: real part to the right, imaginary part to the left. Dashed lines show the effect of including the incident velocity shear correction.

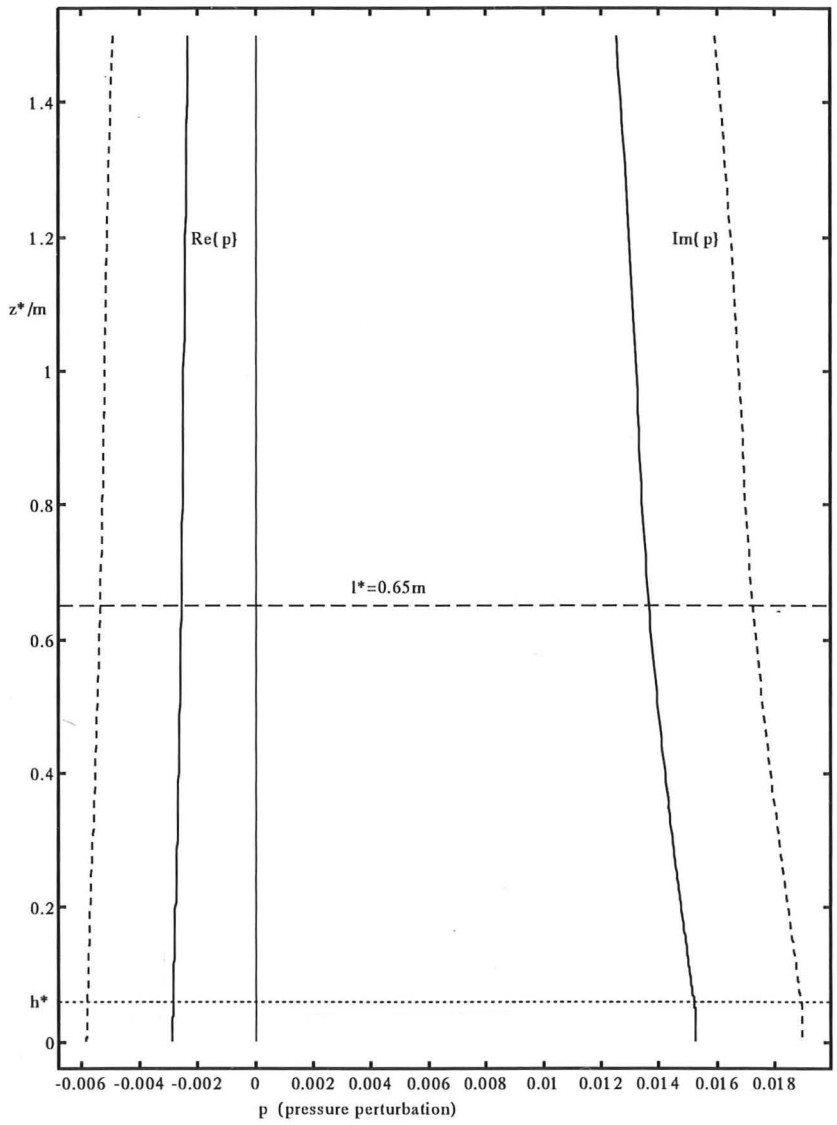

Figure 3.8: Perturbation pressure at small wavenumbers: real part to the left, imaginary part to the right. Dashed lines show the effect of including the incident velocity shear correction.

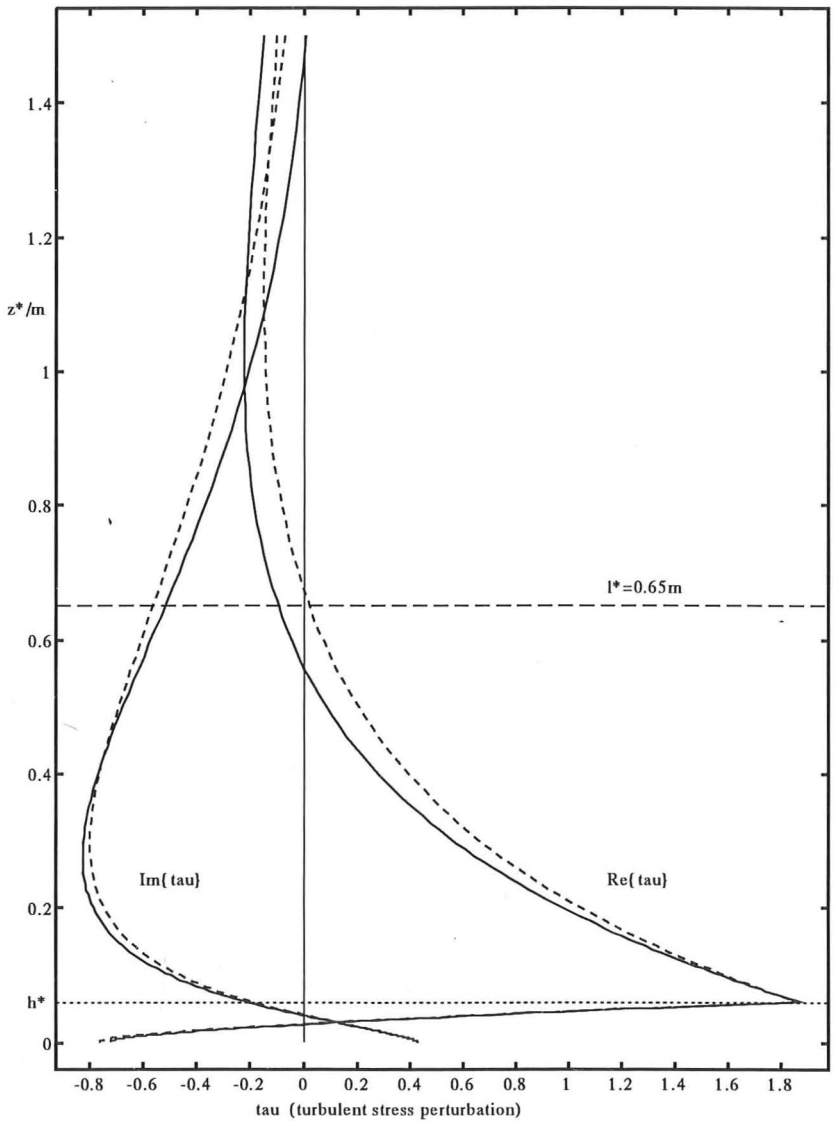

Figure 3.9: Perturbation shear stress at small wavenumbers: real part to the right, imaginary part to the left. Dashed lines show the effect of including the incident velocity shear correction.

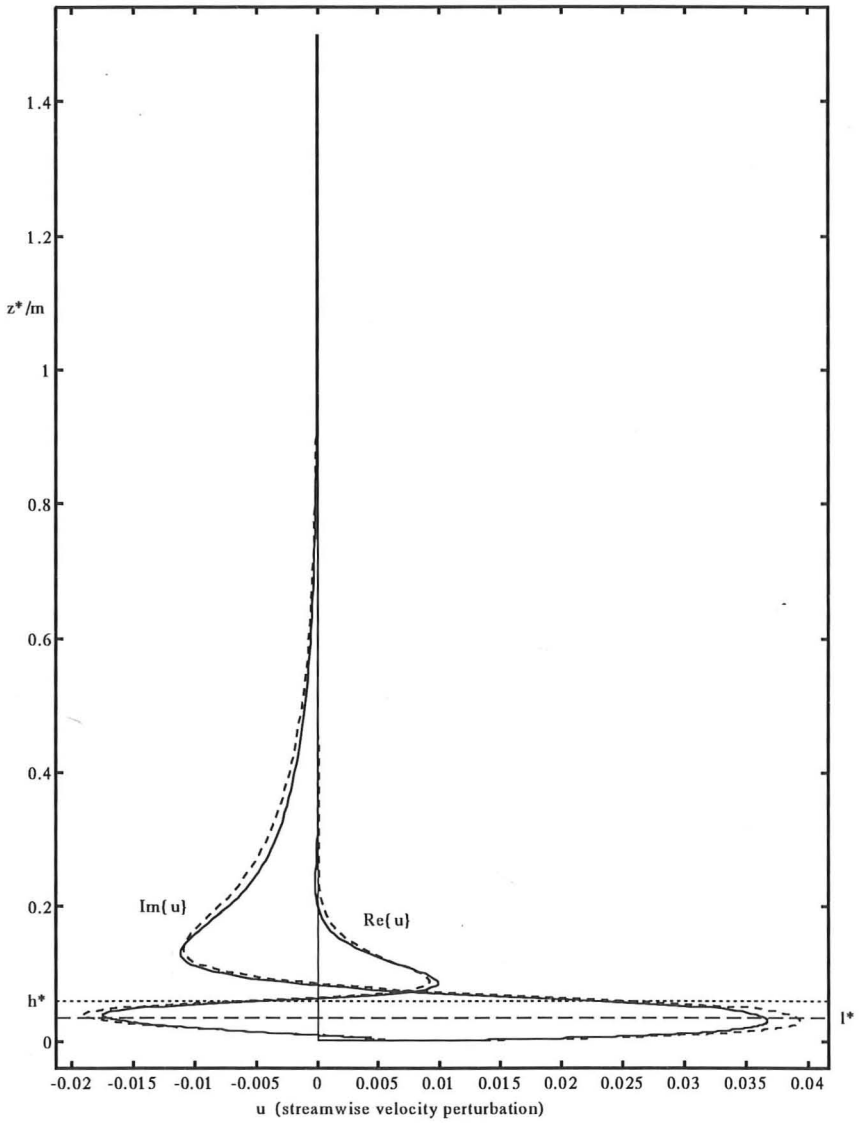

Figure 3.10: Perturbation streamwise velocity at large wavenumbers: real part to the left in $z^* < h^*$, imaginary part to the right. Dashed lines show the effect of including the incident velocity shear correction.

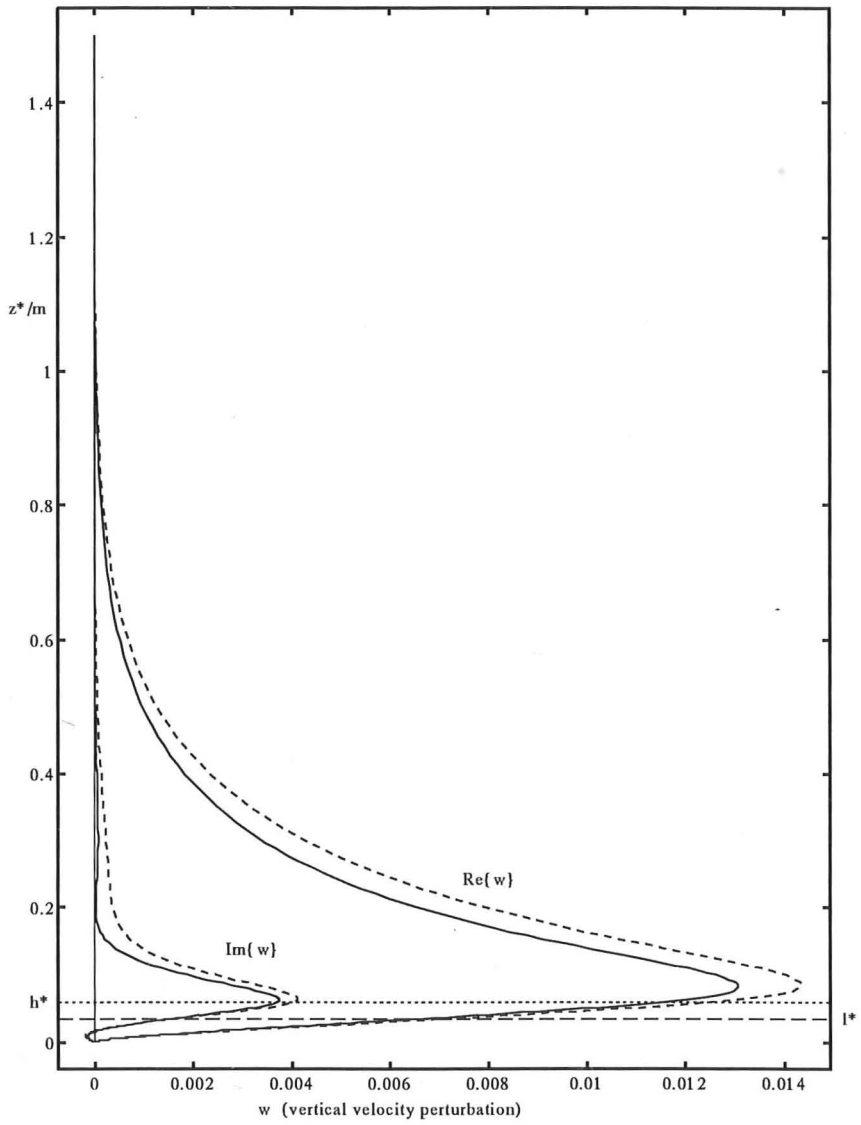

Figure 3.11: Perturbation vertical velocity at large wavenumbers: real part to the right, imaginary part to the left. Dashed lines show the effect of including the incident velocity shear correction.

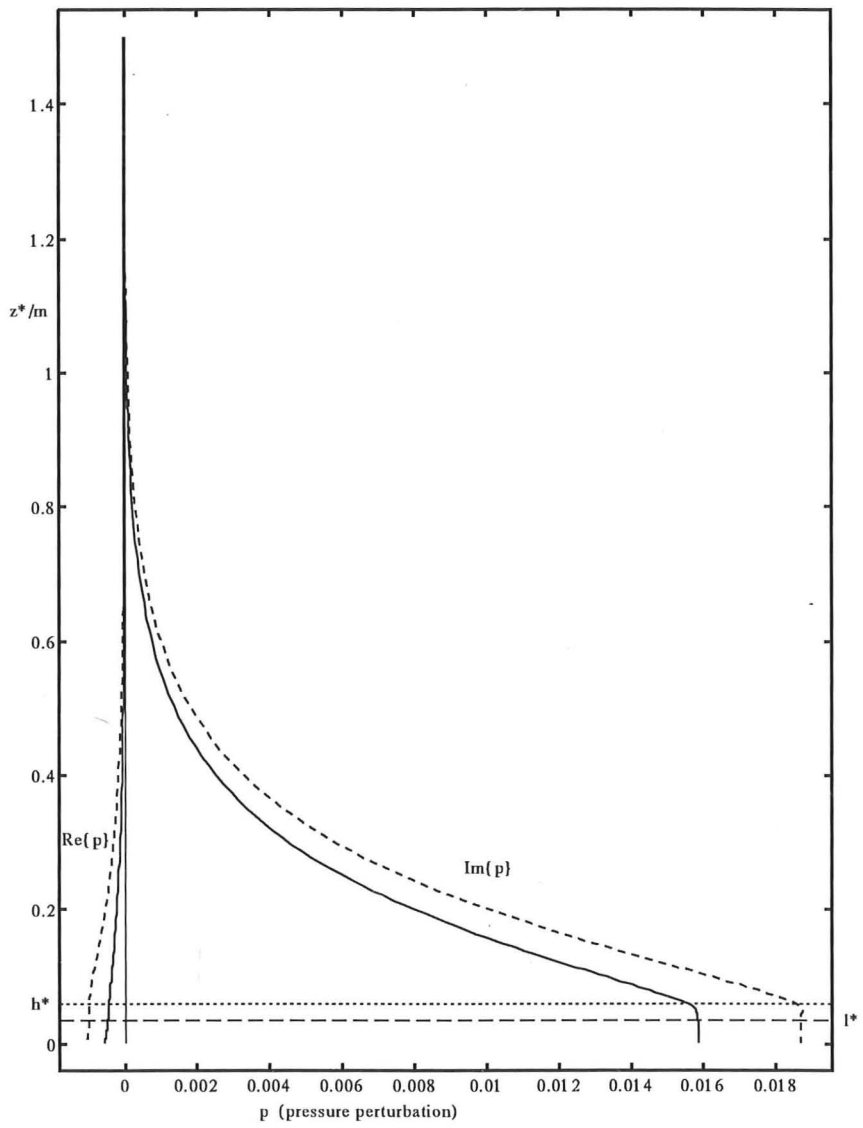

Figure 3.12: Perturbation pressure at large wavenumbers: real part to the left, imaginary part to the right. Dashed lines show the effect of including the incident velocity shear correction.

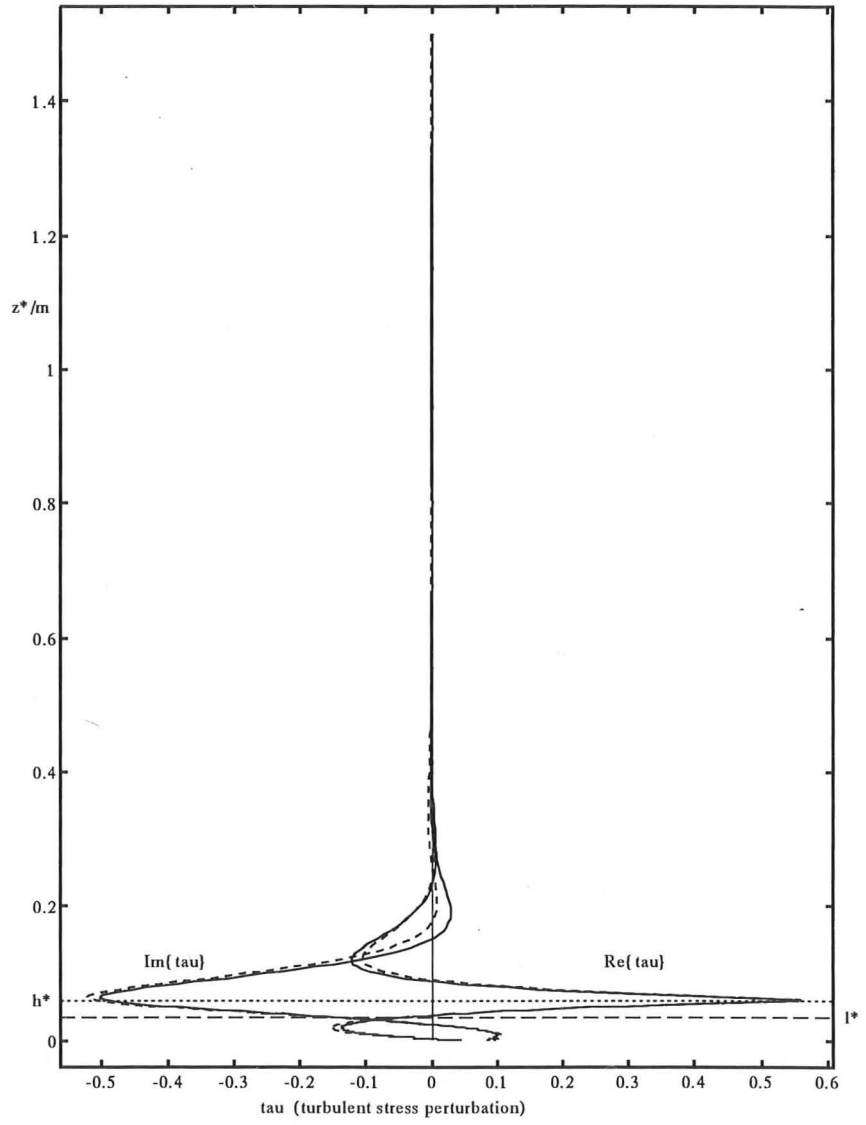

Figure 3.13: Perturbation shear stress at large wavenumbers: real part to the right, imaginary part to the left. Dashed lines show the effect of including the incident velocity shear correction.

3.8 The displaced mixing length turbulence model

According to the discussion of §3.1, the SML turbulence model becomes invalid if mean flow changes are strong enough to change the structure of the turbulence from that in the incident flow. In this section a new turbulence model is developed that takes into account such strong effects of mean flow changes on the turbulence. This "displaced" mixing length model is then used in a new analysis of the flow field perturbations due to a region of distributed resistance.

3.8.1 Effects of a rooftop shear layer

When the buildings in a group have approximately equal heights, the force distribution used to model them has a well-defined, coherent "rooftop," where the distributed force decreases rapidly from its maximum value to zero.

The inviscid response to such a force distribution (chapter 2) includes a strong shear layer around the rooftop height, in which the vertical gradient of streamwise velocity increases following the flow in proportion to the local distributed force gradient:

$$\frac{\partial}{\partial x}\frac{\partial u}{\partial z} \propto \frac{\partial f}{\partial z}. \tag{3.156}$$

In the limit in which the distributed force is discontinuous at the rooftop height, the inviscid response streamwise velocity is discontinuous also. According to the model of §§3.5–3.6, the rooftop shear layer's strength is reduced in the turbulent flow by the mixing action of turbulent shear stresses, but the shear layer is still strong enough to dominate flow around the rooftop height.

Such strong shear layers can have a significant effect upon the turbulence above and below them. Two quite different mechanisms both suggest that a strong shear layer acts to block turbulent motions across it. Firstly there is the dissipation mechanism described by Hunt *et al.* (1988b) and Belcher *et al.* (1991a, 1991b) and illustrated schematically in figure 3.14. Turbulent eddies that enter the shear layer are stretched out by the shear flow to an elongated shape. Hence vertical velocity gradients are amplified and turbulent dissipation increases. The shear flow inhibits motion of tur-

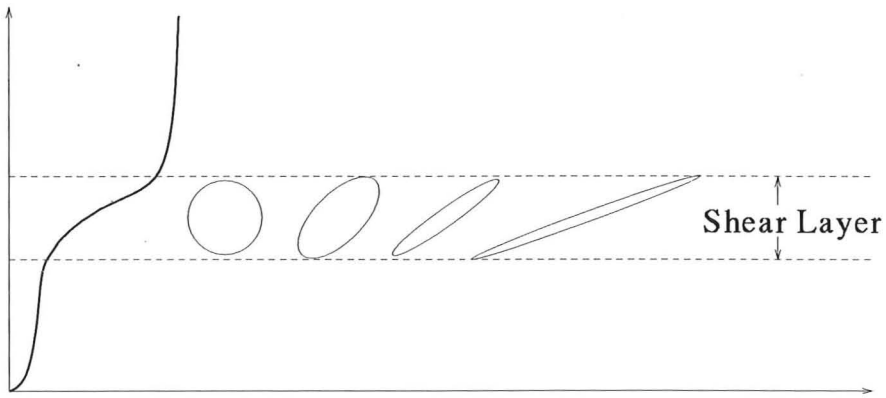

Figure 3.14: The effect of a strong shear layer in increasing turbulent dissipation.

bulent eddies across the shear layer and leads to weak correlation between the flows above and below the shear layer. The increased turbulent dissipation within the shear layer can be modelled as a reduction in the turbulent mixing/dissipation length scale; hence the above authors' shear-dependent mixing length model,

$$\lambda_m^{-1} = \frac{A_B}{\kappa z} + \frac{A_s}{u_*}\frac{\partial U}{\partial z}, \tag{3.157}$$

known as the Shear Blocking Mixing Length model.

Secondly, recent studies by Craik (1991) and Hunt (unpublished) investigate a purely inviscid effect of strong shear layers, illustrated schematically in figure 3.15. Inviscid analysis of a travelling linear disturbance above a vortex sheet shows that there is no induced disturbance *below* the vortex sheet if the phase speed of the disturbance equals the advection velocity U. Extrapolation of this result to the case of turbulent eddies advected by the mean flow above a strong shear layer again suggests that a shear layer acts to block turbulent motions across it and hence provides a reference level for the turbulence above and below.

The effects of these blocking mechanisms will now be investigated in the context of flow through a group of buildings.

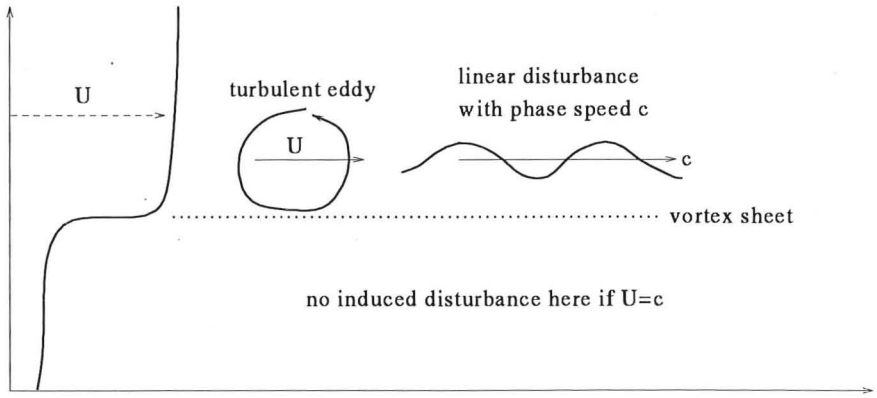

Figure 3.15: The effect of a travelling linear disturbance above a vortex sheet.

3.8.2 The shear layer produced by a group of buildings

There is good reason to suspect that the distributed force model actually underestimates the strength of the rooftop shear layer. To obtain a physical picture of how shear layers are created, it is useful to step back from the distributed resistance model and consider explicitly a group of obstacles in a turbulent boundary layer (figure 3.16). Vorticity created along an obstacle's upper surface is shed from the trailing edge of that surface to form a thin shear layer (cf. the experiments on single surface-mounted obstacles by Castro & Robins 1977). This vorticity is advected downstream towards the next obstacle and also diffuses vertically, so that the shear layer spreads. The shear layer spreads more down towards the ground than upwards because average wind speeds between the obstacles are much lower than those just above them, and because the shed vortices are deflected downwards by their own induced velocity field. Immediately above each building's roof, turbulent eddies are blocked by the roof surface and so the length scale of the turbulence should scale on height above the roof. Hence turbulent mixing here is much less vigorous than that in the SML model used in §§3.2–3.7 and the rooftop surface shear layers are much more concentrated in reality than in the model. Therefore the rooftop shear layer as a whole, comprising boundary layers on building roofs and free shear layers between buildings, is likely to be rather

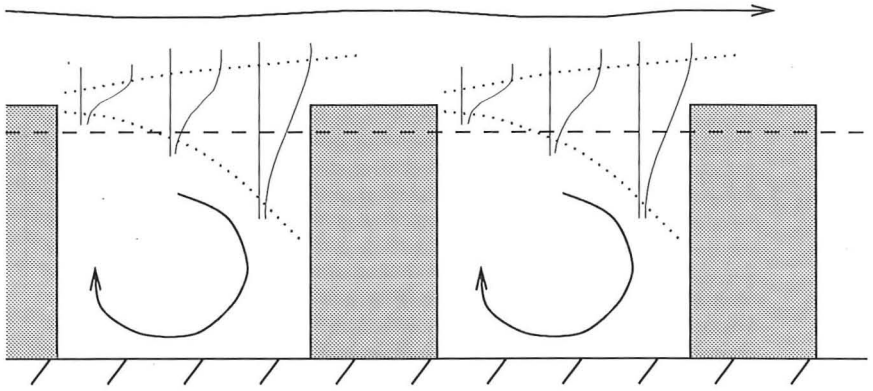

Figure 3.16: The spreading of shear layers shed from obstacle roofs. The dotted lines indicate the approximate extent of the spreading shear layer; the dashed line shows its horizontally averaged mean height.

stronger than that in the SML distributed force analysis.

Clearly a new turbulence model is required to take account of the effects of a concentrated rooftop shear layer. The new formulation is an attempt to account for some of the single obstacle-scale influences on the flow, particularly in the vicinity of the rooftop, that were lost during the horizontal averaging operation.

3.8.3 The displaced mixing length model

The proposed new model is illustrated schematically in figure 3.17. The principal effect of a concentrated shear layer is to inhibit turbulent motions across it: the turbulent length scale within the shear layer is reduced and turbulent eddies above the shear layer appear to be blocked as though by a solid surface at a reference height within or just below the shear layer. This behaviour can be modelled by defining a displacement height d and a roughness height z'_o for the turbulent mixing within and above the shear layer. The displacement height d is the reference level with respect to which eddies above the shear layer appear to be blocked. The roughness height z'_o parameterises the turbulent mixing and dissipation within the shear layer: $\kappa z'_o$ is

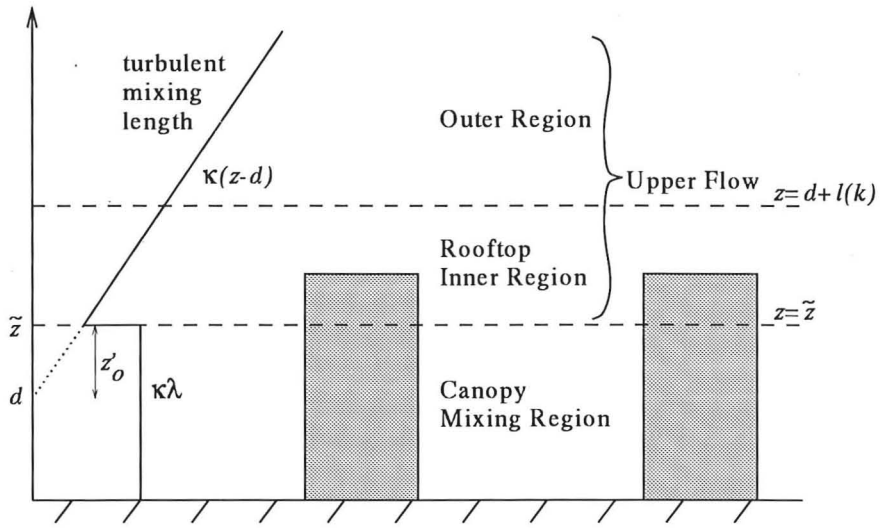

Figure 3.17: Flow structure for the displaced mixing length model.

the minimum value of the turbulent length scale there. Note, following Panofsky & Dutton (1984, chapter 6), how the roughness height is primarily a dynamical measure of turbulent mixing, not a geometrical measure of roughness elements on a surface, and so may be used to parameterise turbulent mixing at any interface whether or not roughness elements are present.

In the "canopy mixing region" below $z = \tilde{z}$ a new model is used. The field and wind tunnel experiments of Davidson *et al.* (1995a,b), on flow through an array of cubical obstacles, showed that the turbulence length scale within the obstacle canopy was much smaller than that in the incident flow. This suggests that the turbulence between obstacles is dominated by high intensity small scale turbulence generated by vortices shed from individual obstacles. In many canopies, where horizontal obstacle dimensions are smaller than obstacle heights, the resultant turbulent mixing will be (i) on a smaller length scale than the blocking length scale κz and (ii) uniform over most of the depth of the canopy (assuming the horizontal obstacle dimensions are approximately constant with height). Thus the turbulence in $z_o < z < \tilde{z}$ is modelled here by a constant eddy viscosity. The laminar viscous analysis of §2.9, which uses a

constant eddy viscosity, is therefore appropriate for the canopy region $z_o < z < \tilde{z}$.

Once general solutions for the upper flow and the canopy mixing region have been obtained, they are matched together at $z = \tilde{z}$ by requiring streamwise velocity, vertical velocity, pressure and shear stress to be continuous. If the turbulent mixing length is discontinuous, as shown in figure 3.17, it follows that the streamwise velocity gradient will be discontinuous also.

3.8.4 Interpretation of the model parameters

According to the discussion of §3.8.2, the new model parameters should be related to the geometry of the rooftop shear layer. The distortion of turbulent eddies illustrated in figure 3.16 suggests that z_o' is of the order of the shear layer thickness and that the sum $\tilde{z} \equiv d + z_o'$ is the mean height of the shear layer. Hence d and z_o' are determined by the distribution of obstacles within a group, in particular by obstacle density. In a dense array with little space for the shear layer to spread between obstacles, d and z_o' are determined mainly by the boundary layer on the obstacle roofs, *i.e.* by the obstacles' height and the surface roughness of their roofs. Conversely, in a sparse array where the shear layer spreads down to the ground between obstacles, $d \ll h$ and z_o' is determined mainly by the roughness of the ground.

Note that the roughness height z_o' used here to describe turbulent mixing within the shear layer is not equivalent to the roughness height z_1 that is obtained by fitting a logarithmic profile,

$$\hat{u}^*(z) = \frac{u_* + \Delta u_*}{\kappa} \ln \frac{z - d_1}{z_1}, \tag{3.158}$$

to the flow above the buildings. The connection between z_o' and z_1 will be examined in chapter 5. The parameter d, on the other hand, can be identified with the displacement height d_1 in (3.158). The question therefore arises: is the notion of d as some measure of a spreading shear layer compatible with other interpretations of the displacement height?

Thom (1971) observed experimentally that the level d_o at which the drag on a rough surface appears to act coincided, to within experimental error, with the dis-

placement height d_1 obtained by fitting the model profile (3.158) to the flow above the surface. That is, he found that

$$d_1 = d_o \equiv \mu_o/\tau_o, \tag{3.159}$$

where μ_o is the streamwise moment per unit area about the surface and τ_o is the streamwise force per unit area. Jackson (1981) showed that the idea of a reference level or displacement height, at or near a rough surface, is implicit in the usual derivation, using dimensional analysis, of the logarithmic profile; otherwise the logarithmic law would not be invariant under a translation of the vertical coordinate system. Following Thom's observation, Jackson then proposed (3.159) as a reliable model for predicting the displacement height over any rough surface. Neither Thom nor Jackson, however, suggested a physical mechanism to explain why the displacement should obey (3.159).

The strong shear layer mechanism discussed in §§3.8.1–3.8.2 could be the missing link. The shear layer determines d by blocking turbulent motions across it, hence providing a reference level for the turbulent eddies above; the reference level then appears as a displacement height in the observed velocity profile (3.158). The shear layer also characterises the flow field that impinges upon downstream obstacles and thus controls the force and moment that act upon the surface. Therefore a relationship such as (3.159) between displacement height and forces on the surface is to be expected.

3.8.5 Velocity profile calculation in $z < \tilde{z}$

The canopy mixing region (CMR) flow is calculated using the analysis of §2.9 with $Re = U_c/(2\epsilon\kappa^2\lambda)$, where $U_c \equiv U(\tilde{z})$ is the canopy velocity scale and λ is the constant mixing length. From (2.29)–(2.31), the general solution for the perturbation streamfunction ψ is expressed in terms of two complementary functions $q_1(k,z)$ and $q_2(k,z)$ and a Green's function $g(k,z;z')$:

$$\psi(k,z) = s_1 q_1(k,z) + s_2 q_2(k,z) + \frac{Re}{U_c}\int_{z_o}^{z} \frac{\partial f}{\partial z}(z')g(k,z;z')\,dz',$$

where

$$q_1(k,z) \equiv \sinh\alpha(z-z_o) - \frac{\alpha}{\beta}\sinh\beta(z-z_o),$$

$$q_2(k,z) \equiv \cosh\alpha(z-z_o) - \cosh\beta(z-z_o),$$
$$\text{and} \quad g(k,z;z') \equiv \frac{\sinh\alpha(z-z')}{\alpha(\alpha^2-\beta^2)} - \frac{\sinh\beta(z-z')}{\beta(\alpha^2-\beta^2)}.$$

Recall from §2.9 that $\beta = |k|$ and $\alpha^2 = k^2 + ikRe$ such that the real part of α is non-negative. Then the perturbation velocities, pressure and shear stress are given in terms of ψ by

$$u = \frac{\partial\psi}{\partial z}; \tag{3.160}$$
$$w = -ik\psi; \tag{3.161}$$
$$p = \frac{2\epsilon\kappa^2\lambda}{ik}\left(\frac{\partial^3}{\partial z^3} - k^2\frac{\partial}{\partial z}\right)\psi - U_c\frac{\partial\psi}{\partial z} - \frac{f}{ik}; \tag{3.162}$$
$$\tau = \frac{2\lambda}{\epsilon}\left(k^2 + \frac{\partial^2}{\partial z^2}\right)\psi. \tag{3.163}$$

These profiles depend implicitly on the constants s_1 and s_2 which are to be determined by matching with the upper part of the flow. Thus at $z = \tilde{z}$ we have

$$\tilde{u} = u(\tilde{z};s_1,s_2); \quad \tilde{w} = w(\tilde{z};s_1,s_2); \quad \tilde{p} = p(\tilde{z};s_1,s_2); \quad \tilde{\tau} = \tau(\tilde{z};s_1,s_2),$$

which are all linear functions of s_1 and s_2.

3.8.6 Velocity profile calculation in $z > \tilde{z}$

The upper flow is analysed using the methods developed for the SML analysis in §§3.5–3.6. The main differences are that (i) the flow is displaced upwards by a distance $\tilde{z} - z_o$ and (ii) the lower boundary condition is $\mathbf{u}(\tilde{z}) = (\tilde{u}, \tilde{w})$ instead of $\mathbf{u} = 0$. Here we focus on the smaller wavenumber analysis, such that there are no strong force gradients in the outer region of the flow. Large wavenumber results may be obtained by following the approach of §3.6 with appropriate modifications.

Asymptotic structure of the upper flow

The upper limit z_l of the rooftop inner region (RIR) is determined, as in §3.3, by the balance between time scales for advection by the mean flow and for turbulent eddy

adjustment. Taking into account the new reference level d for the turbulent eddies of the upper flow, the time scale balance is

$$\frac{1}{kU^*(z_l)} \approx \frac{z_l - d}{u^*}. \tag{3.164}$$

Therefore the vertical size of the RIR, $l \equiv z_l - d$, satisfies

$$kl \ln \frac{d+l}{z_o} = 1. \tag{3.165}$$

The small parameter ϵ is defined as in §3.3, namely $\epsilon \equiv \ln^{-1}(H/z_o)$. It remains true that $kl = O(\epsilon)$ since $d = O(H)$. The RIR velocity scale is defined by

$$U_l \equiv U(d+l) = \epsilon \ln \frac{d+l}{z_o}, \tag{3.166}$$

so then the incident velocity profile in the RIR may be expressed as

$$U(z) = U_l + \epsilon \ln \frac{z}{d+l}. \tag{3.167}$$

It is not necessary to subdivide the RIR because $U(z)$ is well approximated by U_l throughout the region.

The rooftop inner region

In the upper flow, the turbulent mixing length is $\kappa(z-d)$. Therefore the turbulent stress model becomes

$$\tau = \frac{2(z-d)}{\epsilon} \frac{\partial u}{\partial z}. \tag{3.168}$$

Define the RIR coordinate $\zeta \equiv (z-d)/l$; the governing equations are then

$$ikl(U_l + O(\epsilon))u + \epsilon wl/z + iklp = 2\epsilon\kappa^2(\zeta u')' - lf; \tag{3.169}$$

$$ikl(U_l + O(\epsilon))w + p' = 2ikl\epsilon\kappa^2\zeta u'; \tag{3.170}$$

$$iklu + w' = 0. \tag{3.171}$$

The non-zero vertical velocity at $z = \tilde{z}$ means that the leading order streamwise momentum equation differs slightly from (3.38):

$$iklU_l u_o - 2\epsilon\kappa^2(\zeta u_o')' = -lf - iklp_o - \epsilon\tilde{w}l/z. \tag{3.172}$$

The last term in (3.172) is another manifestation of the $O(\epsilon)$ additional force distribution $\epsilon w/z$ that may be applied to the whole of the upper flow. Putting this term to one side (for later correction), the general solution is

$$\begin{aligned} u_o &= A_o J_o(Z) + B_o K_o(-iZ) - \frac{p_o}{U_l} \\ &\quad + \frac{i}{kU_l}\int_{\tilde{Z}}^{Z} Z' f(z') \left\{ J_o(Z) K_o(-iZ') - J_o(Z') K_o(-iZ) \right\} dZ', \end{aligned} \tag{3.173}$$

where

$$Z \equiv e^{3i\pi/4}\sqrt{\frac{2U_l k(z-d)}{\epsilon\kappa^2}}. \tag{3.174}$$

A_o is determined by the constraint of boundedness as $\zeta \to \infty$:

$$A_o + \frac{i}{kU_l}\int_{\tilde{Z}}^{\infty} Z' f(z') K_o(-iZ') dZ' = 0. \tag{3.175}$$

The three contributions to the first order correction u_1 are determined as shown in §3.5 except that now $f_1^{(\mathrm{U})} \equiv iku_o(U - U_l)/\epsilon$. Then the streamwise velocity boundary condition at $z = \tilde{z}$, namely $u(\tilde{z}) = \tilde{u}$, shows that $B_o = 0$ as before and that

$$A_o J_o(\tilde{Z}) + \epsilon B_1 K_o(-i\tilde{Z}) - \frac{p_o}{U_l} = \tilde{u}. \tag{3.176}$$

Differentiation of the streamwise velocities u_o and $u_1^{(\mathrm{cf})}$ gives the shear stresses:

$$\begin{aligned} \tau_{-1} &= -A_o Z J_1(Z) \\ &\quad - \frac{iZ}{kU_l}\int_{\tilde{Z}}^{Z} Z' f(z') \left\{ J_1(Z) K_o(-iZ') + iJ_o(Z') K_1(-iZ) \right\} dZ'; \end{aligned} \tag{3.177}$$

$$\tau_o^{(\mathrm{cf})} = iB_1 Z K_1(-iZ). \tag{3.178}$$

The vertical velocity is $w = \tilde{w} + \epsilon w_1 + \epsilon^2 w_2^{(\mathrm{cf})} + \ldots$, where

$$\epsilon U_l w_1 = ikp_o(z - \tilde{z}) + \int_{\tilde{z}}^{z} f(z')\, dz' - \epsilon\kappa^2(\tau_{-1} + A_o \tilde{Z} J_1(\tilde{Z})); \tag{3.179}$$

$$\epsilon U_l w_2^{(\mathrm{cf})} = -\epsilon\kappa^2(\tau_o^{(\mathrm{cf})} - iB_1 \tilde{Z} K_1(-i\tilde{Z})). \tag{3.180}$$

As in the SML analysis, incorporation of the $O(\epsilon)$ $f_1^{(\mathrm{U})}$ correction at the top of the RIR converts occurrences within these solutions of the RIR velocity scale U_l to the slowly varying incident velocity $U(z)$.

The outer region

Governing equations for the outer region are identical to (3.91)–(3.94). To reflect the displacement of the upper flow, it is convenient however to use $\exp \pm k(z-d)$ as the complementary functions of these equations rather than $\exp \pm kz$ as in the standard mixing length analysis. The leading order solutions are

$$w_o = C_o e^{-k(z-d)} + D_o e^{k(z-d)} + \int_{\tilde{z}}^{z} \frac{f(z') \cosh k(z-z')}{U(z')}\, dz'; \tag{3.181}$$

$$u_o = -iC_o e^{-k(z-d)} + iD_o e^{k(z-d)} + \frac{if}{kU} + i\int_{\tilde{z}}^{z} \frac{f(z') \sinh k(z-z')}{U(z')}\, dz'; \tag{3.182}$$

$$p_o = \frac{if}{k} - Uu_o. \tag{3.183}$$

Here D_o is determined by the condition of boundedness as $kz \to \infty$, namely

$$D_o + \frac{1}{2}\int_{\tilde{z}}^{\infty} \frac{f(z') e^{-k(z'-d)}}{U(z')}\, dz' = 0. \tag{3.184}$$

Matching the rooftop inner and outer regions

The $O(1)$ matching coordinate χ for the overlap region between the rooftop inner and outer regions is defined by

$$k(z-d) = \epsilon^{\alpha}\chi, \qquad \text{where} \quad 0 \le \alpha \le 1. \tag{3.185}$$

Matching the leading order vertical perturbation velocities in the overlap region gives

$$\tilde{w} = C_o + D_o; \tag{3.186}$$

the particular integrals over f match automatically. Matching the perturbation pressures gives

$$p_o = iU_l(C_o - D_o). \tag{3.187}$$

3.8.7 Matching the canopy region and upper flow analyses

The entire upper flow solution is linearly dependent on the velocity perturbations at the top of the canopy mixing region, $\tilde{u}$ and $\tilde{w}$, and therefore on s_1 and s_2. The values

of s_1 and s_2 are determined by requiring that the CMR and RIR pressures and shear stresses are continuous at $z = \tilde{z}$.

In practice it is easiest to do this by taking advantage of the linearity in s_1 and s_2. Calculate the discrepancies in pressure and shear stress when $s_1 = s_2 = 0$ ($\rightarrow \Delta p_{00}, \Delta\tau_{00}$), when $s_1 = 1, s_2 = 0$ ($\rightarrow \Delta p_{10}, \Delta\tau_{10}$) and when $s_1 = 0, s_2 = 1$ ($\rightarrow \Delta p_{01}, \Delta\tau_{01}$). Then the required values of s_1 and s_2 are given by

$$s_1 = \frac{(\Delta p_{01} - \Delta p_{00})\Delta\tau_{00} - (\Delta\tau_{01} - \Delta\tau_{00})\Delta p_{00}}{(\Delta\tau_{01} - \Delta\tau_{00})(\Delta p_{10} - \Delta p_{00}) - (\Delta p_{01} - \Delta p_{00})(\Delta\tau_{10} - \Delta\tau_{00})};$$

$$s_2 = \frac{(\Delta\tau_{10} - \Delta\tau_{00})\Delta p_{00} - (\Delta p_{10} - \Delta p_{00})\Delta\tau_{00}}{(\Delta\tau_{01} - \Delta\tau_{00})(\Delta p_{10} - \Delta p_{00}) - (\Delta p_{01} - \Delta p_{00})(\Delta\tau_{10} - \Delta\tau_{00})}.$$

3.8.8 Sample results

The displaced mixing length analysis introduces three new parameters that describe different aspects of the internal structure of a group of obstacles. These are λ, the constant mixing length within the canopy mixing region, $\tilde{z}$, the depth of the canopy mixing region, and z_o', the roughness height of the interface between the canopy mixing region and the linear mixing length flow above. In figures 3.18–3.20 we attempt to illustrate the impact each parameter has on the streamwise velocity perturbation by varying a single parameter in each figure. Thus figure 3.18 shows results obtained using a "central" parameter set, results with λ less than its central value, and results with λ greated than its central value; similarly figures 3.19 and 3.20 illustrate variation of z_o' and $\tilde{z}$ respectively. The values of all parameter sets are given in table 3.1. In addition, the dotted line in each figure shows the streamwise velocity perturbation predicted by the SML analysis. Figures 3.18–3.20 are calculated for the same force distribution and wavenumber as the small wavenumber SML sample results.

Variation of λ (figure 3.18)

As λ increases there is more efficient mixing over the depth of the canopy region. Hence velocity gradients are increasingly inhibited and the maximum velocity deficit is reduced. By continuity, the streamwise velocity deficit leads to a vertical velocity

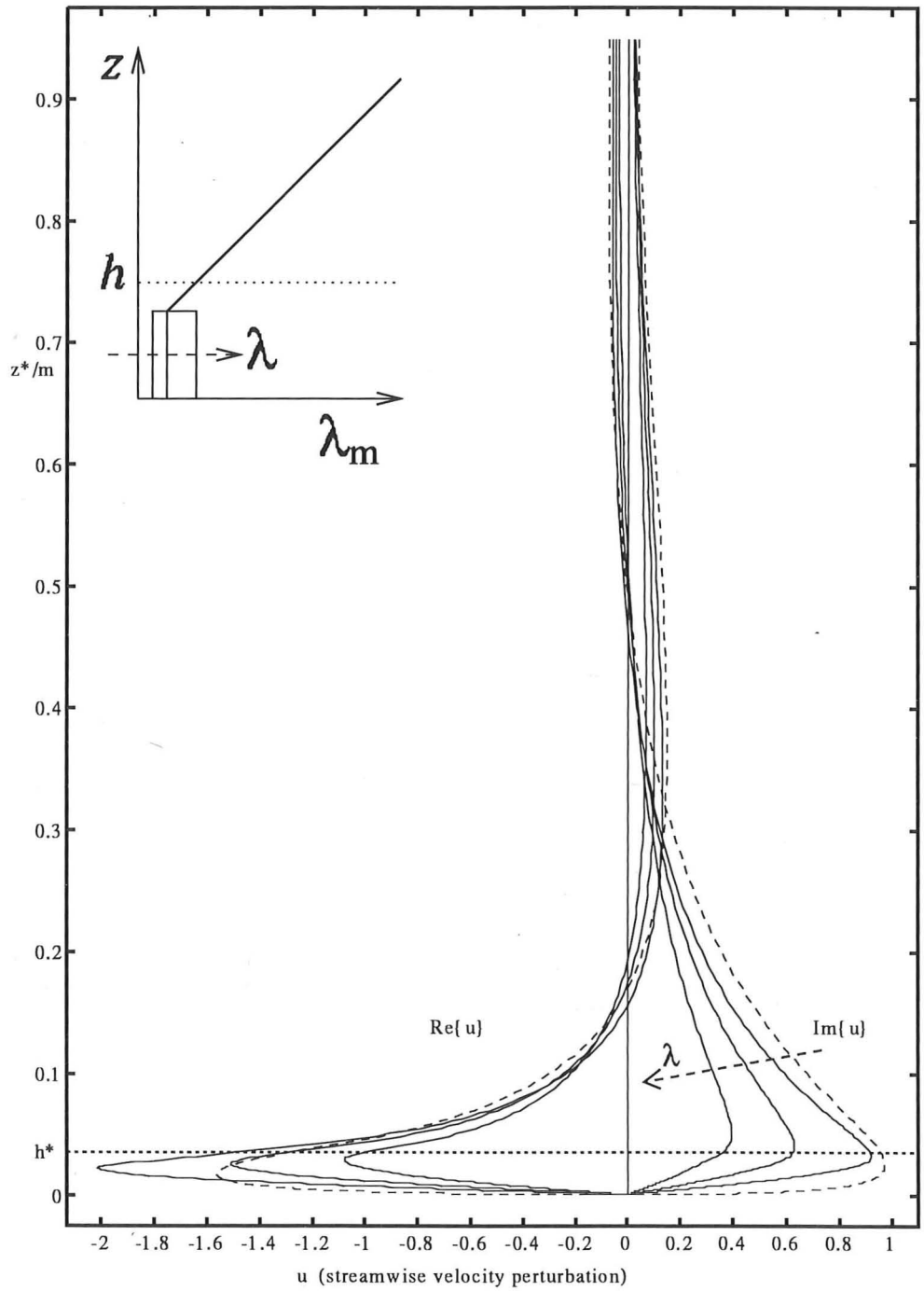

Figure 3.18: Variation of λ. The inset shows the mixing length profiles for each of the results graphed below. The dashed arrows indicate increasing λ.

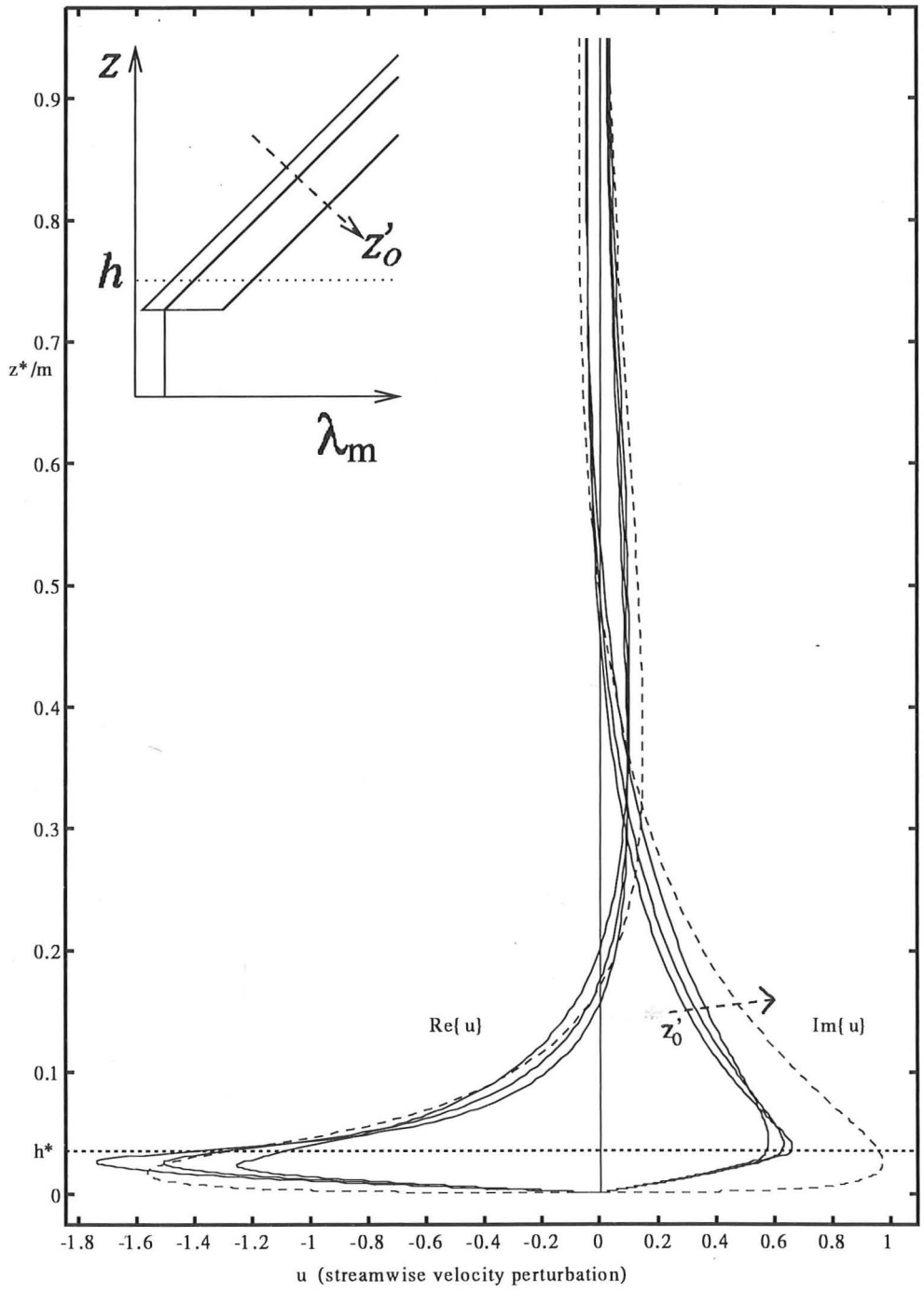

Figure 3.19: Variation of z_o'. The inset shows the mixing length profiles for each of the results graphed below. The dashed arrows indicate increasing z_o'.

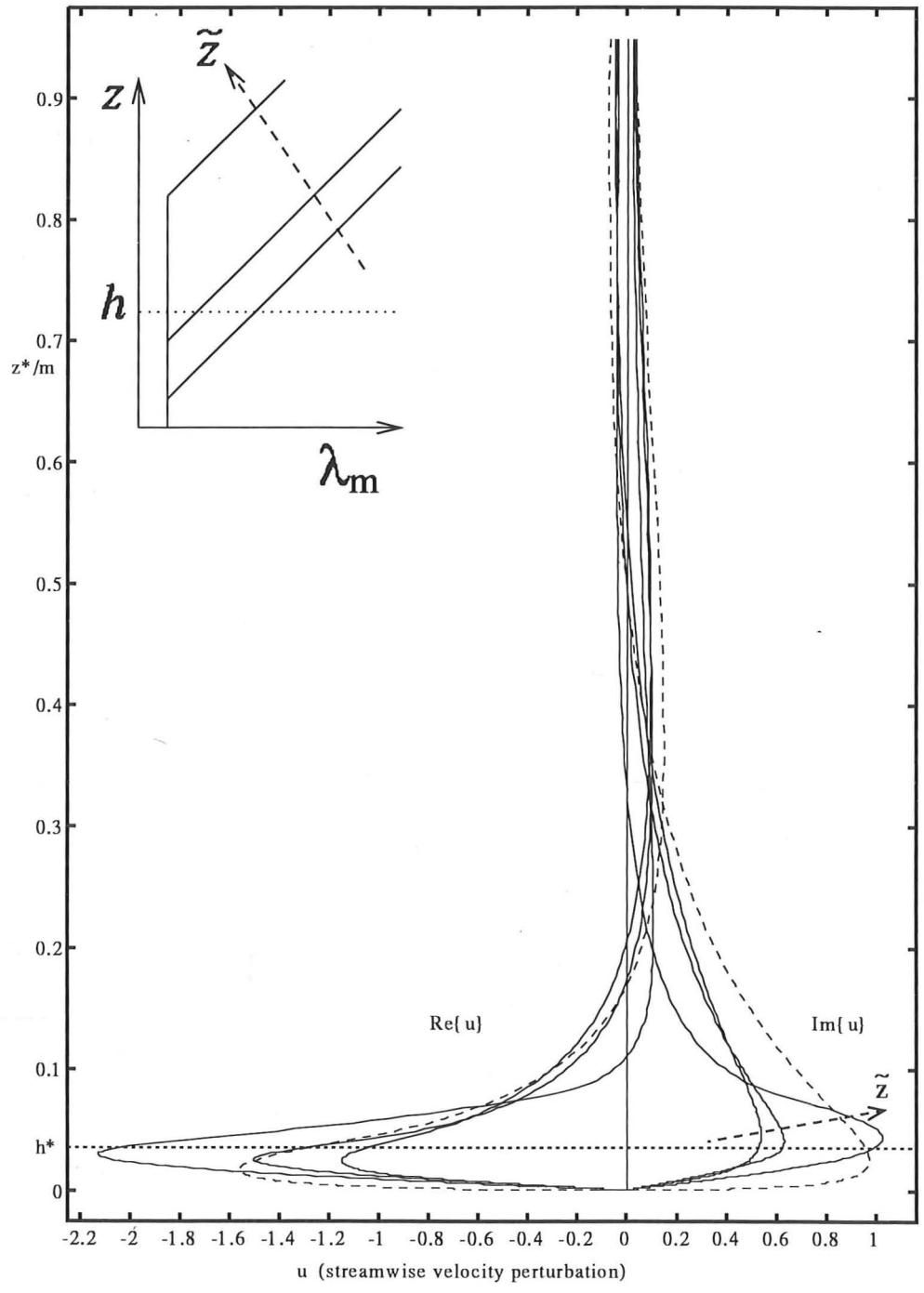

Figure 3.20: Variation of $\tilde{z}$. The inset shows the mixing length profiles for each of the results graphed below. The dashed arrows indicate increasing $\tilde{z}$.

	λ/h	z'_o/h	$\tilde{z}/h$	$\Rightarrow d/h$
Central parameter set	$\frac{1}{4}$	$\frac{1}{4}$	$\frac{3}{4}$	$\frac{1}{2}$
Reduced λ	$\frac{1}{8}$	$\frac{1}{4}$	$\frac{3}{4}$	$\frac{1}{2}$
Increased λ	$\frac{1}{2}$	$\frac{1}{4}$	$\frac{3}{4}$	$\frac{1}{2}$
Reduced z'_o	$\frac{1}{4}$	$\frac{1}{16}$	$\frac{3}{4}$	$\frac{11}{16}$
Increased z'_o	$\frac{1}{4}$	$\frac{3}{4}$	$\frac{3}{4}$	0
Reduced $\tilde{z}$	$\frac{1}{4}$	$\frac{1}{4}$	$\frac{1}{4}$	0
Increased $\tilde{z}$	$\frac{1}{4}$	$\frac{1}{4}$	2	$1\frac{3}{4}$

Table 3.1: The values of λ, z'_o and $\tilde{z}$ used in figures 3.18-3.20.

perturbation at the top of the canopy region, which in turn causes the speed up in streamwise velocity above the canopy. Since the parameters of the flow over this vertical perturbation velocity, z'_o and $d = \tilde{z} - z'_o$, are held constant, the speed up above the canopy increases or decreases with the velocity deficit within the canopy.

In the DML model the mixing length remains constant even very close to the ground where the blocking scale z must eventually dominate the canopy turbulence scale λ based on the dimensions of eddies shed from upstream obstacles. Thus significant velocity gradients that would be permitted near the ground by a mixing length of order z_o, the surface roughness, are inhibited by the constant DML model mixing length. This is a model weakness that could be compensated by reducing λ to a form $\propto z$ near the ground. Such a refinement is not attempted here because it might not be practical to make measurements that are consistent with the distributed force model so close to the ground.

Variation of z'_o (figure 3.19)

The interface roughness height or minimum mixing length in the shear layer, z'_o, determines the gradients of streamwise velocity just above $z = \tilde{z}$: smaller z'_o gives larger

velocity gradients. Since speed up above the canopy is small compared with the maximum velocity deficit, the maximum velocity deficit is influenced by velocity gradients above $z = \tilde{z}$ and hence by z_o'. The canopy mixing region adjusts to meet this velocity deficit by changing its velocity perturbation only very close to $z = \tilde{z}$; cf. figure 3.18, in which variation of λ causes variation of velocity perturbation throughout the canopy mixing region.

Variation of $\tilde{z}$ (figure 3.20)

The inset graph shows how the mixing length starts increasing at $z = \tilde{z}$ from its minimum value in the canopy mixing region. Since $z_o' = \lambda$ for the cases shown in figure 3.20, $\tilde{z}$ determines the extent of the flow domain where the minimum mixing length applies. Increased $\tilde{z}$ means that stronger velocity gradients are allowed over more of the flow. The results with $\tilde{z}/h = 2$ show particularly strong gradients above the canopy; these are effectively laminar viscous results, since velocity variation above $z = 2h$ appears insensitive to the turbulence model.

3.9 Turbulence model sensitivity

Since the DML analysis of §3.8 includes the SML analysis as a special case ($z_o' = \tilde{z} = z_o$), the effects of varying the three DML parameters provide a good indication of the general sensitivity of the turbulent flow problem to changes in the turbulence closure model. On the one hand, the sample results exhibited in §3.8.8 show that dramatic changes in the streamwise velocity perturbation profile, *e.g.* up to 100% change in the maximum velocity deficit, can be effected by varying the DML parameters. On the other hand, they also show that such dramatic changes require extreme parameter values and that there is a large parameter space within which the theoretical predictions vary rather little. Even when extreme parameter values are used, the qualitative shapes of the perturbation quantity profiles remain similar in all cases.

In particular, the sample results show that the DML model with constant mixing

length in the force distribution can give very similar results to the SML model if the DML parameters are chosen appropriately (with the exception of the $z = O(z_o)$ layer near the ground where the SML model gives much stronger velocity gradients). This insensitivity of the turbulent analysis to the way the mixing length varies within the canopy is encouraging: it suggests that reservations over the use of a single length scale in the turbulence model are less relevant than originally expected.

The following chapter presents comparisons of the SML and DML results with experimental data and numerical simulations.

Chapter 4

Comparisons with experimental and numerical data

4.1 Introduction

In this chapter the results for the perturbed flow field derived from the distributed force model and turbulent flow analyses are compared with a numerical simulation of the distributed force model and with several sets of experimental data on obstacle canopies.

Before presenting these comparisons however, it is necessary to consider two interesting details of the practical implementation of the results of chapter 3. It was noted in §1.5 that in most practical problems the distributed force is not known *a priori*. Instead the urban or forest canopy is described by a distribution of drag parameter $D^*(x,z)$ and the distributed force acting at any point is given by D^* times the local wind speed squared. Thus the distributed force depends on the local wind speed, but the local wind speed is determined by distributed forces upstream. This problem is addressed in §4.2 by the concept of distributed force iteration.

The second detail, in §4.3, concerns the transition from Fourier space, in which the results of chapter 3 are given, back to real space where flowfield comparisons are to be made. The inverse Fourier transformation is not straightforward because the

model results contain an unusual singularity at $k = 0$. Similar problems arise in other models that use Fourier synthesis, *e.g.* the "Flowstar" model described by Carruthers *et al.* (1988).

The flowfield comparisons proper begin in §4.4 with a discussion of the validation procedure.

4.2 Distributed force iteration

As originally noted in §1.5, the distributed force in most practical problems is best calculated as the product of a velocity-independent drag parameter $D^*(x, z)$ and the square of the local wind speed. In a strictly linear calculation it is consistent to use the upstream velocity profile $U(z)$ for the local wind speed throughout the canopy. In practice, however, to do so leads to serious overestimation of the streamwise velocity defect, particularly in the downstream parts of a canopy, the overestimate being cumulative with distance downstream. This is an artefact of linearising the drag. For example, the experiments of Davidson *et al.* (1995a) showed that the streamwise velocity in the latter half of the obstacle array was about one half of that upstream, which means that the force acting over a large part of the array was just one quarter of the force acting near the leading edge. This suggests that the results of the linear analysis can be significantly improved if non-linear effects are accounted for in the specification of the drag.

We can allow for the effects of reduced local wind speed by iterating the distributed force calculation. For the first iteration, set

$$f^{(0)}(x, z) = \frac{1}{2}\rho L^* D^* U^2(z) \tag{4.1}$$

and calculate the corresponding streamwise velocity perturbations

$$u^{(1)}(x, z) = \mathcal{U}\{f^{(0)}(x, z)\}, \tag{4.2}$$

where $\mathcal{U}$ represents the analysis of chapter 3. Then on subsequent iterations (starting

from $n = 1$), set

$$f^{(n)}(x,z) = \frac{1}{2}\alpha_r \rho L^* D^* (U(z) + u^{(n)}(x,z))^2 + (1-\alpha_r) f^{(n-1)} \tag{4.3}$$

and calculate

$$u^{(n+1)}(x,z) = \mathcal{U}\{f^{(n)}(x,z)\}. \tag{4.4}$$

Without relaxation the iterative process oscillates owing to negative feedback, since

large velocity defect $\rightarrow$ reduced force $\rightarrow$ reduced velocity defect

and so on. Use of a relaxation factor α_r effectively increases the damping and therefore accelerates convergence of the iterative scheme. Note that the use of complementary relaxation factors α_r and $(1-\alpha_r)$ in (4.3) ensures that the converged result is independent of α_r. For when the iteration converges, $f^{(n)} = f^{(n-1)}$, which substituted into (4.3) gives

$$f^{(n)}(x,z) = \frac{1}{2}\rho L^* D^* (U(z) + u^{(n)}(x,z))^2. \tag{4.5}$$

as required. Experience suggests that $\alpha_r \approx 0.6$ is an efficient value. For most of the force distributions we have so far considered the iterative process then converges in just three or four iterations. The convergence criterion adopted here is that the fractional L2 norm of the force distribution change should be less than 1%, *i.e.*

$$\frac{\iint (f^{(n)} - f^{(n-1)})^2 \, dx \, dz}{\iint (f^{(n)})^2 \, dx \, dz} < 0.01. \tag{4.6}$$

Figure 4.1 demonstrates the importance of this iteration. The curves shown were calculated for a rectangular drag parameter distribution describing the Cardington experiment of Davidson *et al.* (1995a). Curve (a) shows the ratio of force acting after iteration to that acting before iteration. Curves (b) and (c) show the dramatic difference between calculated streamwise velocity perturbations at half canopy height with and without iteration.

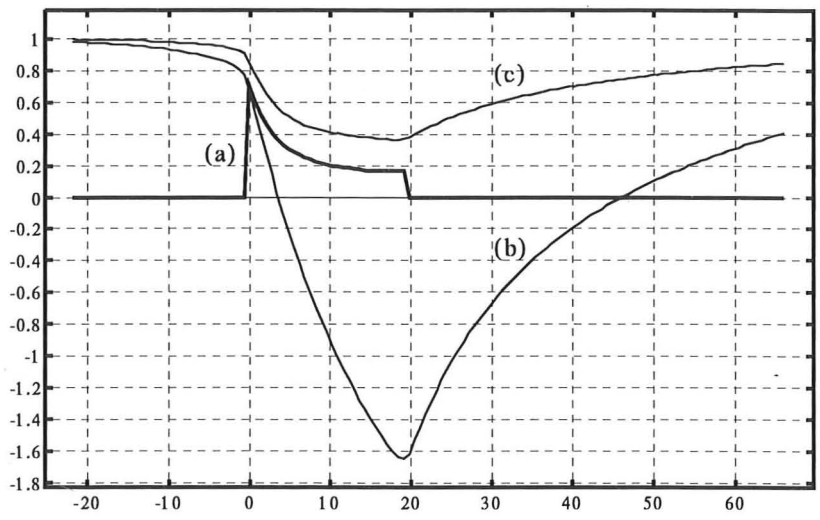

Figure 4.1: The significance of distributed force iteration. (a) The ratio of distributed force after iteration to that before iteration, integrated over the height of the distribution. (b),(c) Streamwise velocity at half canopy height, before and after iteration, normalised by the upwind velocity at half canopy height. The horizontal axis is streamwise distance from the leading edge, normalised by the canopy height.

4.3 Inverse Fourier transformation

The results of the standard mixing length analysis, obtained in chapter 3, contain an interesting singularity at zero wavenumber. To see this, consider just the inner region solution, which may be written as

$$\begin{aligned} u &= \frac{A_o}{K_o(-iZ_o)}\{J_o(Z)K_o(-iZ_o) - J_o(Z_o)K_o(-iZ)\} \\ &\quad + \frac{p_o}{U_l K_o(-iZ_o)}\{K_o(-iZ) - K_o(-iZ_o)\} \\ &\quad + \frac{i}{kU_l}\int_{Z_o}^{Z} Z' f(z')\{J_o(Z)K_o(-iZ') - J_o(Z')K_o(-iZ)\}\, dZ'. \end{aligned} \tag{4.7}$$

Now as $k \to 0$,

$$K_o(-iZ) - K_o(-iZ_o) = -\frac{1}{2}\ln\frac{z}{z_o} + O(k\ln k) \tag{4.8}$$

and

$$J_o(Z)K_o(-iZ') - J_o(Z')K_o(-iZ) = \frac{1}{2}\ln\frac{z}{z'} + O(k). \tag{4.9}$$

Hence

$$\begin{aligned} \frac{A_o}{K_o(-iZ_o)} &= \frac{-i}{kU_l}\int_{Z_o}^{\infty} Z' f(z')\frac{K_o(-iZ')}{K_o(-iZ_o)}\, dZ' \\ &= \frac{-1}{\epsilon\kappa^2}\int_{z_o}^{\infty} f(z')\left\{1 - \frac{\ln(z'/z_o) + O(k\ln k)}{2K_o(-iZ_o)}\right\} dz' \end{aligned} \tag{4.10}$$

and

$$p_o = iU_l\int_{z_o}^{\infty}\frac{f(z')e^{-kz'}}{U_g(z')}\, dz' = i\int_{z_o}^{\infty} f(z')\{1 + O(k)\}\, dz'. \tag{4.11}$$

Therefore the inner region solution may be approximated as $k \to 0$ as

$$\begin{aligned} u &\approx \frac{1}{2\epsilon\kappa^2}\ln\frac{z}{z_o}\int_{z_o}^{\infty} f(z')\left\{\frac{\ln(z'/z_o)}{2K_o(-iZ_o)} - 1\right\} dz' \\ &\quad - \frac{i\ln(z/z_o)}{2U_l K_o(-iZ_o)}\int_{z_o}^{\infty} f(z')\, dz' + \frac{1}{2\epsilon\kappa^2}\int_{z_o}^{z} f(z')\ln\frac{z}{z'}\, dz'. \end{aligned}$$

The singularity at $k = 0$ arises from the k dependence of $K_o(-iZ_o)$ in some of the denominators here, *viz.* $K_o(-iZ_o) \sim -\frac{1}{2}\ln k$ as $k \to 0$. Thus the small k dependence of u may be summarised as

$$u(k) \approx A + \frac{B}{\ln k} \qquad \text{as} \quad k \to 0, \tag{4.12}$$

where A and B are independent of k. The typical form of this singularity is illustrated in figure 4.2 (taking $A = B = 1$). The gradient of $u(k)$ becomes infinite as $u(k)$ approaches the limiting value A at $k = 0$.

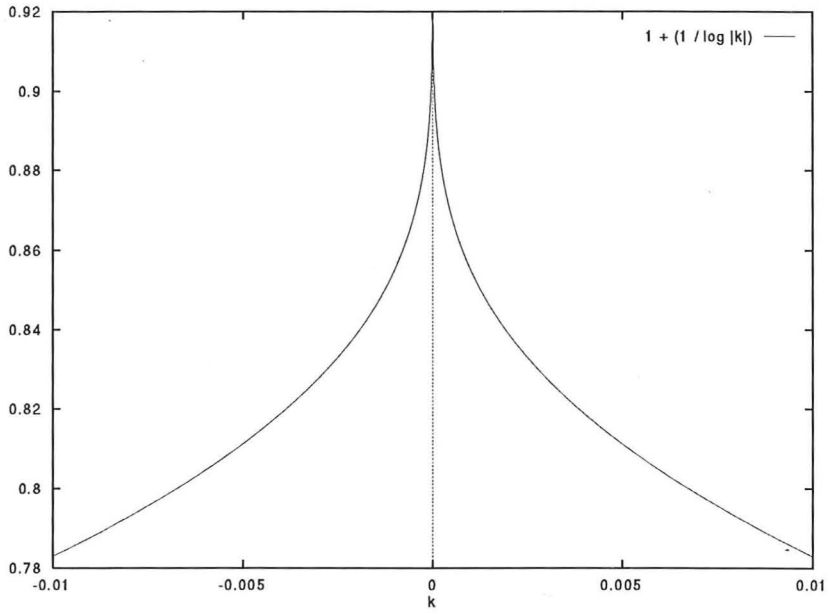

Figure 4.2: The singularity $1+(1/\ln|k|)$. The sharpness of the singularity is illustrated by the fact that the computer-approximated curve uses 2000 samples equi-spaced in the range $-0.01 < k < 0.01$ but reaches a maximum value of only 0.92. The theoretical maximum is of course 1.

The difficulty introduced by this singularity may be understood in two ways. For the usual inverse Fourier transform algorithm, $u(k)$ must be sampled at discrete values of k: $j\Delta k$, $j = 0 \ldots N-1$, where N is the size of the Fourier transform. It is well known that this discrete sampling of $u(k)$ causes aliasing of the real space result $u(x)$ such that the inverse Fourier transform obtained is not exactly $u(x)$ but $\sum_{j=-\infty}^{\infty} u(x-j\Delta x)$, where $\Delta x = 2\pi/\Delta k$.

Another way of interpreting the aliasing problem is to observe that the extreme pointedness of the $\ln^{-1} k$ singularity is not adequately resolved by a finite number of

equispaced samplings.

Such aliasing can often be removed if it is possible to obtain analytically the large $|x|$ behaviour of $u(x)$, which in turn depends upon the singularities of the Fourier transform $u(k)$. A step discontinuity in $u(k)$, for example, would imply that $u(x) \sim x^{-1}$ for large $|x|$ (*e.g.* Lighthill 1958). The $\ln^{-1} k$ singularity is qualitatively intermediate between a step discontinuity and a gradient discontinuity, so the corresponding large $|x|$ behaviour should fall somewhere between x^{-1} and x^{-2}. Unfortunately, however, it is not possible to obtain the exact behaviour in closed form.

For these reasons it is impossible to use the straightforward Fast Fourier Transform (FFT) algorithm to calculate the inverse Fourier transform of $u(k)$. Instead we split the FT integral into two parts, only one of which includes the singularity:

$$\begin{aligned} \int_{-\infty}^{\infty} u(k)e^{ikx}\,dk &= 2\,\mathrm{Re}\int_0^{\infty} u(k)e^{ikx}\,dk \\ &= 2\,\mathrm{Re}\int_0^{\Delta k/2} u(k)e^{ikx}\,dk + 2\,\mathrm{Re}\int_{\Delta k/2}^{\infty} u(k)e^{ikx}\,dk. \end{aligned} \tag{4.13}$$

The second of these integrals may now be computed as the FFT of $u(k)$ with $u(0)$ set to zero. The first integral is calculated by Simpson's rule after a change of variable to $\xi \equiv \ln k$. Thus

$$\int_0^{\Delta k/2} u(k)e^{ikx}\,dk = \int_{\xi_{\min}}^{\ln(\Delta k/2)} u(e^{\xi})e^{ie^{\xi}x}e^{\xi}\,d\xi \approx \frac{\Delta\xi}{30}\sum_{j=0}^{10} S_j u(e^{\xi_j})e^{\xi_j}e^{ixe^{\xi_j}},$$

where $S_0 = S_{10} = 1$, $S_1 = S_3 = S_5 = S_7 = S_9 = 4$, $S_2 = S_4 = S_6 = S_8 = 2$, $\Delta\xi = (\ln(\Delta k/2) - \xi_{\min})/10$ and $\xi_j = \xi_{\min} + j\Delta\xi$. The error involved in choosing a finite negative value for $\xi_{\min}$ rather than $-\infty$ is $O(\exp\xi_{\min})$, so $\xi_{\min}$ can easily be chosen to make the error negligible. The author's current implementation has $\exp\xi_{\min} = 10^{-5}$. The change of variable is advantageous because the error involved in using Simpson's rule to integrate a function $f(q)$ over a range of q is $O((d^4f/dq^4)_{\max})$. If $q = k$ and $f(q) \sim A + B/\ln q$ as $q \to 0$, the fourth derivative of f tends to infinity as $q \to 0$. After the change of variable, however, $q = \ln k$, $f(q) \sim A + B/q$ and $d^4f/dq^4 \sim 24B/q^5$ as $q \to -\infty$. In other words, changing the independent variable dramatically reduces the numerical error because the singularity is sampled at a more

sensible set of points.

4.4 Comparison of model results with experiment

In the recipe described by this thesis, three main ingredients contribute to flowfield prediction for a given group of obstacles:

- the idea that the group of obstacles may be modelled as a region of distributed force;
- the procedure for calculating the appropriate force distribution;
- the analyses of chapter 3 that calculate flow perturbations for a given force distribution.

Any comparison of the recipe's predictions against experimental data is a test of the complete recipe, not of any single ingredient.

On the other hand, numerical simulations have been performed which use a specific distributed force to represent forest or urban canopies (*e.g.* Yamada 1982, Svensson & Häggkvist 1990, Shaw & Schumann 1992). Comparison of these simulations with the predictions of chapter 3, using the same force distribution, provides a direct test of the turbulent flow analysis in isolation. That is, the asymptotic method and turbulence closure model of the analytic approach are compared against the numerical approximations and nominally more sophisticated turbulence closure model of the simulations. Therefore our first comparison, in §4.5, is with the K–ϵ turbulence closure simulation of Svensson & Häggkvist (1990).

The comparisons in §§4.6–4.8 are all with experimental data and so require modelling of a group of obstacles by an appropriate force distribution, using the drag parameter method and iterative process described in §1.5 and §4.2. §4.6 examines the deceleration of average streamwise velocity within the obstacle canopy, measured by Davidson *et al.* (1995a,b) in field and wind tunnel experiments on a group of obstacles. §4.7 compares whole flowfield predictions with the wind tunnel experiment of Meroney

(1968) on a model forest canopy, characterised by a single rectangular drag parameter distribution. Finally, §4.8 presents a qualitative comparison with the observations of Stacey *et al.* (1994) in a clearing in the middle of a forest.

Our objective throughout is predictive. Therefore we proceed by estimating any adjustable parameters on the basis of physical arguments, calculating the flow predictions that result from the estimated parameter set, and comparing these predictions with simulations or experiment. No attempt is made to improve agreement by retrospectively adjusting parameters. Since the DML turbulence model includes three adjustable parameters, this point is most relevant for the comparison using the DML turbulent flow analysis with Meroney's (1968) data, in §4.7.

4.5 Comparison with numerical simulation

Svensson & Häggkvist (1990) performed a numerical simulation of two-dimensional flow through a region of distributed resistance using the K–ϵ turbulence closure model. The distributed resistance was calculated from a drag coefficient C_d, a plant area density a^* and the local wind speed $\hat{u}^*$:

$$f^* = \frac{1}{2}\rho C_d a^* |\hat{u}^*| \hat{u}^*. \tag{4.14}$$

The model canopy was a rectangular region 2.5m high and 250m long. Within the canopy C_d and a^* took constant values 0.3 and 2.1 m^{-1} respectively; outside the canopy $C_d a^* \equiv 0$. To model the increased turbulent dissipation due to small scale wake turbulence generated by canopy leaves, resistance-related source terms based on C_d, a^* and $\hat{u}^*$ were added to the turbulent kinetic energy and dissipation equations as well as to the streamwise momentum equation. The extra coefficients introduced to allow tuning of these extra source terms were adjusted to give good agreement with far downstream velocity profiles measured in the experiment of Raupach *et al.* (1986).

The upstream velocity profile used by Svensson & Häggkvist was

$$U^*(z^*) = 10 \left(\frac{z^*}{110\mathrm{m}} \right)^{\frac{1}{7}} \mathrm{m/s}. \tag{4.15}$$

We fit a logarithmic profile to (4.15) by matching velocities at $z = h$ and $z = h/2$. This gives $z_o^* = 1.604$mm and $u_* = 0.3248$m/s. The fitted logarithmic profile then differs from (4.15) by less than 3% over the height range $0.4\text{m} < z^* < 11\text{m}$, which includes the part of the canopy where the distributed force and velocity perturbations are most significant.

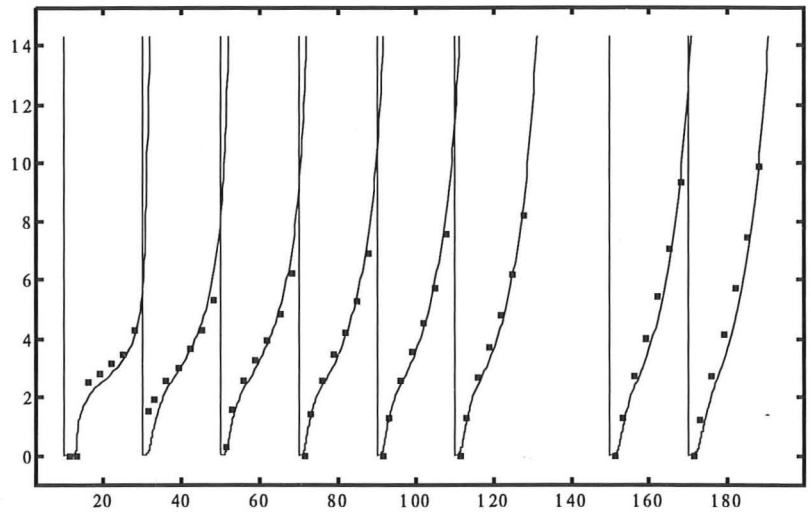

Figure 4.3: Comparison of total streamwise velocity field with the numerical simulation of Svensson & Häggkvist (1990). Points are SH's data; curves are predictions of the current SML theory. Coordinates are in metres.

The predictions of the current SML analysis are compared with Svensson & Häggkvist's simulation results in figures 4.3–4.5. Figure 4.3 shows total streamwise velocity: the points are simulation data measured from Svensson & Häggkvist's figure 4a, the curves are our predictions. Figure 4.4 presents the same comparison after the incident velocity profiles have been subtracted from the total velocities. Clearly the agreement is excellent.

Figure 4.5 shows the turbulent shear stress distribution at $x/h = 85$. So far downstream we would expect the flow to have reached an equilibrium such that the

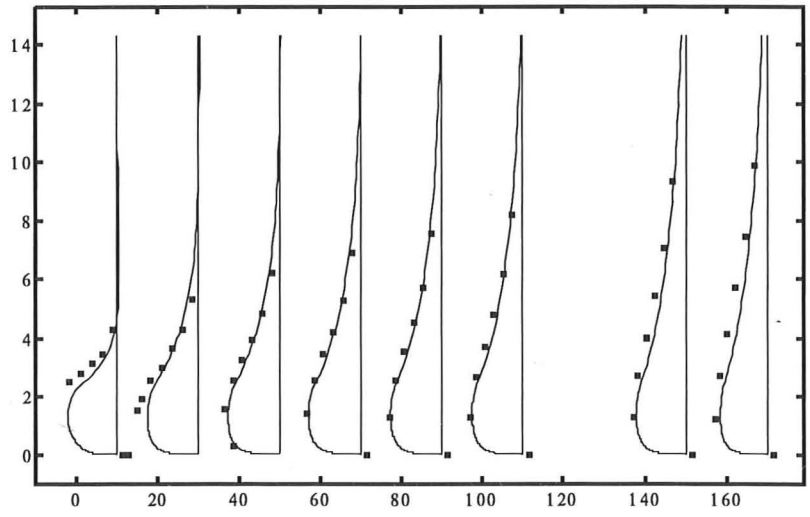

Figure 4.4: Comparison of streamwise perturbation velocity field with the numerical simulation of Svensson & Häggkvist (1990). Points are SH's numerical simulation; curves are predictions of the current SML theory. Coordinates are in metres.

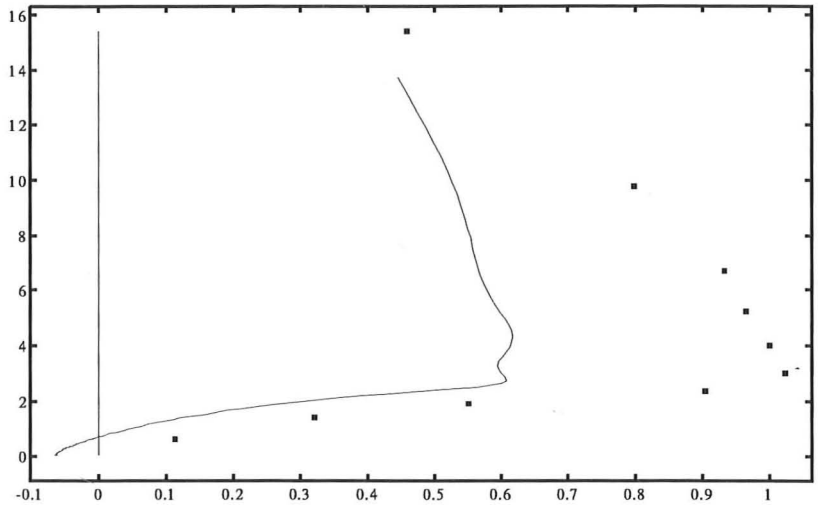

Figure 4.5: A turbulent shear stress profile far downstream from the leading edge but still within the model canopy: comparison of SML theory with the numerical simulation of Svensson & Häggkvist (1990). Points are SH's data; curves are predictions of the current SML theory. Turbulent stress in measured in m^2/s^2. Vertical coordinate is in metres.

dominant streamwise momentum balance is between distributed force and turbulent stress gradient:

$$\frac{\partial \tau}{\partial z} = f. \tag{4.16}$$

The existence of this equilibrium is supported by figures 4.3 and 4.4 and SH's figure 4a, which clearly show that there is minimal development of the perturbed velocity profile downstream of $x^* = 100\text{m}$. Therefore the apparent discrepancy between numerical simulation shear stress and our predictions is rather surprising, given the good agreement for streamwise velocity and hence for distributed force gradient. Svensson & Häggkvist did not say whether their simulation included a non-zero mean pressure gradient in the incident flow, which could account for the shear stress discrepancy.

4.6 Deceleration of the mean canopy wind

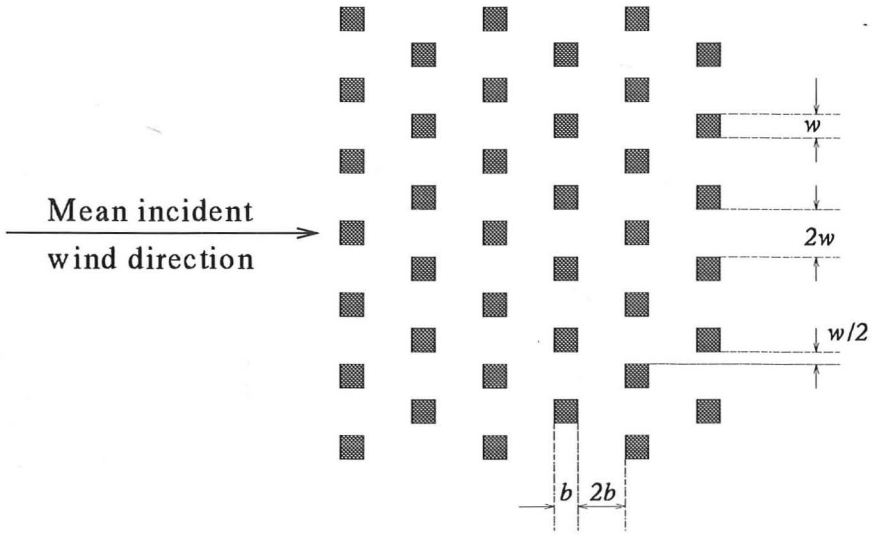

Figure 4.6: The obstacle layout in Davidson *et al.*'s (1995a) experiments.

Davidson *et al.* (1995a,b) conducted two experiments on a staggered array of obstacles arranged as in figure 4.6. One was a full-scale field experiment with obstacle dimensions $w \times b \times h = 2.2\text{m} \times 2.45\text{m} \times 2.3\text{m}$, the other a boundary layer wind tunnel

experiment with $w = b = h = 0.12$m. To quantify the deceleration caused by the array, Davidson *et al.* measured mean streamwise velocities on the array centreline at half canopy height. Assuming that lateral velocity gradients near the array centreline are negligible, so that the centreline flow can be described by two-dimensional theory, the measured velocities can be compared with predictions using the distributed force model.

In both experiments the incident velocity profile was logarithmic, with roughness parameters $z_o^* = 11$mm, $u_* = 0.49$m/s (field) and $z_o^* = 0.4$mm, $u_* = 0.21$m/s (wind tunnel). The area index defined by equation (1.4) is

$$a = \frac{w \times h}{3b \times 3w \times h} = \frac{1}{9b} = 0.045 \text{ (field)}, \ 0.93 \text{ (windtunnel)}. \tag{4.17}$$

The fraction of canopy volume not occupied by obstacles is $\beta = 0.89$. Drag coefficients for the individual obstacles were not measured. Our calculations therefore use two plausible values: $C_d = 3$ and $C_d = 5$; this enables us to assess the dependence of wind deceleration on C_d as well as to see whether our range of predictions includes the experimental data. Thus the obstacle canopies of the two experiments are modelled by rectangular drag distributions with height, length and uniform drag parameter given in the following table.

	Height	Length	D^*, $C_d = 3$	D^*, $C_d = 5$
Field experiment	2.3m	44.1m	0.153m^{-1}	0.255m^{-1}
Wind tunnel experiment	0.12m	1.92m	3.14m^{-1}	5.23m^{-1}

The comparison is shown in figure 4.7. Several points may be noted.

1. The predictions for the two experiments collapse onto each other when non-dimensionalised as in figure 4.7. This is because the model and full scale roughness heights are in approximately the same ratio as the obstacle dimensions.

2. There is good agreement between theory and experiment in the overall form of the deceleration curve. However the experimental wind begins decelerating further upwind and recovers more quickly downwind than the predicted wind.

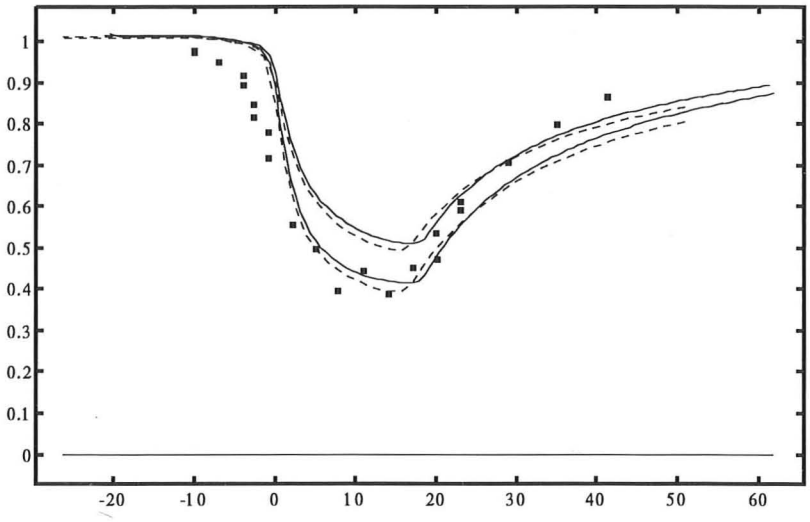

Figure 4.7: Deceleration of the mean wind through an obstacle canopy. $(U + u)/U$ at $z = h/2$ is plotted against streamwise distance from the leading edge of the array non-dimensionalised by obstacle size b. Points: Davidson *et al.*'s experimental data. Solid lines: SML theory results for the field experiment with $C_d = 3$ and $C_d = 5$. Dashed lines: SML theory results for the wind tunnel experiment with $C_d = 3$ and $C_d = 5$.

These discrepancies may be due to the finite lateral dimension of the experimental array, giving weak lateral upstream divergence and downstream convergence over streamwise distances of the order of the lateral dimension. In the case of the wind tunnel experiment, the wind tunnel roof could also be the cause of some discrepancy.

3. The maximum velocity deficit is not linearly related to the drag coefficient C_d.

We conclude that the distributed force model successfully models the mean wind deceleration through the obstacle array.

4.7 Model plant and forest canopies

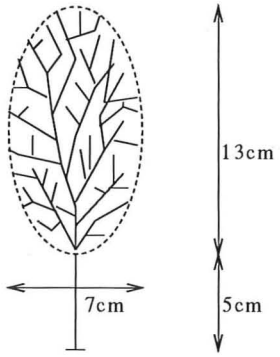

Figure 4.8: Meroney's model tree.

Meroney (1968) investigated the turbulent flow in and above a model forest consisting of trees made from "plastic simulated-evergreen boughs." His forest canopy was 0.18m high and 11m long with tree density one per 36cm^2. Meroney gives the tree drag coefficient as $C_d = 0.72$ and his description of the model tree shape (figure 4.8) gives a frontal area of 71.5cm^2. Hence the projected frontal area of the tree crown is $a_f = 11.0\text{m}^{-1}$. The leaf area index a may be greater or less than a_f depending upon leaf distribution and orientation within the crown. The occupied volume fraction $1-\beta$ is one half times the volume porosity of the tree crown. In the absence of more precise

information, we estimate $a/\beta = a_f$; hence the distributed force model drag parameter is $D^* = 7.94\text{m}^{-1}$.

For a more faithful representation of the model forest, the distributed force model can be refined to reflect the vertical structure shown in figure 4.8. Instead of a single rectangular region with uniform drag parameter $D^* = 7.94\text{m}^{-1}$, we define lower and upper rectangular regions with weaker and stronger drag parameters, namely

$$D^* = 2.58\text{m}^{-1}, \qquad 0 < z^* < 5\text{cm},$$
$$D^* = 10\text{m}^{-1}, \qquad 5\text{cm} < z^* < 18\text{cm}.$$

These numbers ensure that the overall leaf area index is unchanged. In the following comparison with Meroney's data both single region and two region representations are investigated.

Meroney measured vertical profiles of streamwise velocity at $x = -1\text{m}$, 0m, 1m, 2m, 3m, 4m, 5m, 6m, 10m and 11m from the leading edge of the model canopy. He did not specify an incident velocity profile, so we estimate incident flow roughness parameters by fitting a logarithmic profile to his measurements at $x = -1\text{m}$. This gives $z_o^* = 1.77\text{mm}$ and $u_* = 0.391\text{m/s}$.

For a simulation using the DML theory, the estimated parameters are $\lambda/h = 0.2$, $d/h = 0.7$ and $\tilde{z}/h = 0.75$. The low value of λ/h reflects the small horizontal length scale of the model forest ($\sim<$ 5cm) in comparison with canopy height. The value of d/h is an estimate following Thom (1971) and Jackson (1981) of the level of mean momentum absorption, and is typical of the ratios observed in many experiments (*e.g.* Thom 1971, Raupach *et al.* 1980). $\tilde{z}$ and d together imply an interfacial roughness height $z_o' = 0.05h \approx 1\text{cm}$ for the shear layer near the top of the forest canopy.

The comparison between theory and experiment is shown in figures 4.9 (SML theory) and 4.10 (DML theory). In general the agreement is good, more so for the downstream half of the canopy than for the upstream half. The difference between SML and DML results in the overall form of the flow field is not dramatic; specifically, the growth of the maximum velocity defect is similar in both cases. The large

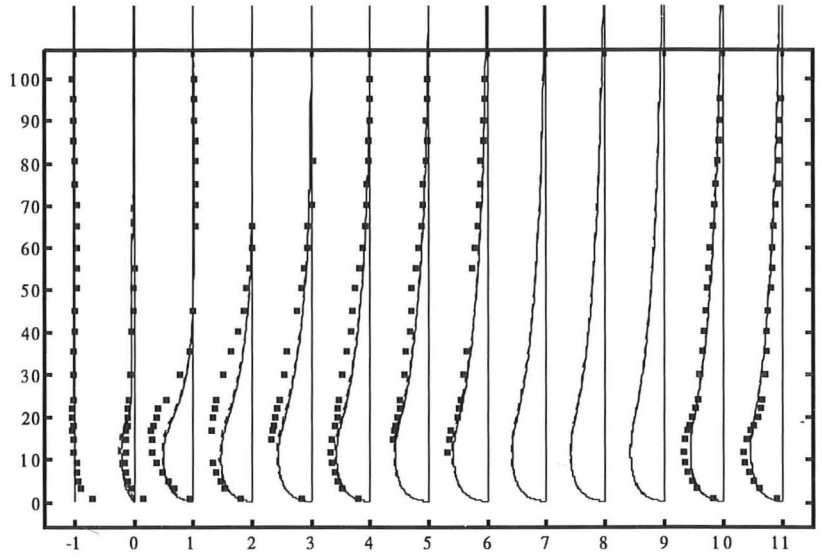

Figure 4.9: Comparison with Meroney's (1968) model forest canopy experiment using SML theory. Perturbation streamwise velocity is plotted against height (in cm) at a series of downstream locations. Points: experimental data. Solid lines: current theory using a single region distributed force model. Dashed lines: current theory using a two region distributed force model.

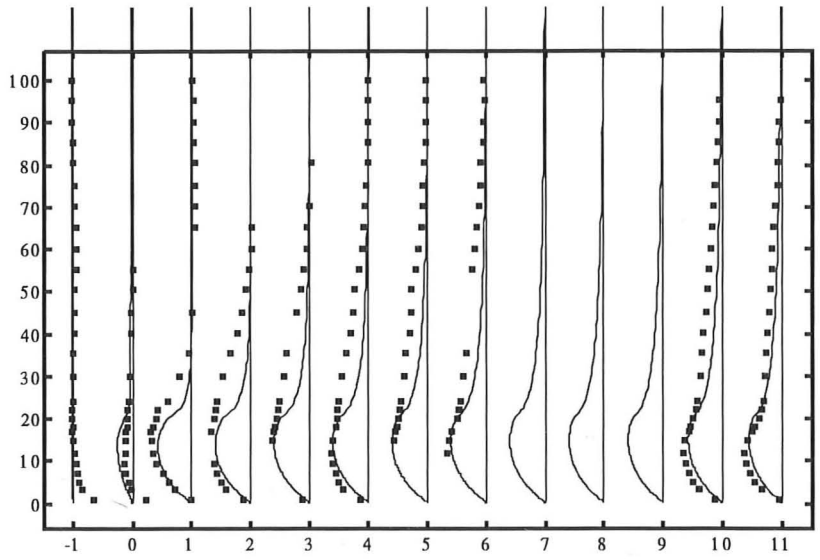

Figure 4.10: Comparison with Meroney's (1968) model forest canopy experiment using DML theory with $\lambda/h = 0.2$, $d/h = 0.7$ and $\tilde{z}/h = 0.75$. Perturbation streamwise velocity is plotted against height (in cm) at a series of downstream locations. Points: experimental data. Solid lines: current theory.

discrepancies near the leading edge may be due to a detail of Meroney's experimental setup which is not reproduced in the distributed force model. The model trees were mounted in holes drilled in an aluminium base plate sitting on the wind tunnel floor, with the leading edge of the base plate a few centimetres upstream of the leading edge of the forest canopy. Meroney does not specify the height of this base plate, but visual examination of photographs in his paper suggests that it could be as much as 3cm. Therefore the flow near the leading edge of the canopy is actually responding to a sudden vertical step about 3cm high as well as to a porous region of resistance 18cm high.

4.8 The effect of a clearing in mid-forest

Finally we apply the distributed force model and turbulent flow analysis to a scenario investigated by Stacey *et al.* (1994) using model trees in a wind tunnel experiment: mean wind acceleration in a clearing in mid-forest. Stacey *et al.* modelled a spruce forest with average height 15m, with far upstream roughness height 0.1m, across which a clearing had been cut 6.7 tree heights (100.5m) wide. They assumed that the full-scale drag of an isolated tree D agreed with an empirical formula due to Mayhead *et al.* (1975), viz.

$$\text{drag in Newtons } D = 0.4352U^2 m^{0.667} \exp(-0.0009779U^2), \tag{4.18}$$

where m is the tree's live branch mass measured in kg and U is the nominal incident wind speed in m/s. In the conditions being modelled, the live branch mass was $m = 49.5$kg and the nominal wind speed 30m/s, hence the drag force on an isolated full-scale tree was 2193N. The lateral and streamwise tree spacings were 1.73m, so the canopy volume per tree was 44.9m^3. Therefore the distributed force model drag parameter may be estimated as

$$D^* = \frac{2193\text{N}}{\frac{1}{2}\rho \times 30^2\text{m}^2/\text{s}^2 \times 44.9\text{m}^3} \approx 0.11\text{m}^{-1}. \tag{4.19}$$

The flow field shown in figure 4.11 is calculated using two regions of distributed force. Both are 15m high and have $D^* = 0.11\text{m}^{-1}$. One extends from $x = -500$m

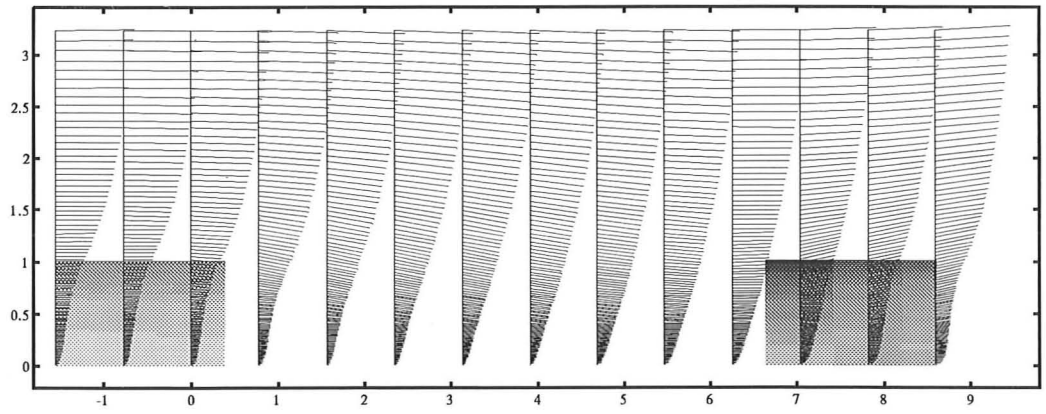

Figure 4.11: Velocity vectors in a clearing in mid-forest. Coordinates are non-dimensionalised on the forest canopy height $h = 15$m.

to $x = 0$ and is intended to set up an equilibrium canopy flow. The other extends from $x = 100.5$m to $x = 300$m. The clearing lies between the two regions. The experimentally measured flow field is shown in Stacey *et al.*'s (1994) figure 13. Detailed numerical comparison is not attempted here, but clearly there is good qualitative agreement between the experimental data and our predictions. The most notable feature is the vertical velocity variation within the clearing. The wind turns downwards to fill out the clearing immediately after its upstream edge and only turns upwards again after the trailing edge when the blocking effect of the downstream resistance has become dominant. Note that the shaded contours in figure 4.11 represent the strength of the local distributed force. The darker contours at the downstream edge of the clearing indicate that the force acting is stronger here than in the equilibrium flow at the left hand edge of the figure. In other words, a clearing in a forest increases the risk of local wind damage, as observed by Stacey *et al.*

4.9 Assessment of the results

These comparisons with numerical simulation and experimental data show that the distributed force concept and the analytical models developed in chapter 3 are useful in practice. The perturbed mean flow field is successfully modelled both within and above an obstacle canopy. In particular, the magnitude of the mean flow deceleration through the array, the tendency to an equilibrium state, and the mean flow recovery after an array are all correctly reproduced by the model theory.

Despite the extra sophistication of the DML turbulence model, the comparisons with Meroney's (1968) data show that the results of the DML theory do not greatly differ from those of the SML theory when the DML turbulence model parameters are estimated on the basis of physical reasoning. Occam's razor requires, therefore, that the SML model is recommended when the intent is to model the broad flow field features that have been considered in this chapter's comparisons.

This recommendation does not mean that the arguments behind the DML model were wrong or superfluous. The following chapter will show that the SML and DML models give dramatically different results when the flow above the canopy is parameterised in terms of effective roughness parameters and that, in general, it is the DML model which gives the better parameterisations.

Chapter 5

Parameterisations

5.1 Introduction

The analytical models developed so far can be used to compute many details of canopy flow, but for many purposes a simple parameterisation of the results may be adequate and more convenient. The results of the analytical models of chapter 3 are now used to develop such parameterisations.

The first parameterisation (§5.3) shows that the flow above the canopy is equivalent to the superposition of two flows, one corresponding to a surface roughness change and the other corresponding to a surface elevation change like a low escarpment. The inclusion of surface elevation as well as roughness in the parameterisation means that the initial blocking region of an obstacle canopy can be represented as well as the farther downstream roughness-like behaviour. Specifically, the parameterisation exhibits detailed agreement, at all heights above the canopy, between the flowfield obtained from the SML distributed force analysis and the flowfields describing flow over roughness and surface elevation changes, details of which are taken from the work of Belcher *et al.* (1990) and Hunt *et al.* (1988a). The roughness heights obtained, however, are unrealistically large because this parameterisation does not include a displacement height.

The second parameterisation (§5.4) follows several experimenters (*e.g.* Thom 1971

and Hsi & Nath 1970) in attempting to fit "equivalent" roughness parameters—friction velocity u_e, roughness height z_e and displacement height d_e—to the predicted total velocity profiles above the canopy. For flows where such a parameterisation is valid, its utility lies in encapsulating all the complexity of the two-dimensional canopy flow in just three functions of streamwise position, such that the flow well above the canopy is entirely determined by $u_e(x)$, $z_e(x)$ and $d_e(x)$.

5.2 Summary of SML results

The results of the SML turbulent flow analysis of §§3.5–3.6 are presented together here for convenience. Uniformly valid solutions for streamwise and vertical perturbation velocities and perturbation shear stress are given by

$$u^{(\mathrm{UVA})} = -iC_o e^{-kz} + iD_o e^{kz} + \int_{z_o}^{z} \frac{if(z')\sinh k(z-z')}{U_g(z')}\,dz' + \frac{if}{kU_g} - \frac{i\epsilon^2\kappa^2\tau'^{(\mathrm{UVA})}}{kU_g}, \tag{5.1}$$

$$w^{(\mathrm{UVA})} = C_o e^{-kz} + D_o e^{kz} + \int_{z_o}^{z} \frac{f(z')\cosh k(z-z')}{U_g(z')}\,dz' - \frac{\epsilon^2\kappa^2\tau^{(\mathrm{UVA})}}{U_g}, \tag{5.2}$$

$$\tau^{(\mathrm{UVA})} = \frac{iZJ_1(Z)}{\epsilon kU_l}\int_{Z}^{\infty} Z' f(z')K_o(-iZ')\,dZ' + \frac{ZK_1(-iZ)}{\epsilon kU_l}\int_{Z_o}^{Z} Z' f(z')J_o(Z')\,dZ' + iB_1 ZK_1(-iZ). \tag{5.3}$$

The coefficients appearing in (5.1)–(5.3) are given by

$$D_o + \frac{1}{2}\int_{z_o}^{\infty} \frac{f(z')\exp(-kz')}{U_g(z')}\,dz' = 0, \tag{5.4}$$

$$C_o + D_o = 0, \tag{5.5}$$

$$p_o = iU_l(C_o - D_o), \tag{5.6}$$

$$A_o + \frac{i}{kU_l}\int_{Z_o}^{\infty} Z' f(z') K_o(-iZ')dZ' = 0, \tag{5.7}$$

$$A_o J_o(Z_o) + \epsilon B_1 K_o(-iZ_o) - \frac{p_o}{U_l} = 0. \tag{5.8}$$

5.3 Surface roughness and elevation changes

Attempting to decompose the distributed force results in terms of equivalent surface roughness and elevation distributions is of interest for two reasons, one practical and the other theoretical. The practical reason is that fluid modellers, in particular meteorologists, have for many years used increased roughness and/or surface elevation to represent complex terrain and terrain-mounted obstacles such as forests and cities. Fiedler & Panofsky (1972), André & Blondin (1986), Taylor *et al.* (1989) and Wood & Mason (1993) discuss aspects of the prediction and use of an equivalent roughness; in the last two papers mentioned the equivalent roughness is closely related to the drag acting on the complex terrain. Clearly one would like to know whether an equivalent roughness for flow through a force distribution is similarly related to the force acting. Previous treatments of two-dimensional flow through a region of resistance have all been numerical (*e.g.* Svensson & Häggkvist 1990, Shaw & Schumann 1992) and so have been unable to investigate such questions analytically.

Roughness alone, however, can only model the large streamwise length scale effects of a group of obstacles; it cannot reproduce the pressure-mediated blocking effects observed around the leading edge of the group. Fung & Hunt (1991) had some success in modelling these blocking effects as well as the usual roughness effects by representing a group of obstacles as a combination of roughness and surface elevation. This suggests that the force distribution flowfield as a whole will also be better represented by a combination of roughness and elevation than by roughness alone. The following parameterisation gives explicit equivalent surface roughness and elevation distributions for any given force distribution.

The second, theoretical reason is that it ought to be possible to simulate the flow perturbations induced by *surface* elevation and roughness changes using a more

general disturbance distributed over a finite *volume*; we shall confirm that this is the case.

5.3.1 Solutions for low hills and roughness changes

Hunt *et al.* (1988a, hereafter "HLR") and Belcher *et al.* (1990, hereafter "BXH") calculated asymptotic solutions for turbulent flow over a low hill and over varying roughness using linear asymptotic methods similar to those of chapter 3. There are three small differences between their method of analysis and that used here. To permit investigation of incident velocity profiles with elevated regions of significant velocity shear, they subdivided the outer region into two layers, "middle" and "upper." The upper layer corresponds to our outer region: flow perturbations are irrotational and inviscid; the middle layer is also inviscid but neglects perturbation streamwise gradients and treats the incident velocity shear U''/U as a leading order term. (A similar refinement could be applied to the analysis of chapter 3 but was omitted in order to simplify the initial investigation; this means that the present theory is limited to logarithmic incident profiles as stated in §3.2.) Secondly, our definitions of U_o^*, ϵ, l and U_l differ slightly from theirs. Thirdly, the uniformly valid first order correction due to wU' is not included in our uniformly valid approximation (3.119), whereas it is included in HLR's and BXH's solutions.

To account correctly for these minor differences, we rederive their results following the method and parameter definitions of chapter 3. Uniformly valid approximations to the hill flow solutions are

$$u^{(\text{hill})} = \text{FT}\left\{U(z-h(x)) - U(z)\right\} - \frac{is(k)}{U_g(z)}\left(e^{-kz} - \frac{K_o(-iZ)}{K_o(-iZ_o)}\right), \tag{5.9}$$

$$w^{(\text{hill})} = \frac{s(k)}{U_g(z)}\left(e^{-kz} + \frac{\epsilon\kappa^2 Z K_1(-iZ)}{U_l K_o(-iZ_o)}\right), \tag{5.10}$$

$$p^{(\text{hill})} = is(k)e^{-kz}, \tag{5.11}$$

$$\tau^{(\text{hill})} = -\frac{s(k)ZK_1(-iZ)}{\epsilon U_g(z)K_o(-iZ_o)}. \tag{5.12}$$

Here $h(x)$ and $s(x)$ are the hill elevation and the hill slope and FT$\{\}$ represents Fourier

transformation. Uniformly valid approximations to the roughness change solutions are

$$u^{(\text{rough})} = A^{(\text{rough})}\left(K_o(-iZ) + \frac{i\epsilon\kappa^2 e^{-kz}}{U_l}\right), \tag{5.13}$$

$$w^{(\text{rough})} = -\frac{\epsilon\kappa^2 A^{(\text{rough})}}{U_l}\left(iZK_1(-iZ) + e^{-kz}\right), \tag{5.14}$$

$$p^{(\text{rough})} = 0, \tag{5.15}$$

$$\tau^{(\text{rough})} = \frac{A^{(\text{rough})} iZK_1(-iZ)}{\epsilon}, \tag{5.16}$$

where $M(x) \equiv \ln(z_1(x)/z_o)$ is the roughness parameter introduced by Townsend (1966) describing the perturbation of the local roughness $z_1(x)$ and

$$A^{(\text{rough})} = \frac{-4\epsilon M}{2\ln(l/z_1) - 4\gamma - i\pi + 2\ln 2\kappa^2} = \frac{-\epsilon M}{K_o(-iZ_1)}. \tag{5.17}$$

5.3.2 Equivalent roughness and elevation distributions

Above the top of the force distribution, the SML distributed force results (5.1)–(5.8) may be simplified and expressed as

$$u^{(\text{above})} = -ie^{-kz}F(k) - \frac{i\epsilon^2\kappa^2\tau'^{(\text{above})}}{kU_g}, \tag{5.18}$$

$$w^{(\text{above})} = e^{-kz}F(k) - \frac{\epsilon^2\kappa^2\tau^{(\text{above})}}{U_g}, \tag{5.19}$$

$$p^{(\text{above})} = ie^{-kz}U_g F(k), \tag{5.20}$$

where

$$F(k) \equiv \int_{z_o}^{\infty} \frac{f(k,z')\cosh kz'}{U_g(z')}\,dz' \tag{5.21}$$

and the shear stress is

$$\tau^{(\text{above})} = \frac{iZK_1(-iZ)}{\epsilon^2\kappa^2}\int_{z_o}^{\infty} f(z')\frac{J_o(Z_o)K_o(-iZ') - J_o(Z')K_o(-iZ_o)}{K_o(-iZ_o)}\,dz' + \frac{ip_o ZK_1(-iZ)}{\epsilon U_l K_o(-iZ_o)}. \tag{5.22}$$

If (5.18)–(5.20) are equivalent to a hill flow and roughness flow, the pressure perturbation $p^{(\text{above})}$ is due entirely to the hill flow component, since BXH's analysis shows that the most significant pressure perturbation in the roughness problem is $O(\epsilon^2)$.

Hence comparison with (5.9) shows that the hill flow contribution to (5.18)–(5.20) is defined by the slope distribution

$$s(k) = U_l F(k). \tag{5.23}$$

Equations (5.9)–(5.12) with $s(k) = U_l F(k)$ account for all the e^{-kz} terms of (5.18)–(5.20) and part of the shear stress terms. Note that the displaced incident velocity perturbation $U(z - h(x)) - U(z)$ is $O(\epsilon)$ outside the inner surface layer, so is not a leading order term over most of the flow. The remaining terms are associated with the shear stress

$$\tau^{(\text{above})} - \tau^{(\text{hill})} = \tau^{(\text{above})} + \frac{U_l F(k) Z K_1(-iZ)}{\epsilon U_g(z) K_o(-iZ_o)}. \tag{5.24}$$

Comparison with (5.13)–(5.16) shows that these terms constitute a roughness flow with

$$A^{(\text{rough})} = \frac{-\epsilon M}{K_o(-iZ_1)} = \frac{\epsilon(\tau^{(\text{above})} - \tau^{(\text{hill})})}{iZK_1(-iZ)}. \tag{5.25}$$

At leading order, therefore, the flow above the force distribution can be formally decomposed into an equivalent hill flow and an equivalent roughness flow, with respective parameters $s(k)$ and $M(k)$ given by (5.23) and (5.25).

The results of the general DML analysis cannot be decomposed into a hill component and a roughness component because the surface elevation and roughness change analyses use a turbulence closure model with no displacement height.

5.4 Equivalent roughness parameters

The equivalent roughness parameterisation follows several experimenters (*e.g.* Thom 1971 and Hsi & Nath 1970) in attempting to fit "equivalent" roughness parameters—friction velocity u_e, roughness height z_e and displacement height d_e—to the predicted total velocity profiles above the canopy.

Standard similarity arguments applied to a slowly developing turbulent boundary layer (*e.g.* Tennekes & Lumley 1972, chapter 5) show that, in a range of heights much greater than the roughness size but much less than the boundary layer depth, the vertical variation of streamwise velocity is logarithmic and can be characterised by the three roughness parameters u_e, z_e and d_e:

$$\hat{u}_m^*(z) = \frac{u_e}{\kappa} \ln \frac{z - d_e}{z_e}. \tag{5.26}$$

When it is the case that height ranges showing logarithmic velocity variation can be found at many successive downstream locations, it becomes natural to think of u_e, z_e and d_e as functions of streamwise position x.

For large scale meteorological computations, (5.26) provides a "ground" boundary condition, specifically a relation between turbulent shear stress and streamwise velocity at the lowest grid point, if values of u_e, z_e and d_e are known for the underlying terrain.

The meteorological literature, however, uses the term "effective roughness length" with different connotations from the "equivalent" roughness lengths used by the experimenters cited above. An "effective" roughness length (*e.g.* Fiedler & Panofsky 1972; Taylor *et al.* 1989, Wood & Mason 1993) is inferred from the areally averaged velocity profiles over a large horizontal area, and is closely related to the drag on that area. Consider for example a range of mountains covered by forest. The *equivalent* roughness parameters at a given horizontal location characterise the forestation and terrain slope immediately around that location, and vary with position on the mountain surface. The *effective* roughness parameters, by contrast, relate to a much larger length scale and characterise the large scale roughness of the mountains themselves. André & Blondin (1986) derive analytical expressions for a large scale effective roughness length in terms of the distribution of small scale equivalent roughness lengths.

In the context of this thesis, however, the distinction between "equivalent" and "effective" roughness parameters is not so clear cut. It appears at first that the roughness parameters derived below from a local velocity profile must be "equivalent" parameters. Recall, though, that horizontal areal averaging is implicit in the distributed force concept and in any results derived from it, and in this sense our roughness parameters are "effective." Moreover, note that the distributed force concept can in principle be used to model the effects of a group of mountains just as it can be used to model the forest on a single mountain—the difference is merely one of horizontal length scale. In the following analysis, therefore, "equivalent" and "effective" are used somewhat interchangeably, and are associated with areal averaging over the horizontal obstacle length scale that was used (at least conceptually) to calculate the model force distribution.

5.4.1 Linear perturbation of the logarithmic profile

For comparison with the analytical results of chapter 3, we express (5.26) in terms of the perturbation u_m^* and an upstream velocity profile characterised by zero displacement height, roughness height z_o and friction velocity u_*; then

$$u_m^*(x,z) = \hat{u}_m^*(x,z) - U^*(z) \approx \frac{u_* \tau_e(x)}{2\kappa} \ln\frac{z}{z_o} - \frac{u_* M_e(x)}{\kappa} - \frac{u_* d_e(x)}{\kappa z}, \tag{5.27}$$

where $\tau_e \equiv u_e^2/u_*^2 - 1$ and $M_e \equiv (1+\tau_e/2)\ln(z_e/z_o)$. In the linearisation of (5.27) second order terms such as products of τ_e and d_e/z have been neglected. The three terms on the right hand side of (5.27) describe perturbations to the friction velocity, roughness height and displacement height. Notice how they are respectively associated with $\ln z$, constant and z^{-1} contributions to the perturbation velocity profile. After Fourier transformation and non-dimensionalisation (5.27) becomes

$$u_m(k,z) \approx \frac{\epsilon \tau_e(k)}{2} \ln\frac{z}{z_o} - \epsilon M_e(k) - \frac{\epsilon d_e(k)}{z}. \tag{5.28}$$

Thus it is possible to define an effective shear stress, roughness parameter and displacement height associated with each wavenumber of the velocity perturbations in Fourier space as well as with each streamwise station in real space.

The dimensionless model perturbation profile (5.28) will be compared with the results of the SML analysis. For comparison with the DML analysis, note that (5.28) is equivalent in the linear approximation to

$$u_m(k,z) \approx \frac{\epsilon\tau_e(k)}{2}\ln\frac{z-d}{z_o'} - \epsilon M_e(k) - \frac{\epsilon d_e(k)}{z} + \frac{\epsilon\tau_e}{2}\ln\frac{z_o'}{z_o}, \tag{5.29}$$

i.e. the difference between (5.28) and (5.29) is quadratic in the small quantities τ_e and d_e/z.

5.4.2 Roughness parameters for the SML analysis

The SML streamwise perturbation velocity profile (5.18) varies approximately logarithmically in the height range $H < z \ll l$, if this range is not empty. For small z/l and H/l, (5.18) may be approximated using (4.8) and (4.9), to give

$$\begin{aligned} u \approx\ & \frac{1}{2\epsilon\kappa^2}\ln\frac{z}{z_o}\int_{z_o}^{\infty}\frac{f(z')\ln(z'/z_o)}{2K_o(-iZ_o)}\,dz' - \frac{i\ln(z/z_o)}{2U_lK_o(-iZ_o)}\int_{z_o}^{\infty}f(z')\,dz' \\ & - \frac{1}{2\epsilon\kappa^2}\int_{z_o}^{z}f(z')\ln\frac{z'}{z_o}\,dz' - \frac{1}{2\epsilon\kappa^2}\ln\frac{z}{z_o}\int_{z}^{\infty}f(z')\,dz'. \end{aligned} \tag{5.30}$$

Hence, putting $z > H$, comparison with (5.28) shows that the effective roughness parameters describing the flow in this height range are

$$\tau_e(k) = \frac{1}{\epsilon^2\kappa^2}\int_{z_o}^{\infty}\frac{f(z')\ln(z'/z_o)}{2K_o(-iZ_o)}\,dz' - \frac{i}{\epsilon U_lK_o(-iZ_o)}\int_{z_o}^{\infty}f(k,z')\,dz'. \tag{5.31}$$

and

$$M_e(k) = \frac{1}{2\epsilon^2\kappa^2}\int_{z_o}^{\infty}f(k,z')\ln\frac{z'}{z_o}\,dz' \tag{5.32}$$

The first term in (5.31) is $O(\epsilon^{-2})$ larger than the second.

5.4.3 Roughness parameters for the DML analysis

In the upper part of the DML flow, where the mixing length is $\lambda_m = \kappa(z-d)$, the solution for the rooftop inner region (3.173) may be written

$$\begin{aligned} u &= \frac{A_o}{K_o(-i\tilde{Z})}\{J_o(Z)K_o(-i\tilde{Z}) - J_o(\tilde{Z})K_o(-iZ)\} \\ &\quad + \frac{p_o}{U_l K_o(-i\tilde{Z})}\{K_o(-iZ) - K_o(-i\tilde{Z})\} \\ &\quad + \frac{i}{kU_l}\int_{\tilde{Z}}^{Z} Z' f(z')\{J_o(Z)K_o(-iZ') - J_o(Z')K_o(-iZ)\}\,dZ' \\ &\quad + \frac{K_o(-iZ)}{K_o(-i\tilde{Z})}\tilde{u}, \end{aligned} \tag{5.33}$$

where

$$p_o = iU_l\left(\tilde{w} + \int_{\tilde{z}}^{\infty} \frac{f(z')e^{-k(z'-d)}}{U(z')}\,dz'\right) \tag{5.34}$$

and A_o is given by (3.175). For small $(z-d)/l$ and $(H-d)/l$, using similar approximations to (4.8) and (4.9), (5.33) becomes

$$\begin{aligned} u &\approx \tilde{u} - \frac{1}{2\epsilon\kappa^2}\int_{\tilde{z}}^{z} f(z')\ln\frac{z'-d}{z'_o}\,dz' - \frac{1}{\epsilon\kappa^2}\ln\frac{z-d}{z'_o}\int_{z}^{\infty} f(z')\,dz' \\ &\quad + \frac{1}{2\epsilon\kappa^2}\ln\frac{z-d}{z'_o}\int_{\tilde{z}}^{\infty}\frac{f(z')}{2K_o(-i\tilde{Z})}\ln\frac{z'-d}{z'_o}\,dz' \\ &\quad - \frac{1}{2K_o(-i\tilde{Z})}\ln\frac{z-d}{z'_o}\left(\tilde{u} + i\tilde{w} + \int_{\tilde{z}}^{\infty}\frac{if(z')}{U_l}\,dz'\right). \end{aligned} \tag{5.35}$$

Hence, putting $z > H$, comparison with (5.29) shows that effective roughness parameters for this part of the DML flow are given by

$$\tau_e(k) = \frac{1}{2\epsilon^2\kappa^2 K_o(-i\tilde{Z})}\int_{\tilde{z}}^{\infty} f(z')\ln\frac{z'-d}{z'_o}\,dz' - \frac{\tilde{u} + i\tilde{w} + \int_{\tilde{z}}^{\infty}\frac{if(z')}{U_l}\,dz'}{\epsilon K_o(-i\tilde{Z})} \tag{5.36}$$

and

$$M_e(k) = \frac{1}{2\epsilon^2\kappa^2}\int_{\tilde{z}}^{\infty} f(z')\ln\frac{z'-d}{z'_o}\,dz' - \frac{\tilde{u}}{\epsilon} + \frac{\tau_e}{2}\ln\frac{z'_o}{z_o}. \tag{5.37}$$

A useful check on the algebra is that the SML results (5.30), (5.31) and (5.32) may be obtained from (5.35), (5.36) and (5.37) respectively by putting $\tilde{u} = \tilde{w} = d = 0$ and $\tilde{z} = z'_o = z_o$. In the remainder of this chapter, where arguments apply equally to the SML and DML analyses, it will suffice to give explicit expressions only for the more general DML analysis.

5.4.4 Relationship with the surface roughness/elevation parameterisation

The SML roughness parameters (5.31) and (5.32) could also have been obtained via the surface roughness/elevation parameterisation of §5.3, since roughness parameters can be derived separately for the surface elevation and roughness change problems. For the flow above a surface slope distribution $s(k)$, approximation of (5.9) gives the roughness parameters

$$M_e(k) = 0 \qquad \text{and} \qquad \tau_e(k) = \frac{-is(k)}{\epsilon U_l K_o(-iZ_o)}. \tag{5.38}$$

Similar approximation of the roughness change streamwise velocity (5.13) for a surface roughnes distribution $M(k)$ gives

$$M_e(k) = M(k) \qquad \text{and} \qquad \tau_e(k) = \frac{M(k)}{K_o(-iZ_o)}. \tag{5.39}$$

These are leading order results valid in the wavenumber-dependent height range $H < z \ll l(k)$. Equation (5.39) confirms that the *surface* roughness parameter M, which appears in BXH's analysis as a surface slip velocity $u(z_o) = -\epsilon M$, is equivalent to the roughness parameter M_e deduced from the streamwise velocity variation above the roughness change. When the distributions $s(k)$ and $M(k)$ given by (5.23) and (5.25) are substituted into (5.38) and (5.39), and the elevation and roughness change contributions added together, the resulting parameters M_e and τ_e are the same at leading order as those given by direct roughness parameterisation of the SML results in (5.31) and (5.32).

5.4.5 Sample results

The distributions of M_e given by (5.32) and (5.37) have been calculated in the simulations of Meroney's (1968) model forest experiment described in §4.7. Strictly speaking it is incorrect to take the inverse Fourier transform of $M_e(k)$ since $M_e(k)$ is only defined at smaller wavenumbers for which $H \ll d + l(k)$ (with $d = 0$ for the SML analysis). However, since (i) the amplitudes of higher wavenumber Fourier components of the

distributed force are relatively small and (ii) the restriction $H \ll d + l(k)$ has a physical basis in Fourier space that can be restated in real space, we calculate the inverse Fourier transform regardless and then consider in what region of the real space flow the resulting $M_e(x)$ has validity.

The physical basis of the restricted height range $H < z \ll d + l(k)$ is that $M_e(k)$ is a valid parameterisation of the flow only for positions both above the force distribution and well within the inner flow region where turbulence is in local equilibrium. Townsend's (1965) arguments, upon which the Fourier space inner region derivation of §3.3.1 was based, were originally stated in real space, and showed that after a sudden change in surface conditions turbulence is in local equilibrium within an internal boundary layer whose height $l(x)$ is given approximately by

$$l \ln \frac{l}{z_o} \sim x \tag{5.40}$$

where x is the distance downstream from the change. For flow with non-zero displacement height d, (5.40) generalises to

$$l \ln \frac{d+l}{z_o} \sim x. \tag{5.41}$$

Hence the real space roughness parameters, $\tau_e(x)$ and

$$M_e(x) = \frac{1}{2\epsilon^2\kappa^2} \int_{\tilde{z}}^{\infty} f(x,z') \ln \frac{z'-d}{z'_o}\, dz' - \frac{\tilde{u}}{\epsilon} + \frac{\tau_e(x)}{2} \ln \frac{z'_o}{z_o}, \tag{5.42}$$

are valid in the region $\{(x,z) : H < z \ll d+l(x)\}$ with $l(x)$ given by (5.41), *i.e.* for flow well downstream of the initial blocking region of the canopy where pressure and inertial effects dominate the flow. Notice that a non-zero displacement height d *increases* the region of validity of the roughness parameterisation and brings the point of origin of the internal boundary layer defined by (5.41) *closer* to the leading edge of the obstacle canopy. (The streamwise coordinate where the IBL emerges from the roof of the obstacle canopy is estimated by putting $l = H - d$ in (5.41).)

Figure 5.1 shows the calculated $M_e(x)$ for the SML and DML simulations of Meroney's (1968) model forest experiment described in §4.7. The DML equilibrium value of about 2.7 corresponds to an effective roughness height of about 2.6cm

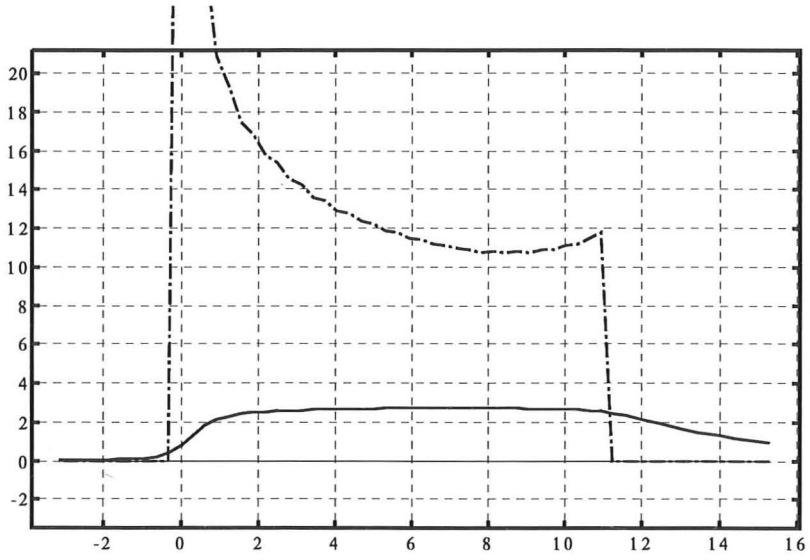

Figure 5.1: The roughness parameter $M_e(x)$ calculated in the SML (dot-dashed line) and DML (solid line) simulations of Meroney's (1968) experiment. The horizontal axis shows streamwise coordinate in metres.

($z_e/H \approx 0.14$). For the same experimental configuration Hsi & Nath (1970) inferred a roughness height of 0.74cm ($z_e/H \approx 0.04$) above the model forest, but they took d to equal the forest height H and their semi-logarithmic plot of $\hat{u}/u_*$ against $\ln(z-H)$ (their figure 10), from which their effective roughness height was estimated, consequently shows a pronounced curve. When their data is replotted using the present model displacement height $d = 12.6$cm ($d/H = 0.7$), estimated following Thom (1971) and Jackson (1981) as the level of mean momentum absorption, the semi-logarithmic curve is straighter and leads to an effective roughness height of about 1.6cm ($z_e/H \approx 0.09$).

The SML value, on the other hand, is far too large to be realistic. This is because the SML turbulence model forces the flow above the canopy to have zero displacement height. Suppose the velocity variation above the canopy is broadly as illustrated in figure 5.2, and recall that the roughness parameter M_e quantifies the slip velocity at the displacement height, as shown by BXH's analysis and the parameterisation of §5.4.4. Clearly the flow above the force distribution in figure 5.2 is displaced with a displacement height d of the order of H, and the slip velocity at $d = O(H)$ is a good velocity scale for the complete profile. The DML parameterisation shows that the effective roughness parameter M_e for the flow above the canopy is related to the magnitude of the velocity defect within it. The SML parameterisation, on the other hand, effectively obtains its velocity scale by extrapolating the logarithmic velocity variation above H down to the ground, as indicated by the dashed line, leading to enormous and unrealistic values of M_e.

Figure 5.1 shows how strongly the value of M_e depends upon the model displacement height. To investigate the sensitivity of M_e to the other DML model parameters, figure 5.3 shows the effect of doubling the canopy mixing length λ and the interfacial roughness height z_o'. The weak dependence of M_e upon λ and z_o' is a robust feature of the present parameterisation because these two parameters are more difficult to estimate in an algorithmic way than the displacement height d.

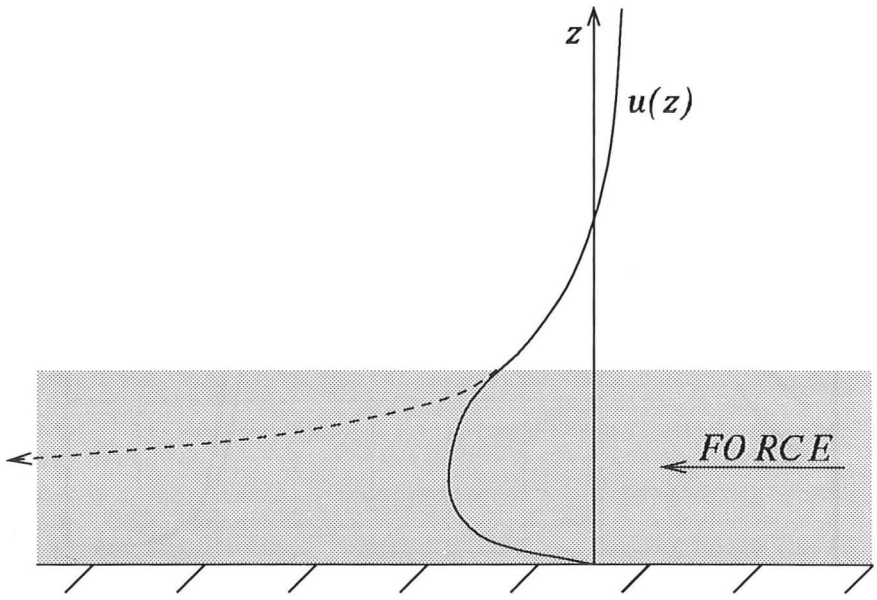

Figure 5.2: A typical low wavenumber streamwise velocity profile (solid line). Values of effective roughness parameter M_e are obtained by fitting a logarithmically varying profile to the velocity above the canopy and taking the value of the fitted logarithmic profile at the displacement height d. Hence the dashed line shows why unrealistically large values of effective roughness parameter M_e are obtained when an appropriate displacement height is not taken into account.

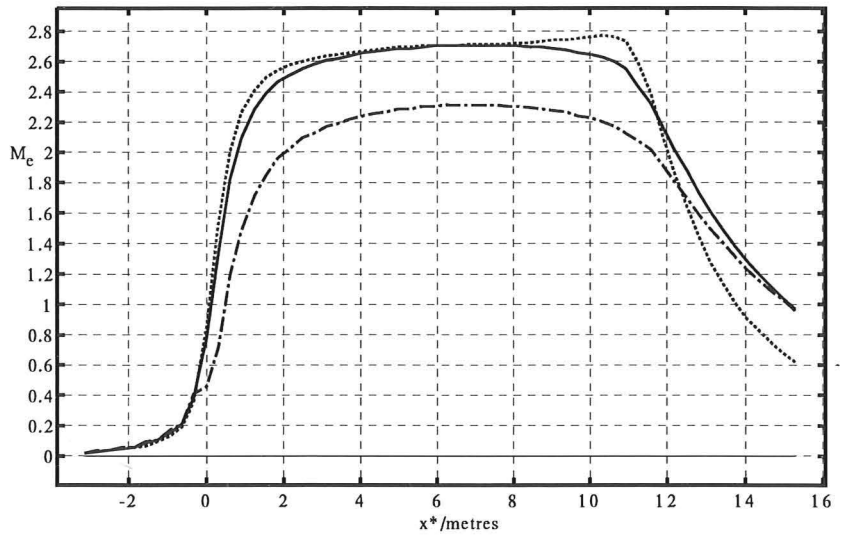

Figure 5.3: Illustrating the sensitivity of M_e to DML model parameters. The solid line is the same as in figure 5.1 ($\lambda/h = 0.2$, $d/h = 0.7$ and $\tilde{z}/h = 0.75$). The dotted line shows M_e calculated with λ/h doubled to 0.4; the dashed line shows M_e calculated with z'_o/h doubled to 0.1.

5.4.6 Far downstream development

One case of specific interest is an obstacle canopy that continues with constant obstacle density for a streamwise distance much larger than the canopy height.

Experiments (*e.g.* Thom 1971, Raupach *et al.* 1986) and the simulations of chapter 4 strongly suggest that the flow in this case attains an equilibrium state in which the streamwise velocity and turbulent stress profiles become independent of streamwise coordinate. The distributed force acting on the flow is balanced by the turbulent stress gradient.

Since this equilibrium state is independent of the drag parameter distribution much farther downstream, it is mathematically convenient to consider a semi-infinite drag distribution. The suffix ∞ will be used in this section to denote the limiting forms of profiles far downstream. Suppose that the equilibrium distributed force profile is $f_\infty(z)$, independent of x. Then the equilibrium streamwise velocity profile $u_\infty(z)$ is given by the limit of the approximate Fourier transform (5.35) as $k \to 0$:

$$u_\infty(z) = \tilde{u}_\infty - \frac{1}{2\epsilon\kappa^2}\int_{\tilde{z}}^{z} f_\infty(z') \ln\frac{z'-d}{z_o'}\,dz' - \frac{1}{2\epsilon\kappa^2}\ln\frac{z-d}{z_o'}\int_{z}^{\infty} f_\infty(z')\,dz'. \quad (5.43)$$

This result does not depend upon the arguments given in (5.4.5) as justification for the general inverse Fourier transform operation, since the far downstream profiles f_∞ and u_∞ are dominated by the k^{-1} singularity in their Fourier transforms as $k \to 0$.

Putting $z > H$ in (5.43) gives the far downstream roughness parameters

$$\tau_\infty = 0 \qquad \text{and} \qquad M_\infty = \frac{1}{2\epsilon^2\kappa^2}\int_{\tilde{z}}^{z} f_\infty(z') \ln\frac{z'-d}{z_o'}\,dz' - \frac{\tilde{u}_\infty}{\epsilon}. \quad (5.44)$$

The vanishing of the far downstream perturbation shear stress was also obtained by Townsend (1976, §7.15) for a surface roughness change.

Equation (5.43) indicates the form of the far downstream velocity perturbation but not its magnitude. Owing to the non-linear dependence of the distributed force on the total velocity, exact calculation of the magnitudes of u_∞ and f_∞ requires the solution of the non-linear differential equation

$$(\zeta \hat{u}_\infty')' = \hat{u}_\infty^2, \quad (5.45)$$

where ζ is a stretched vertical coordinate and $\hat{u}_\infty$ is the total, *i.e.* incident plus perturbation, downstream velocity. This solution has not been obtained here, but an approximation to it may be obtained by noting that $u_\infty(z)$ given by (5.43) is constant above the force distribution and therefore assuming that $u_\infty(z)$ varies only slowly in the upper part of the force distribution where $\ln(z-d)/z'_o$ is large. Then putting $z = H$ in (5.43) gives

$$u_\infty(H) \approx \tilde{u}_\infty - \frac{L^* D^*}{4\epsilon\kappa^2}\left(1 + u_\infty(H)\right)^2 \int_{\tilde{z}}^{H} \ln\frac{z'-d}{z'_o}\, dz', \tag{5.46}$$

the solution of which is

$$u_\infty(H) \approx -1 + \sqrt{\frac{1+\tilde{u}_\infty}{\alpha}}. \tag{5.47}$$

where

$$\alpha = \frac{L^* D^*}{4\epsilon\kappa^2}\left\{(H-d)\ln\frac{H-d}{z'_o} - H + \tilde{z}\right\}. \tag{5.48}$$

In the SML case this simplifies to

$$u_\infty(H) \approx -1 + \frac{2\epsilon\kappa}{\sqrt{H^* D^*}}, \qquad \text{or} \quad \hat{u}_\infty(H) \approx \frac{2\epsilon\kappa}{\sqrt{H^* D^*}}. \tag{5.49}$$

Hence limiting values of streamwise velocity scale with the inverse square root of canopy height and drag parameter and in proportion with ϵ. The asymptotic small parameter ϵ quantifies the incident velocity shear, or equivalently the strength of the turbulent mixing processes, within the force distribution. As ϵ decreases, the capacity of the turbulent stress gradient to balance the force acting is reduced, hence the magnitudes of the equilibrium force and total streamwise velocity profiles must decrease.

The scaling of $\hat{u}_\infty$ with the inverse square root of drag parameter D^* agrees with the results shown in figure 4.7. For two values of D^* in the ratio $5:3 \approx 1.67$, the values of $\sqrt{D^*}$ are in the ratio $\sqrt{5}:\sqrt{3} \approx 1.29$ and the near-equilibrium values of streamwise velocity are in the approximate ratio $5:4 = 1.25$.

5.5 The importance of displacement height

The parameterisation results of §5.4 show that accurate modelling of the displacement height d is crucial to the prediction of realistic roughness parameters M_e and τ_e. The fine details of a practical scheme to estimate d, M_e and τ_e for any given canopy flow are incomplete, since we have not specified algorithms for estimating the DML parameters λ and z_o'. The sensitivity study of §5.4.5, however, suggests that the impact of λ and z_o' on calculated roughness parameters is minor in comparison with that of d. Therefore an interim recipe can be outlined as follows.

1. Calculate a displacement height d for the flow as the level of mean momentum absorption, following Thom (1971), Jackson (1981) and the discussion of §3.8.

2. Estimate λ and z_o' using the physical ideas of §3.8.

3. Calculate effective roughness parameters M_e and τ_e using the results of §5.4.

It is interesting to note that the DML and SML results are very similar in the picture they give of the overall canopy flow field (§4.7) but differ enormously when parameterised in terms of roughness.

Chapter 6

Scalar dispersion within a group of obstacles

6.1 Introduction

Many of the practical situations that motivate investigation of flow through a group of obstacles are concerned with dispersion, for example the accidental release of toxic or radioactive material just upwind of a built-up area. Understanding the changes in the flow field around a group of buildings is a prerequisite for any prediction of the dispersion, but the bottom line for those at risk is expressed in terms of increased or reduced concentrations, not velocities and turbulent shear stresses.

As a preliminary investigation into the problem of dispersion near buildings, and to show how the flow field results of previous chapters can be used in a practical dispersion calculation, this chapter presents a steady, Eulerian analysis of concentration changes based on the time-averaged diffusion equation. Although a mathematically similar analysis has been performed before for flow over low hills (Hunt *et al.* 1988c, Weng 1990), new aspects of diffusive behaviour emerge because the underlying velocity and turbulent stress fields are very different.

6.2 The variety of dispersive processes

The problem of turbulent dispersion around a group of buildings is hugely complex. Different time scales, of the turbulence in the incident wind, of the turbulence generated by obstacles and of the mean flow advection between obstacles, interact to determine the behaviour of parcels of contaminant passing through the array. Rapid advection between obstacles coupled with long residence times in individual obstacle wakes gives rise to a chaotic, random walk process in which parcels of contaminant behave largely independently of each other. Slow advection between obstacles, on the other hand, allows turbulent eddying motions to spread out the concentration field in a more continuous way.

Following the field and wind tunnel experiments of Davidson *et al.* (1995a,b), Jerram *et al.* (1994) discussed some important physical processes that influence dispersion in such flows. For an unobstructed plume, lateral meandering of the mean wind (on the experimental advection time scale) makes the instantaneous plume width much smaller than the time- or ensemble-averaged plume envelope, as described for vertical diffusion from a ground-level source by Hunt & Weber (1979); this meandering effect is clearly visible in the video of the Cardington field experiments shown by Davidson *et al.* (1995a). For a plume passing through the group of buildings, however, the meandering effect is reduced by the creation of secondary wake sources: an obstacle's wake rapidly entrains contaminant while the plume is directed onto that obstacle and detrains contaminant more slowly for some time after the impinging plume has been turned elsewhere by the meandering wind. A second important effect is topological dispersion: the convergence and divergence of mean streamlines as they weave between the obstacles amplifies the effects of turbulent diffusion across the streamlines. Countering this increase in total dispersion, however, the basic turbulent diffusivity within a group of obstacles can be less than in the incident flow when the lateral obstacle dimensions are much smaller than turbulence length scales in the incident wind, as shown in the bubble experiment described by Hinze (1975, pp. 448–449).

Turbulent diffusion near a two-dimensional obstacle and its wake was studied by

Puttock & Hunt (1979) using the diffusion equation: their results included prediction of the average residence time of fluid particles within the recirculating wake. Fung & Hunt (1991) modelled the lateral diffusion through a group of tall cylinders using potential flow for the mean flow field, a random flight model for the turbulence and the criterion that whenever a fluid particle hit an obstacles it was absorbed for a period of time representing residence in the wake and then emitted at a random position around the wake's boundary. Fung & Hunt's model permitted study of the topological dispersion and secondary source effects, but omitted consideration of vertical plume spread and deceleration of the mean flow through the group (since in potential flow the obstacles exert no drag upon the flow). Bartsch (1993) used a similar potential flow model to try to relate particle travel times through an array of cylinders to observed pressure drops across such arrays and to the dispersion of contaminant within the array.

Summaries of the mathematical modelling approaches available for general dispersion problems, without particular reference to groups of obstacles and the associated special effects, are given by Robins & Fackrell (1977), Hunt *et al.* (1979), Chatwin & Allen (1985) and Hunt (1985). Thomson (1986) describes a random walk model for dispersion over complex terrain that might be adaptable for flow through a group of buildings. Kot (1989) considers the application of the various modelling approaches to contaminant dispersion around buildings. The consensus is that statistical methods provide the most authoritative dispersion predictions but require detailed flow field information that is often unavailable. The conceptually simpler diffusion equation does not required such detail but is based on gradient-transfer assumptions that are, in general, unfounded. In many situations, however, statistical analysis can be used to show that the diffusion equation is approximately valid in certain regions of the flow, usually where fluid particles have travelled for a long time from the source of contaminant (*e.g.* Chatwin & Allen).

6.3 Use of the time-averaged diffusion equation

This chapter presents a steady, Eulerian analysis of concentration changes based on the time-averaged diffusion equation

$$\hat{\mathbf{u}}^* \cdot \nabla^* \hat{c}^* + \frac{\partial}{\partial x_i^*} \langle \hat{u}_i' \hat{c}' \rangle = 0. \tag{6.1}$$

Here $\hat{\mathbf{u}}^*$ and $\hat{c}^*$ are the total mean velocity and concentration fields and $\hat{\mathbf{u}}'$ and $\hat{c}'$ are the total fluctuation velocity and concentration fields. In the second term of (6.1), $\langle \hat{u}_i' \hat{c}' \rangle$ is a mean concentration flux due to temporal correlations between the fluctuating concentration and velocity fields. Modelling is required, as in the time-averaged Navier Stokes equations, because there is no closed form equation for $\langle \hat{u}_i' \hat{c}' \rangle$. By arguments similar to those of §3.2, the gradient-transfer model proposes that this flux is linearly related to the mean concentration gradients—

$$\langle \hat{u}_i' \hat{c}' \rangle = -\hat{K}_{ij}^* \frac{\partial \hat{c}^*}{\partial x_j^*} \tag{6.2}$$

—with diffusion coefficients $\hat{K}_{ij}^*$ that depend only on the local flow. For a detailed discussion of this model and the turbulent scalar diffusion equation, see the review of Chatwin & Allen (1985). Observations and theoretical arguments suggest that (6.2) is a reasonable model for far-field diffusion, *i.e.* for diffusion of fluid particles which have moved some distance away from the source of concentration, but fails to describe dispersion close to a source, since fluid particles tend initially to travel in straight lines for a time of the order of the Lagrangian integral time scale T_L^*.

Our analysis calculates the *changes* in concentration that are due to the existence of obstacles obstructing the boundary layer flow. Thus we imagine the concentration distribution of some pollutant that would prevail in the *absence* of any obstacles, and then ask how this distribution would be altered by the addition of a group of obstacles to the flow. The pre-existing, steady concentration field may derive from a localised source upstream of the group, in which case its form may be calculated by reference to the literature on turbulent dispersion in undisturbed boundary layers (*e.g.* Hunt & Weber 1979, Hunt 1985). Alternatively it may be a diffuse cloud of pollution whose

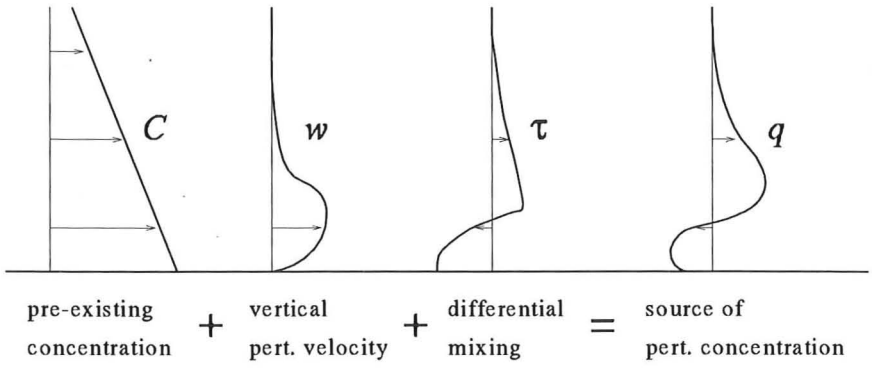

Figure 6.1: The creation of a perturbation source field.

length scales are much larger than those of the perturbing group of obstacles, changing little in the streamwise direction and with a simply varying concentration profile in the vertical (cf. Hunt *et al.* 1988c).

In all cases the perturbation velocity and stress fields cause the pre-existing concentration distribution to be advected and diffused differently to what would happen in the absence of such perturbations, creating patches q within the flow where concentration is higher or lower than it would otherwise be (figure 6.1). These patches then act as sources—both positive and negative—of perturbation concentration which may be advected downstream by the total velocity field and dispersed by turbulent stresses.

Thus the perturbation concentration field to be calculated appears to derive from a virtual source q that is distributed throughout the group of obstacles. If q were a *real* source of concentration, the diffusion equation alone would be a poor model of the resulting concentration distributions, since it is invalid for parcels of contaminant that have not travelled far from their source. Raupach (1989) describes a combined method, using a statistical method for the near field and a diffusion equation for the far field, that could be used to analyse such a distributed real source of contaminant. For the present *virtual* source, however, we believe that the near field restriction does not apply. The distinctive statistical behaviour of fluid particles near a source results from

the initial localisation of fluid particle positions. Fluid particles anywhere in a flow field will tend to move in straight lines for times of the order of T_L^*; what differentiates near-field dispersion is that all dispersing particles are starting from a fixed position. Fluid particles passing through the virtual sources of perturbation concentration do not have such certain positions; having travelled for some time from the actual source their coordinates are described by delocalised probability distributions. Hence dispersion of perturbation concentrations from virtual sources should behave everywhere like far-field dispersion. (Except, of course, for virtual source that lie within T_L^* of the actual source, such that near-field dispersion from the actual source is still in effect. Such cases, which arise when a source of pollution is placed within or very near the group of obstacles, require corrections similar to those used by Raupach (1989) and are excluded from the analysis below.) It follows that (6.1) and (6.2) together should provide a reasonable model of the dispersion process.

6.4 Linearisation conditions and flow structure

The governing equations for perturbation concentration will be linearised as have been the flow equations of previous chapters. This means that products of perturbation concentration with perturbation velocities are neglected in comparison with products of perturbation concentration and incident velocity. This does not require any assumption that perturbation concentrations are much smaller than pre-existing concentrations because the diffusion equation is linear in concentration. Thus the only linearisation assumptions are those on the perturbation velocities and turbulent stresses which have already been used in deriving the flow field information.

The arguments of §3.3, defining the region near the ground where a turbulence closure model based on gradient-diffusion is appropriate, apply equally to the use of (6.2) in modelling turbulent fluxes of perturbation concentration. Therefore the flow domain is divided into inner and outer regions in the same way as for the standard mixing length flow calculations. The problems of multiple length scales discussed in §3.4 are unlikely to be so prevalent as in the flow calculation, as the perturbation

the initial localisation of fluid particle positions. Fluid particles anywhere in a flow field will tend to move in straight lines for times of the order of T_L^*; what differentiates near-field dispersion is that all dispersing particles are starting from a fixed position. Fluid particles passing through the virtual sources of perturbation concentration do not have such certain positions; having travelled for some time from the actual source their coordinates are described by delocalised probability distributions. Hence dispersion of perturbation concentrations from virtual sources should behave everywhere like far-field dispersion. (Except, of course, for virtual source that lie within T_L^* of the actual source, such that near-field dispersion from the actual source is still in effect. Such cases, which arise when a source of pollution is placed within or very near the group of obstacles, require corrections similar to those used by Raupach (1989) and are excluded from the analysis below.) It follows that (6.1) and (6.2) together should provide a reasonable model of the dispersion process.

6.4 Linearisation conditions and flow structure

The governing equations for perturbation concentration will be linearised as have been the flow equations of previous chapters. This means that products of perturbation concentration with perturbation velocities are neglected in comparison with products of perturbation concentration and incident velocity. This does not require any assumption that perturbation concentrations are much smaller than pre-existing concentrations because the diffusion equation is linear in concentration. Thus the only linearisation assumptions are those on the perturbation velocities and turbulent stresses which have already been used in deriving the flow field information.

The arguments of §3.3, defining the region near the ground where a turbulence closure model based on gradient-diffusion is appropriate, apply equally to the use of (6.2) in modelling turbulent fluxes of perturbation concentration. Therefore the flow domain is divided into inner and outer regions in the same way as for the standard mixing length flow calculations. The problems of multiple length scales discussed in §3.4 are unlikely to be so prevalent as in the flow calculation, as the perturbation

source field is derived from velocity and stress fields which vary more smoothly than the underlying force distribution; but if necessary they can be accommodated by the same sort of solution modifications as those used in §3.6.

6.5 Diffusion equation analysis

The analysis presented here closely follows that of Hunt *et al.* (1988c) and Weng (1990), who developed a diffusion equation analysis to model the changes in concentration and scalar deposition rates over the surface of a low hill.

6.5.1 Governing equations

Combining the time averaged diffusion equation (6.1) and turbulent flux model (6.2), and omitting non-perturbation terms (whose balance should describe the pre-existing concentration distribution), we obtain

$$u^* \frac{\partial C^*}{\partial x^*} + w^* \frac{\partial C^*}{\partial z^*} + U^* \frac{\partial c^*}{\partial x^*} = \frac{\partial}{\partial x_i^*} \left(K_{ij}^* \frac{\partial c^*}{\partial x_j^*} \right) + \frac{\partial}{\partial x_i^*} \left(\Delta K_{ij}^* \frac{\partial C^*}{\partial x_j^*} \right). \qquad (6.3)$$

Here the velocity field $\hat{\mathbf{u}}^*$ has been separated into its incident and perturbations parts as in the flow calculations; similarly $\hat{c}^* = C^* + c^*$ and $\hat{K}_{ij}^* = K_{ij}^* + \Delta K_{ij}^*$. Thus ΔK_{ij}^* is the change in ij-diffusivity due to the distributed force. K_{33}^*, which relates the vertical turbulent flux to the vertical concentration gradient, may be modelled by arguments similar to those used for the turbulent shear stress model in §3.2, since eddies contributing to vertical diffusion are blocked by the ground and so have length scales proportional to height.

Eddies contributing to the lateral diffusion coefficient K_{22}^* are not blocked in this way because they may lie in horizontal planes. A length scale λ_y^* for these eddies may be estimated from the obstacle arrangement: since such eddies are created as Karman vortices shed from the obstacles, λ_y^* is related to the average lateral obstacle dimension or the average lateral spacing. Similar arguments apply to the streamwise diffusion coefficient K_{11}^* but in practice this coefficient is less important, firstly because the effects of direct streamwise diffusion are normally swamped by "shear" or "Taylor"

dispersion (the combined effect of differential advection at different heights and vertical diffusion; see *e.g.* Smith 1976) and secondly because the thinness of the inner region makes streamwise turbulent flux gradients negligible in comparison with vertical and lateral flux gradients.

Following Hunt *et al.* (1988c), the velocity scale for the diffusion coefficients is taken to be the perturbed friction velocity, *i.e.* the square root of the locally perturbed turbulent shear stress. So the dynamically important undisturbed and perturbation diffusivities are modelled by

$$K^*_{33} = \kappa z^* u_*; \quad K^*_{22} = \lambda^*_y u_*; \quad \Delta K^*_{33} = \tau K^*_{33}/2; \quad \Delta K^*_{22} = \tau K^*_{22}/2; \tag{6.4}$$

where τ is the perturbation shear stress from the flow calculation. Robins & Fackrell (1977) suggest $K^*_{ij} = \nu_{Tij}/\mathrm{Pr}$, where ν_T is the eddy viscosity and Pr is the turbulent Prandtl or Schmidt number of the scalar under investigation; hence (6.4) effectively assumes $\mathrm{Pr} \approx 1$.

There could be significant turbulent concentration flux gradients associated with off-diagonal elements of the diffusivity tensor, for example $\partial(\hat{K}^*_{23}\partial\hat{c}^*/\partial z^*)/\partial y^*$, but it is difficult to justify such sophistication in the diffusion model when the only available turbulence information is the Reynolds shear stress. The present analysis therefore neglects off-diagonal contributions to the concentration flux. Using the diffusivities (6.4), (6.3) becomes

$$U^*\frac{\partial c^*}{\partial x^*} - \frac{\partial}{\partial y^*}\left(\lambda^*_y u_* \frac{\partial c^*}{\partial y^*}\right) - \frac{\partial}{\partial z^*}\left(\kappa z^* u_* \frac{\partial c^*}{\partial z^*}\right) = -q^*, \tag{6.5}$$

where

$$q^* = u^*\frac{\partial C^*}{\partial x^*} + w^*\frac{\partial C^*}{\partial z^*} - \frac{\partial}{\partial y^*}\left(\lambda^*_y u_* \frac{\tau}{2}\frac{\partial C^*}{\partial y^*}\right) - \frac{\partial}{\partial z^*}\left(\kappa z^* u_* \frac{\tau}{2}\frac{\partial C^*}{\partial z^*}\right). \tag{6.6}$$

q^* is the virtual source field for the perturbation concentration. There may be further contributions to q^* if pollutant can be deposited on or absorbed through obstacle surfaces, such as through a building's open windows; these contributions could be modelled by a source term proportional to the force distribution f.

Equation (6.5) is non-dimensionalised using the length and velocity scales L^* and U_o^* from the flow calculations and a concentration scale C_o^*:

$$U\frac{\partial c}{\partial x} - \epsilon\kappa\lambda_y\frac{\partial^2 c}{\partial y^2} - \epsilon\kappa^2\frac{\partial}{\partial z}z\frac{\partial c}{\partial z} = -q, \tag{6.7}$$

where $c = c^*/C_o^*$ and $q = q^*L^*/(U_o^*C_o^*)$. Finally, to facilitate solution of the diffusion problem for arbitrary distributions of the perturbation source q, we rewrite the physical quantities in (6.7) in terms of their Fourier transforms:

$$ikUc + \epsilon\kappa m^2\lambda_y c - \epsilon\kappa^2(zc')' = -q. \tag{6.8}$$

Here we have used Fourier transforms in both streamwise and lateral directions, with respective wavenumbers k and m. This allows us to consider dispersion of a three-dimensional plume, even though the underlying flow field is two-dimensional.

6.5.2 The outer region

In the outer region the evolution of turbulent eddies responsible for vertical mixing is described by rapid distortion theory (Britter *et al.* 1981); hence the vertical concentration fluxes associated with these eddies are negligible. The same cannot necessarily be said of the eddies responsible for lateral mixing since these eddies are characterised by an independent length scale that does not increase with height. Therefore the third term of (6.8) is ignored and the outer region solution is

$$c = \frac{iq}{kU_m}, \qquad \text{where} \quad U_m(z) = U(z) - \frac{i\epsilon\kappa m^2\lambda_y}{k}. \tag{6.9}$$

6.5.3 The inner region

The SSL analysis proceeds by rescaling the vertical coordinate on l and expanding c as an asymptotic series in ϵ:

$$\zeta = z/l; \qquad c = c_o + \epsilon c_1 + \epsilon^2 c_2 + \ldots \tag{6.10}$$

Then at $O(\epsilon)$ and $O(\epsilon^2)$, (6.8) gives

$$ikU_l c_o + \epsilon\kappa m^2\lambda_y c_o - \epsilon\kappa^2(\zeta c_o')'/l = -q; \tag{6.11}$$

$$ikU_l c_1 + \epsilon\kappa m^2\lambda_y c_1 - \epsilon\kappa^2(\zeta c_1')'/l = -ikc_o\ln\zeta. \tag{6.12}$$

Although the form of (6.11) and (6.12) is similar to that of Weng's (1990) inner region equations, the sample results obtained below are quite different from Weng's because the perturbation source fields q are quite different in the distributed force and hill flow problems. The general solutions to (6.11) and (6.12) are

$$\begin{aligned} c_o &= A_o J_o(Z) + B_o K_o(-iZ) \\ &\quad + \frac{i}{kU_{lm}} \int_{Z_o}^{Z} Z' q(z') \left\{ J_o(Z) K_o(-iZ') - J_o(Z') K_o(-iZ) \right\} dZ', \end{aligned} \tag{6.13}$$

$$\begin{aligned} c_1 &= A_1 J_o(Z) + B_1 K_o(-iZ) \\ &\quad - \frac{1}{U_{lm}} \int_{Z_o}^{Z} Z' c_o(z') \ln \frac{z'}{l} \left\{ J_o(Z) K_o(-iZ') - J_o(Z') K_o(-iZ) \right\} dZ', \end{aligned} \tag{6.14}$$

where

$$Z = e^{3i\pi/4} \sqrt{\frac{4kU_{lm} z}{\epsilon \kappa^2}}. \tag{6.15}$$

Exponentially large terms must cancel each other as $|Z| \to \infty$; hence

$$A_o + \frac{i}{kU_{lm}} \int_{Z_o}^{Z} Z' q(z') K_o(-iZ')\, dZ' = 0, \tag{6.16}$$

$$A_1 - \frac{1}{U_{lm}} \int_{Z_o}^{Z} Z' c_o(z') \ln \frac{z'}{l} K_o(-iZ')\, dZ' = 0. \tag{6.17}$$

Details of the inner surface layer are similar to those in the flow calculation and are not repeated here; the result is that very near the ground

$$c = c_w + \frac{\phi_w}{\kappa} \ln \frac{z}{z_o} + \frac{1}{\epsilon \kappa^2} \int_{z_o}^{z} q(z') \ln \frac{z}{z'}\, dz', \tag{6.18}$$

where c_w is the perturbation concentration at the ground and ϕ_w is the perturbation surface flux non-dimensionalised by $u_* C_o^*$. Matching between the ISL and SSL shows that $B_o = 0$ and that

$$c_w = A_o + \epsilon B_1 K_o(-iZ_o). \tag{6.19}$$

6.5.4 Matching the inner and outer regions

As $z/l \to \infty$ the SSL solutions (6.13) and (6.14) may be approximated as in §3.5.8 by moving $q(z')$ outside the rapidly varying integrals, to give

$$c_o \approx \frac{iq}{kU_{lm}}; \qquad c_1 \approx \frac{-kc_o \ln \zeta}{kU_{lm}}. \tag{6.20}$$

The sum of these leading and first order approximate SSL solutions is

$$c_o + \epsilon c_1 \approx \frac{iq}{kU_m}, \tag{6.21}$$

which is the same as the outer region solution (6.9). Hence the inner region solution is in fact uniformly valid for the whole flow.

Using the matching conditions that determine A_o and A_1 we can write the uniformly valid leading and first order solutions as follows:

$$\begin{aligned} c_o &= -\frac{iJ_o(Z)}{kU_{lm}} \int_Z^\infty Z' q(z') K_o(-iZ')\, dZ' \\ &\quad - \frac{iK_o(-iZ)}{kU_{lm}} \int_{Z_o}^Z Z' q(z') J_o(Z')\, dZ'; \end{aligned} \tag{6.22}$$

$$\begin{aligned} c_1 &= B_1 K_o(-iZ_o) + \frac{J_o(Z)}{U_{lm}} \int_Z^\infty Z' c_o(z') \ln\frac{z'}{l} K_o(-iZ')\, dZ' \\ &\quad + \frac{K_o(-iZ)}{U_{lm}} \int_{Z_o}^Z Z' c_o(z') \ln\frac{z'}{l} J_o(Z')\, dZ'. \end{aligned} \tag{6.23}$$

6.5.5 Surface flux conditions

A vertical concentration flux at the ground results from pollutant sticking to or being absorbed by roughness elements near $z = z_o$. Since roughness elements typically occupy a height range up to about $30z_o$ the average deposition height will be $z_1 \approx 10z_o$ and it is usual to specify a surface flux condition at z_1 rather than at z_o (Hunt *et al.* 1988c).

In a linear calculation, the surface flux of perturbation concentration must in general be a linear function of the various perturbation quantities that occur in the flow. There are obvious reasons for dependence on the local concentration and shear stress:

$$\phi_w = \kappa z_1 \left.\frac{\partial c}{\partial z}\right|_{z_1} = \phi_c c(z_1) + \phi_\tau \tau(z_1) + \ldots \tag{6.24}$$

ϕ_c and ϕ_τ are fixed coefficients: the first describes increased surface flux due to increased local concentration and the second describes increased surface flux due to faster deposition of the pre-existing concentration. Pollutant deposition may also be affected directly by the distributed force near the ground, contributing a third term

to the surface flux:

$$\phi_w = \phi_c c(z_1) + \phi_\tau \tau(z_1) + \phi_f F(z_1), \tag{6.25}$$

where $F(z_1)$ is some integral over the force distribution at $z = O(z_1)$.

The only part of the perturbation concentration solutions (6.22) and (6.23) that gives any surface flux is $\epsilon B_1 K_o(-iZ)$. Thus ϕ_w may be expressed in terms of B_1:

$$\phi_w = \epsilon B_1 \left.\frac{\partial K_o(-iZ)}{\partial \ln z}\right|_{z_1} = \frac{i\epsilon B_1 Z_1 K_1(-iZ_1)}{2} \approx \frac{-\epsilon B_1}{2}. \tag{6.26}$$

Substituting (6.26) into (6.25) we obtain an equation for B_1:

$$\begin{aligned} \frac{-\epsilon B_1}{2}(1 + 2\phi_c K_o(-iZ_1)) &= \phi_c(c_o(z_1) + \epsilon[c_1(z_1) - B_1 K_o(-iZ_1)]) \\ &\quad + \phi_\tau \tau(z_1) + \phi_f F(z_1). \end{aligned} \tag{6.27}$$

6.6 A linear incident concentration profile

To illustrate the results of the analysis, consider a pre-existing concentration distribution that is homogeneous in the streamwise and lateral directions and varies linearly with height:

$$C = 1 + \alpha z. \tag{6.28}$$

Then the perturbation source field $-q$ given by (6.6) simplifies to

$$-q = -\alpha\left(w - \frac{\epsilon\kappa^2\tau}{2} - \frac{\epsilon\kappa^2 z}{2}\frac{\partial\tau}{\partial z}\right). \tag{6.29}$$

Let α be positive, such that the pre-existing concentration increases upwards. Then the interpretation of (6.29) is that (i) upwards perturbation velocities (w) reduce the local concentration by transporting scalar from less concentrated areas, (ii) positive shear stress perturbations (τ) increase local concentration because the diffusivity profile $z\sqrt{1+\tau}$ increases faster than in the undisturbed flow, hence more high concentration scalar is mixed down from above, and (iii) positive shear stress gradients ($\partial\tau/\partial z$) make the diffusivity profile increase faster with height, with the same effect as in (ii).

Even with such a simplified initial concentration distribution as (6.28), it has not so far proved possible to obtain simple expressions for interesting integrated quantities such as the total concentration flux through the roof of an obstacle canopy or the maximum ground level concentration perturbation.

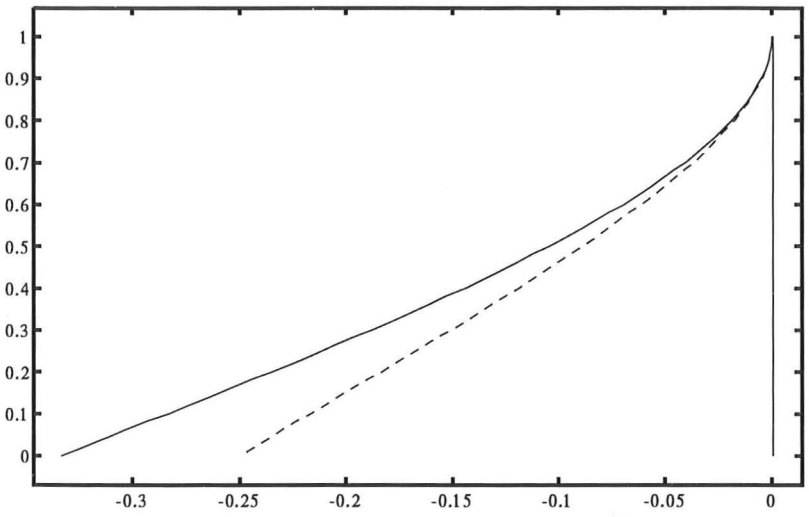

Figure 6.2: Far downstream perturbation concentration profiles within the canopy. $2\epsilon^2\kappa^2 c_\infty/(\alpha H^2 f_{\infty\max})$ is plotted against z/H for linear (solid line) and quadratic (dashed line) equilibrium force profiles.

Some progress can be made, however, in investigating the far downstream form of the perturbation concentration profile for semi-infinite obstacle canopies of the type described in §5.4.6. The limiting far downstream profiles derived here (indicated by the suffix ∞) describe an equilibrium state that will exist in practice in any long obstacle canopy far downstream of its leading edge. Assuming zero perturbation flux at the ground, which is appropriate for a non-adhesive gaseous contaminant, and approximating the leading order inner region solution (6.13) using (4.8) and (4.9), we find

$$c_\infty = \frac{1}{\epsilon\kappa^2}\int_z^\infty q_\infty(z')\ln\frac{z'}{z}\,dz' = \frac{\alpha}{2}\int_z^\infty \tau_\infty(z')\,dz'. \tag{6.30}$$

Here we have used the fact that the integral of q over all z vanishes, which is evident from (6.6) when $\partial/\partial x = \partial/\partial y = 0$. By differentiation of (5.43), τ_∞ is

$$\tau_\infty = -\frac{1}{\epsilon^2\kappa^2}\int_z^\infty f_\infty(z')\,dz'. \tag{6.31}$$

Hence

$$c_\infty = \frac{\alpha}{2\epsilon^2\kappa^2}\int_z^\infty (z-z')f_\infty(z')\,dz'. \tag{6.32}$$

Figure 6.2 shows the perturbation concentration profile within the canopy given by (6.32) when the equilibrium force profile f_∞ takes on idealised linear and quadratic forms. Above the canopy the perturbation concentration is zero, because $\partial u/\partial x$, w and τ all vanish (the latter only for $z > H$) in the equilibrium state.

6.7 Perturbation of an incident Gaussian plume

As a second example of the dispersion analysis, consider a two-dimensional, steady plume of contaminant that would, in the absence of any obstacles, have the reflected Gaussian concentration distribution (*e.g.* Davidson *et al.* 1995a)

$$C(x,z) = \frac{C_o}{\sqrt{2\pi}\sigma_z(x)}\left(\exp\left[\frac{-(z-\bar{z}(x))^2}{2\sigma_z^2(x)}\right] + \exp\left[\frac{-(z+\bar{z}(x))^2}{2\sigma_z^2(x)}\right]\right). \tag{6.33}$$

The progress of the plume is specified by two functions of streamwise coordinate: the vertical plume spread $\sigma_z(x)$ and mean centerline height $\bar{z}(x)$.

Simulation results are now presented using the dispersion analysis of §6.5 to calculate the perturbations to a Gaussian plume given by (6.33) passing through a force distribution that models the staggered obstacle array in Davidson *et al.*'s (1995b) wind tunnel experiment at the Environmental Protection Agency (see §4.6).

Figure 6.3 shows the growth of the undisturbed plume in the absence of any obstacles. The plume centreline height is uniformly $\bar{z} = H/2$, while the plume spread σ_z increases from $0.2H$ at $7H$ upstream of the leading edge of the array to $1.3H$ at $40H$ downstream of the leading edge. Hence the incident plume size is of the same order as the canopy height.

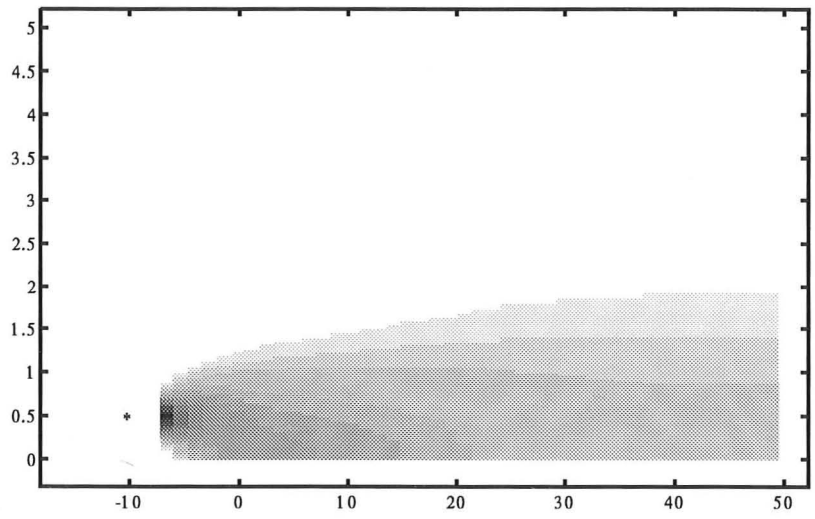

Figure 6.3: Contours of the undisturbed plume concentration C. Streamwise and vertical coordinates are non-dimensionalised by obstacle height $H = 0.12$m. The streamwise coordinate is measured from the leading edge of the array and the obstacle array extends from $x/H = 0$ to $x/H = 16$. $*$ marks the source position.

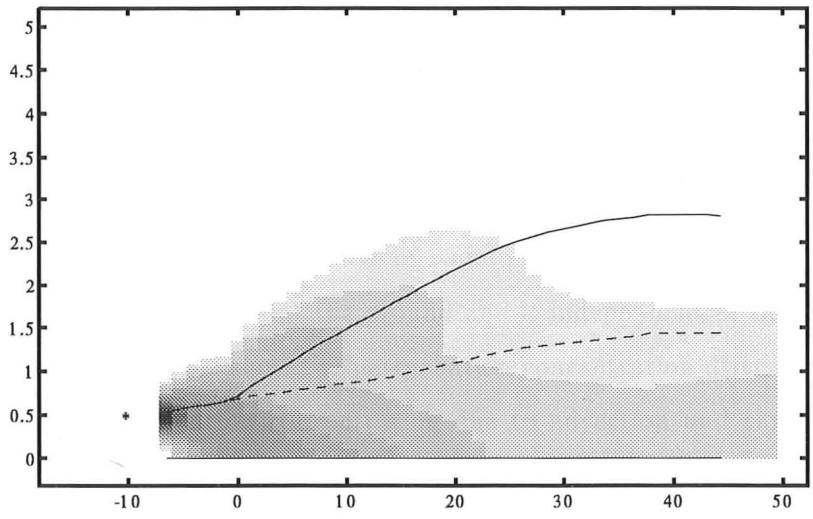

Figure 6.4: The disturbed plume. Total concentration $\hat{c}$ is shown using greyscale contours. The superimposed lines show the standard deviation about the ground of the incident (dashed line) and disturbed (solid line) concentration profiles as a function of x. Axes are as in figure 6.3. $*$ marks the source position.

Figure 6.4 shows the disturbed plume. As expected, the effect of the resistance is to increase the vertical spread of the plume. Figure 6.4 also quantifies the increase by superimposing graphs of the standard deviation about the ground of the undisturbed and disturbed concentration profiles. Although it is conventional and convenient to specify a vertical Gaussian plume profile in terms of $\bar{z}$ and σ_z, as in (6.33), the inverse process—finding the parameters $\bar{z}$ and σ_z which best describe a supplied concentration profile—is rather ill-conditioned, particularly when $\bar{z}/\sigma_z$ is small. Davidson *et al.* (1995a) chose to characterise their measured profiles by fitting values of $\bar{z}$ and σ_z and then adding these together to give the "plume extent" $z_T \equiv \bar{z} + \sigma_z$; the published control and array plume data refers only to z_T. The ill-conditioning of this parameter fitting process means that any attempt to compare Davidson *et al.*'s data with theory is susceptible to large errors. A better way of quantifying plume extent as a single number is to use the sum of the squares of $\bar{z}$ and σ_z: $z_S^2 \equiv \bar{z}^2 + \sigma_z^2$; z_S^2 is the variance of the concentration profile about the ground and is independent of the ratio $\bar{z}/\sigma_z$.

Figures 6.5, 6.6 and 6.7 show the perturbation concentration distribution and the contributions to perturbation concentration due to advection and turbulent mixing respectively. The separate contributions are calculated by excluding terms from the expression (6.6) for the perturbation source field q. Thus for the advection contribution we put

$$q = u\frac{\partial C}{\partial x} + w\frac{\partial C}{\partial z} \tag{6.34}$$

and for the turbulent mixing contribution,

$$q = -\frac{\epsilon\kappa^2}{2}\frac{\partial}{\partial z}\left(z\tau\frac{\partial C}{\partial z}\right). \tag{6.35}$$

For the flow modelled here it is clear that the concentration changes due to enhanced turbulent shear stresse around the top of the obstacle canopy are far more significant than concentration changes due to advection.

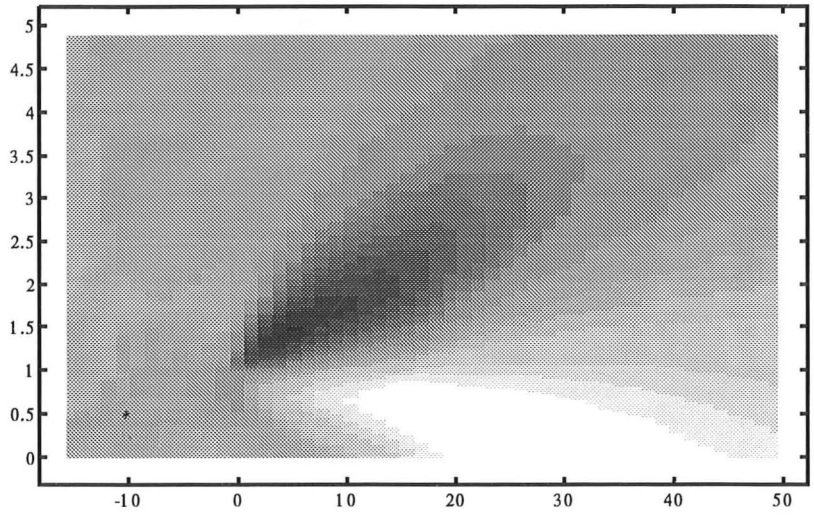

Figure 6.5: Contours of the perturbation concentration distribution c. Contour range is $-0.10C_{\max}$ (white) to $0.13C_{\max}$ (black), where $C_{\max}$ is the maximum concentration in the incident plume (figure 6.3). $*$ marks the source position.

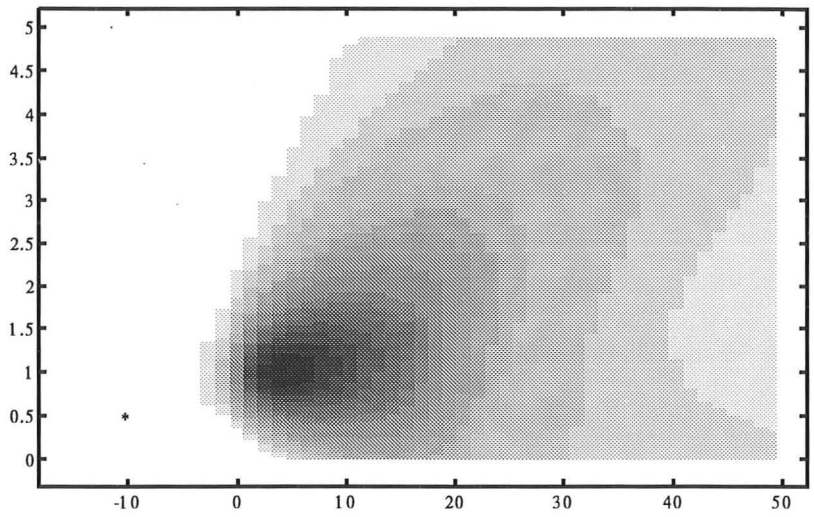

Figure 6.6: The advection contribution to the perturbation concentration distribution. Contour range is $-0.01C_{\max}$ (white) to $0.07C_{\max}$ (black). $*$ marks the source position.

6.8 Concluding remarks

The analysis described here is very general in that it can be applied to any incident concentration distribution and any perturbation flow field. It has been incorporated into the flow field computer software package described in §3.1 so that simulations of plume dispersion changes can be performed for any combination of incident wind and distributed force that is input to the flow field calculation. The limitations of the dispersion analysis are the limitations of the diffusion equation as a representation of real dispersion.

Experimental dispersion data for comparison with the current analysis must satisfy two requirements. Firstly, the data must be perturbation data, *i.e.* they must describe the *changes* in dispersion that result from the addition of obstacles to an initially unobstructed flow. This can be achieved in practice, as in Davidson *et al.*'s (1995a) field experiments, by running a control plume to one side of an array of obstacles

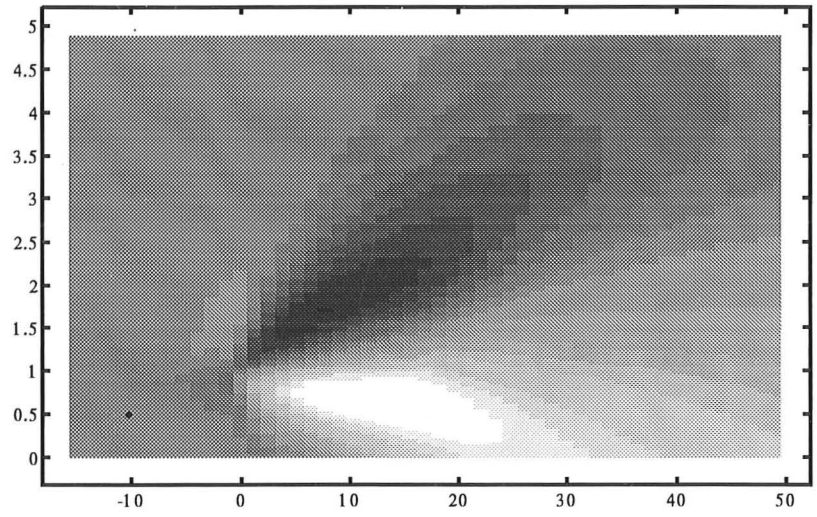

Figure 6.7: The mixing contribution to the perturbation concentration distribution. Contour range is $-0.14C_{\max}$ (white) to $0.08C_{\max}$ (black). $*$ marks the source position.

at the same time as the array plume passes between the obstacles. Secondly, the data must be characterised by convenient and well-conditioned quantities. The usual Gaussian parameters, mean centreline height $\bar{z}$ and vertical plume spread σ_z, are not good characterisation quantities because fitting these parameters to an arbitrary concentration profile is, in general, an ill-conditioned process. The distinction between $\bar{z}$ and σ_z is only clear for thin elevated plumes with $\bar{z} \gg \sigma_z$, a rare case in canopy flows. In the context of canopy flows, where plumes are usually well-mixed over a depth of the order of canopy height, we recommend that plumes be characterised by the mean and standard deviation of their concentration profiles about the ground.

Chapter 7

Summary and conclusions

The main achievement of this thesis has been to give the first analytical treatment of two-dimensional turbulent flow through a region of distributed resistance.

The introductory discussion of chapter 1 set out the need for such a theory, firstly to provide a description of the flow field within a group of obstacles of finite extent, such as a forest or an urban area, secondly to clarify existing parameterisations of the flow above such obstacles and, where relevant, propose new parameterisations. A review of the existing literature on canopy flows showed that the concept of distributed resistance, in which an array of obstacles is modelled as a region without solid obstructions but with distributed body forces, was well known but had only previously been investigated in numerical computations and one-dimensional analytical treatments (*i.e.* for horizontally homogeneous force distributions). Such treatments are insufficient to understand the parameterisation of flow above a group of obstacles of finite size, or whose distribution varies in the streamwise direction. Therefore two key objectives emerged: (i) to construct an analytical theory of two-dimensional canopy flows and (ii) to use the results of this theory to derive accessible parameterisations of broad features of the flow. As the necessary first step in any theory based on distributed resistance, chapter 1 concluded with a simple formulation for calculating the distributed forces corresponding to a given obstacle distribution.

Chapter 2 presents several calculations of inviscid and laminar (or constant eddy

viscosity) flow through a region of distributed force. The most significant result of these calculations is that the structure of the perturbation velocity field depends strongly on the form of the velocity profile incident upon the force distribution. In most cases the perturbation flow structure resembles outflow from a source, as expected given the close mathematical relationship between a point force and a point source. For some incident velocity profiles, however, even for force distributions that are everywhere non-negative (*i.e.* resistive), the source-like structure of the flow field changes to a much weaker quadrupolar flow structure (*i.e.* the far field decays like r^{-3} rather than r^{-1}). The two perturbation flow structures differ significantly in the degree of blocking of the incident flow and in the amount of fluid exchange between the force distribution and the flow above it, and so would have radically different effects on scalar dispersion.

By consideration of the symmetry of the flow, we showed that the vanishing of the source-like structure is associated with the absence of a velocity discontinuity or strong shear layer at the ground. The implication for turbulent flows, which *do* have a strong shear layer at the ground, is that the source-like structure should always prevail. Hence it is crucial that any attempt to model turbulent flow uses an incident velocity profile which is discontinuous or has strong shear at the ground—this specifically rules out linear velocity profiles of the form $U = \sigma z$. The results also suggest that low Reynolds number laminar viscous flows, which *are* linear near the ground, respond to distributed forces in a very different way from turbulent flows. The laminar viscous calculation of §2.9 uses a uniform incident velocity profile (which is interpreted by the symmetry arguments of §2.10 as being discontinuous at the ground) because it was intended as a preliminary model for *turbulent* flow, and was later used as such in the displaced mixing length (DML) theory of §3.8.

The core of the thesis is the asymptotic analysis of chapter 3. Two contrasting turbulence models were investigated, respectively describing strong (DML) and weak (standard mixing length – SML) interaction between the perturbed mean flow and turbulent stress perturbations. Although the SML analysis is similar to previous

analyses of turbulent flow over low hills (Hunt *et al.* 1988a) and roughness changes (Belcher *et al.* 1990), changes were required to reflect the fact that a distributed force extends vertically into the flow and thus imposes its own vertical length scale H (or, in general, several such scales). The appropriate velocity scale for advection is then, for all wavenumbers, $U^*(H)$ rather than $U^*(h_m)$ (where h_m is Hunt *et al.*'s middle layer height), and the asymptotic small parameter $\epsilon = \ln^{-1}(H/z_o)$ quantifies the difference in height scales between H and the roughness height z_o of the incident flow. ϵ must be small, or else it would be inconsistent to distinguish between the canopy obstacles modelled as a distributed force and the surface roughness elements modelled as a roughness height. The imposed length scale H also means that rapidly varying force distributions require a new layer to be added to the hill/roughness flow structure. The new layer includes significant turbulent stresses that are generated in an elevated region of rapid mean velocity variation and then advected downstream.

When the perturbed flow includes an elevated shear layer strong enough to alter the turbulence structure above the canopy, the DML turbulence model is required. The effect on the upper turbulence of a strong elevated shear layer is upward displacement: the mixing length for turbulence above the shear layer is referred to some non-zero displacement height d rather than to the ground. The arguments of §3.8 showed that the creation and spreading of shear layers at rooftop height in a group of obstacles could be the missing physical mechanism to explain Thom's (1971) observations and Jackson's (1981) theoretical conjecture that the displacement height d coincides with the level of mean momentum absorption within the obstacle canopy.

Chapter 4 presented comparisons between the analytical theories of chapter 3 and experimental data or numerical simulations. Good agreement between SML theory and a numerical simulation of turbulent flow through a distributed force using the K–ϵ closure shows that the SML turbulence model and the assumptions made during the asymptotic analysis are justifiable in practice. For the other comparisons, with experimental field and wind tunnel data, the concept of distributed force iteration was introduced. This allows for non-linear sheltering effects in the specification of the

force distribution by using the local velocity instead of the upwind velocity to calculate the force acting at any point. The experimental comparisons are, of course, tests of the distributed force concept and of the recipe for calculating distributed force as well as of the turbulence modelling and asymptotic analysis. The level of agreement, in comparisons of the perturbed streamwise velocity profiles for which most data is available, was very encouraging!

When the additional parameters for the DML theory were estimated according to the physical reasoning of §3.8, no large differences were observed between the SML and DML results. Therefore the less adjustable and simpler SML theory is recommended when the intent is to model the detailed perturbation flow field within and around an obstacle canopy.

In chapter 5 two parameterisations for the flow above the obstacles were derived from the detailed flow field results of chapter 3. The first parameterisation decomposed the SML results in terms of the previously studied hill flow and roughness change problems. This means that an existing computational model for surface elevation and roughness changes, such as "Flowstar" (Carruthers *et al.* 1988), can in principle be used to simulate flow above a region of distributed resistance, using the relations derived in §5.3 to calculate elevation and roughness distributions "equivalent" to a given force distribution. Fung & Hunt (1991) discovered this possibility while trying to model the flow above an array of obstacles using Flowstar: they obtained a better representation of the flow by using a combination of elevation and roughness than by either alone. The parameterisation conversely implies that the hill and roughness problems may each be simulated by using a force distribution calculated such that the unwanted flow component vanishes (but the details of this calculation have not been presented here).

The second parameterisation derived effective roughness parameters for both SML and DML results. Despite the apparent similarity between the results of the two turbulence models in the comparisons of chapter 4, there are dramatic differences between them when it comes to parameterisation. The DML theory, using a realistic

displacement height estimated using Jackson's (1981) definition as the level of mean momentum absorption (in accordance with the physical arguments of §3.8), gives values of effective roughness height z_e that are comparable with those "observed" in experiments by fitting logarithmic velocity profiles to the data. The SML theory, on the other hand, with zero displacement height, gives impossibly large values for z_e. Hence a realistic displacement height is essential for successful estimation of effective roughness parameters. The sensitivity of z_e to the other two DML parameters seems much weaker. More work is required, however, to be sufficiently precise about all three DML parameters that the DML roughness parameterisation could be used as a reliable, predictive model.

It is interesting to note that the expressions derived here for the effective roughness height are strikingly similar to those derived by Wood & Mason (1993) for the flow above a range of hills. The similarity suggests that results of the form

$$\ln \frac{z_e}{z_o} = \frac{C F^*}{\rho u_*^2} \ln \frac{H_F}{z_o} \qquad (7.1)$$

are very widely applicable in the roughness parameterisation of surface disturbances. Here F^* is the force acting on the flow per unit plan area, H_F is the height at which F^* appears to act, and C is an $O(1)$ coefficient.

The region of validity of the roughness parameterisation is naturally expressed in Fourier space and cannot rigorously be translated into real space. Loosely translated, however, for the case of a step change in obstacle density at $x = 0$, there is an internal boundary layer (IBL) that starts from $x = 0$ and grows downstream. The roughness parameterisation is valid when there is a range of heights z within the IBL but above the obstacle canopy such that $H < z \ll l_i(x)$, where $l_i(x)$ is the IBL depth. Note that $l_i(x = 0) = d$, so the region of validity obtained from the DML theory starts at a smaller fetch (*i.e.* closer to $x = 0$) than that obtained from the SML theory.

Chapter 5 concludes with an investigation of the asymptotic equilibrium state that develops in a semi-infinite force distribution far downstream of its leading edge. This idealisation is useful in practice as a model for the downstream parts of any obstacle canopy much longer than its height. The magnitude of the limiting streamwise velocity

was estimated by balancing the force against the turbulent stress gradient and making a reasonable assumption about the shape of the limiting profile, with the result that the limiting total velocity is directly proportional to the small parameter ϵ and inversely proportional to the square roots of canopy height H^* and drag parameter D^*. Direct proportionality can be explained by noting that ϵ quantifies the ability of the turbulent stress gradient to support a residual distributed force profile.

The expression for the limiting velocity can be used to conduct a brief review of the validity of the assumption of linearity. Suppose that linearisation requires $|u| < \alpha$, and take the limiting value (5.49) to be the maximum velocity perturbation. Then (taking $\kappa \approx 0.5$) the drag parameter D^* is constrained by

$$D^* < \frac{1}{(1-\alpha)^2 H^* \ln(H/z_o)}. \tag{7.2}$$

For some purposes (7.2) is unnecessarily restrictive. For example, when approaching the far downstream equilibrium state, the neglected non-linear perturbation terms $u\partial u/\partial x$, $u\partial w/\partial x$, $w\partial u/\partial z$ and $w\partial w/\partial z$ remain negligible even though u is significant because $\partial u/\partial x$ and w both tend to zero in the equilibrium state. Within a long canopy, therefore, the linear theory may give accurate results for values of D^* somewhat larger than those allowed by (7.2). The greatest potential for error due to linearisation arises just after the trailing edge of a long canopy, where $(-u)$ is still close to its maximum but its streamwise gradient $\partial u/\partial x$ and the vertical velocity w are also significant.

Finally, chapter 6 demonstrated application of the flow field results to the modelling of scalar plume dispersion through a group of obstacles. This was a preliminary study only, but even so the results clearly showed several interesting aspects of the interaction between a plume and a group of obstacles. Most notable were the positive concentration perturbations (relative to concentrations in a control plume) around the leading edge of the canopy, due to the blocking effect of the initial resistance, and the dominance of perturbation turbulent stresses around the rooftop height in controlling the evolution of the perturbed plume farther downstream.

References

M. Abramowitz & I.A. Stegun (1972) *Handbook of mathematical functions.* Dover.

B.D. Amiro & P.A. Davis (1988) Statistics of atmospheric turbulence within a natural black spruce forest canopy. *Boundary-Layer Meteorol.* **44** 267–283.

R.A. Antonia & R.E. Luxton (1971) The response of a turbulent boundary layer to a step change in surface roughness. Part 1: smooth to rough. *J. Fluid Mech.* **48** 721–761.

J.-C. André & C. Blondin (1986) On the effective roughness length for use in numerical three-dimensional models. *Boundary-Layer Meteorol.* **35** 231–245.

G.I. Barenblatt (1993) Scaling laws for fully developed turbulent shear flows. Part 1. Basic hypotheses and analysis. *J. Fluid Mech.* **248** 513–520.

C.B. Bartsch (1993) Comparison of pressure drops in two-dimensional arrays of cylinders with the average traveltime of particles through them. *First year report.* Department of Applied Mathematics and Theoretical Physics, University of Cambridge.

G.K. Batchelor (1967) *An introduction to fluid dynamics.* Cambridge University Press.

S.E. Belcher (1990) Turbulent boundary layer flow over undulating surfaces. *Ph.D. thesis,* University of Cambridge.

S.E. Belcher, D.P. Xu & J.C.R. Hunt (1990) The response of a turbulent boundary layer to arbitrarily distributed two-dimensional roughness changes. *Quart. J. Roy. Met. Soc.* **116** 611–635.

S.E. Belcher, W.S. Weng, D.J. Carruthers & J.C.R. Hunt (1991a) The modelling of perturbed turbulent boundary layers. *Advances in Turbulence 3* (ed. A.V. Johansson & P.H. Alfredsson). Springer-Verlag.

S.E. Belcher, W.S. Weng & J.C.R. Hunt (1991b) Structure of turbulent boundary layers perturbed over short length scales. *Eighth Symposium on Turbulent Shear Flows, Munich*

S.E. Belcher, T.M.J. Newley & J.C.R.Hunt (1993) The drag on an undulating surface due to the flow of a turbulent boundary layer. *J. Fluid Mech.* **249** 557–596.

E.F. Bradley (1968) A micrometeorological study of velocity profiles and surface drag in the region modified by a change in roughness. *Quart. J. Roy. Met. Soc.* **94** 361–379.

R.E. Britter, J.C.R. Hunt & K.J. Richards (1981) Air flow over a two-dimensional hill: studies of velocity speed-up, roughness effects and turbulence. *Quart. J. Roy. Met. Soc.* **107** 91–110.

D.J. Carruthers, J.C.R. Hunt & W.S. Weng (1988) A computational model of stratified turbulent airflow over hills — Flowstar. *Computer Techniques in Environmental Studies* (ed. P. Zanetti). Springer-Verlag.

D.J. Carruthers, R.J. Holroyd, J.C.R. Hunt, W.S. Weng, A.G. Robins, D.D. Apsley, D.J. Thomson & F.B. Smith (1994) UK-ADMS: a new approach to modelling dispersion in the earth's atmospheric boundary layer. *J. Wind Eng. Ind. Aerodyn.* **52**

139–153.

I.P. Castro & A.G. Robins (1977) The flow around a surface-mounted cube in uniform and turbulent streams. *J. Fluid Mech.* **79** 307–335.

P.C. Chatwin & C.M. Allen (1985) Mathematical models of dispersion in rivers and estuaries. *Ann. Rev. Fluid Mech.* **17** 119–149.

R.M. Cionco (1965) A mathematical model for airflow in a vegetative canopy. *J. Appl. Meteorol.* **4** 517–522.

R.M. Cionco (1972) A wind-profile index for canopy flow. *Boundary-Layer Meteorol.* **3** 255–263.

P.A. Coppin, M.R. Raupach & B.J. Legg (1986) Experiments on scalar dispersion within a model plant canopy. Part II: an elevated plane source. *Boundary-Layer Meteorol.* **35** 167–191.

J. Counihan (1971) Wind tunnel determination of the roughness length as a function of the fetch and the roughness density of three-dimensional roughness elements. *Atmos. Environ.* **5** 637–642.

J. Counihan, J.C.R. Hunt & P.S. Jackson (1974) Wakes behind two-dimensional obstacles in turbulent boundary layers. *J. Fluid Mech.* **64** 529–563.

A.D.D. Craik (1991) The continuous spectrum of the Orr-Sommerfeld equation: note on a paper of Grosch & Salwen. *J. Fluid Mech.* **226** 565–571.

M.J. Davidson, K.R. Mylne, C.D. Jones, J.C. Phillips, R.J. Perkins, J.C.H. Fung &

J.C.R. Hunt (1995a) Plume dispersion through large groups of obstacles — a field investigation. *Atmos. Environ., in press.*

M.J. Davidson, W.H. Snyder, R.E. Lawson & J.C.R. Hunt (1995b) Plume dispersion from point sources upwind of groups of obstacles — wind tunnel simulations. *Submitted to Atmos. Environ..*

W.P. Elliot (1958) The growth of the atmospheric internal boundary layer. *Trans. Am. Geoph. Union* **39** 1048–1054.

F. Fiedler & H.A. Panofsky (1972) The geostrophic drag coefficient and the 'effective' roughness length. *Quart. J. Roy. Met. Soc.* **98** 213–220.

J.C.H. Fung & J.C.R. Hunt (1991) Modelling flow and dispersion through groups of buildings. *Final report to U.K. Ministry of Defence — part I.*

W. Gao, R.H. Shaw & K.T. Paw U (1989) Observation of organised structure in turbulent flow within and above a forest canopy. *Boundary-Layer Meteorol.* **47** 349–377.

B.A. Gardiner (1994) Wind and wind forces in a plantation spruce forest. *Boundary-Layer Meteorol.* **67** 161–186.

J.R. Garratt (1990) The internal boundary layer: a review. *Boundary-Layer Meteorol.* **50** 171–203.

A.L.M. Grant & P.J. Mason (1990) Observations of boundary-layer structure over complex terrain. *Quart. J. Roy. Met. Soc.* **116** 159–186.

G. Gross (1987) Some effects of deforestation on nocturnal drainage flow and local climate – a numerical study. *Boundary-Layer Meteorol.* **38** 315–337.

G. Gross (1988) A numerical estimation of the deforestation effects on local climate in the area of the Frankfurt International Airport. *Beitr. Phys. Atmosph.* **61** 219–231.

J.O. Hinze (1975) *Turbulence (2nd edition).* McGraw-Hill.

H. Hiraoka (1993) Modelling of turbulent flows within plant/urban canopies. *J. Wind Eng. Ind. Aerodyn.* **46 & 47** 173–182.

G. Hsi & J.H. Nath (1970) Wind drag within simulated forest canopies. *J. Appl. Meteorol.* **9** 592-602.

J.C.R. Hunt, R.E. Britter & J.S. Puttock (1979) Mathematical models of dispersion of air pollution around buildings and hills. *Mathematical Modelling of Turbulent Diffusion in the Environment* (ed. C.J. Harris). Academic Press.

J.C.R. Hunt & A.H. Weber (1979) A Lagrangian statistical analysis of diffusion from a ground-level source in a turbulent boundary layer. *Quart. J. Roy. Met. Soc.* **105** 423–443.

J.C.R. Hunt (1982) Mechanism for dispersion of pollution around buildings and vehicles. *BMFT/TÜV Colloquium on Exhaust Gas Air Pollution caused by Motor Vehicle Emissions.* TÜV Rheinland GmbH.

J.C.R. Hunt (1985) Turbulent diffusion from sources in complex flows. *Ann. Rev. Fluid Mech.* **17** 447–485.

J.C.R. Hunt, S. Leibovich & K.J. Richards (1988a) Turbulent shear flow over low hills. *Quart. J. Roy. Met. Soc.* **114** 1435–1471.

J.C.R. Hunt, D.D. Stretch & R.E. Britter (1988b) Length scales in stably stratified turbulent flow and their use in turbulence models. *Proc. IMA Conf. on Stably Stratified Flow and Dense Gas Dispersion* (ed. J.S. Puttock). Clarendon.

J.C.R. Hunt, W.S. Weng & D.J. Carruthers (1988c) Modelling deposition fluxes on hills. *Air Pollution Modelling and its Application VI* (ed. H. van Dop). Plenum.

P.S. Jackson & J.C.R. Hunt (1975) Turbulent wind flow over a low hill. *Quart. J. Roy. Met. Soc.* **101** 929–955.

P.S. Jackson (1981) On the displacement height in the logarithmic velocity profile. *J. Fluid Mech.* **111** 15–25.

N. Jerram, R.J. Perkins, J.C.H. Fung, M.J. Davidson, S.E. Belcher & J.C.R. Hunt (1994) Atmospheric flow through groups of obstacles and dispersion from localised sources. *Proc. NATO Advanced Study Institute on Wind Climate in Cities, pp. 109–130* (ed. E.J. Plate, J.E. Cermak, A.G. Davenport & D.X. Viegas). Kluwer.

M. Kanda & M. Hino (1994) Organized structures in developing turbulent flow within and above a plant canopy, using a large eddy simulation. *Boundary-Layer Meteorol.* **68** 237–257.

S.C. Kot (1989) Numerical modelling of contaminant dispersion around buildings. *Building and Environment* **24** 33–37.

R. Kowe, J.C.R. Hunt, A. Hunt, B. Couet & L.S.J. Bradbury (1988) The effect of

bubbles on the volume fluxes and the presure gradients in non-uniform steady flow of liquids. *Int. J. Multiphase Flow* **14** 587–606.

J. Laufer (1955) The structure of turbulence in fully developed pipe flow. *Nat. Adv. Ctee Aero., Wash., Rep. no 1174.* [Cited in Townsend (1976)]

B.J. Legg, M.R. Raupach & P.A. Coppin (1986) Experiments on scalar dispersion within a model plant canopy. Part III: an elevated line source. *Boundary-Layer Meteorol.* **35** 277–302.

M.J. Lighthill (1957) The fundamental solution for small steady three-dimensional disturbances to a two-dimensional parallel shear flow. *J. Fluid Mech.* **3** 113–144.

M.J. Lighthill (1958) *An introduction to Fourier analysis and generalised functions.* Cambridge University Press.

A.K. Lo (1990) On the determination of zero-plane displacement and roughness length for flow over forest canopies. *Boundary-Layer Meteorol.* **51** 255–268.

G.J. Mayhead, J.B.H. Gardiner & D.W. Durrant (1975) *Physical properties of conifers in relation to plantation stability.* Unpublished report, Forestry Commission, Edinburgh. [Cited in Stacey *et al.* (1994)]

R.N. Meroney (1968) Characteristics of wind and turbulence in and above model forests. *J. Appl. Meteorol.* **7** 780–788.

P.J. Mulhearn & J.J. Finnigan (1978) Turbulent flow over a very rough, random surface. *Boundary-Layer Meteorol.* **15** 109–132.

T.M.J. Newley, H.J. Pearson & J.C.R. Hunt (1991) Stably stratified rotating flow through a group of obstacles. *Geophys. Astrophys. Fluid Dynamics* **58** 147–171.

H.A. Panofsky & J.A. Dutton (1984) *Atmospheric turbulence.* John Wiley & Sons.

Phillips World Atlas (1993) Phillips.

E.J. Plate & A.A. Quraishi (1965) Modeling of velocity distributions inside and above tall crops. *J. Appl. Meteorol.* **4** 400–408.

J.S. Puttock (1976) Turbulent diffusion in separated and stratified flows. *Ph.D. thesis,* University of Cambridge.

J.S. Puttock & J.C.R. Hunt (1979) Turbulent diffusion from sources near obstacles with separated wakes. Part I: an eddy diffusivity model. *Atmos. Environ.* **13** 1–13.

M.R. Raupach, A.S. Thom & I. Edwards (1980) A wind-tunnel study of turbulent flow close to regularly arrayed rough surfaces. *Boundary-Layer Meteorol.* **18** 373–397.

M.R. Raupach & R.H. Shaw (1982) Averaging procedures for flow within vegetation canopies. *Boundary-Layer Meteorol.* **22** 79–90.

M.R. Raupach, P.A. Coppin & B.J. Legg (1986) Experiments on scalar dispersion within a model plant canopy. Part I: the turbulence structure. *Boundary-Layer Meteorol.* **35** 21–52.

M.R. Raupach (1989) A practical Lagrangian method for relating scalar concentrations to source distributions in vegetation canopies. *Quart. J. Roy. Met. Soc.* **115** 609–632.

A.G. Robins & J.E. Fackrell (1979) Continuous plumes – their structure and prediction. *Mathematical Modelling of Turbulent Diffusion in the Environment* (ed. C.J. Harris). Academic Press.

M.W. Rotach (1993) Turbulence close to a rough urban surface. Part I: Reynolds stress. *Boundary-Layer Meteorol.* **65** 1–28.

A.M. Savill & T. Solberg (1994) Some improvements to PDR/K-Epsilon model predictions for explosions in confined geometries. *Proc. IMA conference on Flow and Dispersion through Groups of Obstacles, Cambridge, March 1994* (ed. S.E. Belcher & R.J. Perkins). Clarendon Press, Oxford, to appear.

R.H. Shaw & U. Schumann (1992) Large-eddy simulation of turbulent flow above and within a forest. *Boundary-Layer Meteorol.* **61** 47–64.

M. Shibata & C.C. Mei (1990) Inertia effects of a localized force distribution near a wall in a slow shear flow. *Phys. Fluids A* **2** 1094–1104.

F.B. Smith, D.J. Carson & H.R. Oliver (1972) Mean wind-direction shear through a forest canopy. *Boundary-Layer Meteorol.* **3** 178–190.

R. Smith (1976) Longitudinal dispersion of a buoyant contaminant in a shallow channel. *J. Fluid Mech.* **78** 677–688..

G.R. Stacey, R.E. Belcher, C.J. Wood & B.A. Gardiner (1994) Wind flows and forces in a model spruce forest. *Boundary-Layer Meteorol.* **69** 311–334.

U. Svensson & K. Häggkvist (1990) A two-equation turbulence model for canopy flows. *J. Wind Eng. Ind. Aerodyn.* **35** 201–211.

R.I. Sykes (1980) An asymptotic theory of incompressible turbulent boundary-layer flow over a small hump. *J. Fluid Mech.* **101** 647–670.

G.I. Taylor (1944) Air resistance of a flat plate of very porous material. *Rep. and Mem. Aero. Res. Council* **2236** [Also G.I. Taylor *Scientific Papers* (ed. G.K. Batchelor) III 383–386, Cambridge University Press (1963)].

P.A. Taylor, R.I. Sykes & P.J. Mason (1989) On the parameterization of drag over small-scale topography in neutrally-stratified boundary-layer flow. *Boundary-Layer Meteorol.* **48** 409–422.

H. Tennekes & J.L. Lumley (1972) *A first course in turbulence.* M.I.T. Press.

W. Theurer & E.J. Plate (1994) Point sources in urban areas: modelling of neutral gas clouds with semi-empirical models. *Proc. NATO Advanced Study Institute on Wind Climate in Cities* (ed. E.J. Plate, J.E. Cermak, A.G. Davenport & D.X. Viegas). Kluwer.

A.S. Thom (1971) Momentum absorption by vegetation. *Quart. J. Roy. Met. Soc.* **97** 414–428.

D.J. Thomson (1986) A random walk model of dispersion in turbulent flows and its application to dispersion in a valley. *Quart. J. Roy. Met. Soc.* **112** 511–530.

A.A. Townsend (1961) Equilibrium layers and wall turbulence. *J. Fluid Mech.* **11** 97–120.

A.A. Townsend (1965) Self-preserving flow inside a turbulent boundary layer. *J. Fluid Mech.* **22** 773-797.

A.A. Townsend (1966) The flow in a turbulent boundary layer after a change in surface roughness. *J. Fluid Mech.* **26** 255–266.

A.A. Townsend (1976) *The structure of turbulent shear flow (2nd edition).* Cambridge University Press.

D.J. Tritton (1988) *Physical fluid dynamics (2nd edition).* Oxford.

W.S. Weng (1989) Turbulent air flow and fluxes over low hills. *Ph.D. thesis,* University of Cambridge.

P.S. Westbury & J.F. Morrison (1994) Bursts and low Reynolds number effects in turbulent boundary layers. *Oral presentation to the 5th European Turbulence Conference, Siena, July 1994.*

N.R. Wilson & R.H. Shaw (1977) A higher order closure model for canopy flow. *J. Appl. Meteorol.* **16** 1197–1205.

N. Wood & P.J. Mason (1993) The pressure force induced by neutral, turbulent flow over hills. *Quart. J. Roy. Met. Soc.* **119** 1233–1267.

T. Yamada (1982) A numerical model study of turbulent airflow in and above a forest canopy. *J. Meteorol. Soc. Jap.* **60** 439–454.